2015

Modelling of gas decompression process for CO2 transmission pipeline

Alhoush Mohmed Elshahomi
University of Wollongong

UNIVERSITY OF WOLLONGONG

Modelling of Gas Decompression Process for CO_2 Transmission Pipeline

A thesis submitted in fulfilment of the requirement for the award of the degree of

DOCTOR OF PHILOSOPHY

From

UNIVERSITY OF WOLLONGONG

By

Alhoush Mohmed Elshahomi

BSc. Eng. (Mechanical Engineering)
MSc. Eng. (Mechanical Engineering)

School of Mechanical, Material and Mechatronic Engineering,

University of Wollongong, Australia

2015

THESIS CERTIFICATION

I, Alhoush Mohmed Elshahomi, declare that this thesis, submitted in fulfilment of the requirements for the award of Doctor of Philosophy, at the School of Mechanical, Materials and Mechatronic Engineering, University of Wollongong, is wholly my own work unless otherwise referenced or acknowledged. The document has been not been submitted for qualification at any other academic institution.

Alhoush Mohmed Elshahomi

August 2015

TABLE OF CONTENTS

ABSTRACT

The decompression behaviour of CO_2 pipelines must be determined accurately in order to estimate the proper pipe toughness for fracture arrest. Anthropogenic CO_2 may contain impurities that can modify the fluid decompression characteristics quite significantly. In this thesis, a simulation study of the decompression behaviour of CO_2 based mixtures is presented. The current research is aimed at developing a new multi-dimensional gas decompression model using the Computational Fluid Dynamics (CFD) software ANSYS Fluent. The thermodynamic properties of CO_2 mixtures must be determined by using an accurate equation of state (EOS). A comparative study between some of widely used equations of state for gas pipelines is conducted. The wide range GERG-2008 EOS is accordingly adopted to provide the thermodynamic properties of CO_2 mixtures. Factors that affect the behaviour of decompression wave speed and the arrest toughness such as operating conditions, fluid compositions and the actual pipe deformation are investigated. The simulation results are validated against measured data obtained from 'shock tube' and 'full-scale burst' tests.

The thesis presents a novel technique to implement a real-gas EOS into ANSYS Fluent. The technique can be used to implement any future developed EOS. For the purpose of validation, the model is employed to simulate the decompression of single-phase flow and two-phase flow for some fluids in 2D geometry. The results prove the capability of the model in dealing with different gas mixtures and multi-phase flow. The influence of wall boundary on the behaviour of some properties and its impact on the local and average decompression wave speed is discussed. It was found that the local decompression wave speed will always differ from that obtained

from pressure-time traces especially at the later stages of the decompression. This difference could be neglected as far as fracture propagation control is concerned, but for longer pipelines and smaller diameters pipelines it may become influential.

A range of representative CO_2 mixtures was examined in terms of the changes in fluid properties from the initial conditions with time and distance, immediately after a sudden pipeline opening at one end. Phase changes that may occur within the fluid due to condensation of 'impurities' in the fluid were successfully predicted. It was found that increasing the initial operating temperature decreases the initial decompression wave speed, and lowering the initial temperature increases the initial decompression wave speed. Also, an increase in the initial temperature leads to a higher pressure plateau for temperatures below the critical temperature. However, a drop in the initial temperature does not always result in a lower pressure plateau level for CO_2 mixtures. Increasing the initial pressure was found to lower the pressure plateau, implying that using lower initial pressure leads to an increase in the required arrest toughness for pipelines transporting CO_2 mixtures. This suggests that it is safer and more efficient to use high initial pressure to transport CO_2 mixtures through pipelines.

Among the impurities investigated, the existence of hydrogen in the CO_2 stream had a maximum impact on the decompression, compared to the other impurities tested (e.g. N_2, O_2, CH_4, Ar, CO and H_2S). The effects of pipe diameter and pipe wall roughness on the decompression wave speed were investigated. The impact was found to be negligible for pipe diameters greater than 250 mm. The effects of initial temperature, initial pressure and pipe diameter on the arrest toughness were also studied. If the CO_2 mixture is initially a dense-phase fluid, the arrest toughness

increases with decreasing initial pressure, increasing initial temperature and increasing pipe diameter. This indicates that small diameter and high pressure are helpful to control the tendency for ductile fractures. In addition, if the CO_2 mixture has decompressed from an initial gas phase, the required arrest toughness is generally low.

Finally, three-dimensional CFD simulations of pressure distribution acting on the flaps behind the crack tip are presented. The geometry of the pipe opening was defined using a 3D pipe deformation model. The results show that the pressure distribution behind the crack tip is affected by the change in the cross-sectional area and mouth opening. The results show that CO_2 fluid pressure acting on the flaps remains high, between 55% and 63% of the initial operating pressure, for several cross-sections behind the crack tip; while for nitrogen, the pressure acting on the flaps is relatively low, ranging between 17% and 37% of the initial pressure for the same range of cross-sections. The effect of the shape of the ‘mouth’ opening on the fluid pressure acting on the flaps was also studied. It was found that the pressure decay in front of the crack tip is affected by the width of the mouth opening until the full-bore condition is reached. For a narrow opening, the pressure along the flaps was up to 75% of the operating pressure.

ACKNOWLEDGEMENTS

I would like to thank all the people who have made this thesis possible. First and foremost, I would like to express my deepest gratitude to my supervisors – Associate Professor Cheng Lu and Dr Guillaume Michal for their support, advice and guidance and especially for their empathy, enduring patience throughout this lengthy journey.

My sincere and special thanks go to Dr Xiong Liu and again Dr Guillaume Michal for writing the Matlab code and for their infinite support and valuable advice during the simulation work. Also, I would like to thank Dr Ajit Godbole for his suggestions during the research and in revising the manuscript.

This work was carried out at the School of Mechanical, Material and Mechatronics Engineering, Faculty of Engineering, University of Wollongong. I would like to thank all my colleagues and fellow PhD students for their precious advice and help during the research.

The funding and in-kind support from the Energy Pipeline Cooperative Research Centre (EPCRC), Australia, is gratefully acknowledged. Sincere thanks to the Libyan Ministry of Higher Education for providing the scholarship.

Finally, my deepest regards to my parents for their unconditional love and support, and to my wife, Wafa Elmabrouk, for her patience, support and understanding. I must also thank my lovely children, Mohamed and Rinad, all my sisters and brothers, and all my friends in Libya and Australia. Without their support and love I could not have completed this research. I dedicate this thesis to them.

LIST OF FIGURES

LIST OF TABLES

NOMENCLATURE

A	Pipe cross-sectional area
At	Area at the crack tip
c	Speed of sound
C_p	Specific heat at constant pressure
C_v	Specific heat at constant volume
D	Pipe diameter
E	Fluid energy
h	Enthalpy
J	Joule
M_w	Molecular weight
p	Pressure
R_0	Pipe radius
s	Entropy
t	Time
T	Temperature
u	Outflow velocity
P_i	Initial pressure
P_{critical}	Critical pressure
T_i	Initial temperature
T_{critical}	Critical temperature
Vc	Fracture velocity
w_{ave}	Average decompression wave speed
w_{exp}	Measured decompression wave speed
w_{local}	Local decompression wave speed
k_{eff}	Effective thermal conductivity
c_p	Specific heat
v_x	Axial velocity
v_y	Radial velocity
V	Volume
$\bar{x}$	Molar composition
Z	Compressibility factor

Greek symbols

α	Helmholtz free energy
ρ	Fluid density
μ	Dynamic viscosity
ε	Surface roughness
σ	Standard deviation of the distribution of the relative error
θ	Circumferential angle
τ_w	Wall shear stress
ψ	Pipe deformation factor
Γ_Φ	Diffusive coefficient
S_Φ	Source term

Abbreviations

AAD	Absolute Average Deviation
AGA	American Gas Association
AS	Australian Standard
AUSM	Advection Upstream Splitting Method
BTCM	Battelle Two-Curve Model
BWRS	Benedict-Webb-Rubin-Starling
CCS	Carbon Capture and Storage
CFD	Computational Fluid Dynamics
CO_2	Carbon dioxide
CVN	Charpy V-Notch
EOS	Equation of State
FDM	Finite Difference Method
FVM	Finite Volume Method
GERG	Groupe Européen de Recherches Gazières
GHG	Greenhouse Gases
ID	Internal Diameter
MOC	Method of Characteristics
ms	Millisecond
PR	Peng-Robinson
REFPROP	REFerence fluid PROPerties

SRK	Soave-Redlich-Kwong
2D	Two-dimensional
3D	Three-dimensional
UDF	User Defined Functions
VLE	Vapour-Liquid Equilibrium
w.r.t.	With respect to

Subscripts

ave	average
cal	calculated
eff	effective
exp	experimental
end	at the end
max	maximum value

PUBLICATIONS

Elshahomi, A., C. Lu, G. Michal, X. Liu, A. Godbole, and P. Venton, 2015, *Decompression wave speed in CO_2 mixtures: CFD modelling with the GERG-2008 equation of state.* Applied Energy. **140**: p. 20-32.

Elshahomi, A., C. Lu, G. Michal, X. Liu, A. Godbole, K.K. Botros, P. Venton, and P. Colvin, 2013, *Two-dimensional CFD Modelling of Gas Decompression Behaviour*, in *the 6th Pipeline Technology Conference*: 7–9 October, Ostend, Belgium.

Chapter 1 Introduction

1.1 Background

The burning of fossil fuels and biomass continues to be the main source of energy worldwide [1, 2]. Such processes emit significant quantities of greenhouse gases (GHG), particularly carbon dioxide (CO_2), which has been identified as the major contributor to global warming and climate change [3, 4]. Carbon Capture and Storage (CCS) technology was introduced as a key CO_2 abatement option to mitigate emissions of GHG by 50% by 2050, while populations and economies are expected to continue to grow globally [5]. This technology will necessitate substantial quantities of CO_2 to be conveyed over long distances from source to storage sites [6]. Transportation infrastructure such as tankers, ships and pipelines are possible options to carry CO_2; however, tankers, trucks, ships and rail options cost more than twice as much as pipelines [3, 7]. In addition, trucks, railways and ships can only carry relatively limited quantities of captured CO_2. Transporting huge quantities of CO_2, as implied by widespread implementation of CCS technologies, will necessitate a dedicated transmission and interstate pipeline network [8]. Worldwide, there has been great interest in constructing CO_2 pipelines to meet future requirements in terms of mitigating the effects of carbon emissions. Using ageing pipeline systems which were mainly designed for natural gas transport will not be a suitable option. This is due to the difference in operating conditions as well as the fact that these pipelines have been under repair and replacement continually.

In terms of operational and economic motivations, the best way to transport CO_2 or CO_2 mixtures via pipes will be in a liquid and/or supercritical state. A purely gaseous-phase transmission would necessitate significantly larger diameter pipelines for the same mass flow rate [9, 10]. Under these operational conditions, the

possibility of running fractures in the pipelines is a major concern. This makes arresting and/or preventing running fractures in pipelines very important for the integrity and safety of the operation of the pipelines [5, 9].

Technically, one of the best methods to control fracture propagation in gas pipelines involves the determination of the toughness required for fracture arrest [7]. Fracture propagation in gas pipelines is commonly analysed using the semi-empirical Battelle Two-Curve Model (BTCM) [11, 12], which aims to estimate the toughness required to arrest crack propagation. This method involves the superposition of two independently determined curves: the *fluid decompression wave speed* and the *fracture propagation speed* (the 'J curve'), each expressed as a function of pressure. According to this approach, to prevent a running ductile fracture in gas pipelines, the gas decompression wave velocity has to be greater than the fracture propagation velocity in the pipe wall [6, 7, 13-15]. Figure 1.1 shows a schematic representation of the BTCM. The shape of the fluid decompression wave speed curve depends on the phase of the fluid, as shown by the red and green curves in Figure 1.1. Curve 1, curve 2 and curve 3 represent the fracture speed curves for different toughness values.

Fracture speed curves 2 and 3 (for relatively low toughness) are shown to intersect the two-phase decompression wave speed curve. This implies that the fracture and the gas decompression wave move at the same speed. In this case, the gas pressure at the tip of the fracture no longer decreases, so that the fracture will continue to propagate. The boundary between arrest and propagation of a running fracture is represented by tangency between the gas decompression wave speed curve and the fracture speed curve (curve 1 with the two-phase decompression wave speed curve and curve 3 with the single-phase decompression wave speed curve). According to

the BTCM, the minimum toughness required to arrest the propagation of a fracture is the value of toughness corresponding to this tangency condition [11, 16].

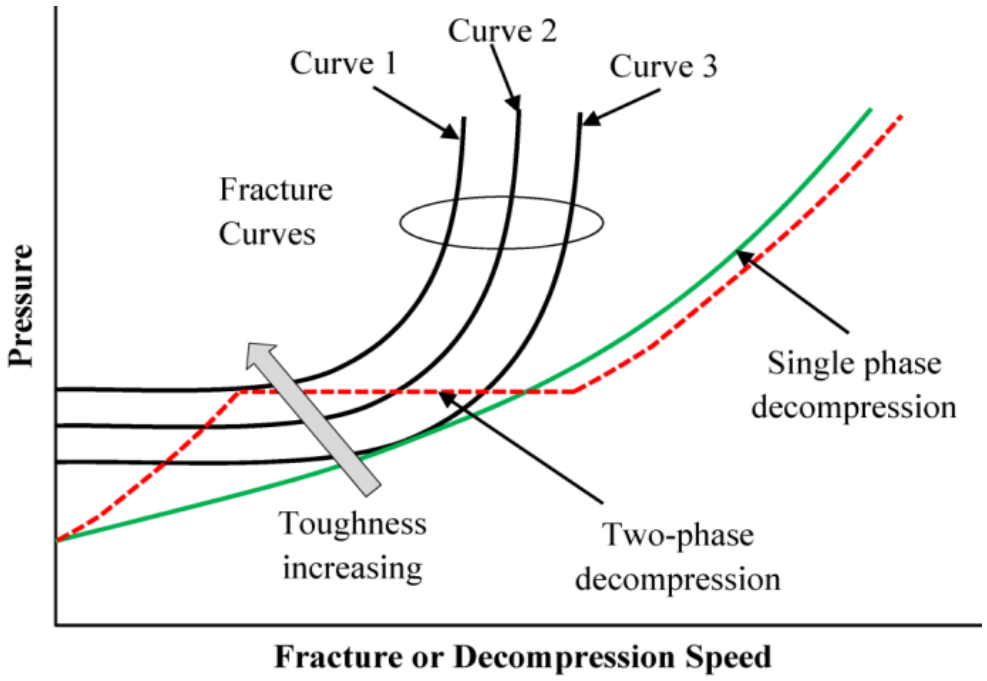

Figure 1.1: Schematic of the BTCM [16]

Sufficient knowledge of the gas decompression behaviour following pipeline rupture is therefore crucial for determining the arrest toughness. The decompression is influenced by the operating conditions, fluid composition and the fracture opening of the pipeline. Understanding of CO_2 decompression behaviour is difficult, because the gas captured from industrial emission sources is not 100% pure CO_2 but contains a range of impurities as a result of the treatment process [17]. These impurities have a significant influence on the decompression due to the change in the phase envelope [6].

The fluid decompression wave speed can be measured in carefully designed experiments involving full-bore rupture of a small diameter pipeline (shock tube tests), or in full-scale burst tests. Those tests are very time consuming and expensive.

A much less expensive is numerical modelling of the process using the Computational Fluid Dynamics (CFD) technique. This has become an increasingly important approach to investigate many industrial problems. This tool can deliver detailed information about fluid flow problems in cases where experimental tests are difficult to conduct. Numerical methods are also more flexible, as they enable testing the effects of several factors on the decompression behaviour before any physical test is carried out. Therefore, developing a CFD tool that can provide a comprehensive understanding of the decompression behaviour of CO_2 pipelines assumes great importance.

To simulate the decompression of CO_2 mixtures, it is important for the modelling tool to handle CCS mixtures efficiently. Without this ability, complex and possibly large simulations of fluid–pipe interactions, hydraulic transients and dispersion will not be possible. To precisely simulate the decompression of CO_2 mixtures, two important features are required for the CFD decompression model: handling transient flows in multi-dimensional geometries and, more importantly, an accurate equation of state (EOS) to calculate the thermo-physical properties of the fluid. Most of the currently available decompression models are simple one-dimensional models. The difference between them is mostly the EOS used.

1.2 Objectives of the Research

The main objective of this research is to comprehensively study the decompression behaviour of CO_2 pipelines. The research aims to investigate how the composition, operating conditions and pipe dimensions influence the decompression behaviour. It is expected that this research will provide greater understanding of the effect of some

impurities on the depressurisation of CO_2 pipelines. The major objectives of the work presented in this thesis are highlighted below:

- A comprehensive literature review on the decompression behaviour of gas pipelines, mainly focusing on CO_2 mixtures and the available methods used to numerically and experimentally determine the decompression wave speed in gas pipelines;
- A comparative study to assess the currently available thermodynamic models (EOS) to handle the thermodynamic properties for CCS mixtures, leading to selection of the most accurate EOS for the current research;
- Development of the first ever multi-dimensional CFD decompression model using the commercial CFD software 'ANSYS Fluent' to predict the decompression behaviour of CO_2 pipelines, taking into account the effects of factors such as pipe diameter, surface roughness, heat transfer and actual pipe deformation;
- Development of a novel technique to implement the real-gas EOS 'GERG-2008' into ANSYS Fluent using a newly developed User Defined Function (UDF) to be able to precisely predict the thermodynamic properties of the CO_2 mixtures. The method can be adapted to any EOS developed in the future;
- Validating the CFD model(s) by comparing the predicted results to those gained from experiments such as shock tube tests and full-scale burst tests;
- Investigating the impact of several factors on predicting the required toughness to arrest fracture propagation in pipelines carrying CO_2 mixtures.

1.3 Organisation of the Thesis

This thesis consists of a total of eight chapters (including this Introduction), followed by a list of References and the Appendices. A brief description of the contents of the remaining chapters is given below:

Chapter 2 presents a review of the relevant literature on the decompression behaviour of CO_2 mixtures and the determination of the decompression wave speed in gas pipelines. It examines the decompression behaviour in terms of fracture propagation control and selection of an appropriate EOS. Currently available methods to analyse the decompression behaviour and their limitations are also outlined. Chapter 2 ends with a summary wherein the gap in the current knowledge is identified.

Chapter 3 presents a comprehensive, comparative study of a total of nine equations of state. Their suitability in handling the thermodynamic properties of pure CO_2 and CO_2 mixtures is examined. The predicted results are compared to some of the currently available measured data. Chapter 3 ends with a summary which identifies the most accurate EOS to be used in the current research.

The first part of Chapter 4 introduces the CFD model with detailed information about the governing equations, boundary conditions and numerical solution methodology. The second part of Chapter 4 focuses on the implementation of a real-gas EOS into the CFD software, ANSYS Fluent. Two methods of implementing an EOS into the model are presented. Two equations of state named ‘PR’ and ‘GERG-2008’ are implemented into this model to calculate the thermodynamic properties. A verification process is performed to evaluate the sub-models adopted for the numerical solution and the accuracy of the models.

Chapter 5 presents a validation of the two-dimensional (2D) CFD model in predicting the decompression process in natural gas pipelines. The technique developed in Chapter 4 to implement the modern multi-component GERG-2008 EOS is tested here against a direct implementation of the PR EOS. The model is used to simulate the decompression of different mixtures involving both single-phase and two-phase flow. The model results are compared to the measured results obtained from three different shock tube tests.

In Chapter 6, the CFD model is used to predict the decompression characteristics of CO_2 mixtures. Validation of the model is carried out using results from two relatively recent shock tube tests using dense-phase CO_2 mixtures. Factors such as initial operating conditions, stream impurities, pipeline diameter and internal surface roughness, which can modify the decompression behaviour of CO_2 mixtures, are investigated. The predicted decompression wave curves are used to obtain the arrest toughness of the three typical mixtures produced by the CCS technology. The effects of initial temperature, initial pressure and pipe diameter on the arrest toughness are also discussed for the three main CCS routes.

Chapter 7 presents a 3D simulation of the pressure distribution behind the crack tip for a fractured CO_2 pipeline. This chapter starts with the implementation of a 3D pipe deformation model that simulates the actual pipe opening. The model is validated against measured data from a full-scale burst test. Unlike the 2D model used in Chapters 5 and 6, the effect of the actual geometry of the pipe opening on the decompression behaviour is taken into account. The fluid pressure acting on the flaps during the decompression process, which is the main responsible parameter that changes the driving force, is investigated. The effect of fracture opening on the

pressure distribution behind the crack tip is studied for CO_2 mixtures and compared to that obtained for pure nitrogen.

Chapter 8 summarises the conclusions of the current research, followed by recommendations for future research.

1.4 Summary

Chapter 1 highlights the significance of this research by outlining the relevant background information, the research goals and the outline of the thesis. In Chapter 2, a detailed overview of the current available literature related to the decompression from CO_2 pipelines is presented.

Chapter 2 Literature Review

2.1 Introduction

This chapter discusses and reviews the different factors that affect the determination of the decompression behaviour of carbon dioxide (CO_2) and presents the importance of its accurate determination in terms of pipeline integrity against fracture propagation. This is addressed in terms of the design considerations of CO_2 pipelines, fracture propagation and control, and reviewing the existing methods used to measure and predict gas decompression behaviour. It analyses the applicability of currently available thermodynamic 'equations of state' models to the most likely CO_2 mixtures; the potential of existing studies to predict the decompression behaviour of CO_2; and finally, a summary of the identified gaps in the current knowledge.

2.2 Importance of Design Considerations in CO_2 Transmission Pipelines

CO_2 capture and storage technology (CCS) can limit anthropogenic impact on climate [6]. Engineering a CCS solution requires a significant quantity of CO_2 to be transported from the industrial emitters to pressurised storage sites such as geological wells [6] using efficient pressurised pipelines capable of transporting large volumes of fluids over long distances. Enhanced Oil Recovery (EOR) applications are 30 years old, and the pipelines are considered suitable for anthropogenic CO_2 mixtures, however, with some technological development needed [3, 18, 19].

The CO_2 liquid-vapour phase boundary is largely within the typical temperature range of pipeline operations. With two-phase flow being generally unstable, single-phase flow [3] is the preferred transport method either in a gas form (~3.5 MPa) or in a liquid form at high pressure (>10 MPa) or in supercritical form. The latter has liquid-like density and gas-like viscosity [5, 6, 18, 20-30], making it the most economical method since it requires much smaller cross-sectional pipes for carrying

high mass flow rates [2][9]. However, supercritical phase means that the fluid must be pressurised to a value above the critical pressure [5]. Hence, CO_2 supercritical phase has the potential to damage the surrounding environment as it is deemed a volatile and explosive material [31].

Recent studies indicate that CCS-related pipelines will be constructed in more populated areas than current CO_2 pipelines, and reviews of the risks have been conducted [18, 19, 32]. Pipeline failure due to possible running fractures is a major concern, and therefore, arresting and/or preventing such an issue is essential to the integrity and safety of the pipeline's operation [5, 9]. CO_2 for CCS can carry a variety of impurities that alter the decompression characteristics of pure CO_2 and consequently change the properties of the steel required for fracture arrest. Impurities are only one aspect of decompression characteristics. A drop in temperature of the pipe; accompanying condensation of the fluid during the phase change; friction interactions between the fluid and the pipe wall [8]; and the physics of the fluid during a transient flow, are interrelated and will affect the decompression speed. A better understanding of CO_2 decompression behaviour due to these factors using full-scale burst tests, shock tube tests and/or numerical modelling has both safety and economic benefits.

2.3 Properties of Pure CO_2 and CO_2 Mixtures

Chemically, one molecule of CO_2 consists of one atom of carbon and two atoms of oxygen. In its natural state, CO_2 is a colourless, odourless, non-poisonous and non-flammable substance; but being approximately 50% heavier than air, CO_2 collects at low points of topography with potentially asphyxiating consequences. When the temperature of a plume of CO_2 is lower than the dew point temperature of the

atmosphere into which it is being released, it is difficult to distinguish CO_2 solids from condensed water within the cloud. A plume of CO_2 is invisible to the human eye when its temperature is higher than the dew point temperature of the atmosphere into which it is being released [6, 33]. The phase diagram of pure CO_2, in Figure 2.1 shows:

- The 'triple point' (TP) is at P=~0.5 MPa and T=~-56°C, while the 'critical point' (CP) is at P=~7.38 MPa and T=~31°C); compared to other gases the CP is located at relatively high pressure, which needs special attention in terms of pipelining applications;
- The triple and the critical points lie on the vapour-liquid equilibrium (VLE) line that divides the gaseous and liquid phases;
- Beyond CP, CO_2 exists in a supercritical phase and not in distinct gaseous or liquid phases. In this region, both $P>P_{critical}$ and $T>T_{critical}$ are satisfied;
- For $T>T_{critical}$, increases in pressure no longer produce liquids.
- For $T<T_{critical}$ and $P>P_{critical}$, CO_2 becomes liquid; as temperature decreases, the density of this liquid increases.

Figure 2.2 illustrates the phase envelope of CO_2 in a binary combination with 5% methane, which shows [24, 34]:

- Adding other components to the pure CO_2 varies the phase envelope;
- Impurities generally increase the size of the phase envelope, give rise to a phase mixture gas-liquid region, and increase $P_{critical}$;

- Some components such as H_2 and NO_2 generate a substantial increase in the size of the phase envelope, whereas others like N_2 and H_2S produce a much slighter increase.

The binary and ternary (i.e. CO_2 with two other impurities) mixtures that involve NO_2, raise the critical point both in pressure and temperature [34].

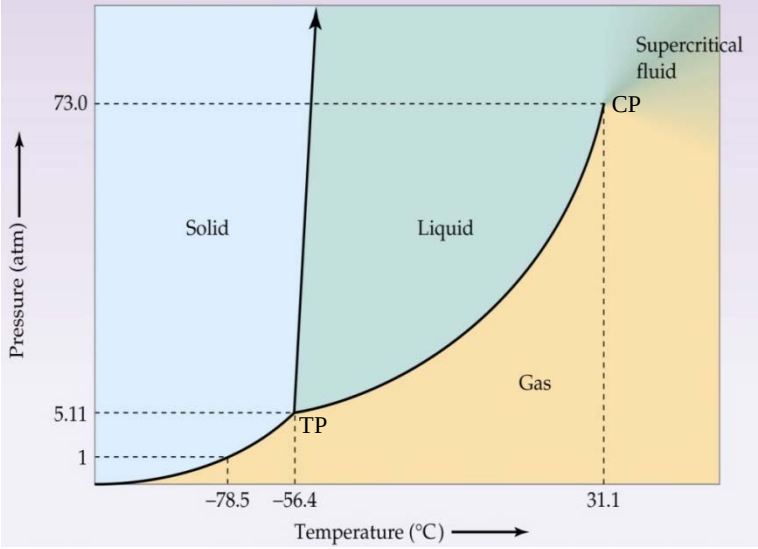

Figure 2.1: Phase diagram for pure CO_2 [35] showing Triple Point (TP) and Critical Point (CP)

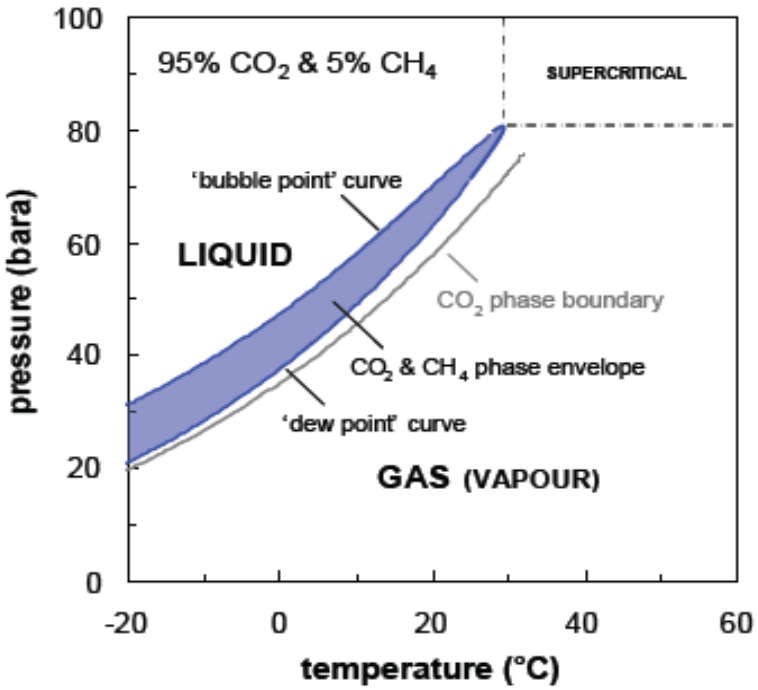

Figure 2.2: Phase diagram for 100% CO_2 and for CO_2 with 5% impurity [24]

2.4 Mechanisms of Fracture Propagation in Gas Pipelines

Running fractures are considered the most disastrous kind of gas pipeline failure. Fracture propagation is the rapid growth of a crack once it has initiated or penetrated the thickness of the pipeline wall [36]. A crack could run for several kilometres causing substantial environmental damage, loss of tens of millions of dollars and sometimes loss of life [16, 37]. Fracture initiation may occur in a gas pipe wall due to manufacturing defects (i.e. rolling defects, welding defects, defects during piping), design errors (pipe material incapable of withstanding the operating conditions such as pressure, temperature or corrosion resistance) and/or because of damage by a third party [38].

There are two fracture mechanisms for gas pipelines:

1) A *brittle fracture* is initiated at low stress and it travels at high velocity, which occurs when the steel changes from a ductile material to a brittle

material as the temperature decreases below a ductile-to-brittle transition temperature;

2) A *fast-tearing fracture* (running ductile fracture) occurs at temperatures where the steel is above the ductile-to-brittle transition temperature, but its toughness is insufficient to slow down the tearing velocity below the fluid decompression velocity.

Figure 2.3 illustrates brittle and ductile running fractures [39]

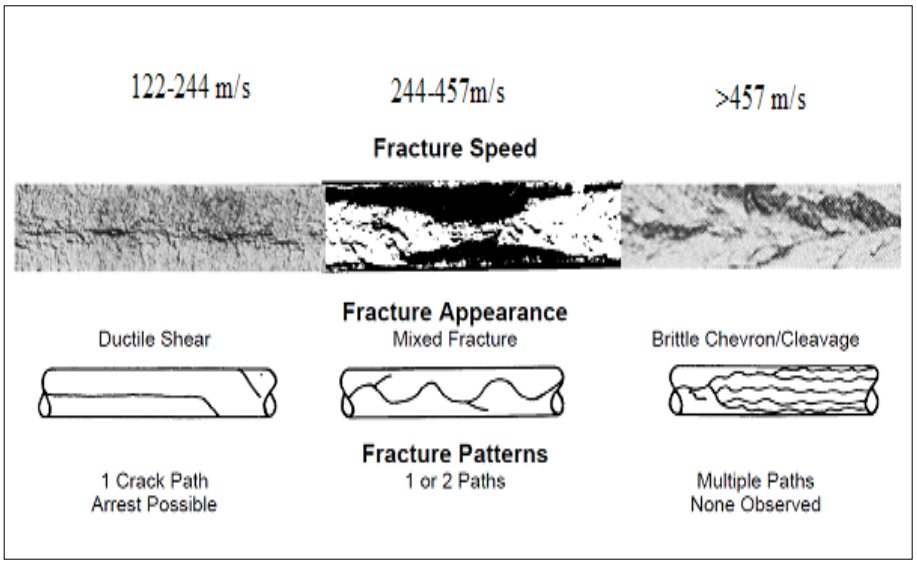

Figure 2.3: Fracture patterns [39]

2.5 Fracture Propagation Control

In pressurised gas pipelines, fracture propagation is a complex interaction of the structural behaviour of the cracking pipe and the fluid mechanics of the escaping gas [11, 16, 38, 40]. While methods for controlling brittle fractures are well established and applicable to all fluids, including CO_2 mixtures, methods for controlling ductile fractures must be further developed for CO_2 mixtures.

2.5.1 Mechanical Collar Devices (Crack Arrestors)

Figure 2.4 shows an example of a crack arrestor. Crack arrestors – either clock springs or a thicker-walled section of pipe – are typically installed to halt a propagating fracture within three pipe spools [5]. They are installed along the length of some CO_2 pipelines – for example, in the USA there are crack arrestors positioned every 3.2 km in remote areas and also within 100 m to 400 m of infrastructure such as road crossings [41] as line-pipe of sufficient toughness was not accessible when the pipelines were constructed [25]. However, fitting crack arrestors for transmission pipelines is too expensive [7].

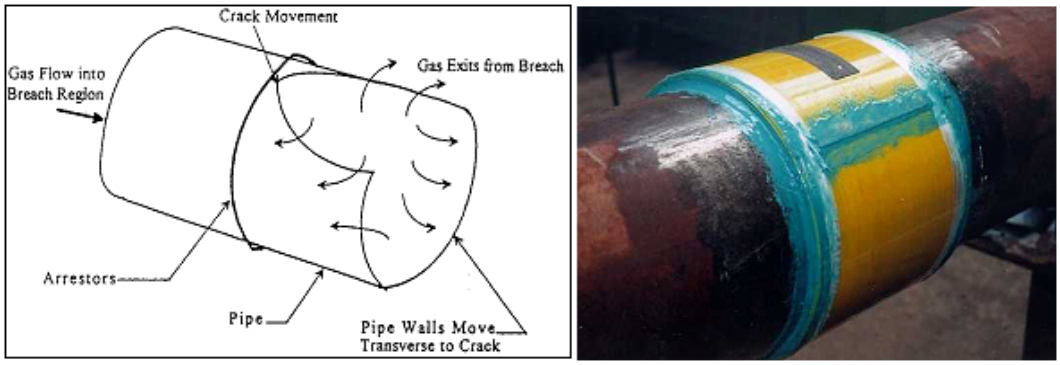

Figure 2.4: Crack arrestor in gas pipelines [34, 42]

2.5.2 Battelle Two-Curve Model (BTCM)

Ductile fracture propagation control of high pressure gas pipelines is commonly treated using the semi-empirical Battelle Two-Curve Model (BTCM) [11, 12]. BTCM assesses the required toughness to suppress crack propagation by superposing two independently determined curves: the *fluid decompression wave speed* and the *fracture propagation speed* (the 'J curve'), each expressed as a function of pressure (see Figure 1.1 in Chapter 1). In the BTCM, the fracture propagation speed V_f derived from analysis of plastic wave propagation is expressed as [15]:

$$V_f = C\frac{\bar{\sigma}}{\sqrt{C_V}}\left[\frac{P}{P_a} - 1\right]^a \tag{2.1}$$

$$R = \frac{C_V}{A_C} \tag{2.2}$$

$$P_a = \frac{2\bar{\sigma}t}{3.33\pi r} cos^{-1}\left(e^{-\left(\frac{\pi BRE}{24\sqrt{rt\bar{\sigma}^2}}\right)}\right) \tag{2.3}$$

where V_f is the fracture speed; $\bar{\sigma}$ is the flow stress; P is the operating pressure; P_a is the arrest pressure; R is the specific Charpy V-notch (CVN) toughness; C_V is the CVN toughness (energy); A is the cross-sectional area of the CVN specimen; r is the pipe diameter; t is the pipe wall thickness; E is the Young's modulus; and C and α are two constants.

The decompression of the fluid, generally considered isentropic, takes the form of a decompression wave that initiates at the point of fracture. If c is the speed of sound behind the decompression wave and u is the average outflow speed behind the decompression wave, then:

$$w = c - u \tag{2.4}$$

where w is the speed of the front of the wave, which moves in both directions away from the crack. c is directly related to the properties and local conditions of the fluid. While ideal gases allow for an analytical estimation of the decompression wave speed, a more complex fluid necessitates the use of an elaborate EOS to estimate the speed of sound along the isentropic decompression. The thermodynamic state of the fluid characterised by temperature, densities and speed of sound is calculated from a step-change in the pressure. The outflow velocity u is obtained through numerical integration of the following equation:

$$u = \sum_{\rho} (\Delta u)_s \tag{2.5}$$

where

$$(\Delta u)_s = C \frac{(\Delta \rho)_s}{\rho} \tag{2.6}$$

ρ is the density, and the subscript s signifies a value on the isentrope. The initial state of the fluid (T, P) gives the starting point of the isentropic decompression, and the characteristics of the decompression wave speed as a function of the pressure is obtained.

2.6 Gas Decompression Behaviour

The decompression behaviour of a pressurised fluid is greatly affected by whether the fluid is an ideal gas such as methane or air, a single-phase gas that undergoes two-phase decompression such as rich natural gas with heavy hydrocarbons, or a sub-cooled fluid undergoing two-phase decompression such as liquid CO_2 [43]. Several decompression modes are witnessed for CO_2 between -10°C and 40°C with the presence of the liquid-vapour phase boundary in the region of operating pressures. The CP and the phase boundary are vital for studying CO_2 decompression behaviour [3]. As the pressure in a pipeline falls to the phase boundary line (saturation pressure), the decompression wave velocity w rapidly decreases, as schematically shown in Figure 2.5. For liquid CO_2, w may be substantially higher than that of natural gas but drops considerably as vapour begins to form. In this regard, running ductile fractures are a greater issue for pipelines carrying CO_2 [6, 7].

Analysis and comparison of the results from full-scale burst tests, shock tube tests and numerical modelling have been instrumental in the past to advance natural gas pipeline techniques and safety, and are necessary for the development of CO_2

pipelines for the application of CCS, particularly to control ductile fracture propagation [13].

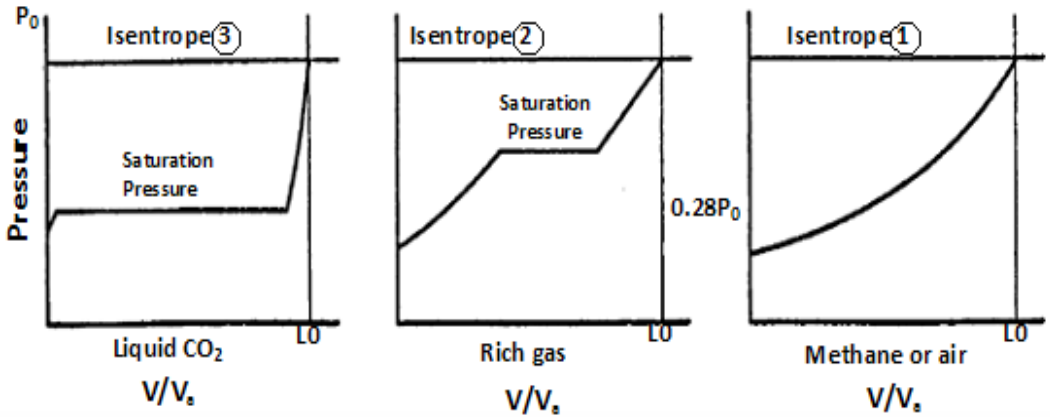

Figure 2.5: Schematic of gas decompression behaviour for ductile fracture arrest considerations [43]

2.6.1 Measurement of the Gas Decompression Wave Speed

The shock tube test is designed to determine the velocity of the decompression wave once rupture is initiated at one end of the tube. This test cannot establish fracture arrest criteria. On the other hand, the full-scale burst test is designed to calculate the decompression velocity away from a ruptured pipe. Pipes of increasing toughness are used to identify the toughness necessary to suppress the fracture. Figure 2.6 shows an example of full-scale burst tests (JGA experiment) conducted on a steel pipeline grade X80 [43] using pressurised N_2 with different levels of sand backfill (depth and moisture) to enhance the performance of BTCM in predicting the minimum required pipe toughness for fracture propagation arrest. Full-scale burst tests [43-56] are very time consuming and expensive, requiring several millions of dollars.

Figure 2.6: JGA full-scale burst test on X80 pipeline

A great deal of insight into decompression wave speed can be gained from shock tube testing at a fraction of the cost of a full-scale burst test. Shock tube sites are composed of a compression station capable of setting the different pressures and temperatures for a variety of fluids and mixtures, allowing observation of different decompression paths. The sudden decompression is triggered by a ruptured disc calibrated to burst at a precise pressure. Figure 2.7 shows an example of a Fike ruptured disc [57].

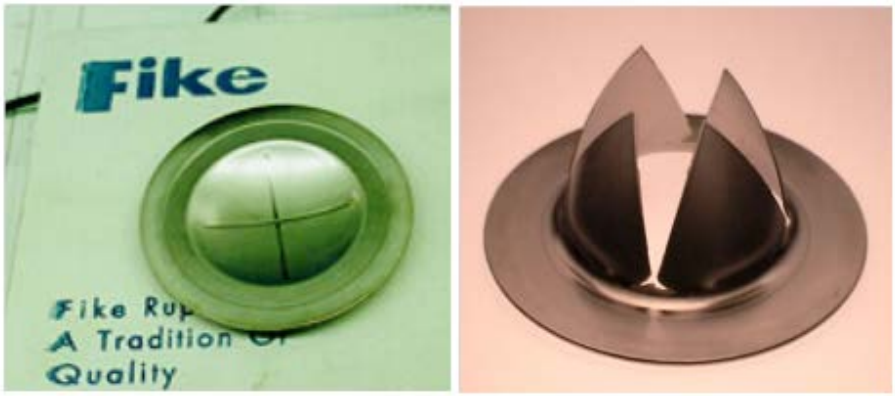

Figure 2.7: Fike ruptured disc before and after rupture [57]

This consumable disc is placed in a holder at one end of the shock tube. On rupturing, the decompression wave develops towards the other end of the tube with the propagation monitored over time by a series of strategically placed pressure transducers along the pipe at known intervals, which measure pressure-time traces.

The arrival time of the decompression wave at the location of each pressure transducer is measured for several pressures lower than the initial pressure. A simple linear relationship between distance and arrival time is assumed to compute the corresponding decompression wave velocity *w*, which is plotted as a function of static pressure *P* (see Figure 1.1).

An example of such a decompression tube was presented by Botros et al. [54, 58-60] using NPS 2 tubes, as schematically shown in Figure 2.8. Phillips and Robinson reported the measured decompression wave speed using NPS 6 shock tubes [61]; and Cosham et al. [55] studied the decompression behaviour of CO_2 and CO_2-rich mixtures also using shock tube testing.

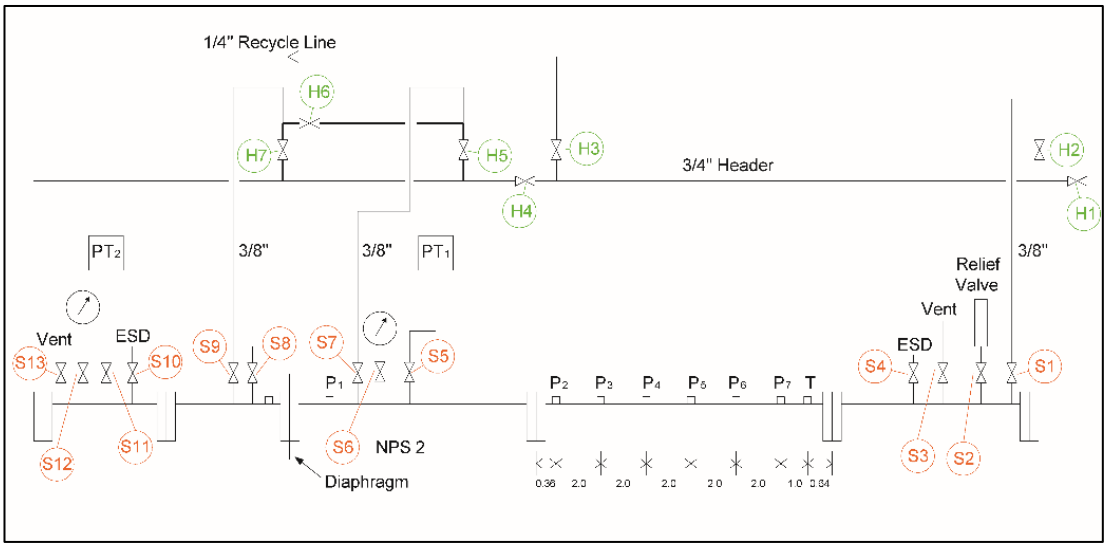

Figure 2.8: Schematic representation of the shock tube test facility [57]

The main section of the shock tube of Botros et al. [54, 58-60] was 42 m long with a maximum pressure of 30 MPa. The pressure chain comprised of eight pressure transducers; these have an accuracy of +/-40 kPa [60]. The shock tube was evacuated and enriched with gas as which was allowed to flow freely up to line pressure. It was subsequently compressed to a pressure slightly below the disc rupture pressure,

followed by recycling at the high pressure end to ensure good mixing. The gas was then sampled and the disc ruptured by slow pressurisation with base-gas from the main line followed by isolation.

Figure 2.9 shows the typical output from the pressure transducers obtained from a shock tube test [62]. The pressure drop starts from the transducer closest to the rupture disc and then successively reaches the following transducers. For a given isobar, the times at different pressure transducers were noted and the decompression wave speed was estimated at various pressures using the regression between w and the location of transducers. For a given point, the characteristics of the decompression wave speed against the pressure is plotted, as depicted in Figure 2.10 [62].

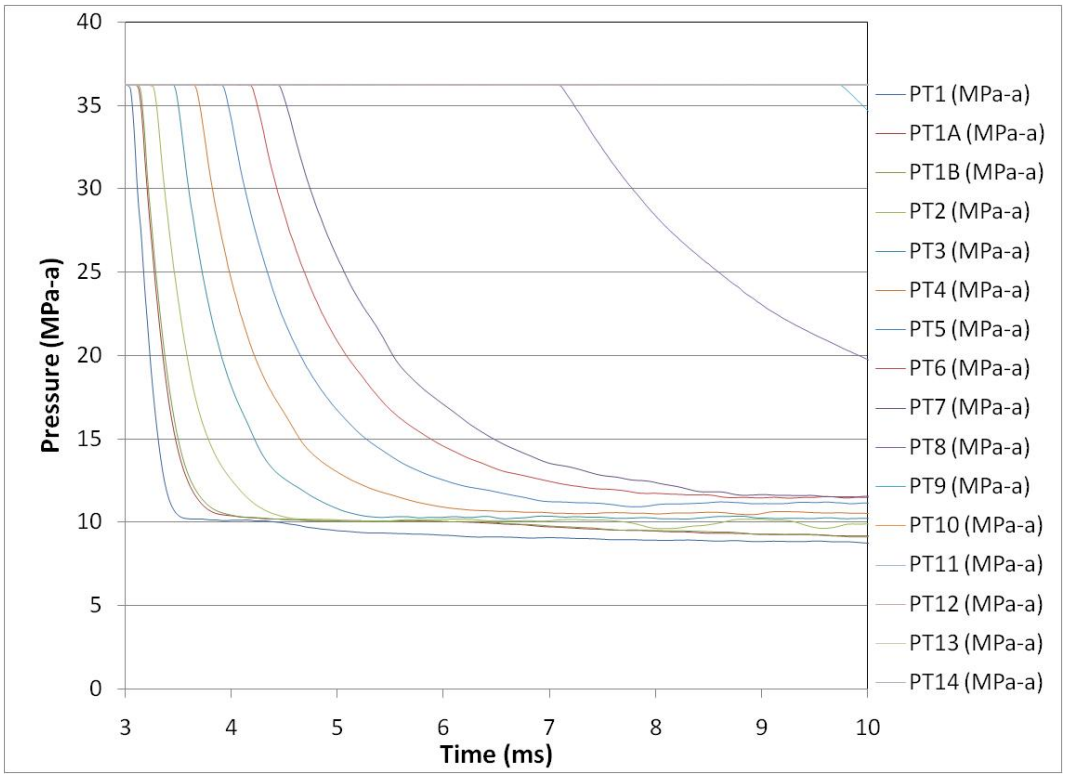

Figure 2.9: Example of typical pressure-time traces obtained from a shock tube test [62]

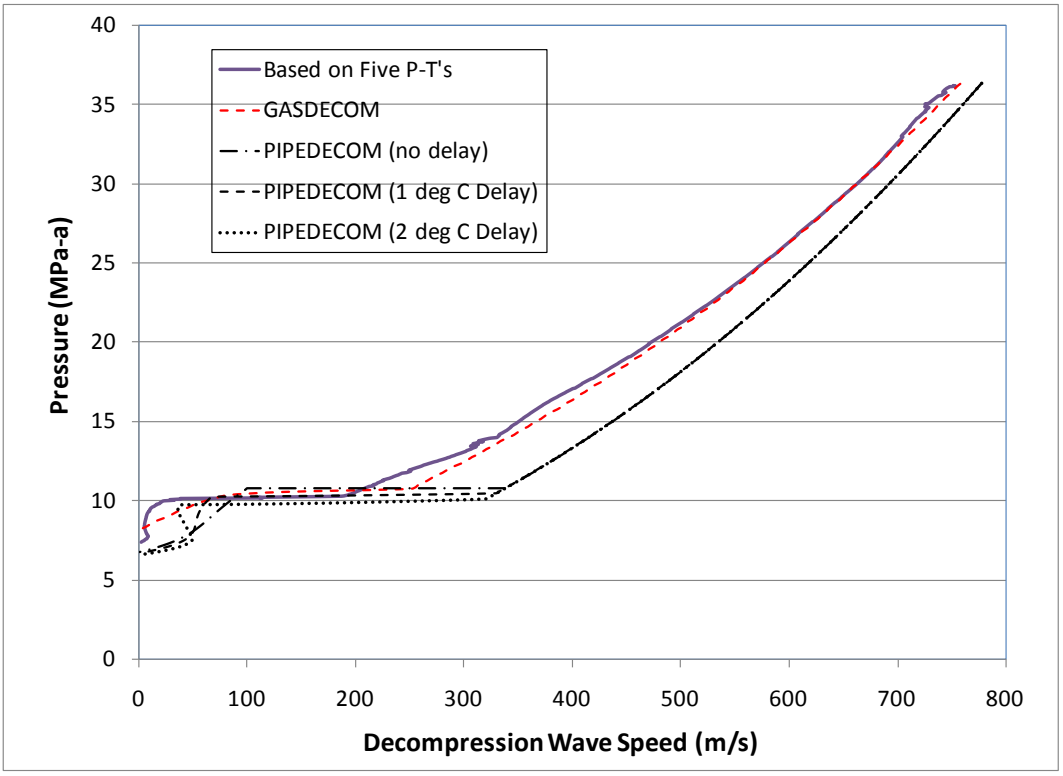

Figure 2.10: Measured decompression wave speed [62]

2.6.2 Modelling of the Gas Decompression Wave Speed

Experiments such as shock tube and full-scale burst tests are limited in the amount of parameters that are possible to investigate and in the quantity of data that can be acquired. Modelling offers the opportunity to probe a wider parameter space quickly and inexpensively, and provides greater insights into the interaction between various parameters.

Of the several numerical models proposed to predict the decompression wave speed, mainly for natural gas pipelines, only those with built-in EOS valid for CO_2 mixtures can be useful. One such model is GASDECOM [63], which uses an analytical expression for the propagation of an infinitesimal decompression front to establish the speed of decompression wave w. In GASDECOM, w can be calculated by Equations 2.4–2.6. GASDECOM uses the Benedict-Webb-Rubin-Starling (BWRS)

EOS [64] with adjusted constants to estimate the thermodynamic properties of the gas (speed of sound and density) during isentropic decompression.

A number of assumptions are implicit within GASDECOM:

- One-dimensional inviscid flow;
- Frictionless and isentropic;
- Pipe rupture is immediate;
- Gas is considered stationary initially (u_i=*0 m/s*);
- Condensation occurs when the decompression trajectory intersects the two-phase envelope;
- Equilibrium prevails at condensation;
- Homogeneous fluid for mixtures (gas and liquid phases flow at the same velocity).

The treatment of mixtures by GASDECOM where the percentage of CO_2 is high, suffers from numerical instabilities, which are due to software coding limitations and are not fundamental. Hence, GASDECOM cannot be used for mixtures containing hydrogen, oxygen and argon – the components regularly added to CO_2 in CCS-related operations – since these components were not originally included in the BWRS EOS [15, 65] development.

Several other models have followed the approach of GASDECOM [66]. The main differences between these models are outlined below.

- The Advantica model [67] uses the cubic London Research Station (LRS) EOS [68], which is similar to the Soave-Redlich-Kwong (SRK) EOS [69]. It employs the Peng-Robinson (PR) equation [70] to precisely forecast the

initial speed of sound and uses a constant multiplication factor to match that value at the initial conditions;

- Groves et al.'s PipeDecom model adopted the SRK EOS [71] to determine the thermodynamic properties and allows for the effects of non-equilibrium thermodynamics [49] to be represented in the calculation. However, delayed liquid droplet formation could be included in the calculation of w only by manually changing the nucleation temperature [61];
- DECAY developed by Jones and Gough [72] followed the GASDECOM approach in modelling single-phase decompression in a pipe undergoing fracture propagation. The two-phase flow was modelled by solving Navier-Stokes equations with the properties calculated using the PR EOS in DECAY;
- Makino et al.'s [73] model based on the theoretical approach of British Gas, a la the DECAY model but with BWRS EOS [64], simulated the two-phase decompression behaviour of natural gas pipelines;

The DECOMWAVE model [74] predicts the decompression wave velocity of poor and rich gases with assumptions similar to GASDECOM. The model uses four equations of state (PR [70], SRK [71], BWRS-PR and BWRS-SRK) to calculate the required thermodynamic properties. The model calculates the speed of sound based on the fluid state. For the gas phase, the speed of sound is obtained using:

$$c = \left(\frac{\partial P}{\partial \rho_g}\right)_s^{1/2} \tag{2.7}$$

For the gas-liquid phase, a united speed of sound model developed by Xu and Gong [75] is used:

$$c = \pm \left\{ \frac{\left(\frac{C_{vm}\rho_L}{R_G R_L^2} + \frac{\rho_G}{R_G} + \frac{\rho_L}{R_L}\right)}{\left(\frac{\rho_L}{R_L c_G^2} + \frac{\rho_G}{R_G c_L^2}\right)\left[1 + C_{vm}\left(\frac{R_G}{R_L} + \frac{\rho_L}{\rho_G}\right)\right]} \right\}^{1/2} \quad (2.8)$$

Equation 2.7 was demonstrated to be functional in calculating the speed of sound in the two-phase region, since a homogeneous mixture is assumed;

- DECOM [55] was developed to predict the decompression wave speed in CO_2 mixtures, and is also based on assumptions identical to those considered in GASDECOM. The only difference is the use of the NIST Standard Reference Database 23 (REFPROP version 9.0) [76], along with the built-in Span and Wagner EOS [77] for pure CO_2 and the GERG-2004 EOS [78] for multi-component CO_2 mixtures.

Some complex decompression accounting for non-isentropic effects using the Computational Fluid Dynamics (CFD) technique (Picard and Bishnoi [79, 80], PipeTech [81, 82] and CFD-DECOM [83]) are based entirely on assumptions of one-dimensional homogeneous-equilibrium fluid flow. They include heat transfer, friction, and pipe diameter, which are particularly relevant for smaller diameter and longer pipelines where friction could lead to a range of complex effects on local flow conditions, temperature, and pressure within the pipeline [58, 82, 84-86].

CFD involves discretising the governing partial differential equations of fluid flow, namely the Navier-Stokes and constitutive equations. The Finite Difference Method (FDM) [87, 88], the Method Of Characteristics (MOC) [89], and the Finite Volume Method (FVM) [83] are examples of discretisation methods. The MOC solves the fluid flow conservation equations by following the Mach-line characteristics inside the pipe. It is claimed that numerical diffusion related to the FDM approximation of partial derivatives is reduced by this method [90, 91], but the MOC needs much

longer computation runtimes and cannot predict non-equilibrium or heterogeneous flows [37, 83], while the FVM is better at dealing with multi-dimensional flows. In the existing CFD models, the cubic Peng-Robinson (PR) EOS [70] is often used due to its relatively simple mathematical form compared to other more complex (but more accurate) equations of state, such as AGA-8 [92], BWRS [64] and GERG [78].

2.7 Equations of State Used in the Gas Pipelines Industry

Many types of equations of state are used in the gas pipelines industry. The use of a certain EOS is based on the fluid status where the calculation of the thermodynamic properties is required. Modern work on the development of equations of state to describe the pressure-volume-temperature (PVT) behaviour of real gases can be traced to pre-industrialised Europe [93]. The best known and simplest EOS is the ideal-gas equation, written mathematically as:

$$P = \frac{nRT}{V} \tag{2.9}$$

where P is the pressure; T is the absolute temperature; n is the number of moles of material; V is the molar specific volume; and R is the universal gas constant.

An ideal gas is one [94] whose constituent molecules are mutually inert (i.e. no forces between them) and have a volume that is negligible in comparison to the volume that the gas occupies. The ideal-gas EOS that is a good approximation for gases operating at low pressures and moderate temperatures, becomes increasingly inaccurate outside that region at higher pressures and lower temperatures, and fails to predict condensation from a gas to a liquid [95]. Hence, other more accurate equations of state have been developed for gases and liquids. Most of them reflect

empirical or semi-empirical relationships, which were firstly based on the ideal-gas law and adjusted to conform to experimental data [96].

Two major groups of EOS will be reviewed in the following sections:

(1) Cubic equations of state;

(2) Virial equations of state.

Special attention is given to comparison of the accuracy of different equations of state for pure CO_2 and CO_2 mixtures.

2.7.1 Cubic Equations of State

2.7.1.1 The van der Waals EOS

Using a hard sphere model of molecules, van der Waals [97, 98] improved the ideal-gas EOS by eliminating the two assumptions made in the ideal-gas EOS and added 'correction' terms $\frac{a}{V^2}$ (impact of molecular attraction forces especially high pressures) and b (effect of molecular volume) to variables pressure (P) and volume, (V) respectively, in the ideal-gas equation for one mole of the gas. [70, 95]. The van der Waals EOS is expressed as:

$$\left(P + \frac{a}{V^2}\right)(V - b) = RT \tag{2.10}$$

or

$$Z = \frac{V}{V - b} - \frac{a}{RTV} \tag{2.11}$$

where Z is the compressibility factor ($Z=PV/RT$). The parameters a and b can be obtained from the critical properties of the fluid:

$$a = \frac{27R^2T_c^2}{64P_c^2}, \quad b = \frac{RT_c}{8P_c} \tag{2.12}$$

where T_c and P_c are the critical temperature and critical pressure, respectively.

Equation (2.10) can be rewritten in a cubic form in terms of the molar specific volume V as follows:

$$V^3 - \left(b + \frac{RT}{P}\right)V^2 + \left(\frac{a}{P}\right)V - \left(\frac{ab}{P}\right) = 0 \tag{2.13}$$

Equation 2.13 yields one real root for V in the single-phase region (gas-phase region or liquid-phase region) and three real roots in the two-phase region [97]. In the latter case, the largest root value corresponds to the volume of the gas phase, while the smallest positive root corresponds to that of the liquid phase.

The most significant feature of the van der Waals EOS is its ability to predict the existence of the critical point and to simultaneously consider the gas and liquid phases, phase equilibrium below the critical point. The accuracy of the van der Waals EOS is improved by modifications to the attractive term or/and the repulsive term.

2.7.1.2 The Redlich-Kwong (RK) EOS

The Redlich-Kwong equation [69] improved the original van der Waals equation but retained the hard-sphere terminology with the addition of a temperature-dependent attractive term.

$$P = \frac{RT}{V-b} - \frac{a}{\sqrt{T}V(V+b)} \tag{2.14}$$

where the two coefficients a and b are defined in terms of critical pressure P_c and critical temperature T_c and are calculated using:

$$a = \frac{0.42747 R^2 T_c^{2.5}}{P_c}, \quad b = 0.08664 \frac{RT_c}{P_c} \tag{2.15}$$

The RK EOS performs relatively well for simple fluids such as noble gases Argon (Ar), Krypton (Kr) and Xenon (Xe) for which the acentric factor is equal to zero, but it does not perform well for complex fluids with non-zero acentric factors. The acentric factor (ω) is defined as:

$$\omega = -log_{10}(p_r^{sat}) - 1 \quad at\ T_r = 0.7 \tag{2.16}$$

where $T_r = \frac{T}{T_c}$ is the reduced temperature and $p_r = P/P_c$ is the reduced saturation pressure of gas.

2.7.1.3 The Soave-Redlich-Kwong (SRK) EOS

Beyond ideal-gas van der Waals and RK models, the EOS models become less theoretical and more empirical. Some like Giorgio Soave [71] produced incremental improvements. Soave replaced the term $a/\sqrt{T}$ in Equation 2.14 with a more generalised temperature-dependent term, as denoted by $\alpha(T)$ [71], to give:

$$P = \frac{RT}{V - b} - \frac{a\alpha(T)}{V(V + b)} \tag{2.17}$$

where

$$\alpha(T) = \left(1 + (0.48508 + 1.55171\omega - 0.17613\omega^2)\left(1 - \left(\frac{T}{T_c}\right)^{0.5}\right)\right)^2 \tag{2.18}$$

and $$a = \frac{0.42747 R^2 T_c^{2.5}}{P_c}, \qquad b = \frac{0.08664 RT_c}{P_c} \tag{2.19}$$

By letting:

$$A = \frac{aP}{R^2T^2}, \qquad B = \frac{bP}{RT}, \qquad and\ Z = \frac{PV}{RT} \tag{2.20}$$

the Soave-Redlich-Kwong (SRK) EOS is written in a cubic form as:

$$Z^3 - Z^2 + Z(A - B - B^2) - AB = 0 \tag{2.21}$$

Soave's modification fitted the experimental curve better than RK and was able to predict the phase behaviour of some mixtures (excluding CO_2 and hydrogen sulphide) in the critical region [98]. The calculated vapour densities were generally acceptable whereas liquid densities were not.

2.7.1.4 The Peng-Robinson (PR) EOS

Peng and Robinson [70] enhanced Soave's equation by reproducing the $\alpha(T,\omega)$ function and by modifying the volume-dependency of the attractive term. They achieved more accurate results for liquid volumes and good representations of vapour-liquid equilibrium (VLE) for many mixtures [97]. The PR EOS is written as:

$$P = \frac{RT}{V - b} - \frac{a\alpha(T,\omega)}{V(V + b) + b(V - b)} \tag{2.22}$$

where

$$\alpha(T,\omega) = \left(1 + (0.37464 + 1.54226\omega - 0.26992\omega^2)\left(1 - \left(\frac{T}{T_c}\right)^{0.5}\right)\right)^2 \tag{2.23}$$

and

$$a = \frac{0.45724R^2T_c^{2.5}}{P_c}, \qquad b = \frac{0.07780RT_c}{P_c} \tag{2.24}$$

The PR and SRK equations of state require only the critical properties and acentric factor to represent the relationship among temperature, pressure and phase compositions in binary and multi-component systems, and are thus used widely in the gas industry [98].

2.7.1.5 Mixing Rules

Strictly speaking, all of the aforementioned equations of state can only be used for pure components. For mixtures, mixing rules must be used. Many mixing rules have been proposed. For example, Van der Waals' mixing rule is:

$$a = \sum_i \sum_j x_i x_j a_{ij}\,, \qquad b = \sum_i \sum_j x_i x_j b_{ij} \tag{2.25}$$

where x_i and x_j are the molar fractions of components *i* and *j*, respectively; a_{ii} and b_{ii} are the constants of the equation for pure component *i*; and cross parameters a_{ij} and b_{ij} ($i \neq j$) are determined by an appropriate combining rule with or without binary parameters [98]. A common approach is to include composition-dependent binary interaction parameters in calculating the parameter *a* in the van der Waals mixing rule and leave the *b* parameter rule unchanged. Margules, and later Van Laar, proposed mixing models by relating the Excess-Gibbs-Free-Energy to the activity coefficients [99]. Some examples of mixing models are summarised in Table 2.1.

Table 2.1: Composition-dependent mixing rules [98]

Reference	a_{ij} Term
Adachi and Sugle (1986)	$(a_{ii}a_{jj})^{1/2}\left[1 - I_{ij} + m_{ij}\left(x_i - x_j\right)\right]$
Panagiotopoulos and Reid (1986)	$(a_{ii}a_{jj})^{1/2}\left[1 - k_{ij} + \left(k_{ij} - k_{ji}\right)x_i\right]$
Stryjek and Vera (1986) (Margules-type)	$(a_{ii}a_{jj})^{1/2}\left[1 - x_i k_{ij} - x_j k_{ji}\right]$
Stryjek and Vera (1986) (Van Laar-type)	$(a_{ii}a_{jj})^{1/2}\left[1 - \dfrac{k_{ij}k_{ji}}{x_i k_{ij} + x_j k_{ji}}\right]$
Schwartzentruber et al. (1987)	$(a_{ii}a_{jj})^{1/2}\left[1 - k_{ij} - I_{ij}\dfrac{m_{ij}x_i - m_{ji}x_j}{m_{ij}x_i + m_{ji}x_j}(x_i + x_j)\right]$ $k_{ji} = k_{ij}; I_{ji} = -I_{ij}; m_{ji} = 1 - m_{ij}; k_{11} = I_{11} = 0$
Sandoval et al. (1989)	$(a_{ii}a_{jj})^{1/2}\left[1 - (x_i k_{ij} + x_j k_{ji}) - 0.5\left(k_{ij} + k_{ji}\right)(1 - x_i - x_j)\right]$

2.7.2 Virial Equations of State

Virial equations of state is another category which are non-analytic equations applicable over much broader ranges of pressure and temperature than the analytic equations [95], but require many parameters that require fitting to large amounts of data of several properties. The virial EOS is commonly expressed by a Taylor-Series-like expansion:

$$= \frac{PV}{RT} = 1 + \frac{B(T)}{V} + \frac{C(T)}{V^2} + \cdots \tag{2.26}$$

where $B(T)$ and $C(T)$ are the temperature-dependent functions expanded as power series in temperature T.

2.7.2.1 The Benedict-Webb-Rubin (BWR) EOS

The Benedict-Webb-Rubin (BWR) equation [100] is a non-analytical multi-parameter EOS which was developed for the isothermal variation with density of light and pure hydrocarbons in the gaseous or liquid state [100].

$$Z = 1 + \left(\frac{B_0 RT - A_0 - C_0/T^2}{RTV}\right) + \left(\frac{bRT - a}{RTV^2}\right) + \frac{\alpha a}{RTV^3} + \left(\frac{c}{RT^3V^2}\right)\left(1 + \frac{\gamma}{V^2}\right)\exp\left(-\frac{\gamma}{V^2}\right) \tag{2.27}$$

where A_0, B_0, C_0, a, b, c, α, γ are eight adjustable parameters. The BWR EOS could treat supercritical components and was able to work limitedly in the critical area, but introduced huge errors in predicting pressure-volume-temperature (P-V-T) behaviour of fluids at the critical region and at density more than 1.5 times the critical. Additionally, the representation of the caloric properties (e.g. enthalpy and heat capacity) was not satisfactory [101].

2.7.2.2 The Benedict-Webb-Rubin-Starling (BWRS) EOS

Starling [71] retained the density dependence of BWR but modified the temperature dependence of the coefficient in the BWR EOS by adding three constants and a binary interaction parameter, thus making an 11 parametric, non-cubic EOS applicable for 15 substances (light gases and hydrocarbons) [102, 103]. The form of the equation is:

$$Z = 1 + \left(\frac{B_0 RT - A_0 - \frac{C_0}{T^2} + \frac{D_0}{T^3} + \frac{E_0}{T^4}}{RTV}\right) + \left(\frac{bRT - a - \frac{d}{T}}{RTV^2}\right) + \frac{\alpha\left(a + \frac{d}{T}\right)}{RTV^3} + \left(\frac{c}{RT^3V^2}\right)\left(1 + \frac{\gamma}{V^2}\right)\exp\left(-\frac{\gamma}{V^2}\right) \quad (2.28)$$

where A_0, B_0, C_0, D_0, E_0, a, b, c, d, α, γ are 11 adjustable parameters.

Starling conducted multi-property regression analysis to determine the 11 parameters for each of the 15 substances (light gases and hydrocarbons) [71]. The binary interaction parameters were determined from experimental data on liquid-vapour equilibrium. Lin and Hopke [103] and Hopke and Lin [65] conducted a simultaneous multi-property regression analysis on pure-component, binary mixture and multi-component mixture data to develop an optimised set of pure-component parameters and binary interaction parameters for the BWRS EOS. The substances considered were methane, ethane, propane, iso-butane, n-butane, iso-pentane, n-pentane, nitrogen and CO_2. A generalised correlation to determine the parameters for heavy hydrocarbon fractions (hexane and above) was also developed [65] .

Probably due to its ability to cover both liquids and gases and the availability of coefficients and mixing rules for many hydrocarbons in one place, BWRS is the most

widely used EOS for simulation of the pipeline processes [15] along with GASDECOM for gas decompression.

2.7.2.3 The AGA8-DC92 EOS

Starling and Savidge introduced a new semi-empirical EOS named AGA8-DC92 [92] to represent the thermodynamic properties of natural gases (for the American Gas Association), explicit in compressibility factor (ISO 12213 [25]), later expanded to compute other important physical properties such as the speed of sound and related thermo-physical quantities [92, 93]. AGA8-DC92 is expressed by:

$$Z = 1 + \delta\frac{B}{K^3} - \delta\sum_{n=13}^{18} C_n^*\tau^{u_n} + \sum_{n=13}^{58} C_n^*\tau^{u_n}(b_n - c_n k_n \delta^{k_n})\delta^{b_n}\exp(-c_n\delta^{k_n}) \quad (2.29)$$

where δ is the reduced density; $\delta = K^3\rho$; $\tau = \frac{1}{T}$; B is the second virial coefficient; K is the mixture size coefficient; C_n^* is the temperature-dependent coefficient; and b_n, c_n and k_n are the parameters. B is calculated by means of binary parameters for the 21 considered components according to:

$$B = \sum_{n=1}^{18} a_n\tau^{u_n}\sum_{i=1}^{21}\sum_{j=1}^{21} x_i x_j E_{ij}^{u_n}\left(K_i K_j\right)^{3/2} B_{nij}^* \quad (2.30)$$

The size parameter K relays on the component of the mixture and is estimated by using binary parameters. The coefficients C_n^* and B_{nij}^* are also based on the components and have further binary parameters which take into account different physical properties – for instance, dipole and quadrupole characteristics – of the considered components. The structure of the AGA8-DC92 EOS is quite complex, as

it depends on a total of 58 polynomial terms and polynomial terms in conjunction with exponential functions, which require 860 different parameters. Despite this huge requirement, significant deviations between calculated and measured caloric properties occur at temperatures below 270 K, even for typical natural gases. For example, speed of sound deviations increase at higher pressures and reach a value of about ~1% at a pressure of 20 MPa. Similarly for gases containing higher fractions of nitrogen, CO_2, ethane, or heavier alkanes, larger uncertainties loom in the lower temperature range. The range of validity of AGA8-DC92 covers the gas phase at temperatures 143 K<T<673 K and pressures up to 280 MPa.

2.7.2.4 The Span and Wagner EOS

Span and Wagner developed an EOS for the representation of the thermodynamic properties of CO_2 [77], which are expressed in the form of the Helmholtz energy A with the two independent variables, density ρ and temperature T. The dimensionless Helmholtz energy $\phi=A/(RT)$ is commonly split into a part depending on the ideal-gas behaviour ϕ^o and a part which takes into account the residual or the non-ideal fluid behaviour ϕ^r, namely:

$$\phi(\delta,\tau) = \phi^o(\delta,\tau) + \phi^r(\delta,\tau) \tag{2.31}$$

where $\delta=\rho/\rho_c$ is the reduced density and $\tau=T_c/T$ is the inverse reduced temperature. The formulations of Helmholtz energy of an ideal gas, and the residual part of the Helmholtz energy, can be found in [77]. Using Maxwell's [104] relations, all the thermodynamic properties of a pure substance can be obtained by combining derivatives of Equation 2.31.

The Span and Wagner EOS has 42 terms. The coefficients in this equation have been obtained by fitting the reliable experimental data for pure CO_2 in the homogeneous

region (i.e. single phase) and in liquid-vapour equilibrium states (i.e. the liquid-vapour phase boundary) with a total of 5508 data points (from 59 papers, the earliest published in 1903) which covered the fluid region (i.e. the gas and liquid states) from the triple point temperature, 216.692 K to 1100 K, and pressures up to 800 MPa. The uncertainties in the Span and Wagner EOS for pure CO_2 compared to the experimental data are shown in Table 2.2. In the region of interest to pipelines, the uncertainty in the prediction of density is reported not to exceed ±0.05%.

Table 2.2: Uncertainties in the Span and Wagner EOS for pure CO_2

Property	Nomenclature	Errors (%)
Density	ρ	±0.03 - 0.05%
Speed of sound	W	±0.03 - 1%
Isobaric heat capacity	C_p	±0.15 - 1.5%
Triple temperature point	T_t	±0.003 K
Triple pressure point	ρ_t	±0.00010 MPa
Triple saturated liquid density point	ρ_t'	±0.18 kg/m^3
Triple saturated vapour density point	$\rho t''$	±0.0034 kg/m^3
Critical temperature	T_c	±0.015 K
Critical pressure	P_c	±0.0030 MPa
Critical density	ρ_c	±0.6 kg/m^3
Melting pressure	p_m	$\Delta p_m/p_m$: ± 1.5% (T_t<T<225K) ± 0.5% (225K<T<270K)
Sublimation pressure	p_{sub}	Δp_{sub}: ±250 Pa (185K<T<T_t) ±100 Pa (170K<T<185) ±50 Pa (T<170K)
Vapour pressure	p_{σ}	Δp_{σ}: ± 0.012%
Saturated liquid density	ρ'	$\Delta \rho'$:

Saturated vapour density	ρ''	±0.015% (T_t<T<295K) ±0.04% (295K<T<303K) ±1% (303<T<T_c) $\Delta\rho''$: ±0.025% (T_t<T<295K) ±0.08% (295K<T<303K) ±1% (303<T<T_c)

The Span and Wagner EOS was designed for pure CO_2 and is not applicable to CO_2 mixtures.

2.7.2.5 The GERG EOS

GERG-2004, developed by the Groupe Européen de Recherches Gazières (GERG) in 2004 [78, 105], is effective for wide ranges of temperature, pressure and composition, and covers the gas phase, the liquid phase, the supercritical region, and vapour-liquid equilibrium states for natural gases and other mixtures consisting of 18 components: methane, nitrogen, CO_2, ethane, propane, n-butane, iso-butane, n-pentane, iso-pentane, n-hexane, n-heptane, n-octane, hydrogen, oxygen, carbon monoxide, water, helium, and argon. GERG-2004 replaces the AGA8-DC92 EOS in ISO standards. The drafts ISO 20765-2 and ISO 20765-3 are based on GERG-2004.

Both GERG-2008 [106] and the extended version of GERG-2004 are expressed in terms of the Helmholtz free energy as a function of temperature and density, and consider three additional components n-nonane, n-decane, and hydrogen sulphide, resulting in a total of 21 components [105]. GERG-2004 and GERG-2008 are based on pure substance EOS for each of the considered mixture components and correlation equations for binary mixtures consisting of these components.

$$\alpha(\delta,\tau,\bar{x}) = \alpha^o(\rho,T,\bar{x}) + \alpha^r(\delta,\tau,\bar{x}) \tag{2.32}$$

where α^o denotes the properties of the ideal-gas mixture at a given mixture density ρ, temperature T, and molar composition $\bar{x}$; while α^r in Equation 2.32 of the reduced Helmholtz free energy represents the residual part of the mixture [78].

A database of more than 100,000 experimental data points for the thermodynamic properties of binary mixtures, natural gases and other multi-component mixtures was used to develop the structure, coefficients and parameters of the correlation equations for binary mixtures, and to evaluate the behaviour of the EOS. Thus GERG-2008 is able to represent the most accurate experimental binary and multi-component data for gas-phase and gas-like supercritical densities, speeds of sound, and enthalpy differences, mostly to within their low experimental uncertainties. The pure substance EOS in GERG-2004/GERG-2008 is simpler (22 terms) compared to the Span and Wagner EOS (42 terms) [105].

.

- GERG-2008 is valid over 90 K $\leq T \leq$ 450 K and pressures of $P \leq$35 MPa for natural gases and similar mixtures for pipeline transport, natural gas storage, and processes with liquefied natural gas [105]. In their gas phase and for 250 K/270 K <T< 450 K given P<35 MPa, the uncertainty of the equation in density and speed of sound is less than 0.1%;
- For many binary and multi-component mixtures in the liquid phase, the uncertainty of GERG-2008 in density is below 0.1–0.5% and uncertainty in the liquid phase (isobaric) enthalpy differences is less than 0.5–1%;
- Accurate vapour pressure data and thus VLE data for binary and ternary mixtures consisting of the natural gas main components are reproduced by

GERG-2008 to within their experimental uncertainty, which is approximately 1–3%.

2.7.3 Comparisons of Equations of State

To date, no EOS is specifically recommended for CO_2 mixtures, but the ability to accurately predict the VLE, density and speed of sound is considered the best way to gauge any weaknesses or strengths of an EOS [2, 10, 107, 108]. The following sections will introduce previous attempts to evaluate the accuracy of different equations of state.

2.7.3.1 Li and Yan's work - 1

Li and Yan [2] evaluated the reliabilities of five cubic equations of state, including PR [70], Patel-Teja (PT) [109], Redlich-Kwong (RK) [69], Soave-Redlich-Kwong (SRK) [71] and 3P1T [110] for predicting the VLE of CO_2 and binary CO_2 mixtures containing CH_4, H_2S, SO_2, Ar, N_2 or O_2, based on comparisons with collected experimental data. All equations of state employed the conventional random van der Waals mixing rules, where the binary interaction parameter k_{ij} – which accounts for the attraction forces between pairs of dissimilar molecules – was determined from VLE data. Since k_{ij} is more sensitive to derivative or partial properties such as fugacity coefficients than to total properties such as mixture molar volumes, k_{ij} is considered to be independent of temperature, composition and density, and it is determined by matching the predicted values with experimental data.

The following conclusions were obtained from their study:

- For the VLE properties of pure CO_2, SRK is superior in the calculations on saturated pressure with an Absolute Average Deviation (AAD) of 1.05%. AAD is defined as:

$$AAD = \frac{\sum \left| \frac{v_{cal} - v_{exp}}{v_{exp}} \right| \times 100\%}{N} \tag{2.33}$$

where v_{cal} and v_{exp} are the calculated and experimental values of the property v, respectively, and N is the number of data points. In general, RK is not recommended for VLE calculations;

- For the VLE properties of binary CO_2 mixtures, PR, PT and SRK are generally superior to RK and 3P1T. Comparatively, PR is recommended for the calculations of CO_2/CH_4 and CO_2/H_2S; PT is recommended for the calculations of CO_2/O_2, CO_2/N_2 and CO_2/Ar; while 3P1T is recommended for the calculations of CO_2/SO_2.

The new calibrated k_{ij} led to better estimates of saturated vapour composition, although the accuracy of saturated pressure estimation may not be improved.

2.7.3.2 Li and Yan's work - 2

Li and Yan [10] extended their earlier study and compared seven cubic equations of state, including PR, PT, RK, SRK, MPR, MSRK and ISRK, to evaluate their reliabilities for predicting volume (density) of binary CO_2 mixtures containing CH_4, H_2S, SO_2, Ar and N_2. The following conclusions were drawn from the comparison:

- The binary interaction parameter k_{ij} clearly influences the accuracy of an EOS in the volume calculations of CO_2 mixtures. To improve the accuracy, k_{ij} was calibrated for all of the equations of state regarding the gas and liquid phases of all the studied binary CO_2 mixtures, respectively;

- For calculations on the volume properties of binary CO_2 mixtures, PR and PT are generally superior to others for all of the mixtures studied. PT is recommended for the calculations of CO_2/CH_4, V_l of CO_2/H_2S, CO_2/Ar and CO_2/SO_2, and V_g of CO_2/N_2; PR is recommended for the calculations of V_l of CO_2/N_2 and V_g of CO_2/Ar; MPR and ISRK are recommended for the calculations of V_l of CO_2/H_2S and V_g of CO_2/SO_2, respectively;
- If the calibrated k_{ij} is not available, generally PR and PT are more likely to give accurate results for the density of both vapour and liquid phases than other equations of state studied in this work.

2.7.3.3 Span and Wagner

Span and Wagner [77] compared the thermodynamic properties of pure CO_2 predicted by their model and other models. The Span and Wagner EOS is valid for equilibrium thermodynamic properties of CO_2 in the fluid region up to temperatures of 1100 K (827°C) and pressures up to 800 MPa (8000 bar). The Span and Wagner EOS was developed with special attention given to the behaviour of thermal properties in the critical region and extrapolation behaviour of empirical equations of state. It is therefore able to represent thermal properties and speed of sound in the immediate vicinity of the critical point.

Figure 2.11 shows the relative density deviations of very accurate P-ρ-T data at subcritical temperatures from values calculated from the Span and Wagner EOS. Values calculated from the equations of Ely et al. [111] and Angus et al. [112] are plotted for comparison, while other values in the figure are the experimental results. For pressures up to 13 MPa and temperatures up to 360 K, the Span and Wagner EOS is able to reproduce the experimental data within their experimental uncertainty

(±0.02% in density). Note that Ely et al. [111] was demonstrated to be the best EOS for CO_2, while Angus et al. [112] was widely recognised as an international standard for CO_2.

The equation of Ely et al. yields a suitable description of the gas region at low temperatures, but it has problems for temperatures above about 250 K. The equation of Angus et al. is not able to reproduce the experimental data in the gas region. In the liquid region, none of the equations of Ely et al. and Angus et al. are able to represent the reference data of Duschek et al. [113] and Gilgen et al. [114], at least roughly to within their experimental uncertainty.

Figure 2.12 shows the relative deviations of speed of sound data at supercritical temperatures from values calculated from the Span and Wagner EOS. Values calculated from the equations of Ely et al. and of Pitzer and Schreiber [115], and, in the range of validity, from the equation of Chen et al. [116], are plotted for comparison. The data of Novikov and Trelin [117] describes the caloric behaviour within the gas and supercritical region. Figure 2.13 illustrates the representation of speed of sound values on two representative isotherms of this data set. While all the considered formulations represent the data within their uncertainty at 373 K, only the Span and Wagner EOS is able to reproduce the measurements at 308 K. In the extended critical region, the deviations of the Span and Wagner EOS do not exceed ±0.7%. On the 308 K isotherm, the equation of Chen et al. yields deviations up to 2%.

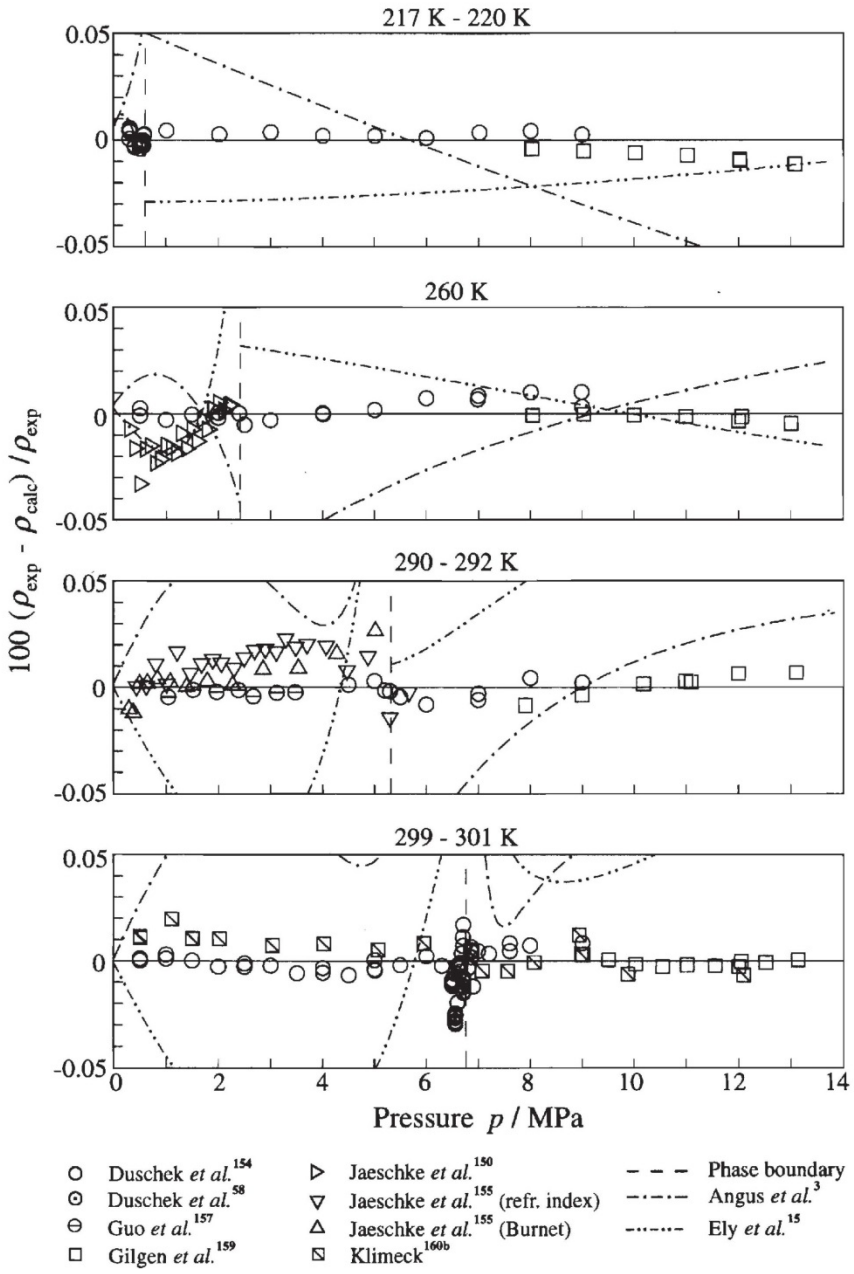

Figure 2.11: Relative density deviations of very accurate $P\rho T$ data at subcritical temperatures from values calculated using the Span and Wagner EOS [77]

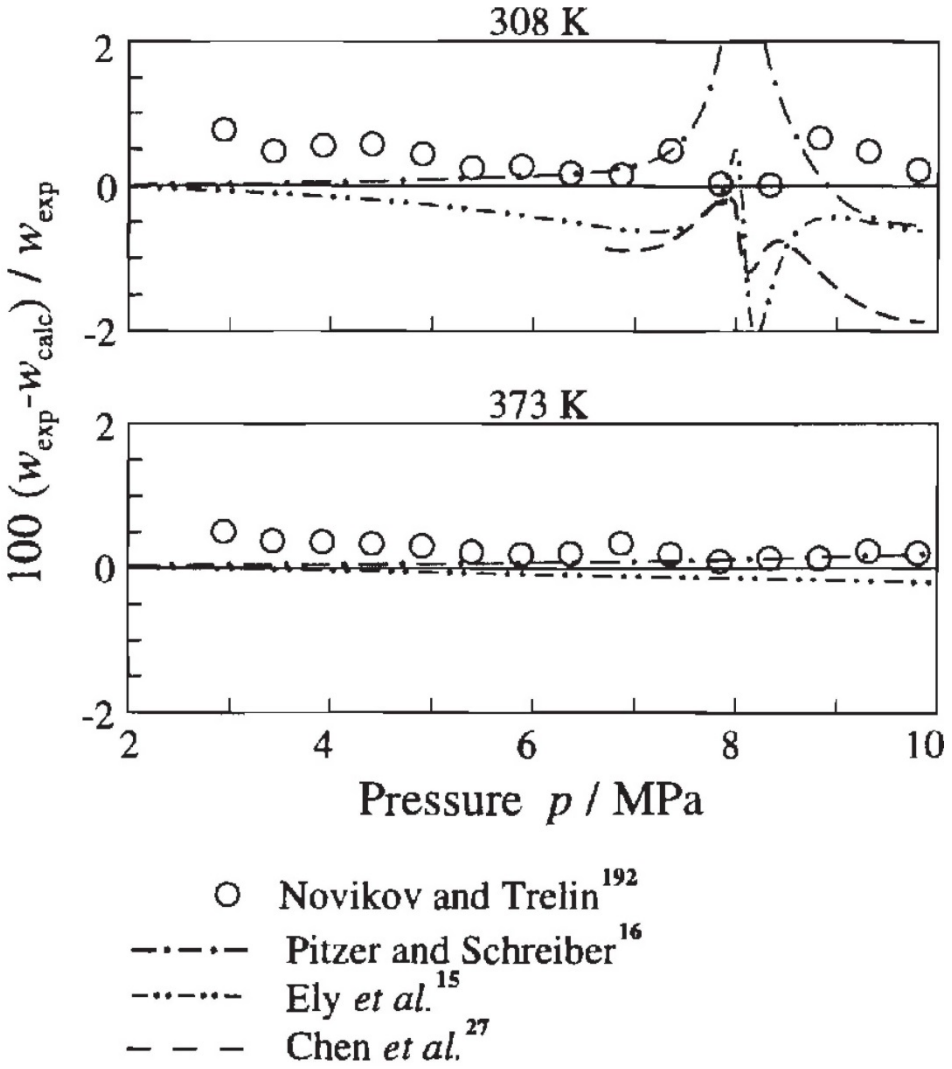

Figure 2.12: Relative deviations of speed of sound data at supercritical temperatures from values calculated using the Span and Wagner EOS [77]

Thus, the Span and Wagner EOS is now generally regarded as the preferred method for calculating equilibrium thermodynamic properties of pure CO_2. This equation was designed for pure CO_2 and thus may only be used with very high purity CO_2 streams. It is therefore not applicable to CO_2 mixtures.

2.7.3.4 Cosham et al. - Work 1

Cosham et al. [15] compared the decompression wave speeds obtained from using different equations of state for pure CO_2 (Span and Wagner, BWRS and PR) and CO_2 mixtures (BWRS and GERG-2004) for one-dimensional flow with isentropic

decompression and in homogeneous equilibrium. The accuracy of the BWRS and PR was considered in relation to the Span and Wagner EOS. As seen in Figure 2.13, the variation between the forecasts of the saturation pressure at a specified temperature is minor, excluding in the vicinity of the critical point. The BWRS EOS over-predicts the pressure and temperature at the critical point.

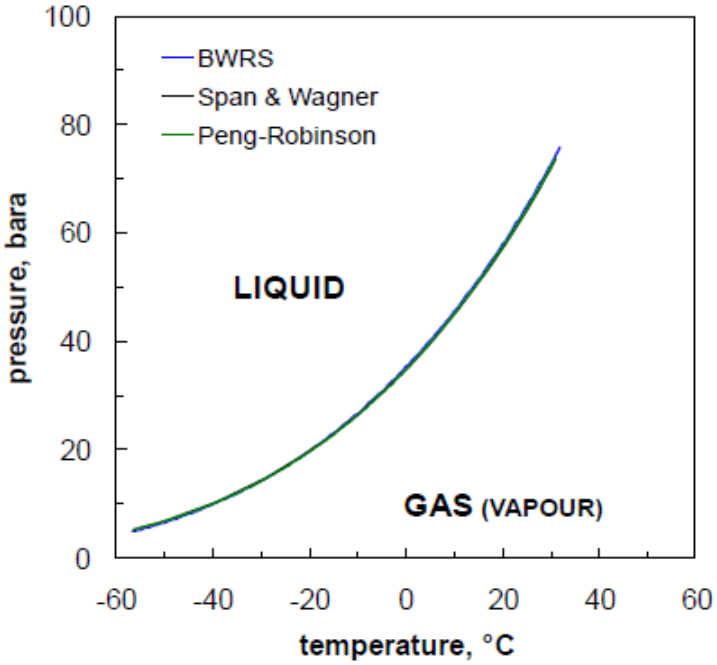

Figure 2.13: The pressure-temperature phase diagram for pure CO_2 [15]

Figure 2.14 illustrates the pressure-density phase diagrams of pure CO_2. While the vapour-phase density predictions of the three models hardly differ, BWRS shows closer predictions of the density of the saturated liquid phase than PR does to the reference i.e. Span and Wagner EOS. Accordingly, a lower saturated liquid density in the critical region is predicted by the PR EOS than the other two.

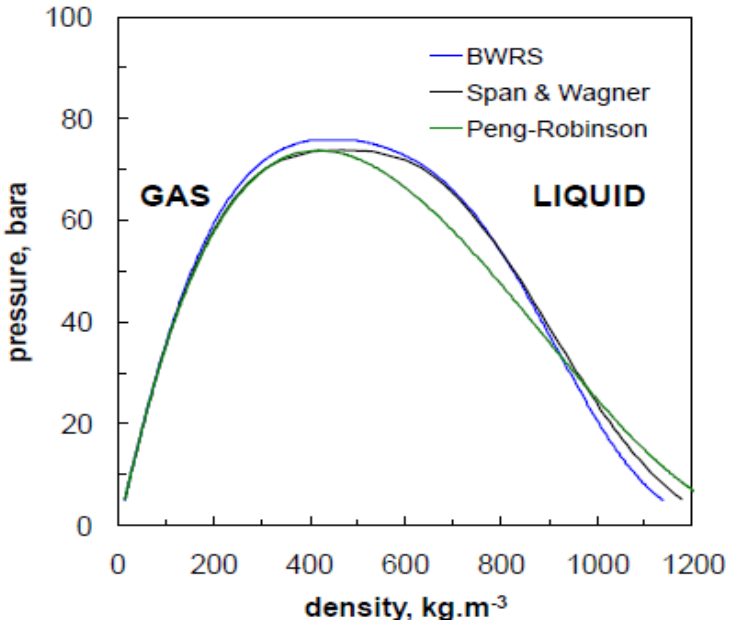

Figure 2.14: The pressure-density phase diagram for pure CO_2 [15]

For binary mixtures that include N_2 and CH_4, while the trends in the results of both BWRS and GERG-2004 equations of state are identical, the BWRS EOS consistently predicts a higher saturation pressure for given initial conditions (see Figure 2.15). However, the predictions have not been validated against experimental data.

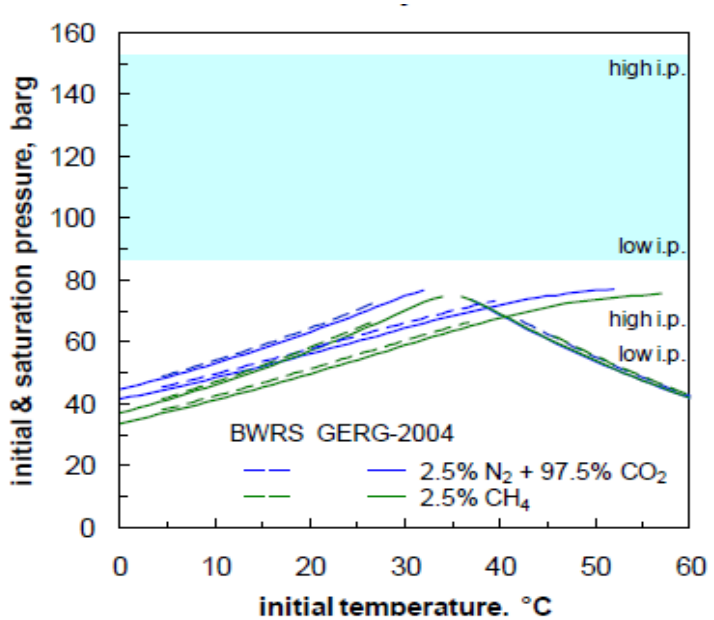

Figure 2.15: The effect of initial pressure and initial temperature on the saturation pressure for two CO_2 mixtures with 2.5% N_2 and 2.5% CH_4 [15]

2.7.3.5 Kamal K. Botros

Kamal K. Botros [118] predicted the speed of sound for different hydrocarbon mixtures using five different equations of state: GERG, AGA-8, BWRS, PR and SRK, and compared the predicted results with the measured values obtained from 42 shock tube tests (see Figure 2.16). The deviation between the predicted and the measured speed of sound was determined using the following formula:

$$\text{Deviation (\%)} = \left(\frac{C_{EOS} - C_m}{C_m}\right) \times 100 \tag{2.34}$$

where C_{EOS} and C_m represent the predicted and the measured values of speed of sound, respectively. The predictions of speed of sound by BWRS, AGA-8 and GERG equations of state were consistent and within ±2% compared to 5% to 6% of PR and SRK equations of state for all tests considered in this work. It was determined that the GERG EOS outperformed the others in the region up to P=30 MPa and T>-8°C, which is similar to the conditions of CO_2 pipeline transport.

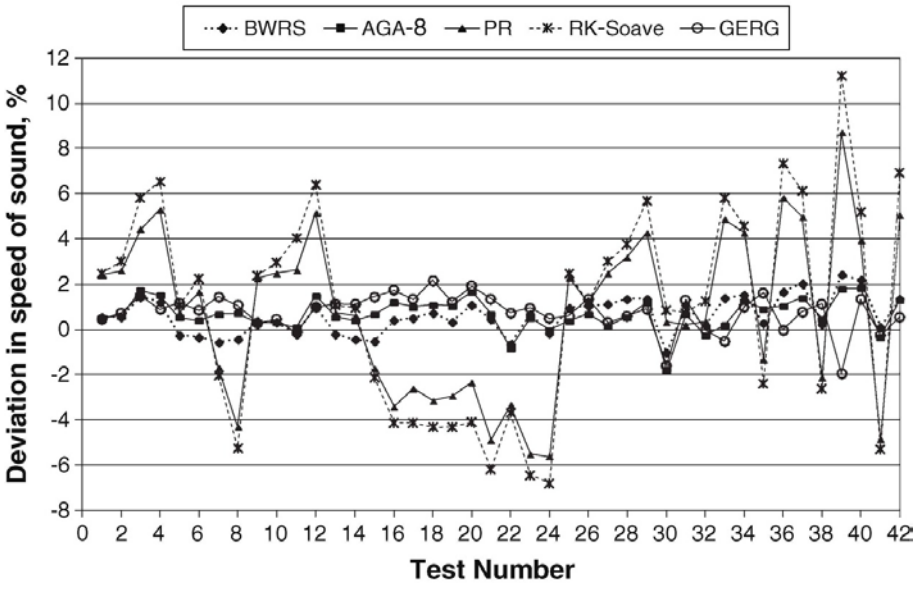

Figure 2.16: Deviations in the predictions of speed of sound using the five EOS

2.8 Previous Studies of CO_2 Decompression Behaviour

2.8.1 Cosham et al. - Work 2

Cosham et al. [15] investigated the isentropic decompression behaviour of pure CO_2 and the effect of the initial pressure and initial temperature on the decompression velocity curves. In a pressure-temperature graph, the different isentropic decompression paths converge onto the phase boundary. The effect of the initial pressure and initial temperature on the saturation pressure and the shape of the decompression velocity curve, depend on whether the isentropic decompression path passes through the liquid phase or the vapour phase. For isentropic decompression paths that pass through:

(a) The vapour phase, the saturation pressure will increase as the initial pressure increases or as the initial temperature decreases. The decompression velocity curve will exhibit a short plateau;

(b) The liquid phase, the saturation pressure will increase as the initial pressure decreases or as the initial temperature increases. The decompression velocity curve will exhibit a long plateau;

(c) The effect of the initial pressure is greater than the effect of the initial temperature.

Cosham et al. [2] explained that although CO_2 can have counterintuitive trends, it is possible to bind the value of the saturation pressure without much effort. For pipelines designed to transport CO_2 in the vapour (liquid) phase, the limiting condition for fracture propagation control is the maximum (minimum) pressure and the minimum (maximum) temperature. For the vapour (liquid), the saturation pressure increases as the initial pressure increases (decreases) or as the initial

temperature decreases (increases). The toughness required to arrest a running ductile fracture (the arrest toughness) depends on the arrest pressure, set equal to the saturation pressure, and the diameter, wall thickness and grade of the line pipe steel. The same trends are observed for impure CO_2, although the definition of the saturation pressure will be influenced by the shape of the phase boundary.

2.8.2 Seevam and Hopkins

Seevam and Hopkins [34] compared and contrasted the current experience of transporting CO_2 onshore with the proposed transport onshore and offshore for CCS. They studied the effect of physical and transport properties (hydraulics) on key technical aspects of pipeline transportation, and the implications for designing and operating a pipeline for CO_2 containing impurities. The addition of impurities to the CO_2 product stream changes the phase envelope (see Figure 2.17), calculated using the PR EOS – a standard in CCT, namely, post-combustion (capture of CO_2 from flue gas); pre-combustion (capture of CO_2 before combustion) or IGCC (Integrated Gasification Combined Cycle); and oxyfuel. Table 2.3 illustrates the possible impurities for each capture technology.

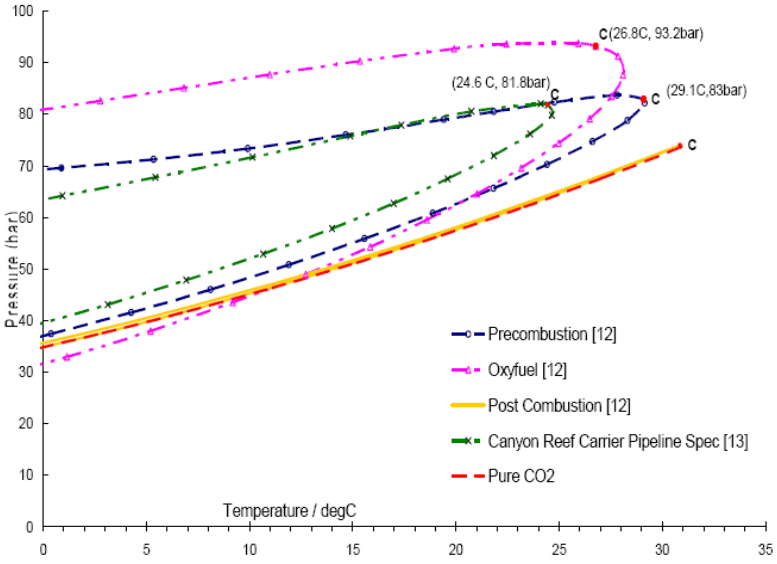

Figure 2.17: Phase envelope for different capture technologies [34]

Table 2.1: The possible composition for the three capture technologies [34]

Composition	Mole fraction %		
	Post-Combustion	Pre-Combustion	Oxyfuel
CO_2	>99% v%	>95.6% v%	>90% v%
CH_4	<100ppmv	<350ppmv	0
N_2	<0.17v%	<0.6v%	<7v%
H_2S	Trace	<3.4v%	Trace
C2+	<100ppmv	<0.01v1%	0
CO	<10ppmv	<0.4v1%	Trace
O_2	<0.01v1%	Trace	<3v%
NO_X	<50ppmv	0	<0.25v%
SO_X	<10ppmv	0	<2.5v%
H_2	Trace	<3v1%	Trace
Ar	Trace	<0.05v1%	<5v%
S	N/A	N/A	N/A

The following can be drawn from this study:

- Impurities generally increase the width of the phase envelope and result in the formation of a two-phase gas-liquid region; however, the magnitude of increase varies e.g. H_2 and NO_2 induce a high increase whilst others e.g. N_2 and H_2S induce a much smaller increase. Generally, the critical pressure increases but the critical temperature decreases;
- The binary and ternary (i.e. CO_2 and two other impurities) system involving NO_2 increases both the critical pressure and temperature. The ternary system – 90% CO_2, 5% N_2 and 5% NO_2 – shows a more significant effect on the phase envelope in terms of the size of the two-phase area, the critical pressure and temperature;
- The phase envelopes formed for a composition involving NO_2 are all below the pure CO_2 vapour-liquid line, in contrast to the CO_2-N_2 and CO_2-N_2-CH_4 phase envelopes. This would slightly reduce the pressure drop gradient for the CO_2-5% NO_2 combination;
- The addition of another component such as N_2, in this case, changes the initial phase behaviour of the two-component system due to the interactions that occur;
- Compared to pure CO_2, the three capture technology combinations reveal a decrease in the critical temperature while the critical pressure increases;
- The compositions of the post-combustion have the closest critical point to that of pure CO_2. It also shows a similar phase diagram to that of pure CO_2;
- The highest increase in the critical pressure (~9.32 MPa) and the highest decrease in the critical temperature (26.8°C) resulted from the oxyfuel impurity combinations.

The above effects will have a direct influence on the decompression behaviour of CO_2. The results of this study show that oxyfuel is the most detrimental in terms of changing the hydraulic properties of the transported CO_2.

2.8.3 Munkejord et al.

Munkejord et al. [119] used a combination of the SRK EOS and the two-phase drift-flux model to calculate the one-dimensional flow of multi-component CO_2 mixtures, wherein each chemical component was tracked explicitly. The drift-flux model is a system of coupled non-linear hyperbolic differential equations. The pressure and mass waves inherent in the model were resolved numerically by using the multistage (MUSTA) centred scheme. Example calculations indicated that their model along with constitutive relations had the potential to describe the depressurisation of multi-component CO_2 mixtures in pipelines. Different mixture compositions affected the bubble and dew temperatures significantly (see Figure 2.18).

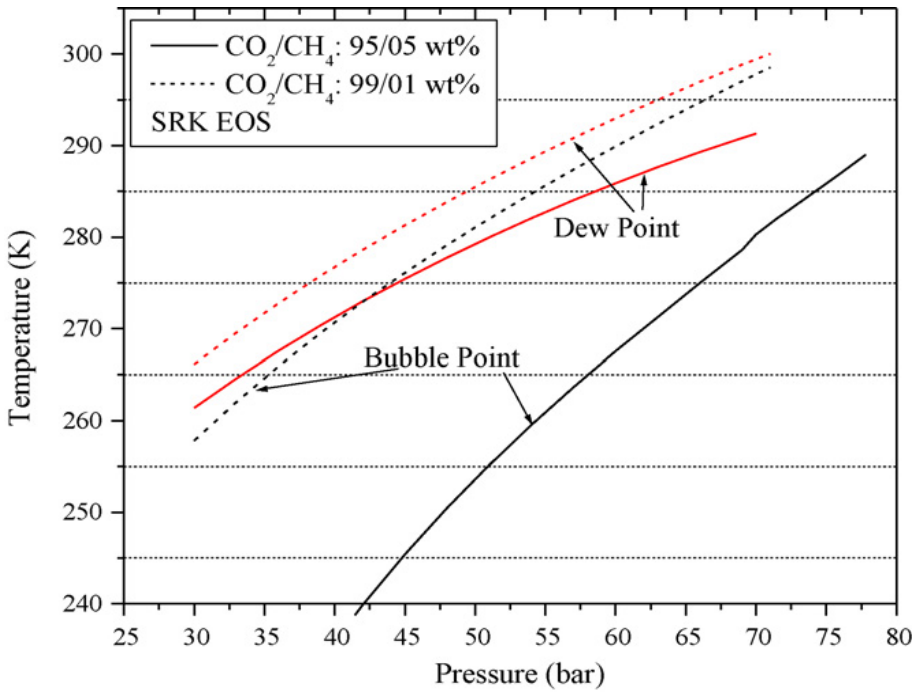

Figure 2.18: Phase envelope of CO_2 binary mixture contains 1%/5% CH_4 [119]

Figure 2.19 illustrates the results of pressure drop as a function of distance (a), and the difference between the initial and the final temperature as a function of distance (b). On graph (a), the propagation velocity of the pressure is lower for the 95% CO_2 mixture. The impact of cooling of evaporation is highest for the mixture with the highest CO_2 content, as depicted on graph (b). The impurity impacts the pressure-propagation speed and the amount of cooling exerted by the decompression process and should be considered for the design and operation of CO_2 transport systems.

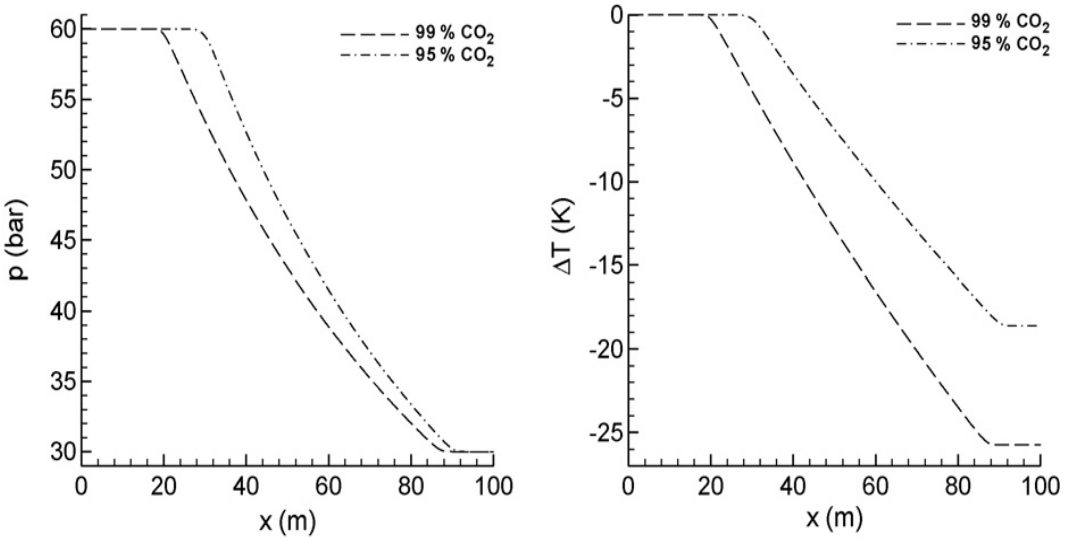

Figure 2.19: Depressurisation of two CO_2-methane mixtures (a) pressure; (b) difference between initial and final temperature [119]

2.8.4 Cosham and Eiber

In this work, GASDECOM was used to examine the influence of methane and nitrogen on the decompression behaviour of CO_2 [9]. Figure 2.20 shows the theoretical decompression curves of the CO_2-N_2 mixture (0–10% N_2). The results illustrate the significant increase in the saturation pressure as the proportion of N_2 increases. Figure 2.21 shows the decompression curves for pure CO_2 and CH_4, based on an initial temperature of 10°C and initial pressures of 10 MPa and 18 MPa. The results showed that the arrest toughness was dependent on both the pipe diameter and

the material transported. For example, CO_2 in the 24 inch pipeline and CH_4 in the 18 inch pipeline showed higher arrest toughness than vice-versa. With CH_4, the decompression wave speed was more affected using higher initial pressure. In contrast, the decompression curve of the CO_2 pipeline changed dramatically when using lower initial pressure. Such results indicate that fracture propagation in a CO_2 pipeline can be controlled using high design pressure.

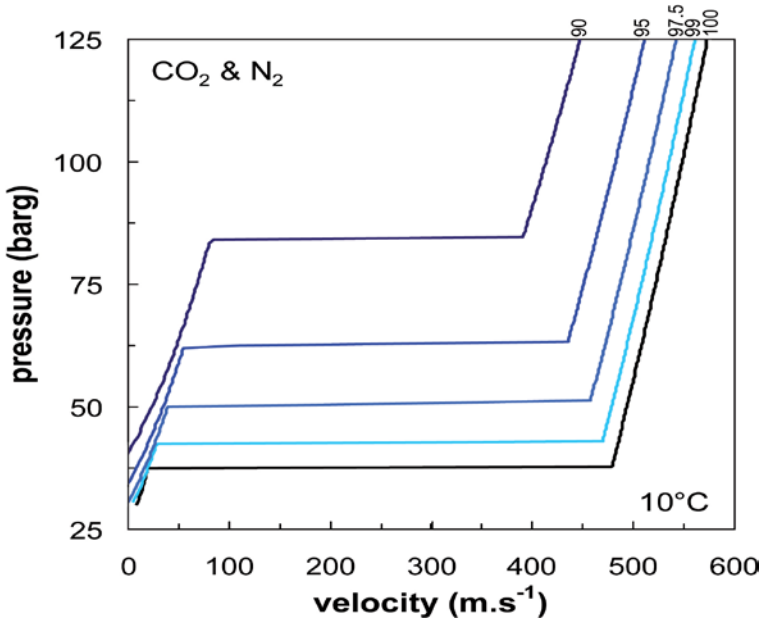

Figure 2.20: The theoretical decompression curves of the CO_2-N_2 mixture (0–10% N_2) [9]

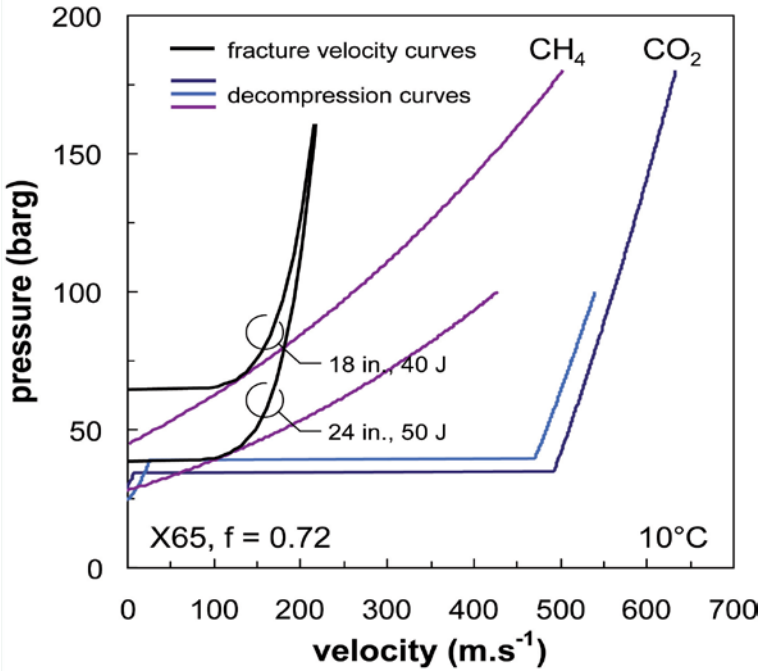

Figure 2.21: Theoretical decompression curves for pure CO_2 and pure CH_4, and fracture speed curves for the 18 and 24 inch pipelines [9]

2.8.5 Cosham, Eiber and Clark

Cosham et al. [15] investigated the consequence of impurities on the decompression behaviour of CO_2 pipelines using GASDECOM. The chosen impurities depend on the three capture technologies (post-combustion, pre-combustion and oxyfuel). The post-combustion method produces an approximately pure CO_2. The other capture methods result in a less pure stream which consists of impurities such as hydrogen, nitrogen, carbon monoxide, argon, oxygen, methane, and hydrogen sulphide. However, components such as hydrogen, oxygen and argon cannot be included using GASDECOM. To circumvent this issue, the GERG-2004 EOS implemented in REFPROP 9.0 [120] was used to include the missing components in GASDECOM. Figure 2.23 shows the predicted decompression wave velocity curves for each of the six binary mixtures and that of 100% CO_2. The saturation pressure was different in each case, and all were higher than that of pure CO_2, i.e. H_2, N_2, CO, Ar, O_2 and CH_4 all have an adverse effect on the decompression curve.

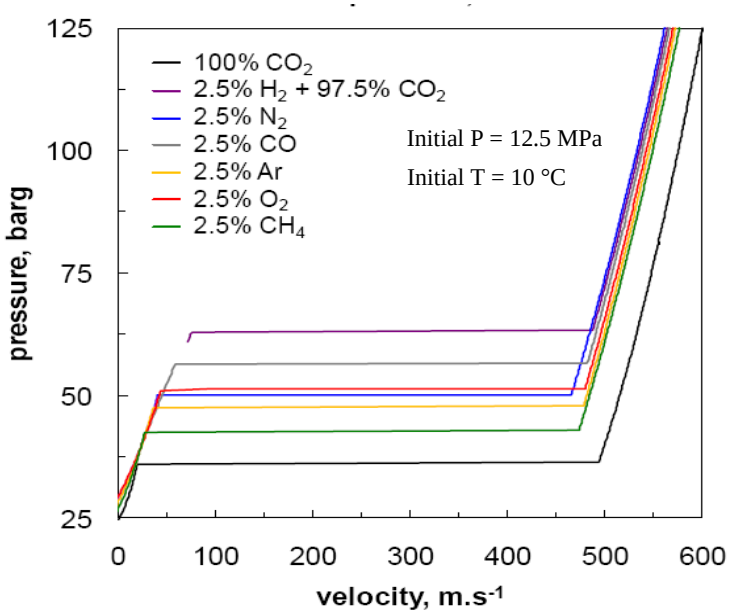

Figure 2.22: Decompression speed curves for binary mixtures of CO_2 and H_2, N_2, CO, Ar, O_2 and CH_4 based on the GERG-2004 EOS

Figure 2.23 presents the decompression curves predicted for the different capture technologies. The coal-fired pre-combustion stream gave the highest pressure plateau (saturation pressure) on the decompression curve. While for the pre-combustion and oxyfuel streams, the saturation pressures were significantly higher than those for the post-combustion streams (or 100% CO_2); nevertheless, the difference between the pre-combustion and oxyfuel streams is trivial. The saturation pressures for the post-combustion streams and 100% CO_2 are nearly identical.

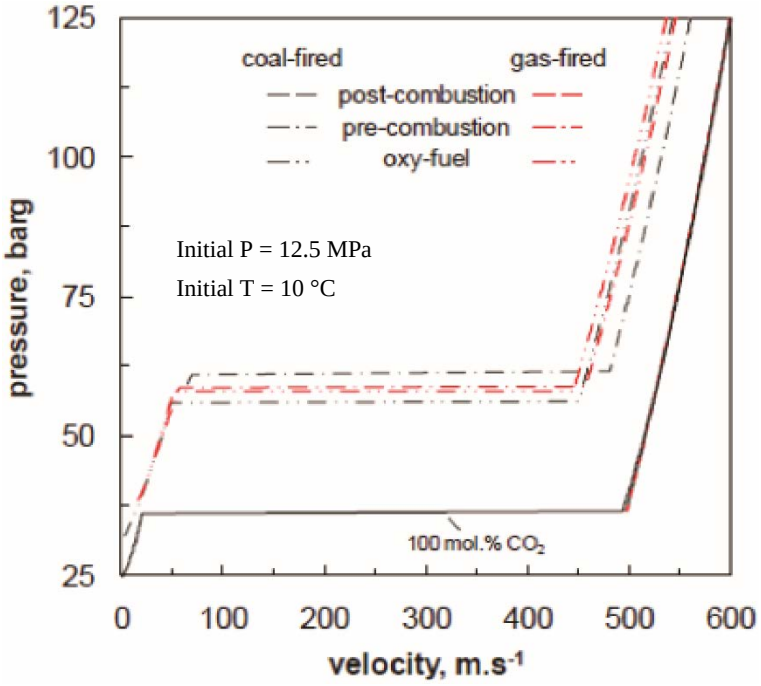

Figure 2.23: Theoretical decompression speed curves for post-combustion, pre-combustion and oxyfuel [15]

Figure 2.24 shows that higher toughness material will be required for pipelines designed to carry the pre-combustion stream (more impurities) than those used for the post-combustion stream (less impurities), the difference between the two cases decreasing as the wall thickness of the pipe increases. This was tested for a pipeline with a design pressure of 15 MPa and a design factor of 0.72 using a maximum operating temperature of 20°C. Here, the post-combustion stream (~pure CO_2) needs a CVN value of less than 100 J; while the pre-combustion stream would necessitate the use of crack arrestors.

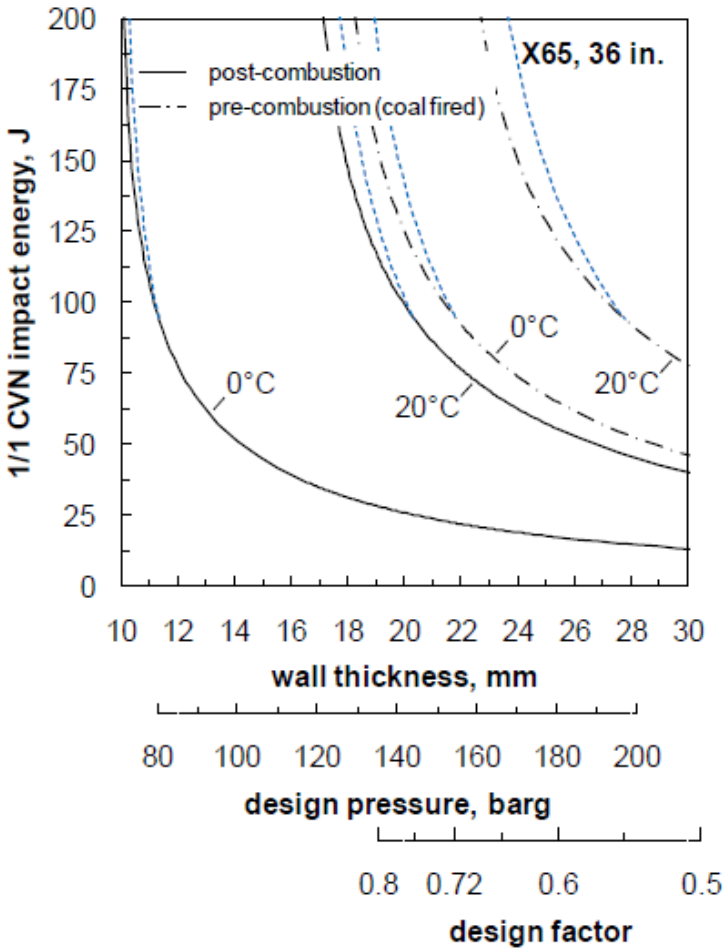

Note:
1. The design pressure is calculated for a design factor of 0.72.
2. The design factor is calculated for a design pressure of 150 barg.

Figure 2.24: The effect of wall thickness, design pressure and design factor on the full-size CVN impact energy required to arrest a running ductile fracture [15]

2.8.6 Mahgerefteh et al.

Mahgerefteh et al. [82] studied the influences of friction, heat transfer and stream impurities on the decompression behaviour in CO_2 pipelines. For CO_2 mixtures, the investigation was done for a decompression from the gas phase using initial pressures below 4 MPa. They used a one-dimensional transient multi-phase outflow model named PipeTech, developed previously at University College London [91], in conjunction with the PR EOS, to predict the decompression wave speed. Figure 2.25 shows the impact of internal pipe roughness on the decompression behaviour of pure

CO_2. Curves A, B and C represent values of roughness of 0.05, 0.005 and 0 mm, respectively. It was found that the effects of pipe wall roughness and fluid/wall heat transfer become evident at the later stages of the decompression, but were found to be ignorable in terms of fracture propagation control philosophy. However, this is valid for conditions used in that study and cannot be marginal when simulating long pipelines where a longer depressurisation process is taking place. The study concluded that higher fracture toughness will be required for streams containing various impurities than for streams of pure CO_2 or binary mixtures.

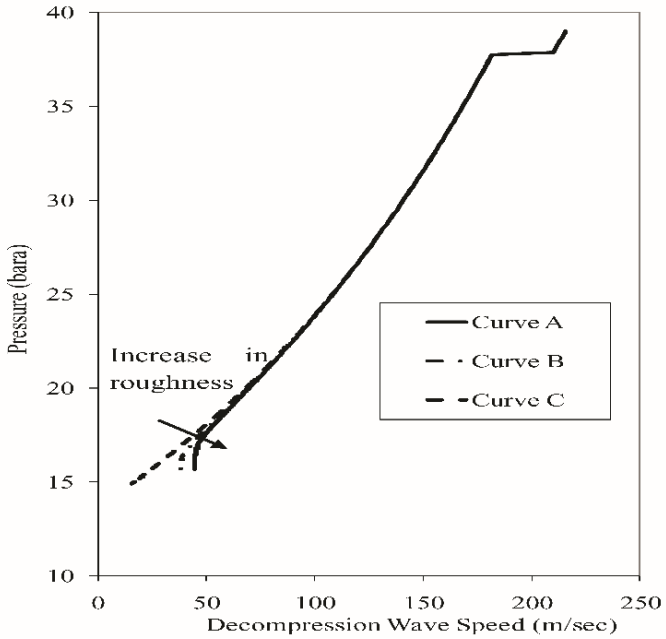

Figure 2.25: The influence of pipe roughness on the decompression behaviour of pure CO_2 [82]

2.8.7 Jie et al.

A CFD model was developed by Jie et al. [83] to simulate multi-phase flows of ruptured pipelines transporting CO_2. The Peng-Robinson-Stryjek-Vera (PRSV) [121] EOS, the PR EOS and SW EOS were adopted in this model. The model results were validated by comparing them against the measured data of shock tube tests commissioned by National Grid for dense phase CO_2 mixtures. Figure 2.26 shows

the predicted pressure-time curves and the decompression wave speed curve compared to the measured results.

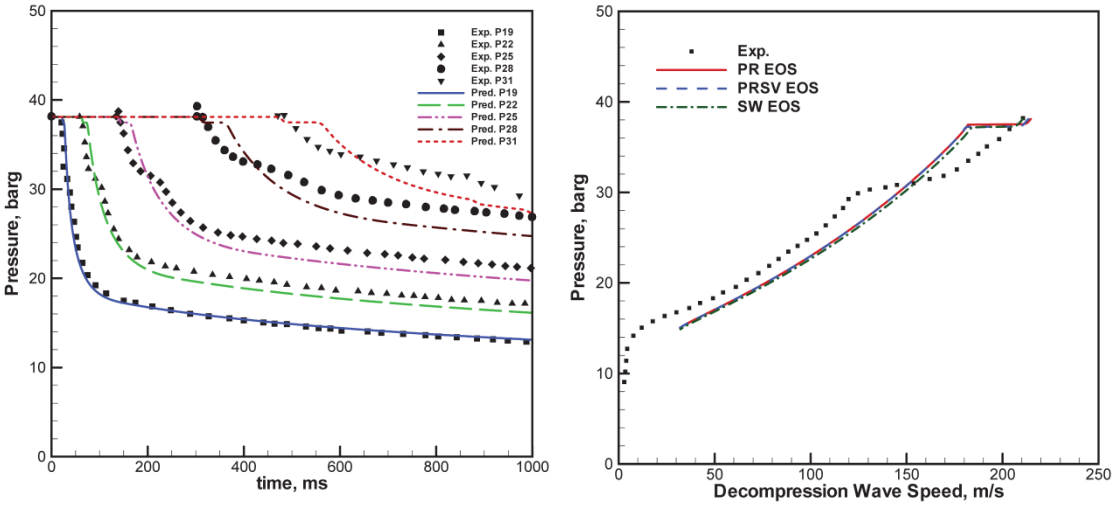

(a) (b)

Figure 2.26: (a) Comparison of the predicted results of pressure-time traces, and (b) comparison of the decompression wave speed of Test 03 [83]

In this work, the effects of friction and heat transfer on the predicted decompression curves were found to be negligible. The impact of impurities on the decompression from the gaseous phase was a decrease in the plateau level, while the decompression from the dense phase led to an increase in the level of the plateau. The performance of the equations of state was investigated as well. It was determined that the SW EOS [77] is the most accurate among the tested equations (PRSV and PR), however, it can be used for pure CO_2 only.

2.8.8 Cosham et al.

National Grid [55] conducted 31 shock tube tests with CO_2 or CO_2-rich mixtures. Five different components were used in the formation of test mixtures, including H_2, N_2, SO_2, O_2, and CH_4. Figure 2.27 is a schematic diagram of the shock tube test facility, while Figure 2.28 illustrates a comparison between the measured and predicted decompression wave speed for three different mixtures.

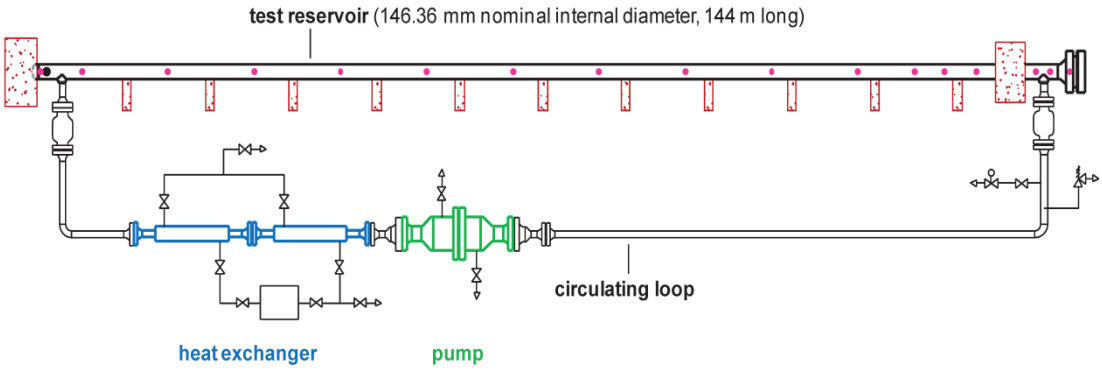

Figure 2.27: Shock tube test rig [55]

The following conclusions were drawn from the study [55]:

- When T_i increases, the arrest toughness will increase;
- The arrest toughness increases with lowering of the initial pressure;
- Components including hydrogen, oxygen, nitrogen and methane lead to an increase in the arrest toughness.

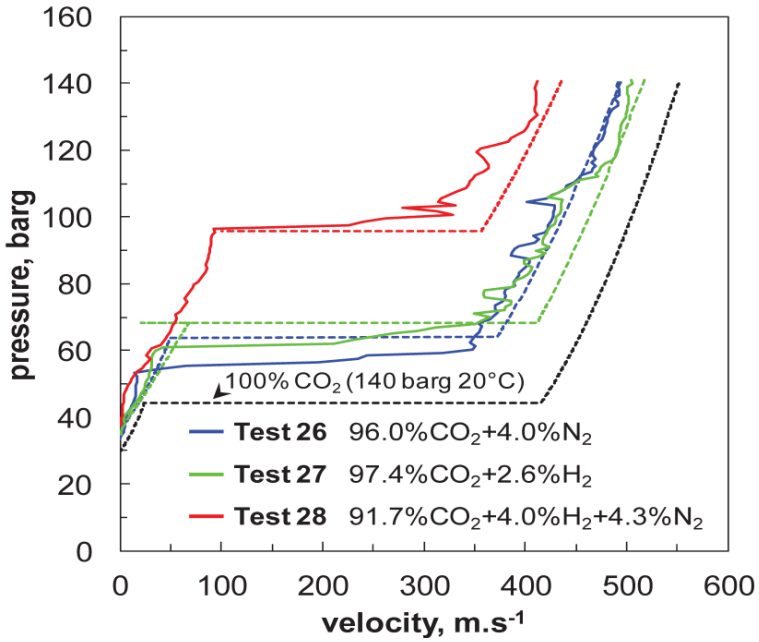

Figure 2.28: A comparison of measured and predicted decompression wave speeds [55]

2.8.9 Cosham et al.

In this work, three West Jefferson Tests [56] were performed for dense-phase CO_2 and a CO_2-rich binary mixture to characterise the difference in the rupture behaviour between liquid or dense-phase CO_2 and that which occurs in a liquid or a gas pipeline. Large diameter and thick-wall (914 mm x 25.4 mm) line pipe was used in each test. A schematic representation of the three vessels used in the tests is illustrated in Figure 2.29. The test conditions are listed in Table 2.4.

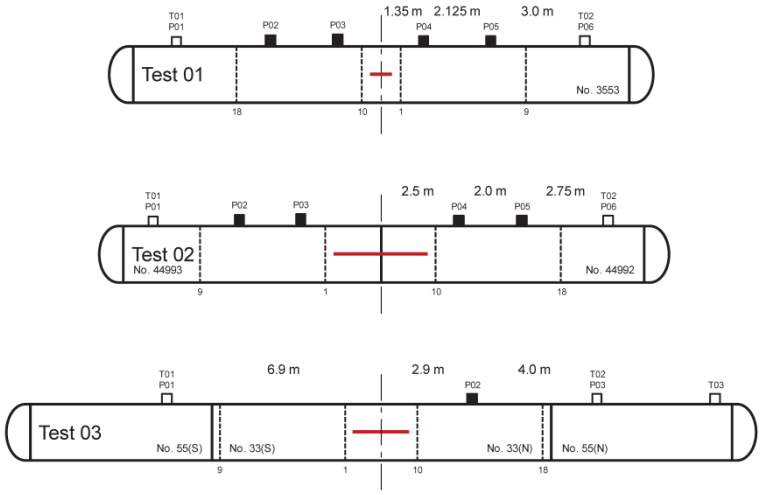

Figure 2.29: Set-up of three West Jefferson Tests

The results of the three tests are shown in Figure 2.30. Fractures have been arrested in the initiation pipes in Tests 01 and 02, as shown in Figure 2.31. In Test 03, the fracture propagated through the initiation pipe (Pipe No. 33) and was arrested in the second pipe (Pipe No. 55). The fracture appearance of the initiation pipe in Test 03 is shown in Figure 2.31 (c).

Table 2.3: West Jefferson Test composition and initial conditions

Test No.	Mixture components (mole %)		P_i (MPa)	T_i (°C)
	CO_2	N_2		
01	100	0	14.82	16.8
02	100	0	15.09	8.2
03	87.5	12.5	14.90	15.2

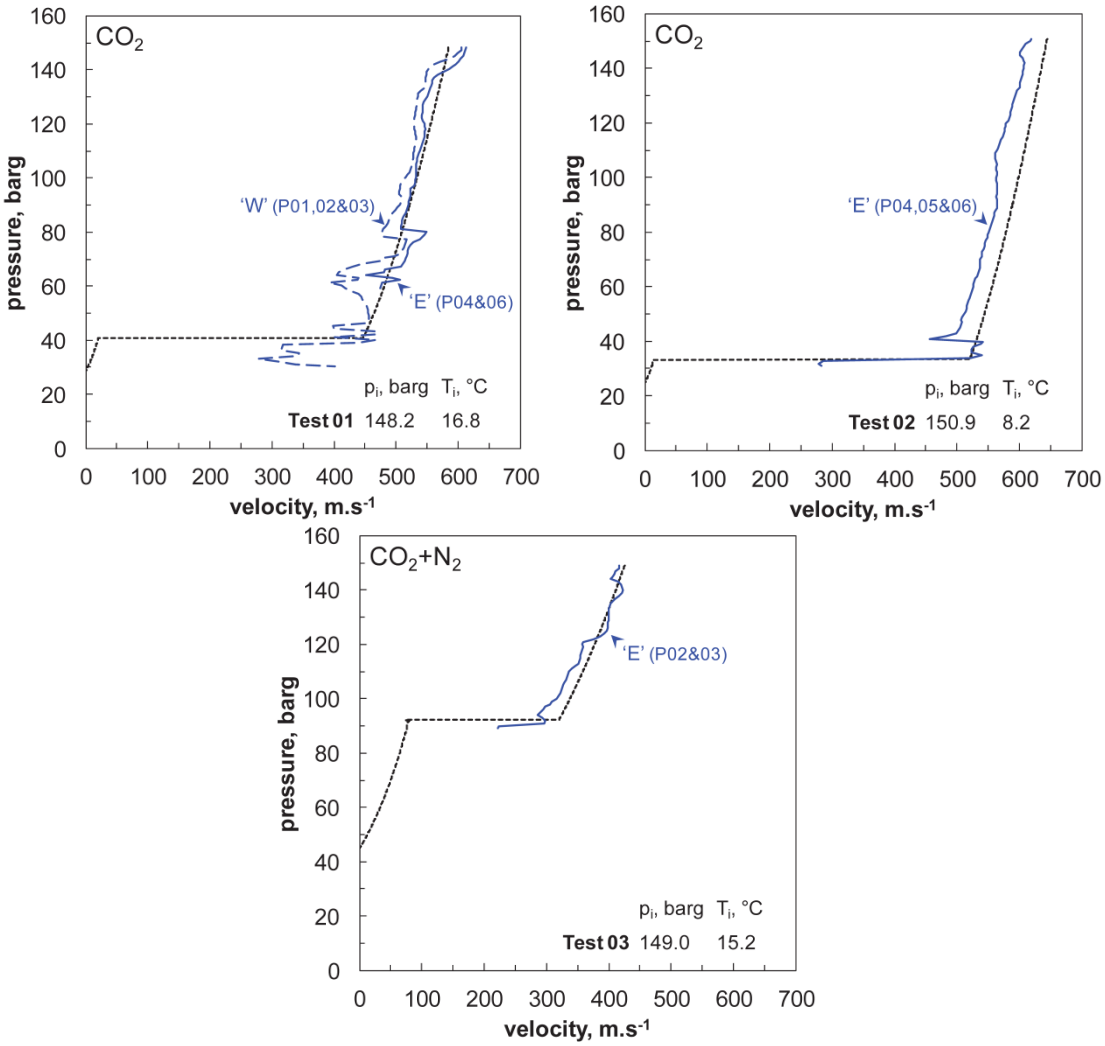

Figure 2.30: Measured and predicted decompression curves for the three West Jefferson Tests [56]

It was found that the resulting rupture in Tests 01 and 02 (pure CO_2) is short, similar to that in a liquid pipeline, while Test 03 produced a long and wide rupture, similar

to a rupture observed in a gas pipeline. However, the actual toughness of the pipe used in Tests 01 and 02 was significantly higher than the toughness required for arresting the propagation of the fracture. In contrast, the pipe toughness used in Test 03 was lower than the minimum required toughness to arrest a running fracture. This indicates that the minimum required pipe toughness must be determined accurately before installing the pipelines transporting CO_2 mixtures in order to avoid the issue of running fractures.

(a)

(b)

(c)

Figure 2.31: Rupture appearance of the three West Jefferson Tests

2.9 Summary

This chapter presented the current available knowledge concerning the decompression behaviour of CO_2. The development of CO_2 pipelines for Carbon Capture and Storage (CCS) raises new questions regarding the control of ductile fracture propagation and fracture arrest toughness criteria. However, the literature revealed that the concerns were mostly focused on natural gas and petroleum pipelines. Fracture propagation has not been considered in detail for CO_2 mixtures, and the safe engineering of CO_2-transmitting pipes asks for a refined understanding of the decompression speed behaviour of the mixtures.

More experimental and theoretical investigations of gas decompression behaviour in CO_2 pipelines are required. The experimental procedure is quite expensive and can be used to investigate limited factors. Theoretical prediction (i.e. using the CFD approach) is a valuable option in order to improve our knowledge. Anthropogenic CO_2 will contain impurities that can modify the fluid decompression characteristics quite significantly; it is therefore important for the modelling tools to handle CCS CO_2 mixtures efficiently. The feasibility of complex and possibly large simulations of fluid-pipe interactions, hydraulic transients and dispersion will otherwise be restricted.

The decompression behaviour in gas pipelines is predicted using simple models which are limited to the assumptions that they are one-dimensional, frictionless and isentropic, and have a homogeneous-equilibrium fluid flow and only differ in the choice of EOS. These models do not take into account the influence of actual pipe deformation and were mainly developed and validated for natural gas pipelines.

The proposed methodology in this research utilises the development of a new multi-dimensional CFD decompression model that takes into account several parameters that affect the decompression process in a CO_2 pipeline. To accurately predict the decompression behaviour of CO_2 mixtures, accurate means of predicting the thermodynamic properties of these mixtures using accurate equations of state is essential. To date, no EOS is specifically recommended for CO_2 mixtures. A comprehensive comparative study between some equations of state will be conducted in Chapter 3. The model will be provided by the accurate EOS based on the results of comparisons, and the model will be developed using the CFD software, ANSYS Fluent. The model results will be verified and validated against measured data of several shock tube tests. Factors such as initial conditions, fluid compositions, heat transfer, friction, phase change and actual pipe deformation will be covered and investigated using the proposed model.

Chapter 3 Equations of State for CO2 Mixtures

3.1 Introduction

To precisely predict the decompression behaviour of CO_2 mixtures, accurate means of predicting the thermodynamic properties of these mixtures using a reliable EOS is essential. To date, no EOS is specifically recommended for CO_2 mixtures, but the ability to accurately predict the density and speed of sound is considered the best way to gauge any weaknesses or strengths of equations of state. In this chapter, the applicability of currently available thermodynamic models to the most likely CO_2 mixtures is evaluated. The objective is to select the most accurate EOS for predicting the thermodynamic properties for CO_2 mixtures related to CCS applications. Three equations of state widely used in gas pipeline applications have been tested and evaluated in predicting the densities and speeds of sound. To validate the equations of state, the predicted results are compared to some of the current available experimental data.

3.2 Equations of State Studied in this Research

In this research, three equations of state are tested: GERG-2008 [105, 106] EOS developed by Prof. Wagner; PR implemented in the software REFPROP [76]; and BWRS implemented in the software Simulis Thermodynamics [122]. A brief description about the equations of state is presented in the following sections.

3.2.1 GERG-2008 EOS

The GERG-2008 EOS [105, 106] has been described in Chapter 2 section 2.7.2.5. The validity of this EOS agrees with the requirements of transporting CO_2 through pipelines, as it provides a satisfactory result for temperatures in the range (90 K – 450 K) and pressures up to 35 MPa. GERG-2008 calculations match the most accurate measured data of density, sound speeds, and enthalpy differences for

mixtures in both gas and supercritical phases, mostly within their low experimental uncertainties.

3.2.2 REFPROP

REFPROP [123] is an abbreviation for REFerence fluid PROPerties. This software is established at the National Institute of Standards and Technology (NIST) to provide calculations for the thermodynamic and transport properties of fluid mixtures. For mixture calculations, REFPROP applies mixing rules to the Helmholtz energy of the fluid components, and a departure function is used to consider the deviation from ideal mixing.

In REFPROP, the PR EOS, which is referred to as REFPROP_PR, is selected for the current comparison. This equation has lower accuracy compared to some other modern equations of state [106], yet it has been extensively used in most of the current gas decompression models. In general, this EOS is not recommended in REFPROP; nevertheless, it is much faster than other built-in equations of state for calculating the properties of some mixtures, particularly at the saturation states.

3.2.3 Simulis Thermodynamics

Simulis Thermodynamics [122] is a software package developed to calculate thermophysical properties and Vapour-Liquid Equilibrium (VLE) of pure/multi-component fluids. The code can be incorporated into any other programs anticipated for wider fields of application (e.g. modelling).

The equations of state and their software packages used in this study are listed in Table 3.1.

Table 3.1: Equations of state studied in the project

Name of EOS	Software package
GERG-2008	Stand alone
REFPROP_PR	REFPROP
SIMULIS_BWRS	Simulis Thermodynamics

3.3 Validation of Equations of State

The composition of the CO_2 stream transported in the pipeline for CCS will depend on its source. There are three methods available for capturing CO_2 from industrial sites (e.g. power plants): post-combustion, pre-combustion and oxyfuel. Table 3.2 lists three typical compositions of CO_2 mixtures captured from three process routes, which represent typical CO_2 compositions for Australian conditions [124].

Table 3.2: Typical compositions of CO_2 mixtures captured from post-combustion, pre-combustion and oxyfuel [124]

Gas components	Post-combustion (Mole %)	Pre-combustion (Mole %)	Oxyfuel (Mole %)
CO_2	99.97	95.66	95.87
N_2	0.01	0.43	1.38
O_2	0.01	0.43	1.38
CH_4	-	2	-
H_2	-	1	-
Ar	0.01	0.43	1.37
CO	-	0.04	-
H_2S	-	0.01	-

It can be seen from Table 3.2 that

- The CO_2 streams from all three capture processes are CO_2-rich mixtures ($CO_2\% > 90\%$);

- The CO_2 stream from the post-combustion capture process is very close to pure CO_2;
- The major impurities include N_2, O_2, CH_4, H_2, Ar, CO and H_2S.

To examine the validity of the equations of state listed in Table 3.1, the calculated results have been compared with:

(a) The measured densities and sound speeds of pure CO_2;

(b) The measured densities for binary CO_2 mixtures (CO_2+N_2, CO_2+O_2, CO_2+CH_4, CO_2+H_2, CO_2+Ar, CO_2+CO and CO_2+H_2S).

The deviation between the predicted and the measured property is determined using the following formula:

$$\text{Deviation (\%)} = \left(\frac{Y_{cal} - Y_{exp}}{Y_{exp}}\right) \times 100 \tag{3.1}$$

while the absolute average deviation is obtained using:

$$AAD = \frac{\sum \left|\frac{Y_{cal} - Y_{exp}}{Y_{exp}}\right|}{N} \times 100\% \tag{3.2}$$

where Y_{cal} and Y_{exp} are the calculated and experimental values of the property Y, respectively, and N is the number of data points.

For calculating the standard deviation of the distribution of the relative error between the predicted and the measured data, the following formula is used:

$$\sigma = \sqrt{\frac{\sum (E - AAD)^2}{N}} \tag{3.3}$$

where σ is the standard deviation and E represents the deviation (error value).

3.3.1 Prediction for Pure CO_2

Figure 3.1 shows the deviations of the densities calculated by the EOS (ρ_{cal}) from the measured values (ρ_{exp}) published in reference [125] for various pressures (P). The value of the Absolute Average Deviation (AAD) for each EOS is inserted in the corresponding figure. Figure 3.2 displays the relative deviations of the calculated speeds of sound (C_{cal}) from the measured values (C_{exp}) published in reference [126] w.r.t. pressure (P).

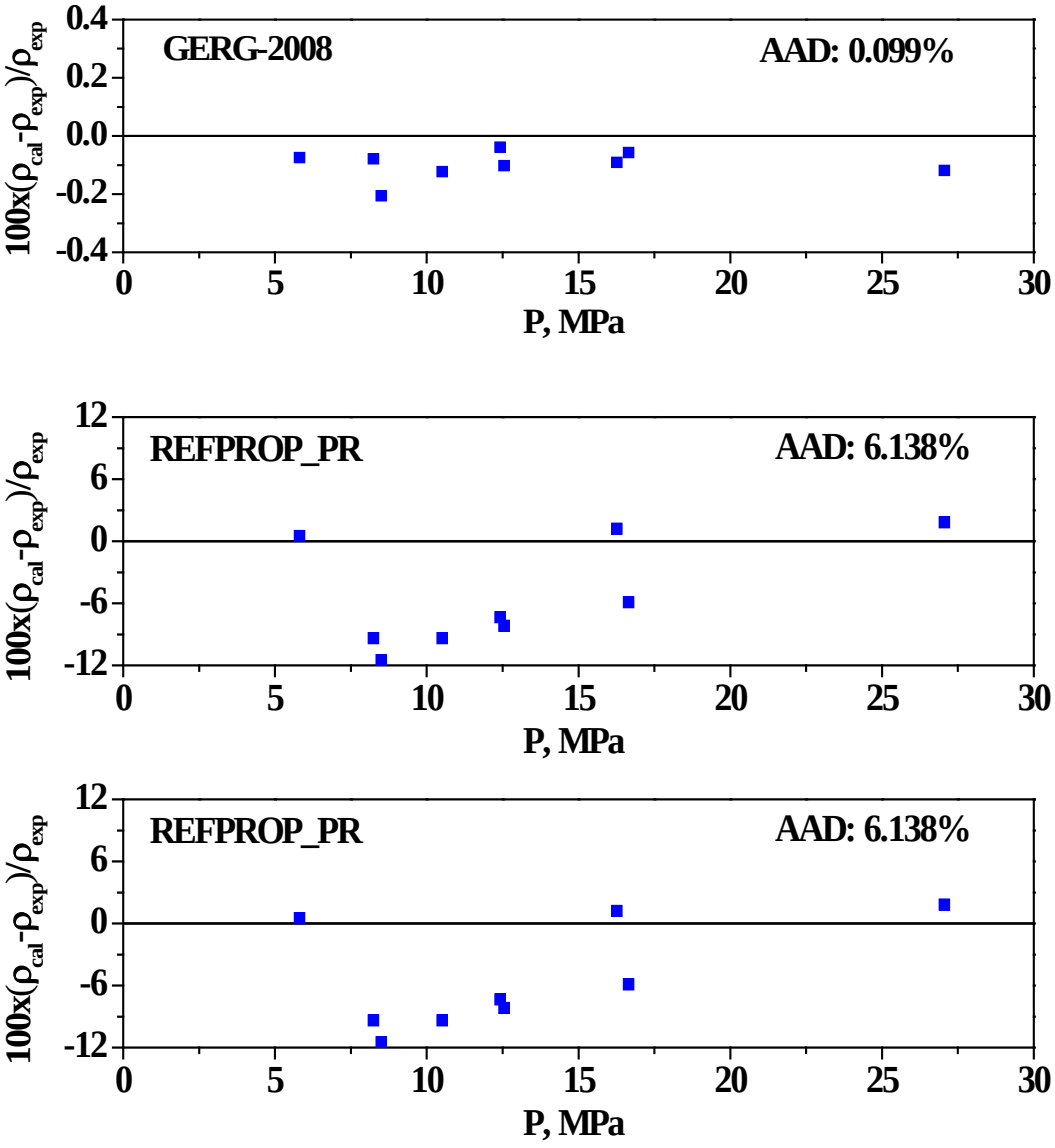

Figure 3.1: Comparisons between measured densities and calculated densities for pure CO_2

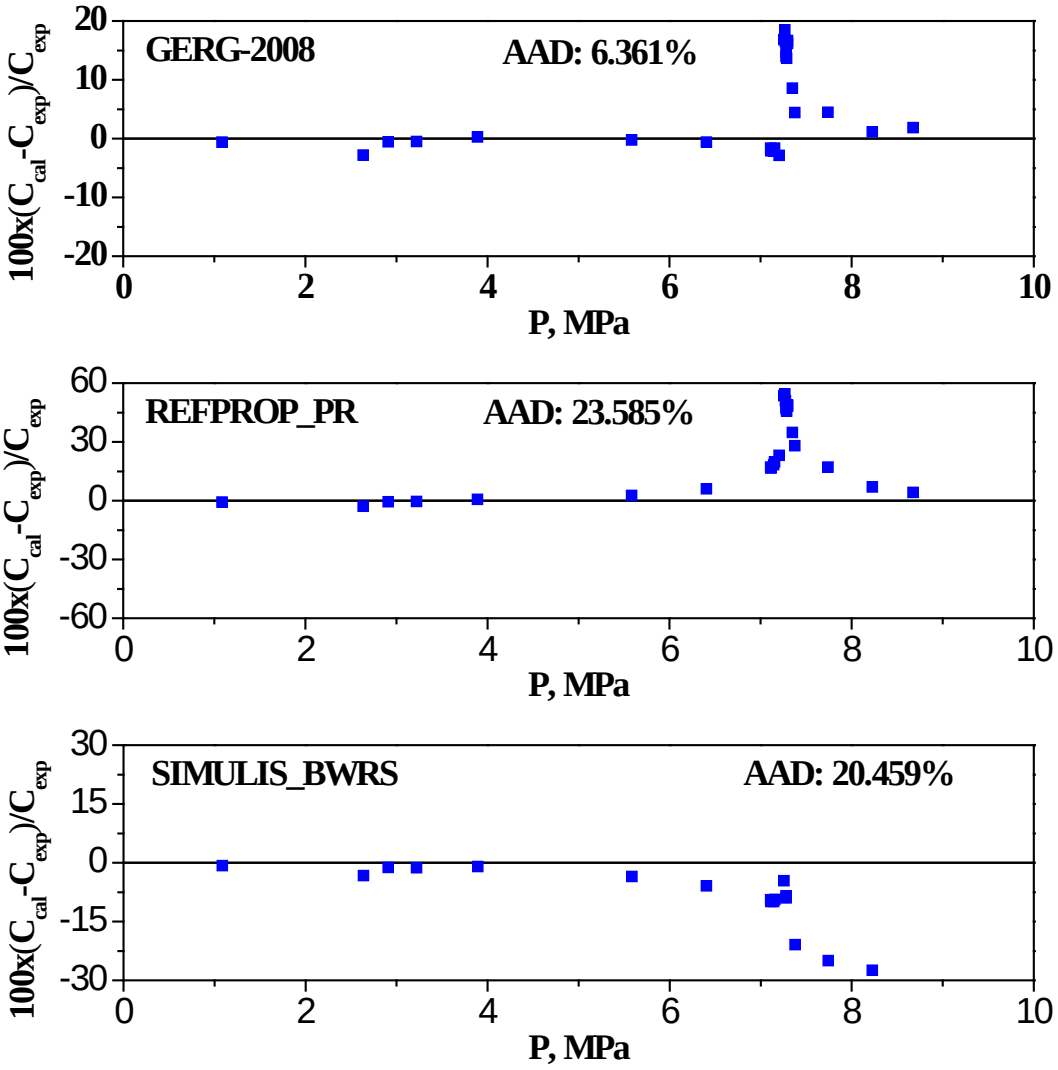

Figure 3.2: Comparisons between measured and calculated speeds of sound for pure CO_2

The AADs displayed in Figures 3.1 and 3.2 are collected and listed in Tables 3.3 and 3.4 for the purpose of comparison. Comments are given on the prediction accuracies in the tables. Tables 3.3 and 3.4 also show the temperature range, pressure range and number of total points used in the calculations. For some points, the EOS fails to predict the result due to a convergence issue. These points are named the dead points. The number of dead points gives an indication of the efficiency of the optimisation engine used in the EOS software. If the EOS is implemented in the CFD simulation,

the convergence of the optimisation algorithm plays a crucial role. Failure to converge at a single point may cause the collapse of the whole simulation.

Table 3.3: Results of comparisons with the measured densities for pure CO_2

EOS	Temp.(K)	Press.(MPa)	Total points	Dead points	AAD %	Comment
GERG-2008	250~310	5.8~27.1	9	0	0.099	Very good
REFPROP_PR				0	6.138	Poor
SIMULIS_BWRS				0	3.075	Medium

Table 3.4: Results of comparisons with the measured speeds of sound for pure CO_2

EOS	Temp.(K)	Press. (MPa)	Total points	Dead points	AAD %	Comment
GERG-2008	303.15	1.09~8.67	26	0	6.361	Medium
REFPROP_PR				0	23.585	Very poor
SIMULIS_BWRS				7	20.459	Very poor

The following points summarise the observations from Figures 3.1 and 3.2, and Tables 3.3 and 3.4:

- GERG-2008 can predict very accurate densities. AADs are around 0.1%;
- The density predictions by REFPROP_PR and SIMULIS_BWRS EOS are less accurate than the GERG-2008 EOS;
- Compared to the density calculations, all the equations of state have larger AADs for the predictions of the speed of sound;

- GERG-2008 more accurately predicts speed of sound compared to REFPROP_PR and SIMULIS_BWRS;
- REFPROP_PR and SIMULIS_BWRS produce very bad speed of sound predictions (AAD > 20%);
- A detailed inspection of Figure 3.2 indicates that the poor predictions of the speed of sound are mainly located close to the critical point (P = ~7.37 MPa);
- SIMULIS_BWRS has seven dead points out of a total 26 points, while the other equations of state can predict the speed of sound for all the points.

3.4 Prediction for CO_2 Mixtures

In this section, the studied equations of state are examined in terms of predicting the density of several CO_2 binary mixtures. The calculated results will be compared with the measured data for validation purposes. This comparison will lead to selection of the best EOS that will be recommended for the calculation of CCS streams. Due to the unavailability of speed of sound measurements for CO_2 mixtures, this property will not be considered for the comparison.

The calculated densities were compared with the measured values for various binary CO_2 mixtures (CO_2+N_2 [127], CO_2+O_2 [128], CO_2+CH_4 [129], CO_2+H_2 [130], CO_2+Ar [131], CO_2+CO [132] and CO_2+H_2S [133]). The components most frequently existing in all CCS streams are N_2 and O_2. Figures 3.6 and 3.7 show the deviations for all the equations of state for CO_2+N_2 and CO_2+O_2.

AADs and comments on the calculation accuracy are given in Tables 3.8–3.14 for all the binary mixtures. The temperature range, pressure range, fraction of CO_2, number of total calculation points and number of dead points are also listed in the tables.

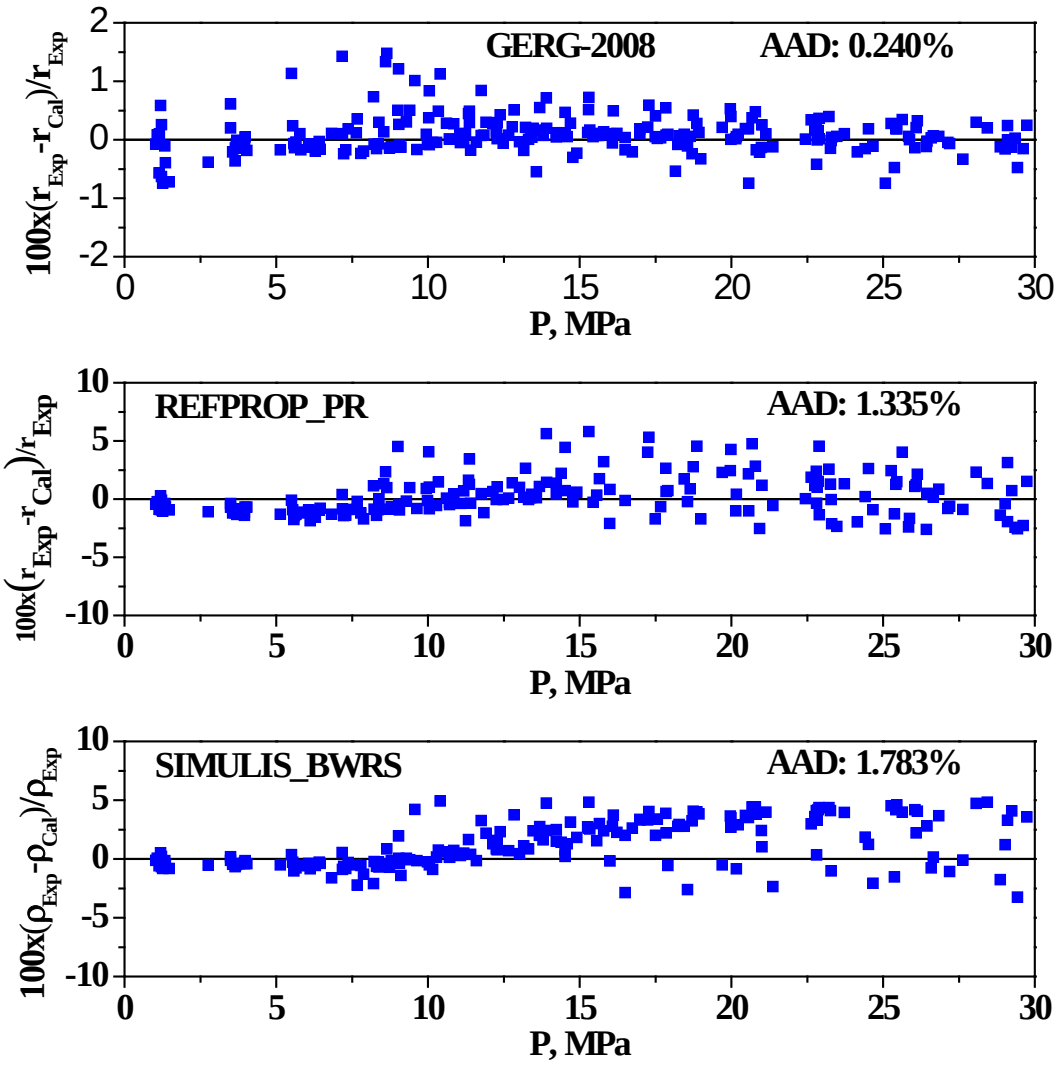

Figure 3.3: Comparisons of densities between experiment and calculation for CO_2+N_2 mixture

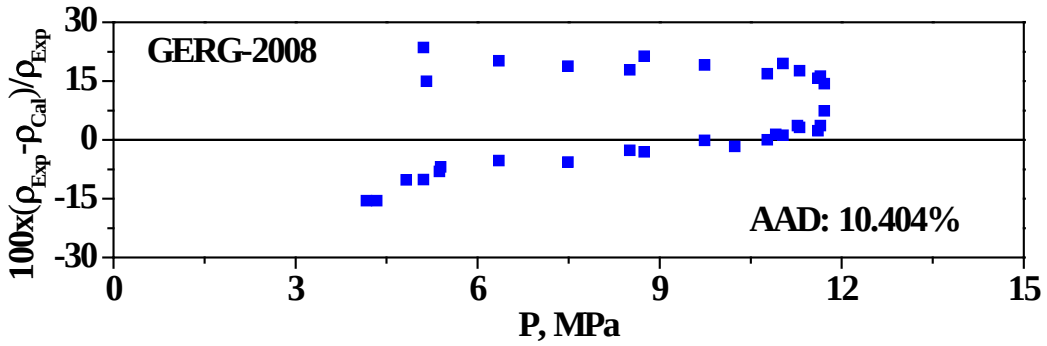

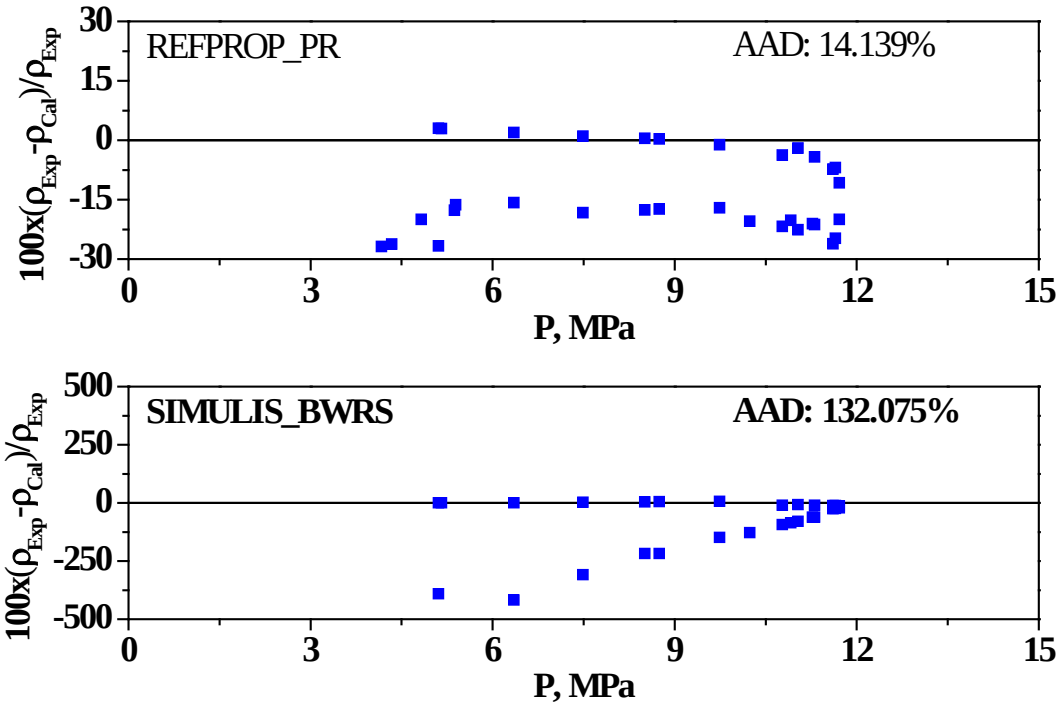

Figure 3.4: Comparisons of densities between experiment and calculation for CO_2+O_2 mixture

The following points summarise the major findings:

- In general, all the equations of state can predict good or reasonable densities for CO_2+N_2, CO_2+CH_4, CO_2+H_2, CO_2+Ar and CO_2+CO. Yet the predictions for CO_2+O_2 and CO_2+H_2S are bad;
- AADs of GERG-2008 are better than those of other equations of state for most binary mixtures. GERG-2008 has a slightly higher AAD than SIMULIS_BWRS EOS for CO_2+H_2S;
- GERG-2008 has been carried out for all the calculations without any dead points, while the other two equations encounter convergence problems, resulting in several dead points, for some calculation conditions and mixtures;

- It was determined that the GERG-2008 EOS outperformed the other equations of state in predicting the density of all tested binary mixtures except for CO_2+H_2S.

Table 3.5: Results of comparisons with the measured densities for CO_2+N_2

EOS	Temp (K)	Press. (MPa)	CO_2 fraction	Total points	Dead points	AAD (%)	Comment
GERG-2008	225 ~ 350	1.03 ~ 30.7	0.5-0.9	238	0	0.24	Very good
REFPROP_PR					41	1.335	Good
SIMULIS_BWRS					43	1.783	Good

Table 3.6: Results of comparisons with the measured densities for CO_2+O_2

EOS	Temp (K)	Press. (MPa)	CO_2 fraction	Total points	Dead points	AAD (%)	Comment
GERG-2008	273.15	4.17 ~ 11.71	0.594 ~ 0.965	33	0	10.404	Poor
REFPROP_PR					0	14.139	Poor
SIMULIS_BWRS					2	132.075	Very poor

Table 3.7 : Results of comparisons with the measured densities for CO_2+CH_4

EOS	Temp (K)	Press. (MPa)	CO_2 fraction	Total points	Dead points	AAD (%)	Comment
GERG-2008	273.15 ~ 288.15	2.42 ~ 14.52	0.679 ~ 0.942	54	0	1.137	Good
REFPROP_PR					3	1.062	Good
SIMULIS_BWRS					6	4.403	Medium

Table 3.8: Results of comparisons with the measured densities for CO_2+H_2

EOS	Temp (K)	Press. (MPa)	CO_2 fraction	Total points	Dead points	AAD (%)	Comment
GERG-2008	323.1	0.1 ~ 6.0	0.766	13	0	0.894	Good
REFPROP_PR					0	1.298	Good
SIMULIS_BWRS					0	0.213	Very good

Table 3.9: Results of comparisons with the measured densities for CO_2+Ar

EOS	Temp (K)	Press. (MPa)	CO_2 fraction	Total points	Dead points	AAD (%)	Comment
GERG-2008	288.14	2.48 ~ 14.53	0.7 ~ 0.94	88	0	1.659	Good
REFPROP_PR					3	4.549	Medium
SIMULIS_BWRS					*	*	*

Note that (*) means Argon is not available in Simulis Thermodynamics.

Table 3.10: Results of comparisons with the measured densities for CO_2+CO

EOS	Temp (K)	Press. (MPa)	CO_2 fraction	Total points	Dead points	AAD (%)	Comment
GERG-2008	323.15	0.1 ~ 6.5	0.299	15	0	0.194	Very good
REFPROP_PR					0	0.513	Good
SIMULIS_BWRS					0	0.431	Very good

Table 3.11: Results of comparisons with the measured densities for CO_2+H_2S

EOS	Temp (K)	Press. (MPa)	CO_2 fraction	Total points	Dead points	AAD (%)	Comment

GERG-2008	220.54 ~ 342	0.61 ~ 24.22	0.707 ~ 0.939	40	0	10.246	Poor
REFPROP_PR					16	20.55	Very poor
SIMULIS_BWRS					0	8.738	Poor

3.5 Summary

This chapter provided an evaluation study of three equations of state. The comparisons were conducted in terms of predicting the thermophysical properties for CO_2 and CO_2-based mixtures. The key sections of the chapter have provided a critical comparison which shows the validity of each of the tested equations of state in calculating the properties of some mixtures related to CCS technology, against the currently available measured data found in the literature. The following points present the major conclusions of the present comparative study:

- GERG-2008 has the best computing efficiency compared to other equations of state;
- GERG-2008 is more accurate and flexible in dealing with all mixtures for all the tested properties.

Based on the outcomes of this comparison study, it has been concluded that GERG-2008 exhibits better calculation accuracy and better computing convergence than other equations of state, mostly over the whole range of tested conditions. For the considerations above, the GERG-2008 EOS will be used in the current research as the main thermodynamic property calculation model for CO_2 mixtures. In the following chapter, the GERG-2008 EOS will be implemented into the CFD package, ANSYS Fluent, which will be used to develop a multi-dimensional CFD

decompression model. Some problems encountered with GERG-2008 calculations will be solved in Chapter 4.

Chapter 4 Development of Computational Fluid Dynamics (CFD) Gas Decompression Model

4.1 Introduction

This chapter describes the methodology used to develop a gas decompression model using the Computional Fluid Dynamics (CFD) technique. It starts with a physical description of the gas decompression process. Modelling of gas decompression in an initially pressurised gas pipeline can be conducted by solving the transient form of the governing equations of fluid flow. The main modelling assumptions used to develop the present decompression model are introduced. The mathematical equations describing the process in terms of the conservation for mass, momentum and energy used by the model are presented in section 3.2.2. This is followed by an overview of the creation of the computational domain, a description of the boundary conditions, setting up of the equations, the numerical solution of the equations, solver selection and its sub-models.

The second part of this chapter focuses on the process of implementing two real-gas equations of state, the Peng Robinson (PR) EOS and the GERG-2008 EOS in the CFD software, ANSYS Fluent. In this section, a novel technique that can overcome issues related to the modern multi-component GERG-2008 EOS library is introduced. This implementation permits flexibility to conduct numerical studies for several gas mixtures. The development of a multi-dimensional CFD decompression model in conjunction with the GERG-2008 EOS allows an investigation of the effects of several parameters on the decompression behaviour of CO_2 pipelines. These parameters include a wide range of initial conditions, gas compositions, internal pipe roughness, pipe diameter, and heat transfer between the gas and the pipe wall. Unlike the currently available decompression models, investigating the effect

of the pressure distribution behind the crack tip and the actual pipe deformation, which is a 3D phenomenon, becomes feasible using this model.

4.2 Methodology

In the event of a rupture at a particular location in a gas pipeline, an expansion wave (decompression wave) is set up, and will propagate in both directions of the pipeline away from the fracture location, as depicted schematically in Figure 4.1. The gas will rapidly escape from inside the pipeline into the ambience due to the difference in pressure. The flow is choked (attains sonic speed) at the exit if the initial pressure drop is high enough. The decompression wave travels at a speed nearly equal to the speed of sound in the fluid.

The decompression wave speed (w) can be determined if the speed of sound (c), the 'outflow' velocity (u) and the pressure profile ($p(x)$) can be determined as a function of time along the length of the pipeline. This requires a detailed analysis of the dynamics, the thermodynamic properties and the composition of the fluid. During the decompression, the accompanying low temperature could lead to partial condensation of the compressed gas. The model must account for the phase change and the real behaviour of gases under such conditions.

The rapid outflow from a pressurised gas pipeline following rupture can be predicted by numerically solving the transient form of the governing equations of fluid flow (mass, momentum and energy conservation), in conjunction with a suitable EOS. Recent advancements in technology have significantly increased the available computing power, allowing more accurate modelling of gas decompression in pipelines.

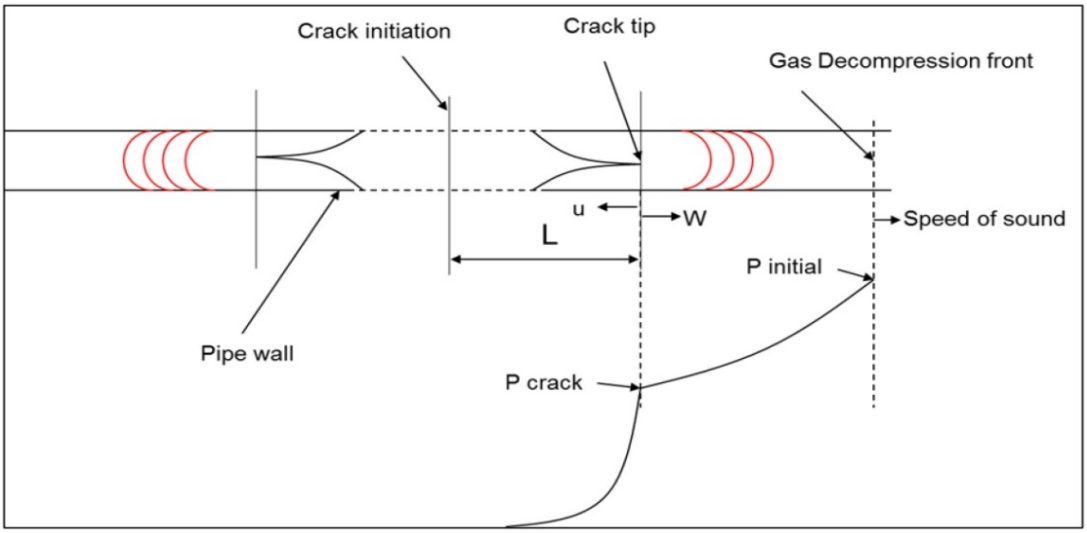

Figure 4.1:Schematic of decompression wave in fractured gas pipeline

In this research, the CFD technique is used to solve the governing equations and thus to simulate the flow. The CFD technique was chosen over other possible methods (such as using MATLAB) due to the availability of the necessary CFD software, and the advantages it offers.

The CFD software, ANSYS Fluent, was chosen to numerically solve the fluid flow governing equations. This tool can simulate a wide range of compressible, laminar or turbulent, steady-state or transient flows of ideal or real fluids, in multi-dimensional geometries [134]. This CFD software was used in this research because it satisfies the three main demands required for real fluid decompression analysis:

- Ability to simulate transient flows;
- Possibility of invoking an accurate real-gas EOS;
- Ability to handle multi-dimensional geometries.

Even though ANSYS Fluent does not have a default EOS that can accurately simulate the decompression of multi-component mixtures, and does not provide access to the source code, subroutines can be added to the main program through

User Defined Functions (UDFs). This allows users to implement a suitable EOS, define the boundary conditions and/or source terms using the 'C' programing language.

4.2.1 Model Assumptions

The CFD technique will be used to simulate real-gas pipeline decompression experiments such as 'shock tube' and also full-scale burst tests. The physical flow domain in the shock tube test consisted of the initially highly pressurised gas in a horizontal pipe, which undergoes a 'full-bore' opening at one end using a rupture disc. The following assumptions were made when developing the current decompression model:

- Horizontal pipeline with no intersections or subdivisions;
- Instantaneous rupture;
- 2D flow for shock tube test and 3D flow for burst test simulations;
- Non-isentropic flow;
- Gas velocity before the rupture negligible compared with the conditions post-rupture;
- 'No-slip' condition between the wall and the fluid;
- Adiabatic wall (no heat transfer between the pipe wall and the surrounding).

4.2.2 Governing Equations

This section describes the 2D form of unsteady, governing differential equations of conservation of mass, momentum and energy. More details about the derivation of the equations can be obtained from Bird et al. [135].

4.2.2.1 The Continuity Equation

The continuity (conservation of mass) equation [135] can be written as:

$$\frac{\partial \rho}{\partial t} + \frac{\partial}{\partial x}(\rho v_x) + \frac{\partial}{\partial y}(\rho v_y) = S_m \tag{4.1}$$

where t is the time; ρ the density; x the axial coordinate; y the radial coordinate; v_x the axial velocity; v_y the radial velocity; and S_m the source term.

4.2.2.2 The Conservation of Momentum Equations

Applying the law of conservation of momentum gives the basic set of equations governing the fluid motion. These sets of equations are employed to calculate the velocity and pressure field within the computational domain. The conservation of momentum is represented in 2D form, so the following equations represent the axial and radial momentums, respectively:

x-momentum:

$$\frac{\partial}{\partial t}(\rho v_x) + \frac{\partial}{\partial x}(\rho v_x v_x) + \frac{\partial}{\partial y}(\rho v_y v_x) = -\frac{\partial p}{\partial x} + \frac{\partial}{\partial x}\left[\mu\left(2\frac{\partial v_x}{\partial x} - \frac{2}{3}(\nabla.\vec{v})\right)\right] + \frac{\partial}{\partial y}\left[\mu\left(\frac{\partial v_x}{\partial y} + \frac{\partial v_y}{\partial x}\right)\right] + F_x \tag{4.2}$$

y-momentum:

$$\frac{\partial}{\partial t}(\rho v_y) + \frac{\partial}{\partial x}(\rho v_x v_y) + \frac{\partial}{\partial y}(\rho v_y v_y) = -\frac{\partial p}{\partial y} + \frac{\partial}{\partial y}\left[\mu\left(2\frac{\partial v_y}{\partial y} - \frac{2}{3}(\nabla.\vec{v})\right)\right] + \frac{\partial}{\partial x}\left[\mu\left(\frac{\partial v_y}{\partial x} + \frac{\partial v_x}{\partial y}\right)\right] + F_y \tag{4.3}$$

where F includes the gravitational and external body force, and contains other source terms, and:

$$\nabla.\vec{v} = \frac{\partial v_x}{\partial x} + \frac{\partial v_y}{\partial y} \tag{4.4}$$

4.2.2.3 The Conservation of Energy Equation

ANSYS Fluent solves the general energy equation in the following form [136]:

$$\frac{\partial}{\partial t}(\rho E) + \nabla.\left(\vec{v}(\rho E + p)\right) = \nabla.\left(k_{eff}\nabla T - \sum_j h_j \vec{J}_j + \left(\bar{\bar{\tau}}_{eff}.\vec{v}\right)\right) + S_h \qquad (4.5)$$

where E is the fluid energy defined by:

$$E = h - \frac{p}{\rho} + \frac{v^2}{2} \qquad (4.6)$$

and h is the sensible enthalpy and can be expressed as:

$$h = \int_{T_{ref}}^{T} C_p dT \qquad (4.7)$$

where in Fluent, T_{ref} is 298.73 K and k_{eff} is the effective thermal conductivity (=k + k_t), where k and k_t are the laminar and turbulent thermal conductivities, respectively; h_j is the specific enthalpy of species j; and $\vec{J}_j$ the diffusion flux of species j.

The first three terms in the bracket on the right hand side of Equation 4.5 represent the energy flow due to conduction, species diffusion, and viscous dissipation, respectively. The term $\sum_j h_j \vec{J}_j$ ('species diffusion') can be simplified to $h\vec{J}$ assuming a homogeneous fluid with only one species. Similarly, S_h can be neglected if there is no chemical reaction, combustion or radiation involved. These four equations (4.1, 4.2, 4.3 and 4.5) involve five unknowns: velocity components v_x, v_y, pressure p, temperature T and density ρ. For closure, a fifth equation is needed: this is the EOS (invoked using UDFs).

4.2.3 Geometry Creation

The geometry has been created using the ANSYS module DesignModeler, a CAD

(Computer Aided Design) tool which is part of the ANSYS 'Workbench' console. This application is designed to be used as a geometry editor, similar to the other existing CAD models such as GAMBIT. The DesignModeler application is a parametric feature-based solid modeller so the user can intuitively and quickly modify the physical dimensions of geometries for the purpose of other analysis. It is possible to import pre-defined CAD properties and/or geometry based on coordinate systems or work points using a text file. Such features allow, for example, to 'create' an opening in the pipeline.

In CFD simulations, identifying the physical flow domain that will be modelled is an important step because the corresponding computational domain can be created accordingly, and the initial and boundary conditions imposed. The shock tube test described in [13] is used to develop the geometry for the purposes of verification and the validation of the model. In the shock tube test, the flow was through a long, constant diameter pipe. Figure 4.2 shows the physical domain used to study the decompression process, the computational domain, and the physical boundary conditions used to carry out the simulation.

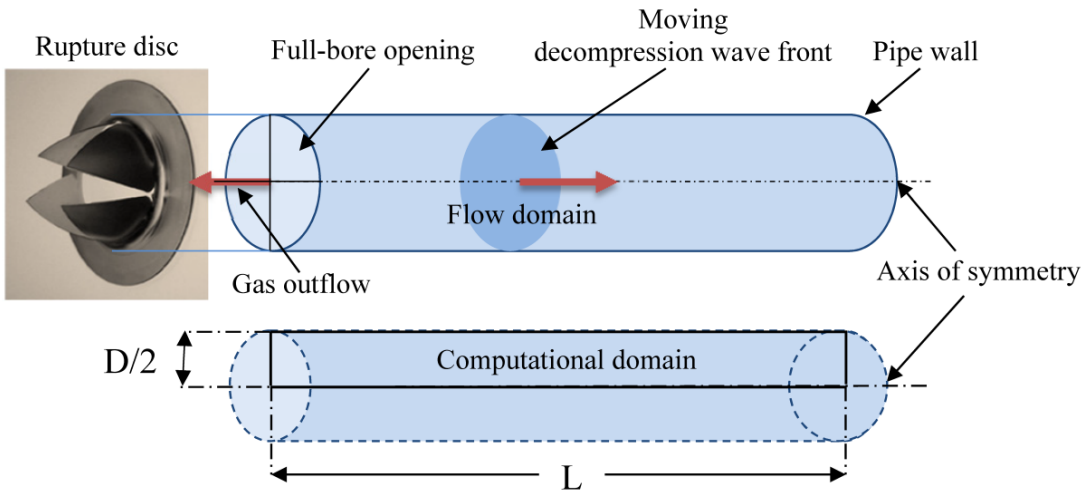

Figure 4.2: Domain dimensions and boundary conditions for 2D simulation

In the simulation, the length of the pipe (L) is not always identical to the pipe length; in the experimental tests the aim is to reduce the computational runtime. The sufficient pipe length in the simulation can be determined using the location of the last pressure transducer on the shock tube and the initial decompression wave speed in that particular fluid mixture. The aim is to ensure that the reflected decompression wave from the far end of the pipe will not affect the pressure reading at the last monitoring point. So the time taken by the reflected decompression wave front to reach the last pressure transducer's location can be determined using the following developed formula:

$$t_w = \frac{L}{w} + \frac{(L - x)}{w} \geq t_{exp} \tag{4.8}$$

where t_w is the time taken by the decompression wave to reach location x after reflecting from the wall (pipe end); t_{exp} is the total time used in the experimental test to determine the decompression wave speed; L is the total pipe length; and w is the decompression wave speed (equal to the initial speed of sound before rupturing). The value of L will be changed until the condition ($t_w \geq t_{\text{exp}}$) is satisfied.

4.2.4 Boundary Conditions

The governing differential equations need to be supplemented by boundary conditions before they can be solved. The boundary conditions define a fluid or heat flow problem. It conveys the necessary information about the quantity of the fluid entering the computational domain, where it can leave, and what its pressure and/or temperature on entry is, and so on. For an axisymmetric 2D pipe geometry, there are four edges bounding the computational domain: outlet boundary, two wall boundaries and the symmetry boundary. The above boundary conditions are used to

model the decompression process from the shock tube test, although other boundary conditions can be used based on the physical problem to be modelled.

4.2.4.1 Outlet Boundary Condition

The outlet boundary is set to model the outflow from the rupture disc. At the rupture end (x=0), the fluid was considered to be exposed to ambient pressure (p_{static}=101325 Pa, or 0 Pa g). This boundary condition allows the gas to flow out from inside the pipe due to the variation between the operating and the atmospheric pressure.

4.2.4.2 Wall Boundary Condition

Based on the computational domain of the pipe, the 'wall' boundary condition is specified on two sides of the flow domain representing the end and the top of the computational domain (at $x=L$ and $y=D/2$). The no-slip condition is specified at the wall boundary. Accordingly, the velocity will be zero at the interior cell-face adjacent to the wall. ANSYS Fluent automatically considers this condition if a viscous flow is assumed.

4.2.4.3 Symmetry Boundary Conditions

As the gas flow takes place in a straight circular cross-section pipe with outflow from a full-bore opening (rupture disc), as shown in Figure 4.2, the axial symmetry allows the creation of a 2D computational domain. ANSYS Fluent specifies that all quantities have zero flux across the symmetry boundary.

4.2.5 Meshing

Grid creation was performed using the ANSYS Mesher platform, which is a component of ANSYS Workbench. To ensure an accurate solution, the mesh is

refined in regions of large flow gradients, i.e. near the outlet and in the boundary layer adjacent to the wall. A mesh size independence study was conducted to ensure the accuracy of the model. In order to properly predict the velocity profile close to the wall, the dimensionless distance y^+ (theoretical) was used to determine the appropriate location of the cell next to the wall. The dimensionless wall distance y^+ for a wall tube-bounded flow is defined as:

$$y^+ = \frac{\rho U_\tau y}{\mu} \tag{4.9}$$

where ρ, y, U_τ and μ are fluid density, the distance to wall, the friction velocity and the dynamic viscosity, respectively.

The following calculations were performed to determine the proper y-value considering the recommendation of y^+ ($30 \leq y^+ \leq 300$). Since the aimed y^+ value and the properties of the fluid are known, it becomes possible to find the friction velocity (U_τ), which is defined by:

$$U_\tau = \sqrt{\frac{\tau_w}{\rho}} \tag{4.10}$$

where τ_w is the wall shear stress and can be determined from the skin friction coefficient (C_f):

$$\tau_w = \frac{1}{2} C_f \rho U^2 \tag{4.11}$$

The skin friction coefficient C_f can be determined from the experimental formula of Blasius for turbulent flow in smooth pipes [137]:

$$C_f = 0.079 Re_D^{-0.25} \tag{4.12}$$

where Re_D is the Reynolds number based on pipe diameter, and can be calculated as:

$$Re_D = \frac{\rho U D}{\mu} \tag{4.13}$$

The first cell location (y) can then be estimated by assuming a value of y^+ within the range of limitation specified above. Several cells are generated to cover the boundary layer thickness. The cell adjacent to the wall was set based on the dimensionless distance with a defined mesh-growth factor (i.e. 1.25). An example of the generated mesh distribution of flow domain near the outlet is shown in Figure 4.3.

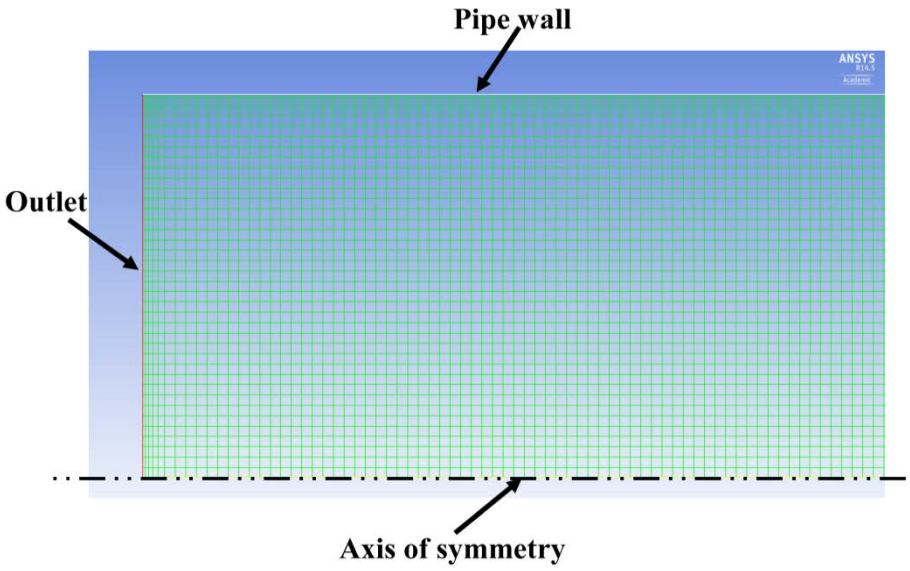

Figure 4.3: An example of 2D computational grid

4.2.6 Numerical Method

ANSYS Fluent uses the Finite Volume Method (FVM) to discretise the governing differential equations described in section 4.2.2. In this method, the computational domain is divided into a number of sub-regions called ‘control volumes’ or ‘cells’, as depicted in Figure 4.4.

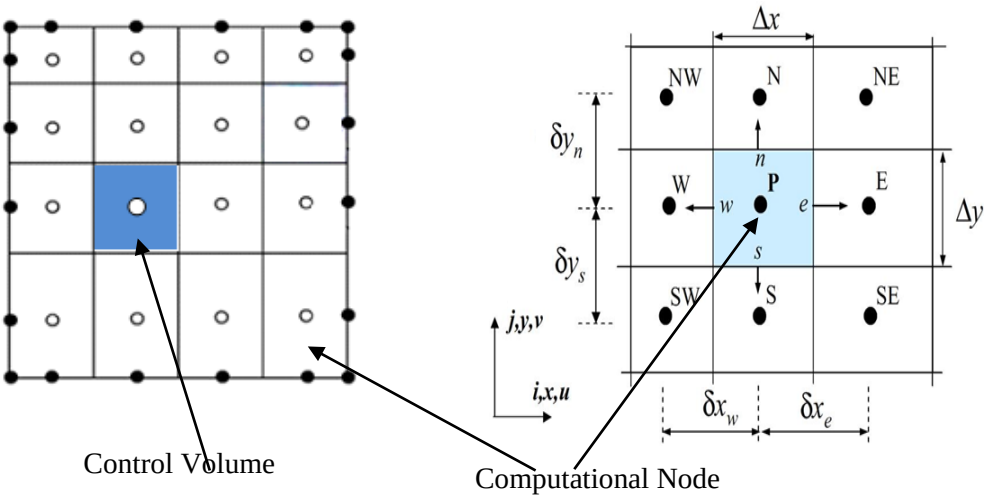

Figure 4.4: 2D Finite volume method [138]

The above conservation equations for the transport of a fluid variable in an unsteady multi-dimensional flow can be generalised in the following form:

$$\underbrace{\frac{\partial}{\partial t}(\rho\ \Phi)}_{Unsteady} + \underbrace{div\left(\rho\ \overrightarrow{V}\ \Phi\right)}_{Convection} = \underbrace{div(\Gamma_{\Phi}\ grad\ \Phi)}_{Diffusion} + \underbrace{S_{\Phi}}_{Sources} \qquad (4.14)$$

where,

- Φ is the fluid variable (=1 for the continuity equation; =*u* for the x-momentum equation; =*v* for the y-momentum equation; =*w* for the z-momentum equation; and =*h* for the energy equation);
- ρ is the density;
- $\overrightarrow{V}$ is the Velocity vector ($\overrightarrow{V} = v_x.\ \overrightarrow{i} + v_y.\ \overrightarrow{j} + v_z.\ \overrightarrow{k}$);
- Γ_{Φ} is the diffusive exchange coefficient;
- S_{Φ} is the source term of Φ;

and

- $grad\ (\nabla) = \frac{\partial}{\partial x} + \frac{\partial}{\partial y} + \frac{\partial}{\partial z}$

The governing equations are integrated over all the control volumes of the computational domain. The unsteady conservation equation for transport of a scalar quantity Φ is written in integral form for an arbitrary control volume as follows:

$$\int_{CV}\left(\int_{t}^{t+\Delta t}\frac{\partial}{\partial t}(\rho\Phi)dt\right)dV+\int_{t}^{t+\Delta t}\left(\int_{A}\left(\rho\vec{V}\Phi\right)dA\right)dt = \int_{t}^{t+\Delta t}\left(\int_{A}(\Gamma_{\Phi}\nabla\Phi)dA\right)dt+\int_{t}^{t+\Delta t}\left(\int_{CV}S_{\Phi}dV\right)dt \quad (4.15)$$

In discretised form, the above equation can be expressed in the form of a linear algebraic equation of the form:

$$a_P\phi_P = a_W\phi_W + a_E\phi_E + a_S\phi_S + a_N\phi_N + a_L\phi_L + a_H\phi_H + a_T\phi_T + Source\ terms \quad (4.16)$$

where,

- $a_P = a_W + a_E + a_S + a_N + a_L + a_H + a_T \cdots\cdots$
- *a*'s denote the influence of the corresponding neighbour term, corresponding to the physical meaning of Φ;
- Subscripts *P, N, S, E, W, H, L & T* represent the current Point, the North and South neighbour (y axis), the East and West neighbour (x axis), the High and Low neighbour (z axis) and the current cell at the earlier time, respectively.
- Source terms can be the pressure gradient and body forces in the momentum equations where the variable is the velocity, heat addition/losses due to external sources in the energy equation where the variable is enthalpy.

The total number of cell neighbours in Equation 4.11 will rely on grid topology, however, typically identical to the number of faces surrounding each cell within the

control volume (cells at the domain boundaries are an exception). For each computational cell within the domain, such equations will be written.

4.2.7 Solver Selection and Sub-Models Setting

There are two options provided by ANSYS Fluent to numerically solve the governing equations, named *pressure-based* and *density-based* solvers. The pressure-based solver was designed for incompressible and mildly compressible flows, while the density-based was mainly established for high-speed compressible flow problems [139]. It was claimed that the density-based formulation has better accuracy in dealing with shock resolution and acoustic wave propagation [136, 140]. The density-based solver allows the use of a user-defined real-gas model (UDRGM), which means a suitable and more accurate thermodynamics model can be implemented. In the case of outflow from high pressure gas pipelines, the variation of density is large, so the density-based solver is used in the current CFD model.

In the density-based solver, the governing flow equations of mass, momentum and energy conservation, supplemented by the auxiliary equation (EOS), were solved simultaneously (in a fully coupled manner), while the turbulence equations were treated sequentially. Here, the momentum equations were used to obtain the velocity field, while the continuity equation was used to determine the density field and the pressure field was determined from the EOS.

There are two formulations – named *coupled-implicit* and *coupled-explicit* – existing under the solver to linearise the coupled sets of flow equations. Those formulations differ in the way that they linearise the coupled equations [136]. The coupled implicit formula solves for all variables (i.e. pressure, temperature & velocity components) in the whole mesh domain simultaneously, while the explicit method determines the

variables for one cell at a time. The coupled-implicit method necessitates significantly larger computer memory, while the explicit method has a stability limitation for time step size in the simulation [140].

For the spatial discretisation, the second-order upwind scheme [141] was used. The method uses Taylor series expansion to achieve higher-order accuracy at the faces of the cell. It interpolates the values of the variables at the cell faces which are needed by the convection terms using the data at the cell centre, because ANSYS Fluent stores all the variables at the cell centre. Here, the gradient $\nabla\Phi$ has to be obtained firstly at each cell to be able to compute the values at the cell faces. The gradients of the scalar Φ in the conservation equations (i.e. the velocity derivatives in Equation 4.9) are obtained using the Least Squares Cell-Based approach [136]. This method is recommended for both structured orthogonal and unstructured meshes, and it consumes less time during the calculation compared to other available methods such as the Green-Gauss Cell-Based and Green-Gauss Node-Based, of which the solutions may produce false diffusion [136].

The convective fluxes in the conservation equation can be evaluated using one of the two schemes: the Advection Upstream Splitting Method (AUSM+) [142] or the Roe Flux-Differences Splitting (Roe-FDS) [143]. The AUSM approach computes the convective fluxes by computing a cell interface Mach number based on the characteristic speed of the flow in the surrounding cells. It is claimed that the AUSM scheme can provide exact resolution of contact and shock discontinuities. The performance of those flux schemes was examined in terms of predicting the transient pressure drop from gas pipelines. This will be further illustrated in the model verification section.

Since the flow is unsteady, Equation (4.14) is discretised in both space and time. Under the coupled-implicit formulation, there are two-temporal discretisations methods (first- and second-order implicit formulation).

The time rate of change of Φ is (Equation 4.9): $F(\Phi) = \frac{\partial \Phi}{\partial t}$

The first-order discretisation is obtained by:

$$\frac{\Phi^{n+1} - \Phi^{n}}{\Delta t} = F(\Phi) \tag{4.17}$$

While the second-order accurate discretisation is determined by:

$$\frac{3\Phi^{n+1} - 4\Phi^{n} + \Phi^{n-1}}{2\Delta t} = F(\Phi) \tag{4.18}$$

where

- *n* signifies value at the current time step (*t*);
- *n-1* signifies value at the previous time step (t-Δt);
- *n+1* signifies value at the next time step (t+Δt).

The accuracy of those methods was tested in terms of capturing the precise time of pressure wave propagation at a certain location during gas pipelines release conditions.

4.2.8 Turbulence Modelling

In the case of outflow from a compressed gas pipeline, the flow will range from no flow (before rupturing, Mach number = 0) to high speed flow (Mach number ~1) at the outlet (rupture location). In the case of 'internal' flows, the effect of wall shear is of vital importance, since the flow undergoes transition to turbulent flow at a certain

Reynolds number (i.e. $Re_D \geq 10^6$). Several models provided by ANSYS Fluent account for the effects of turbulence on the flow. These turbulence models include the Spalart-Allmaras model [144], k-ε models [145-147], Standard and Shear-Stress Transport (SST) k-ω models, k-kl-ω Transition model, Transition SST model, the v^2-f model, Reynolds Stress model (RSM), Scale-Adaptive Simulation (SAS) model, Detached Eddy Simulation (DES) model, Large Eddy Simulation (LES) model, Embedded Large Eddy Simulation (E-LES) model and Near-Wall Treatments for Wall-Bounded Turbulent Flows.

The *k-ε* is widely used for engineering applications because of its simplicity and reduced computational time as well as facility of convergence compared to more sophisticated turbulence models. This model is claimed to be the most accurate in dealing with internal flows [136]. In this study, the standard *k-ε* turbulence model is used.

The effect of surface roughness on the flow in turbulent wall-bounded flows can be taken into account in ANSYS Fluent. This can be included through the law of the wall modified for roughness, which depends on the experiments with sand-grain roughness. The law of the wall for mean velocity modified for roughness is expressed as:

$$\frac{u_p u_*}{\tau_w/\rho} = \frac{1}{k}\ln\left(E\frac{\rho u_* y_p}{\mu}\right) - \Delta B \qquad (4.19)$$

where u_p and y_p represent the velocity and the height, respectively, at the centre point P of the closest cell to the wall. *E* is an empirical constant for smooth wall equal to 9.793; τ_w is the shear stress of the wall; ρ is the density of the fluid; μ is the kinematic viscosity; and u_* is the wall friction velocity and expressed as:

$$u_* = C_\mu^{0.25} k_p^{0.5} \tag{4.20}$$

In this equation, k_p is the turbulent kinetic energy at the centre point P in the cell adjacent to the wall, while C_μ is a constant equal to 0.09.

The fundamental for the modification of wall function (Equation 4.19) results from the experiments of Nikuradse [148] on the impact of roughness on flow in pipes roughened/honed with sand grains. In ANSYS Fluent, the roughness function ΔB is defined in terms of the dimensionless sand-grain roughness height K_s^+:

$$K_s^+ = \frac{u_* K_s}{\mu} \tag{4.21}$$

where K_s is the equivalent sand-grain roughness height.

In ANSYS Fluent, the roughness is defined by specifying the values of sand-grain roughness K_s and roughness constant C_s in the wall boundary condition. The default value of $C_s = 0.5$ is used. In this research, the equivalent sand-grain roughness K_s is calculated from the semi-empirical relation developed by Adams and Grant [149] as:

$$K_s = 5.863 y_0 \tag{4.22}$$

where y_0 is the roughness height.

4.3 Implementation of Real-Gas EOS in ANSYS Fluent

To be able to precisely simulate the decompression behaviour of CO_2 mixtures, the thermodynamic properties of the fluid must be predicted using an accurate 'real-gas' EOS. ANSYS Fluent provides built-in implementations for several cubic equations of state such as RK, SRK and PR, and the more complex EOS of NIST REFPROP. However, these built-in equations of state do not determine the saturation conditions and thus cannot model a two-phase flow where liquid and vapour coexist and limit

the temperature to above the triple point. To overcome this issue, an EOS that is capable of predicting the thermodynamic properties of gas mixtures and accounts for phase change during the rapid decompression in the pipeline following fracture must be implemented into the CFD software, ANSYS Fluent. This can be done using the feature 'User Defined Real Gas Model' (UDRGM) feature, which allows the calculation to be performed in all regimes, i.e. gas, liquid, supercritical fluid and the two-phase region.

A real-gas EOS can be implemented in ANSYS Fluent using a library of functions written by the end user in the 'C' programming language. These functions are compiled and grouped in a shared library, which is later linked to ANSYS Fluent at runtime. The functions represent several thermodynamic properties required by Fluent to solve the system of governing equations. In the UDRGM, the properties of the fluid – such as density, enthalpy, entropy, specific heat, speed of sound, etc. – can be determined for given pressure and temperature at runtime using the real-gas EOS. The required properties and their derivatives that need to be calculated from the EOS for ANSYS Fluent are shown in Table 4.1. Note that the properties must be defined within the UDF in the sequence shown in Table 4.1, otherwise, the real-gas model will not be loaded properly into the ANSYS Fluent code.

Based on the comparison in Chapter 3, the GERG-2008 EOS [78, 150] was selected to be implemented into ANSYS Fluent. The simpler cubic PR EOS [70] was also implemented for comparison.

Table 4.1: Thermodynamic properties required for a real-gas model in ANSYS Fluent

Property	Symbol
Density	ρ
Enthalpy	h
Entropy	s
Specific heat at constant pressure	c_p
Molecular weight	M_w
Speed of sound	c
Viscosity	μ
Thermal conductivity	k
Partial derivative of ρ w.r.t. T	$\partial \rho / \partial T$
Partial derivative of ρ w.r.t. P	$\partial \rho / \partial P$
Partial derivative of h w.r.t. T	$\partial h / \partial T$
Partial derivative of h w.r.t. P	$\partial h / \partial P$

4.3.1 Implementation of PR EOS

The PR EOS was employed based on its proven accuracy in modelling the vapour-liquid behaviour of gases [2] and its relatively simple mathematical structure. The built-in version of the PR EOS in ANSYS Fluent does not determine the saturation conditions and thus does not model the two-phase flow where the liquid and vapour phases coexist and limit the temperature to above the triple point. It was necessary to re-define the EOS through a UDRGM to overcome this limitation. The PR EOS is described by [70]:

$$P = \frac{RT}{V-b} - \frac{a(T)}{V(V+b)+b(V-b)} \tag{4.23}$$

where P is the absolute pressure; T the absolute temperature; V the specific volume; and R the universal gas constant. a and b are empirical parameters accounting for the intermolecular attraction forces and the molecular volume, respectively.

The calculation of ANSYS Fluent requires the determination of density as a function of pressure and temperature, so Equation 4.23 is solved for the specific volume in the form of a cubic equation:

$$Z^3 - (1 - B)Z^2 + (A - 3B^2 - 2B)Z - (AB - B^2 - B^3) = 0 \qquad (4.24)$$

where the constants A, B and Z are defined as:

$$A = \frac{aP}{R^2T^2}, B = \frac{bP}{RT} \; and \; Z = \frac{PV}{RT} \qquad (4.25)$$

The density ρ can then be obtained from:

$$\rho = \frac{1}{V} \qquad (4.26)$$

The enthalpy H and the entropy S of the fluid are determined using the 'departure functions' for PR EOS [104] as:

$$H - H^* = RT(Z - 1) + \frac{T(da/dT) - a}{2\sqrt{2b}} ln\left[\frac{Z + \left(1 + \sqrt{2}\right)B}{Z + \left(1 - \sqrt{2}\right)B}\right] \qquad (4.27)$$

$$S - S^* = Rln(Z - B) + \frac{da/dT}{2\sqrt{2b}} ln\left[\frac{Z + \left(1 + \sqrt{2}\right)B}{Z + \left(1 - \sqrt{2}\right)B}\right] \qquad (4.28)$$

where H^* and S^* are the enthalpy and entropy of an ideal gas, respectively.

The specific heat for the real gas can be determined by differentiating Equation 4.27 with respect to temperature at constant pressure:

$$C_p = \left|\frac{\partial H}{\partial T}\right|_p \tag{4.29}$$

The molar weight of a mixture is obtained using the following formula [151]:

$$M_w = \sum_{i=1}^{k} y_i M_i \tag{4.30}$$

where y_i and M_i are the mole fraction and the molar weight of each component in the mixture, respectively.

The speed of sound is estimated using the following thermodynamic formula:

$$c = V\sqrt{-\left(\frac{C_p}{C_p - \Delta C}\right)\frac{1}{\left|\frac{\partial V}{\partial p}\right|_T}} \tag{4.31}$$

where $\Delta C = C_P - C_v$.

The dynamic viscosity of the fluid is obtained using the following semi-empirical formula [152]:

$$\mu = 6.3 \times 10^7 \frac{M^{0.5}(P_C/101325)^{0.6666}}{T_C{}^{0.1666}}\left(\frac{(T/T_C)^{1.5}}{(T/T_C)+0.8}\right) \tag{4.32}$$

where M is the molar weight of the fluid; T_C the critical temperature; and P_C the critical pressure. Knowing the viscosity, the thermal conductivity can be obtained by [153]:

$$k = \mu\left(C_p + 1.25R\right) \tag{4.33}$$

Finally, the derivatives of density with respect to pressure (at constant temperature) and density with respect to temperature (at constant pressure) can be obtained using the following relations:

$$\left|\frac{\partial \rho}{\partial p}\right|_T = -\rho^2 \left(\frac{\partial V}{\partial p}\right)_T \tag{4.34}$$

$$\left|\frac{\partial \rho}{\partial T}\right|_p = -\rho^2 \left(\frac{\partial V}{\partial p}\right)_p \tag{4.35}$$

while the derivative of enthalpy with respect to pressure (at constant temperature) is obtained using:

$$\left|\frac{\partial H}{\partial p}\right|_T = V - T \left(\frac{\partial V}{\partial T}\right)_p \tag{4.36}$$

4.3.2 Implementation of GERG-2008

The complexity of property behaviour of gas mixtures under the decompression process cannot be described with sufficiently high accuracy using the cubic EOS that can be solved analytically for the specific volume (hence density), from given values of T and P. This section describes the approach used to implement the modern multi-component GERG-2008 EOS [78, 150], which was chosen to provide the thermodynamic properties of CO_2 mixtures based on the comparison study outlined in Chapter 3.

This EOS covers the gas phase, the liquid phase, the supercritical region, and vapour-liquid equilibrium states for mixtures consisting of up to 21 components. Table 4.2 illustrates the list of all components provided by the GERG-2008 EOS library. The highlighted components represent the impurities most frequently produced from the

three available technologies of carbon capture (post-combustion, pre-combustion and oxyfuel).

Table 4.2: List of components provided by GERG-2008 EOS

No.	*Component Name*	*Formula*
1	*Methane*	CH_4
2	*Nitrogen*	N_2
3	*Carbon dioxide*	CO_2
4	*Ethane*	C_2H_6
5	*Propane*	C_3H_8
6	*n-Butane*	$n\text{-}C_4H_{10}$
7	*Iso-Butane*	$i\text{-}C_4H_{10}$
8	*n-Pentane*	$n\text{-}C_5H_{12}$
9	*Iso-Pentane*	$i\text{-}C_5H_{12}$
10	*n-Hexane*	$n\text{-}C_6H_{14}$
11	*n-Heptane*	$n\text{-}C_7H_{16}$
12	*n-Octane*	$n\text{-}C_8H_{18}$
13	*n-Nonane*	$n\text{-}C_9H_{20}$
15	*n-Decane*	$n\text{-}C_{10}H_{22}$
15	*Hydrogen*	H_2
16	*Oxygen*	O_2
17	*Carbon monoxide*	CO
18	*Water*	H_2O

19	*Hydrogen sulphide*	*H_2S*
20	*Helium*	*He*
21	*Argon*	*Ar*

The GERG-2008 EOS is based on pure substance equations of state for each component of the considered mixture, and correlation equations for binary mixtures consisting of these components. It is expressed in the form of a fundamental equation explicit in the Helmholtz free energy *a* [15], expressed as a function of density and temperature *a(ρ,T)*, and all thermodynamic properties can be calculated from it [77, 78].

The basic structure of the GERG-2008 EOS is divided into two parts: (1) representing the properties of the ideal gas at a given temperature and density, and (2) representing the 'residual' behaviour, i.e. departure from the behaviour of an ideal gas [77, 78, 95, 100, 154, 155]. The Helmholtz free energy is usually used in its dimensionless form ($\alpha = a/RT$). Theoretically, the Helmholtz free energy of the ideal gas can be determined [95]; however, the residual part has to be determined empirically, by optimising the structure of the residual part of the Helmholtz free energy and fitting its coefficients to experimental results [15, 77, 78, 154].

The 'reduced' dimensionless Helmholtz free energy α is expressed in the GERG-2008 EOS as:

$$\alpha(\delta, \tau, \bar{x}) = \alpha^o(\rho, T, \bar{x}) + \alpha^r(\delta, \tau, \bar{x}) \quad (4.37)$$

where α^{o} denotes the properties of the ideal-gas mixture at a given mixture density ρ, temperature T, and molar composition $\bar{x}$ and given by:

$$\alpha^{o}(\rho, T, \bar{x}) = \sum_{i=1}^{N} x_i [\alpha_{oi}^{o}(\rho, T) + ln x_i] \tag{4.38}$$

while the residual part α^{r} in Equation 4.19 of the reduced Helmholtz free energy of the mixture is given by:

$$\alpha^{r}(\delta, \tau, \bar{x}) = \sum_{i=1}^{N} x_i \alpha_{oi}^{r}(\delta, \tau) + \sum_{i=1}^{N-1} \sum_{j=i+1}^{N} x_i x_j F_{ij} \alpha_{ij}^{r}(\delta, \tau) \tag{4.39}$$

where δ and τ are the reduced density and the inverse reduced temperature for the mixture, and are given by:

$$\delta = \frac{\rho}{\rho_r(\bar{x})} \text{ and } \tau = \frac{T_r(\bar{x})}{T} \tag{4.40}$$

The dimensionless form of the Helmholtz free energy in Equation 4.38 for the ideal-gas state of component i is given by:

$$\begin{aligned} \alpha_{oi}^{o}(\rho, T) = \frac{R^*}{R} \Bigg[& ln\left(\frac{\rho}{\rho_{c,i}}\right) + n_{oi,1}^{o} + n_{oi,2}^{o} \frac{T_{c,i}}{T} + n_{oi,3}^{o} ln\left(\frac{T_{c,i}}{T}\right) \\ & + \sum_{k=4,6} n_{oi,k}^{o} ln\left|sinh\left(\vartheta_{oi,k}^{o} \frac{T_{c,i}}{T}\right)\right| \\ & - \sum_{k=5,7} n_{oi,k}^{o} ln\left|cosh\left(\vartheta_{oi,k}^{o} \frac{T_{c,i}}{T}\right)\right| \Bigg] \end{aligned} \tag{4.41}$$

where $\rho_{c,i}$ and $T_{c,i}$ are the critical parameters of the pure component i.

While the residual part of the reduced Helmholtz free energy in Equation 4.39 of component i is given by:

$$\alpha_{oi}^{r}(\delta,\tau) = \sum_{k=1}^{K_{Pol,i}} n_{oi,k}\delta^{d_{oi,k}}\tau^{t_{oi,k}} + \sum_{k=K_{Pol,i}+1}^{K_{Pol,i}+K_{Exp,i}} n_{oi,k}\delta^{d_{oi,k}}\tau^{t_{oi,k}}\, e^{-\delta^{c_{oi,k}}} \qquad (4.42)$$

where the function $\alpha_{ij}^{r}(\delta,\tau)$ in Equation 4.39 is given by

$$\alpha_{ij}^{r}(\delta,\tau) = \sum_{k=1}^{K_{Pol,ij}} n_{ij,k}\delta^{d_{ij,k}}\tau^{t_{ij,k}} + \sum_{k=K_{Pol,ij}+1}^{K_{Pol,ij}+K_{Exp,ij}} n_{ij,k}\delta^{d_{ij,k}}\tau^{t_{ij,k}}\, e^{-\eta_{ij,k}(\delta-\varepsilon_{ij,k})^{2}-\beta_{ij,k}(\delta-\gamma_{ij,k})} \qquad (4.43)$$

The values of the coefficients $n_{ij,k}$ and the exponents $d_{ij,k}$, $t_{ij,k}$, $\eta_{ij,k}$, $\varepsilon_{ij,k}$, $\beta_{ij,k}$, and $\gamma_{ij,k}$ were determined by non-linear multi-property regression analysis. A database of more than 100,000 experimental data points for the thermodynamic properties of binary mixtures, natural gases and other multi-component mixtures was used to develop the structure, coefficients and parameters of the correlation equations for binary mixtures, and to evaluate the performance of the EOS [78].

The required thermodynamic properties can then be obtained by combining the derivatives of Equation 4.37. For a homogeneous fluid mixture, the pressure *p*, enthalpy *h* and the entropy *s* can be obtained using the following formulas:

$$\frac{p(\delta,\tau,\vec{x})}{\rho RT} = 1 + \delta\alpha_{\delta}^{r} \qquad (4.44)$$

$$\frac{h(\delta,\tau,\vec{x})}{RT} = 1 + \tau(\alpha_{\tau}^{o} + \alpha_{\tau}^{r}) + \delta\alpha_{\delta}^{r} \qquad (4.45)$$

$$\frac{s(\delta,\tau,\vec{x})}{R} = \tau(\alpha_{\tau}^{o} + \alpha_{\tau}^{r}) - \alpha^{o} - \alpha^{r} \qquad (4.46)$$

Since the Helmholtz free energy of the mixture is a function of density, the density can be determined by inverting the function as:

$$\rho = \alpha^{-1}\big(\alpha(\delta, \tau, \vec{x})\big) \tag{4.47}$$

As the pressure and temperature are known, we can find the density from the following formula:

$$p = \rho RT\left[1 + \delta\left(\frac{\partial \alpha}{\partial \delta}\right)_{\tau}\right] \tag{4.48}$$

This equation is solved for density using an iterative method by setting an initially guessed value for density until the equation approaches an identity, for a known pressure value.

For calculating the specific heat, GERG-2008 uses the following equation:

$$\frac{c_p(\delta, \tau, \vec{x})}{R} = -\tau^2(\alpha^{o}_{\tau\tau} + \alpha^{r}_{\tau\tau}) + \frac{(1 + \delta\alpha^{r}_{\delta} - \delta\tau\alpha^{r}_{\delta\tau})^2}{1 + 2\delta\alpha^{r}_{\delta} + \delta^2\alpha^{r}_{\delta\delta}} \tag{4.49}$$

The GERG-2008 EOS determines the speed of sound from the reduced Helmholtz free energy by:

$$\frac{w^2(\delta, \tau, \vec{x})M}{RT} = 1 + 2\delta\alpha^{r}_{\delta} + \delta^2\alpha^{r}_{\delta\delta} - \frac{(1 + \delta\alpha^{r}_{\delta} - \delta\tau\alpha^{r}_{\delta\tau})^2}{\tau^2(\alpha^{o}_{\tau\tau} + \alpha^{r}_{\tau\tau})} \tag{4.50}$$

4.3.2.1 Direct Implementation of GERG-2008 EOS Library

The complex mathematical structure of the GERG-2008 EOS would adversely affect the complexity of the UDF. This is because a number of additional correlation equations have to be programmed in the ‘C’ code to accurately describe the behaviour of binary and multi-component mixtures. An alternative strategy for implementing the GERG-2008 EOS into ANSYS Fluent is to facilitate a *direct call* to the EOS library through a UDF. The advantage is that instead of re-coding the

above complex equations and the extra correlation equations within the UDF, the software package, which contains an executable FORTRAN program and a dynamic link library (DLL), is linked to ANSYS Fluent via the UDF. The properties are supplied to Fluent for given values of pressure and temperature, using the exported functions and subroutines of the dynamic link library 'GERG-2008.DLL' [150]. Table 4.3 shows the thermodynamic properties and their respective functions in GERG-2008 EOS required for activating the UDRGM in ANSYS Fluent [105].

Table 4.3: Thermodynamic properties and their respective functions in GERG-2008 EOS

Property	Function or sub-routine depending on T, P & $\bar{x}$
ρ	*DOTPX*
h	*HOTPX*
s	*SOTPX*
c_p	*CPOTPX*
M	*XMOLOX*
c	*WOTPX*
$\partial \rho / \partial T$	*DDDTOTPX*
$\partial \rho / \partial P$	*1/DPDDOTPX*
$\partial h \, \partial T$	*cp*
$\partial h / \partial P$	*DHDPOTPX*

Note that viscosity and thermal conductivity are not defined in the GERG-2008 library. Therefore, these properties are determined using Equations 4.32 and 4.33, respectively, while Equation 4.30 is used to calculate the molar weight of the mixture.

The procedure of how the ANSYS Fluent solver works with the UDF is illustrated schematically in Figure 4.5.

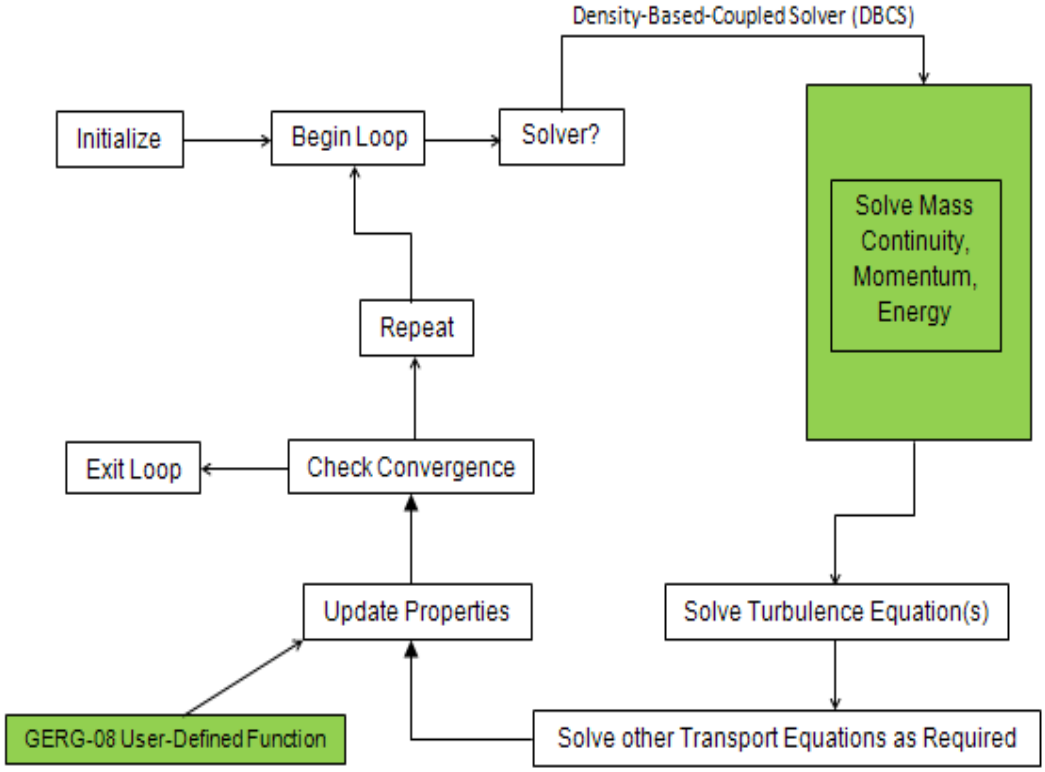

Figure 4.5: ANSYS Fluent density-based solver integrated with GERG-2008 EOS

In large-scale multi-dimensional simulations, the performance encounters a bottleneck. Since the EOS library is called to calculate the properties at each node in the flow domain an enormous number of times, the resulting computing cost of the direct call to the library during simulation can be a major limitation. In addition, the library occasionally fails to produce some properties at certain P-T values and enters an infinite optimisation loop that causes the library to crash. In such cases, the program becomes unresponsive and it must be terminated. Moreover, some properties (e.g. speed of sound) are not defined in the two-phase region, so an error is reported. Most modern multi-component equations of state suffer from this

drawback; this has prompted the need to develop an alternative way of implementing the EOS.

There are several ways to speed up the calculations and overcome the associated obstacles of the EOS library. For instance, generation of tables prior to the simulations for the most extensively used functions – either for a complete operating region or in combination with adaptive grid generation – can be used. This method has proved to be 300 times faster than direct calls to EOS [156] and can save up to 70% of the total computational runtime [157].

4.3.2.2 Indirect Implementation of GERG-2008 EOS Library

Complex EOS libraries carry out numerous optimisations to find a thermodynamic state. There are cases where they will fail to converge to the desired solution, enter an endless optimisation loop, crash suddenly or deliver an incorrect result without warning. Failure to obtain the thermodynamic state at a given point does not mean that the decompression wave velocity cannot be estimated accurately. In this section, mechanisms and methods that are employed to circumvent such issues are presented.

The second strategy of implementation is to use the EOS library indirectly for the purpose of speeding up the calculations and managing some errors from the EOS library. This can be achieved by reference to pre-compiled tables of the relevant thermodynamic properties generated by the GERG-2008 EOS. This replaces a direct call to the dynamic link library GERG-2008.DLL [105]. A linear interpolation scheme is also implemented within the UDF to extract values of the other thermodynamic parameters based on the P-T values solved for by Fluent.

The indirect implementation is based on developing a structured 2D array for the

chosen ranges of pressures and temperatures. Regular structured meshes are very efficient. Linear and higher-order interpolation schemes are simple to implement for structured meshes. The initial conditions and the phase envelope of a mixture are the key parameters used to establish the boundary of the main P-T table. Table 4.4 provides the composition of a mixture and its initial conditions, which will be used as an example for developing the 2D structured array. Table 4.5 illustrates the structure of the P-T table established for the five-component mixture. The total number of nodes generated within the 2D table was 84,300. Figure 4.6 shows the boundary of the domain, which includes the phase envelope of the mixture. As illustrated in the figure, the gas, liquid, supercritical and two-phase regions are taken into account.

Table 4.4: Mixture composition and initial conditions

Composition, mol.%					Initial conditions	
CO_2	H_2	N_2	O_2	CH_4	P (MPa)	T (K)
91.03	1.15	4.00	1.87	1.95	14.95	283.15

Table 4.5: 2D grid table

	Pressure (MPa)	Temperature (K)
Min.	0.05	180
Max.	30	320
Increment	0. 1	0.5
No. of nodes	300	281

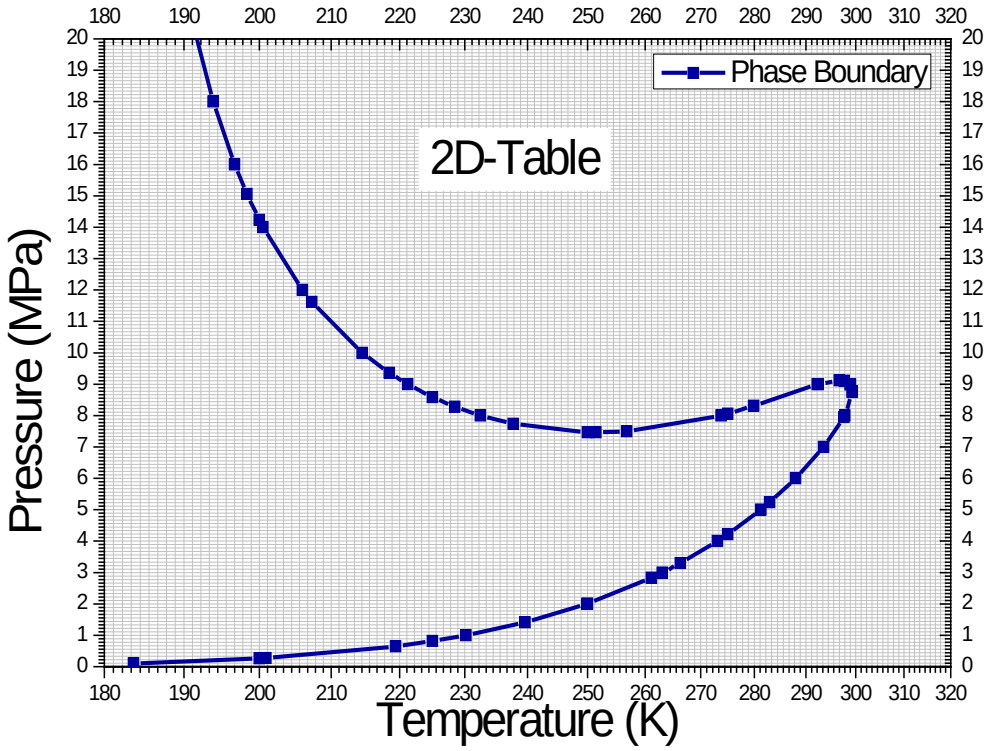

Figure 4.6: 2D structured mesh of five-component mixture

4.3.2.2.1 Management of GERG-2008 EOS Library Crash

The GERG-2008 EOS library is called for each pressure-temperature node in the 2D table to produce tables of the properties listed in Table 4.1. At some P-T values, the EOS library fails to calculate the properties. The reason behind this failure in the calculation is an internal issue and cannot be identified and/or solved if a direct implementation of the EOS library is used.

However, this issue can be avoided using the indirect implementation of the EOS library. Where the EOS library failed to produce data, 'hole(s)' will be displayed in the corresponding table cell(s). To avoid termination of the calculation process, a code was developed to automatically begin the calculation from the next P-T increment and complete the rest of the table so the remaining properties are displayed normally. The red cell in Figure 4.7 represents the node where the EOS library failed

to calculate the property. The corresponding gaps in the table grid are then filled using interpolation based on the values at the neighbouring nodes. Accordingly, the sudden crash of the library which terminates the ANSYS Fluent calculation is avoided using this strategy.

4.3.2.2.2 Management of GERG-2008 EOS Errors

There are many possible situations where the EOS will fail to return a satisfactory result and will return an error code. The most frequent error encountered during the preparation of property tables was related to the speed of sound. The latter is not defined in the two-phase region, so the error code -95555 is displayed within the corresponding cell, as shown in Figure 4.7.

Most equations of state will return an error flag instead of a result. For the simulation of the gas decompression process, a homogeneous-equilibrium fluid is assumed. With this assumption, it is acceptable to estimate the speed of sound of the two-phase fluid as that of a single-phase fluid. For a single phase, the speed of sound is defined as the square root of the partial derivative of the pressure with respect to the density at constant entropy. The speed of sound in the two-phase region is defined within the UDF as:

$$c = \sqrt{\frac{\partial p}{\partial \rho}\Big|_s} \tag{4.51}$$

The calculated properties are then saved into readable files linked to ANSYS Fluent through the UDF as *LOOK-UP* tables. Once the files are produced, they can be used for various simulations involving that mixture. Figure 4.8 shows schematically the computing strategy of fluid properties using the GERG-2008 EOS library. This

method of implementation is a standard method that features the possibility of using any other EOS library.

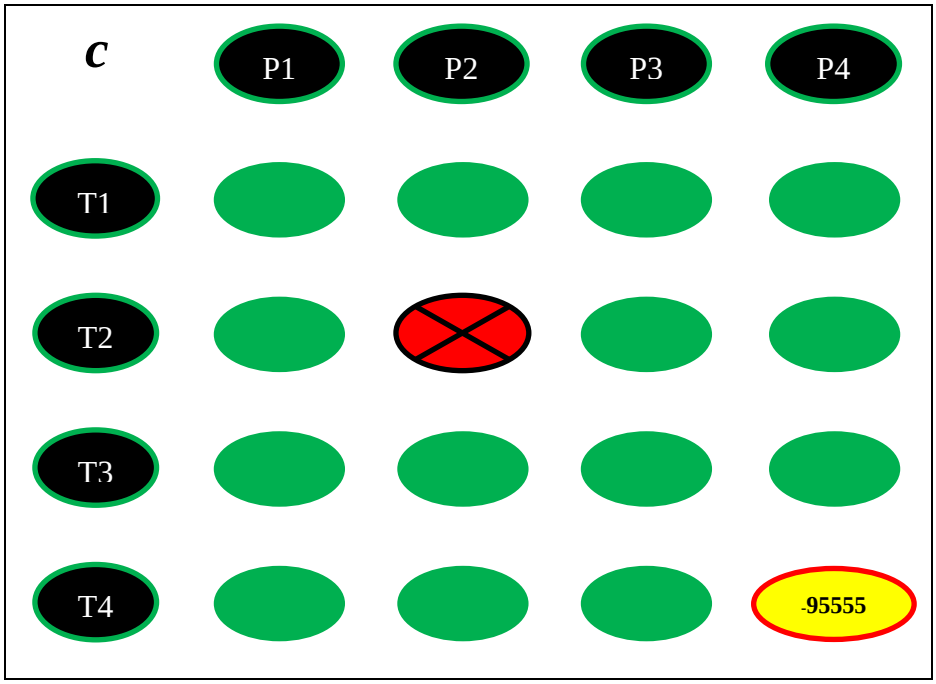

Figure 4.7: Schematic representation of speed of sound '*c*' table showing a 'failed' cell and an error code

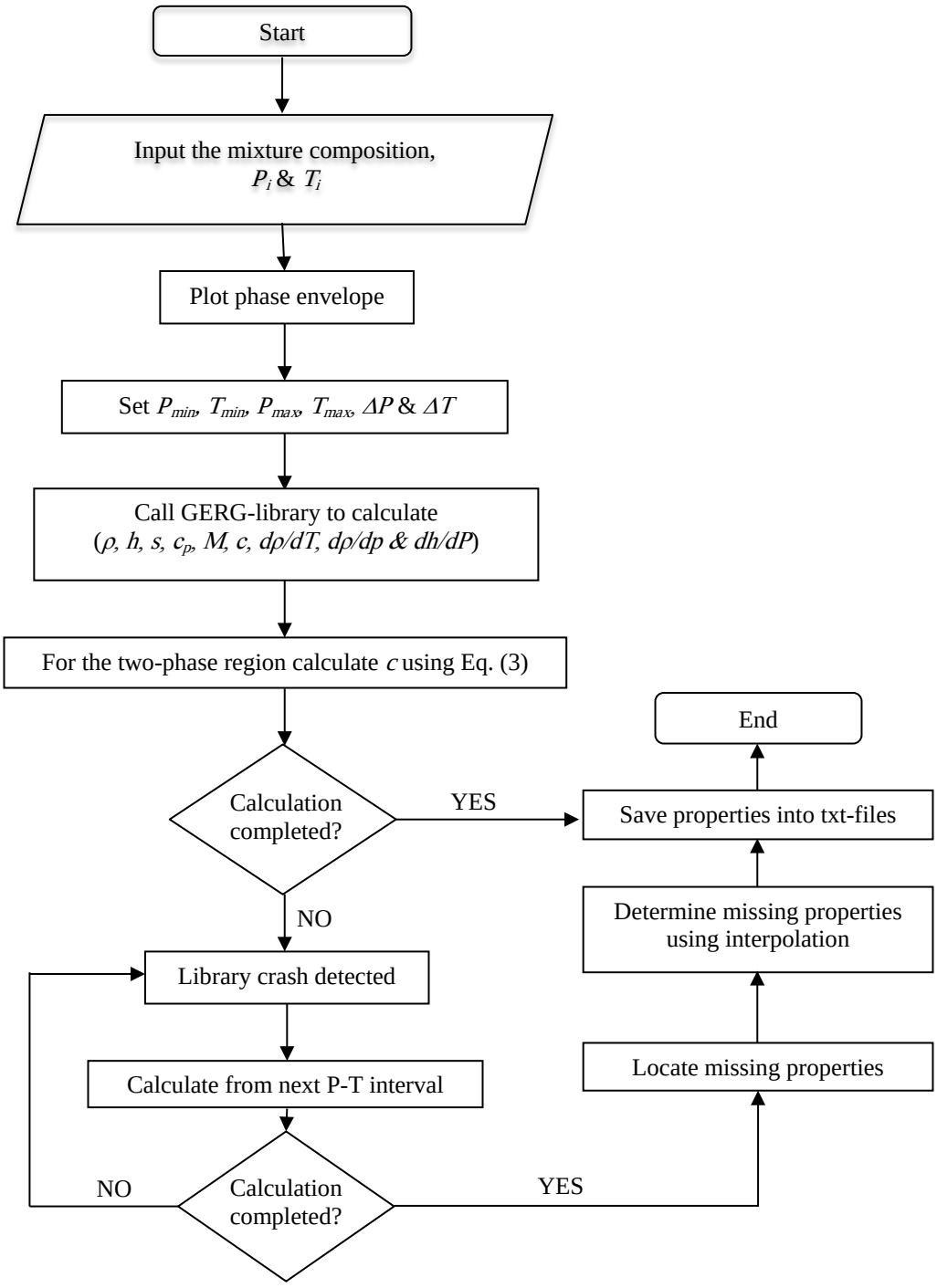

Figure 4.8: Property calculation flow chart

4.3.2.2.3 Accuracy and Performance of Indirect Implementation

The UDFs were used in a standalone test program to test the accuracy and the computing performance of the scheme. The accuracy was assessed by comparing the

properties calculated by the GERG-2008 EOS library, against the properties obtained from mesh interpolation at several P, T points on the decompression path, which includes the region under the two-phase curve. The assessment was conducted for the mixture shown in Table 4.4. A thermodynamic domain spanning a range of temperatures from 180 K to 320 K and a range of pressures from 0.05 MPa to 30 MPa was meshed. Figure 4.9 shows the decompression path as depicted on the phase envelope of this mixture. For all nodes within this domain, the density, enthalpy, entropy, specific heat, speed of sound and the derivatives of density and enthalpy are calculated and saved into readable tables.

The maximum deviation (%) between the mesh interpolation and the properties obtained from the GERG-2008 standalone library is calculated using the following formula:

$$dev = \left| \frac{y_{tables} - y_{GERG-2008}}{y_{GERG-2008}} \right| * 100 \tag{4.52}$$

Tables 4.6 and 4.7 present the maximum deviation of the above properties obtained from mesh interpolation and the GERG-2008 EOS library for a decompression occurring within the two-phase region and a decompression occurring above the two-phase region, respectively. The results are shown for four node densities (660; 12,130; 23,454 and 84,300 nodes). Figure 4.10 shows the 3D plots of each of the thermodynamic properties calculated by GERG-2008 based on the 2D structure table for the case of 84,300 nodes. Due to the fact that the mesh was dense enough, a smooth transient between the phases was observed in all properties.

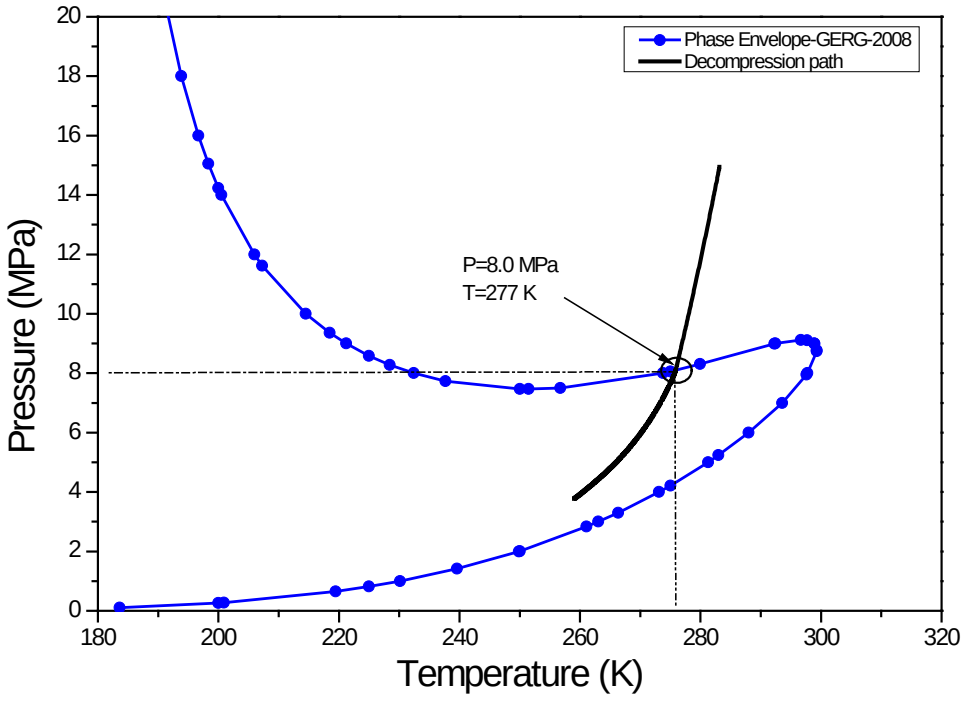

Figure 4.9: Thermodynamics path following decompression

Table 4.6: Maximum deviation of the properties (%) within the two-phase region

Property \ No. of nodes	660	12130	23454	84300
Density	1.907	0.439	0.115	0.017
Enthalpy	2.514	1.260	0.343	0.0088
Entropy	1.634	0.861	0.235	0.0049
Cp	0.906	0.533	0.147	0.0031
Speed of sound	125.080	2.563	0.694	0.0272
dDdP	9.067	3.742	1.002	0.293
dDdT	1.696	1.152	0.322	0.0911
dhdP	22.661	9.347	2.479	0.219

Table 4.7: Maximum deviation of the properties (%) above the two-phase region

Property \ No. of nodes	660	12130	23454	84300
Density	0.981	0.031	0.009	0.0049
Enthalpy	0.209	0.018	0.005	0.0034

Entropy	0.112	0.011	0.003	0.0012
Cp	1.431	0.222	0.064	0.0191
Speed of sound	8.762	0.085	0.024	0.0096
dDdP	15.837	0.688	0.196	0.049
dDdT	2.438	0.406	0.116	0.017
dhdP	8.576	0.917	0.257	0.072

As expected, the deviation decreases as the number of nodes increases. With more than 12,000 nodes in the domain, the maximum interpolation error is below 1% for all properties. Density, enthalpy and entropy are the most accurately estimated parameters. The properties defined through partial derivatives are susceptible to larger deviations. Using more than 23,000 nodes leads to deviations less than 0.3%. It is concluded that the scheme is sufficiently accurate for the application. The accuracy can be arbitrarily controlled through the density of nodes inside the domain, as expected.

The performance of the indirect implementation is tested against the direct call of the GERG-2008 EOS library during a real simulation environment. This is illustrated by considering a 25 m shock tube made of 10,000 elements. In the best scenario, the solution requires one call to the library for each element, at each time step. The time step is equal to 1 μs and the total simulation flow time is equal to 10 m/s. The GERG-2008 EOS library needs ~10 m/s for a mixture involving five components to calculate the thermodynamics properties. The computing time is a function of the numbers of components in the mixture. This simulation needs ~11 days to obtain the thermodynamic properties alone. This time must be added to the time necessary to solve the equations of conservation for the flow.

The time required to produce the thermodynamics mesh files is equal to the product of the number of nodes and the computing time of the EOS library. It is noted that the creation of the mesh produces a pre-processing overhead. Once the files are produced, they can be used for various simulations involving this mixture. For all properties, the search in tables during the simulation was found to be about 20 times faster than a direct call to the library to calculate one property.

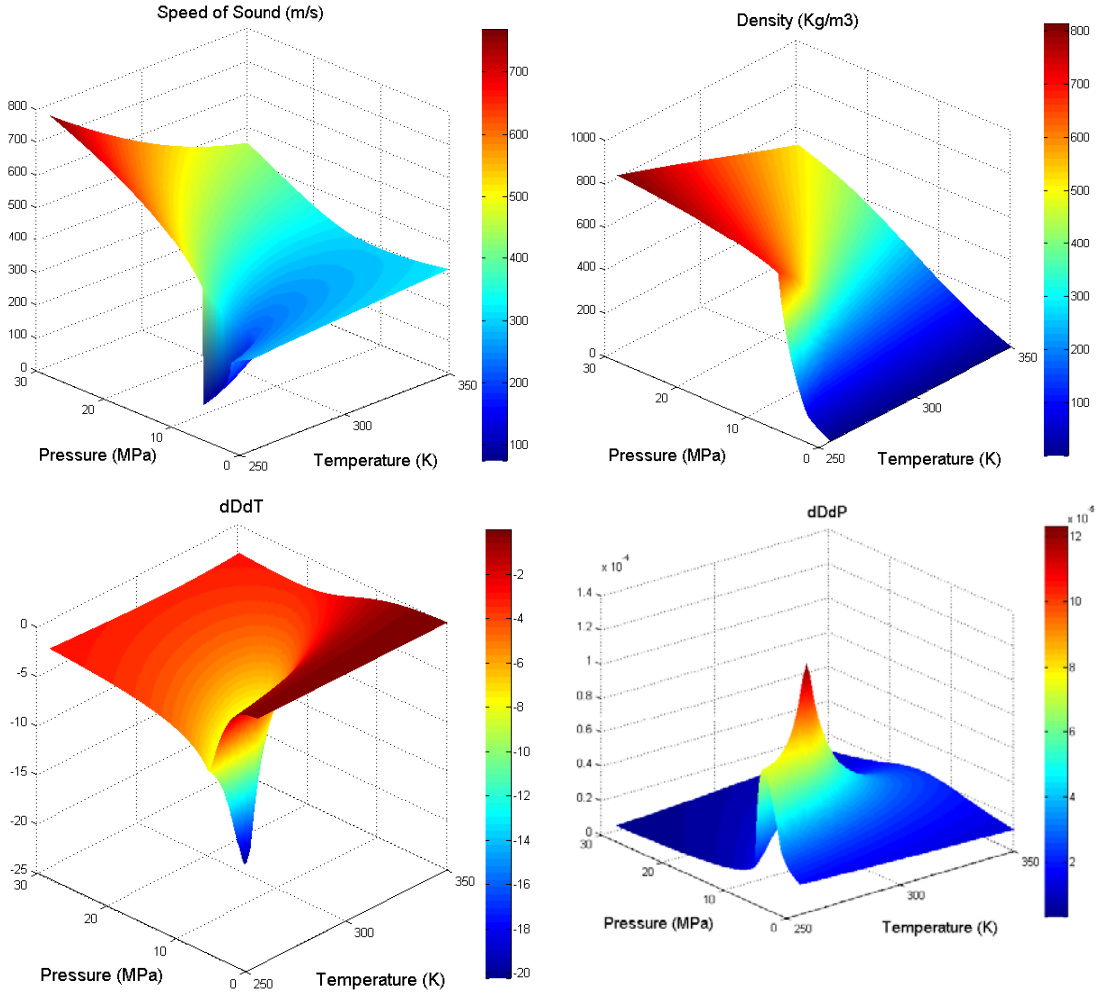

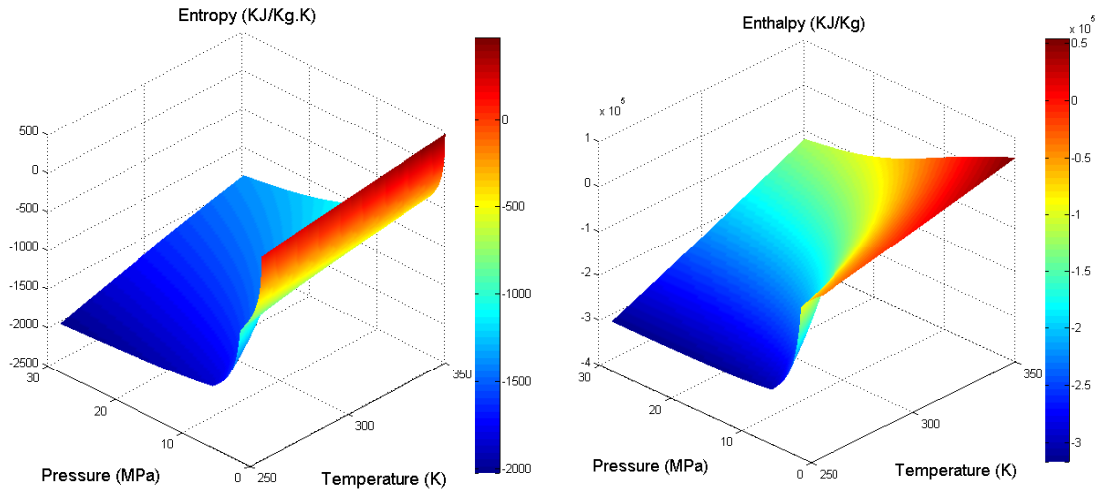

Figure 4.10: 3D plots of thermodynamic properties calculated by GERG-2008

4.4 Model Accuracy and Verification

The general methodology for obtaining the decompression wave speed from experimental tests is to monitor the pressure drop as a function of time at several locations along the pipeline. The pressure transients and other properties of gas mixture escaping from a fractured pipeline therefore must be predicted with sufficient accuracy. In order to verfiy the current CFD model, the following steps were taken:

- A mesh independence study was undertaken by comparing several element sizes and time step values;
- The convective fluxes in the conservation equation were obtained using two flux schemes (Roe-FDS and AUSM) available in ANSYS Fluent;
- The first and the second upwind discretisation schemes were tested for obtaining the momentum equation, turbulent kinetic, turbulent dissipation energy;

- Two-temporal discretisations methods (first- and second-order implicit formulation) were evaluated in terms of calculating the transient part in Equation 4.14.

The model verification was carried out using the mixture in Table 4.4. Figure 4.11 presents the predicted pressure-time using several element sizes (2, 3, 5, 10, 20, 50 and 100 mm). An optimum element size was found to be 2 mm.

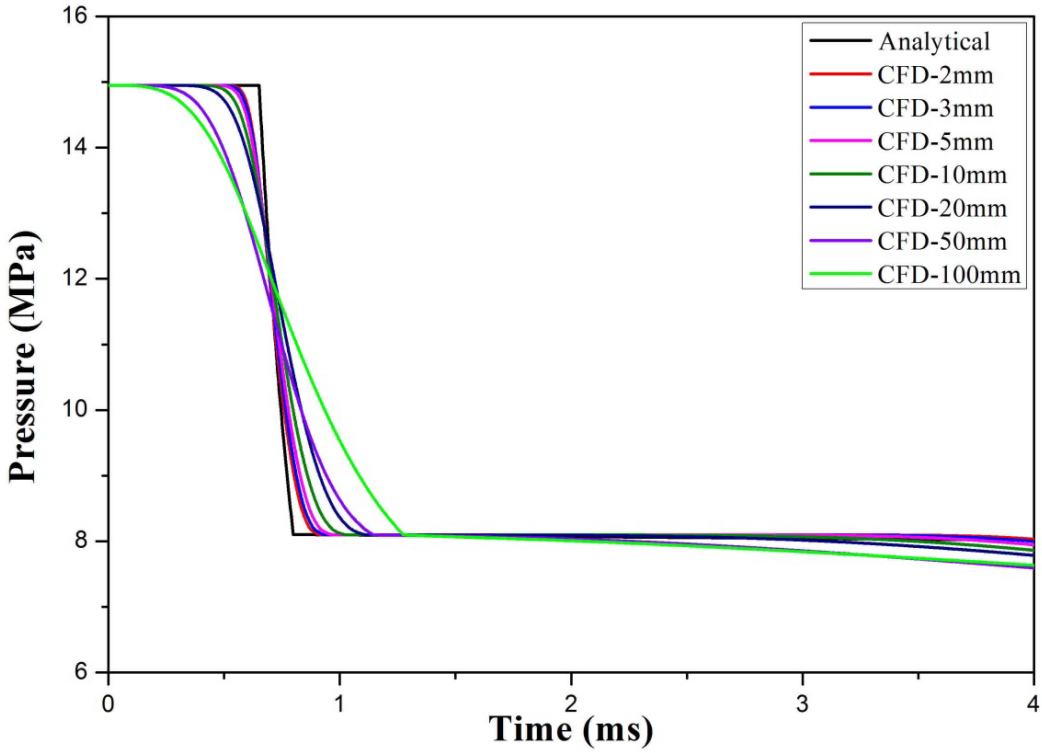

Figure 4.11: Spatial mesh independence tests

Figure 4.12 illustrates the effect of time-step size on the pressure-time drop. Three times have been used (10^{-5}, 10^{-6} and 10^{-7} sec). The results of the tested mixture show that no difference can be seen between the results of 10^{-6} sec and 10^{-7}sec. The pressure-time variation was predicted using both Roe-FDS and AUSM flux schemes, as shown in Figure 4.13. A result closer to the analytical solution was obtained from the AUSM scheme. Note that all the above results were obtained using the default setting in ANSYS Fluent, which is ROE-FDS for flux type, and first-order

discretisation schemes for the momentum equation, turbulent kinetic, turbulent dissipation energy and first-order for temporal discretisation.

Figure 4.14 presents the accurcy of the current model when the second-order schemes are selected. It can be seen that the predicted pressure-time traces using the second-order scheme are almost identical to the analytical solution. However, some convergence difficulties were encountered when using second-order schemes. It can be noticed from Figure 4.15 that even though an element size as large as 20 mm was used, a more accurate transient is predicted using the second-order scheme. This suggests that relatively large elements can be used in conjunction with the second-order shceme, especially when simulating 3D cases where a large number of cells are needed. This finding will eventually be beneficial in terms of reducing the total time needed for simulation.

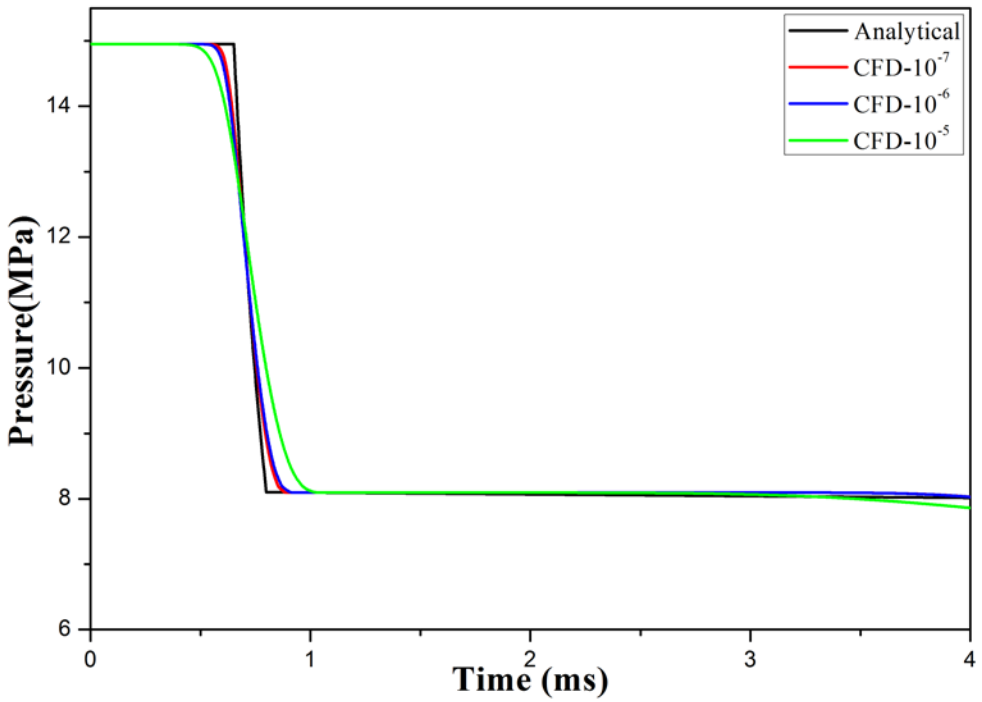

Figure 4.12: Temporal mesh independence tests

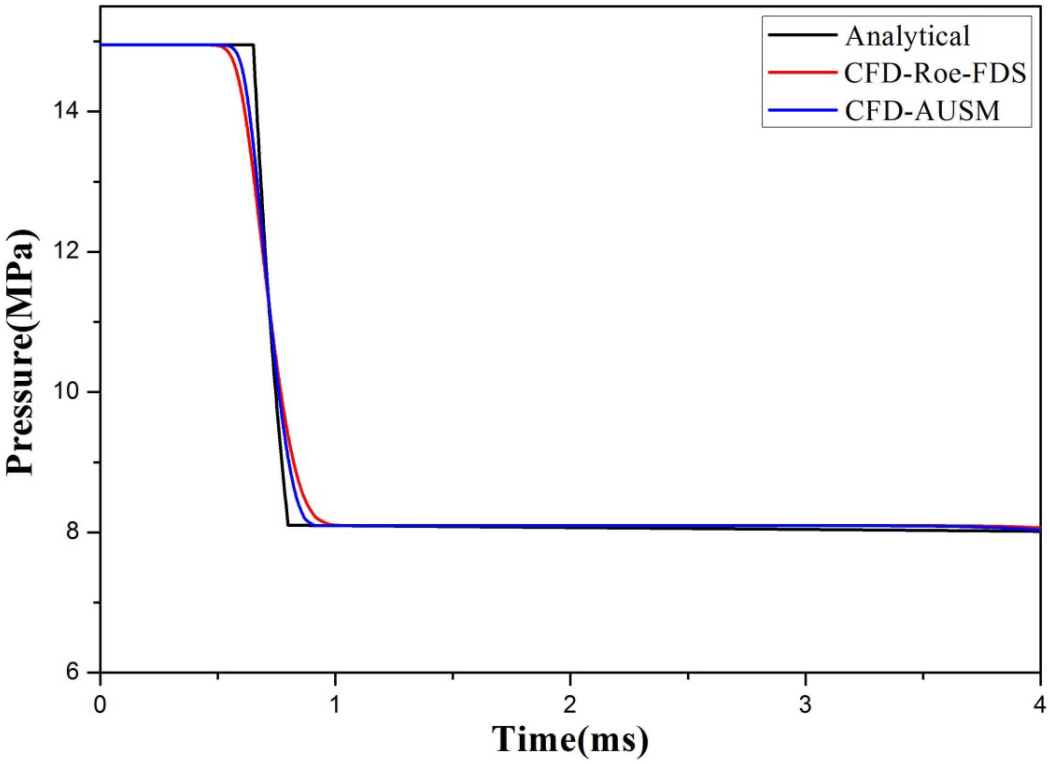

Figure 4.13: Accurcy in terms of flux scheme

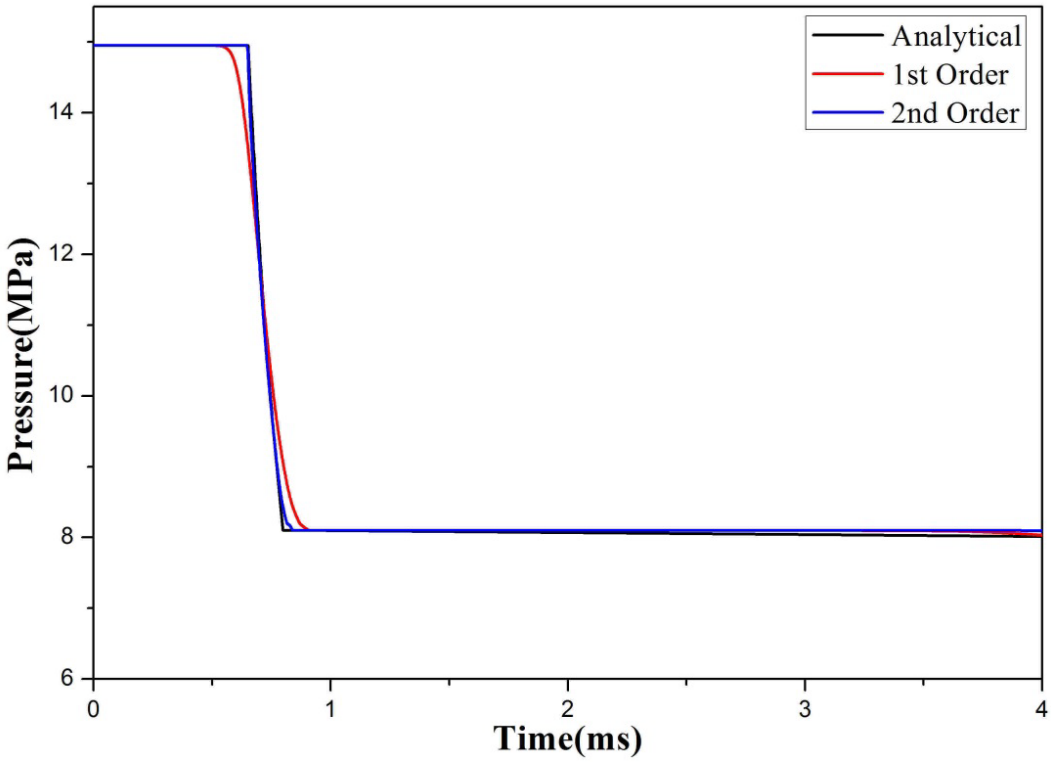

Figure 4.14: Comparsion between first- and second-order schemes

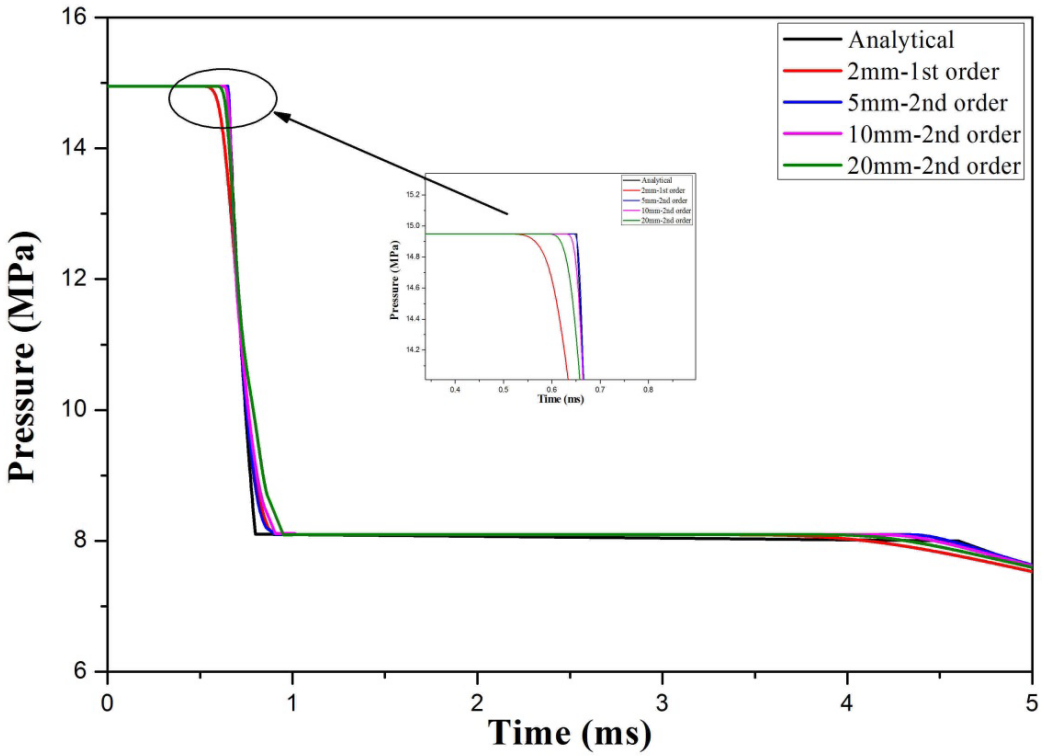

Figure 4.15: Accuracy of the second-order schemes using larger element sizes

4.5 Summary

This chapter outlined (a) the process of developing a multi-dimensional CFD decompression model using the CFD package ANSYS Fluent, and (b) the implementation of an accurate real-gas EOS into the model. The development of the model was based on the numerical simulation of a real decompression experiment using a 'shock tube'. Solver features and sub-models settings were discussed in order to select the accurate and more efficient sub-models available by ANSYS Fluent. The accuracy of the sub-models was verified in terms of predicting the pressure drop as a function of time. For example, the AUSM flux model improves the accuracy of the simulation by about 7.5% to that of Roe-FDS flux model. In the same time, the second order scheme improves the accuracy by 6% compared to the first order scheme.

Two equations of state (PR and GERG-2008) were incorporated into the CFD model to predict the thermodynamic properties. Due to its relatively simple mathematical structure, the PR EOS was implemented first in order to set the stage for implementation of the more complex GERG-2008 EOS. To avoid re-coding of the complex structure of the GERG-2008 EOS, two novel techniques were developed. The first method was a direct implementation by calling the exported functions and subroutines of the dynamic link library 'GERG-2008.DLL'. This method presented several difficulties related to the computational time and the convergence of the EOS solver. The second method involved replacing the calling of the exported functions and sub-routines by a pre-complied thermodynamics table representing all the necessary properties. The advantage of the second technique is that it can be used to implement any future-developed EOS into ANSYS Fluent.

The current CFD model permits to determine the effect of different parameters on the decompression behaviour of fluids including: a wide range of initial conditions, gas mixtures consisting of up to 21 different components, internal pipe roughness, pipe diameter and the actual pipe deformation. In Chapter 5, the model will be firstly validated for modelling natural gas mixtures. A verification of the implementation of the real-gas EOS will be conducted through a comparison between the PR and GERG-2008 equations of state. The model will also be used in Chapter 6 to study the decompression behaviour of CO_2 mixtures. A 3D simulation will be described in Chapter 7 in order to investigate the effect of pipe deformation and other parameters, such as pressure distribution acting on the flaps behind the crack tip, on the decompression from CO_2 pipelines.

Chapter 5 CFD Model Validation

5.1 Introduction

In this chapter, the CFD model developed in Chapter 4 is validated against measurements carried out in three shock tube tests. Three different gases undergoing decompression are simulated using the CFD model: pure nitrogen, conventional (lean) natural gas and rich natural gas. The objective is to examine whether the current CFD model can predict the decompression behaviour of a pure gas and gas mixtures. The implementation of a real-gas EOS is also verified by comparing the predicted results obtained from using the GERG-2008 EOS to those using the PR EOS.

5.2 CFD Simulation

5.2.1 Flow Domain

Based on the physical dimensions of the shock tube test facility described in [59], a horizontal pipe 30 m long and having 49.3 mm internal diameter was chosen as the flow domain for the simulation. The length of the pipe was reduced from the original 172 m to 30 m based on Equation 4.8 developed in Chapter 4, to limit the computational runtime. The 30 m length was sufficient to ensure that the decompression wave would not be reflected off the closed far end in the simulated time of the decompression. The experiment described in reference [59] is modelled using a 2D, axisymmetric setup. The physical flow domain is shown in Figure 5.1, along with the corresponding computational domain.

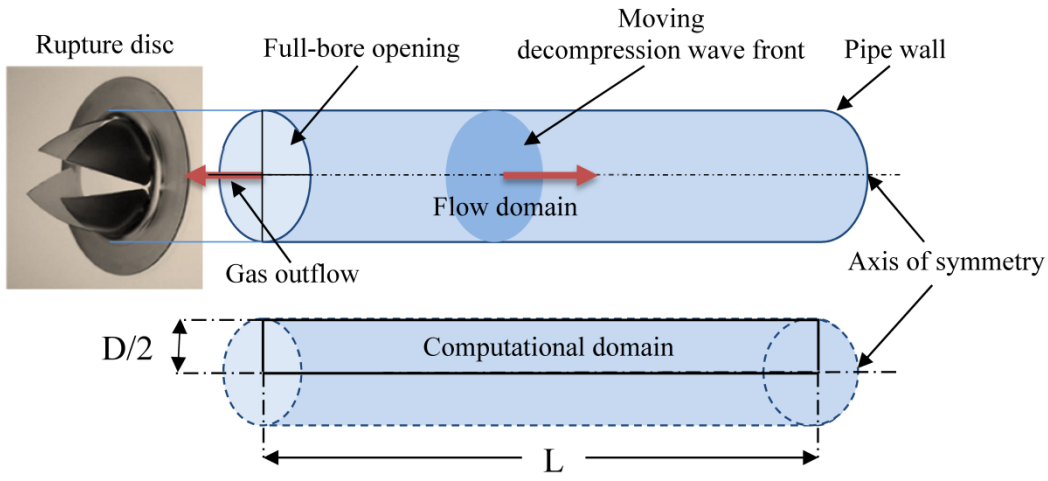

Figure 5.1: Schematic of flow domain and computational domain of the shock tube

5.2.2 Boundary Conditions and Computational Mesh

The boundary conditions and the physical dimensions used to carry out the simulations are illustrated in Figure 5.2. The scored rupture disc in the shock tube test was modelled using the 'pressure-outlet' boundary condition at atmospheric pressure. A boundary condition of axial symmetry was imposed at the centre of the tube. Wall boundary conditions are specified at the top and the far end of the pipe, as depicted on Figure 5.2 by the red colour. The no-slip condition was specified at the wall boundaries.

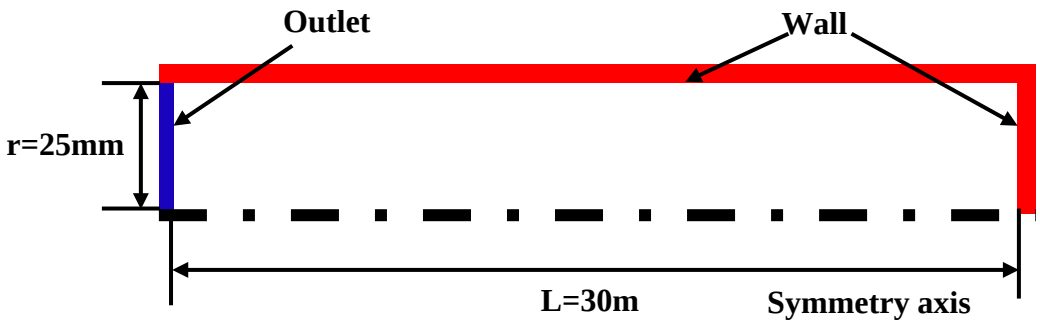

Figure 5.2: Computational domain and boundary conditions

Since axial symmetry was assumed, the computational grid was generated over the 30 m length of the pipe and for r=25 mm. At both 'wall' boundaries, five cells were

generated to cover the boundary layer. The cell adjacent to the wall was set at 0.05 mm from the wall with a mesh-growth factor (from the wall) of 1.2. Following the fifth cell in both radial and axial directions, the cells' dimensions were kept constant at 2 mm up to the pipe axis and the outlet boundary, respectively. Overall, ~250,000 rectangular cells of quadratic mesh distribution were generated for the entire 2D axisymmetric pipe. Details of the mesh distribution of flow domain near the top wall boundary and the outlet is shown in Figure 5.3.

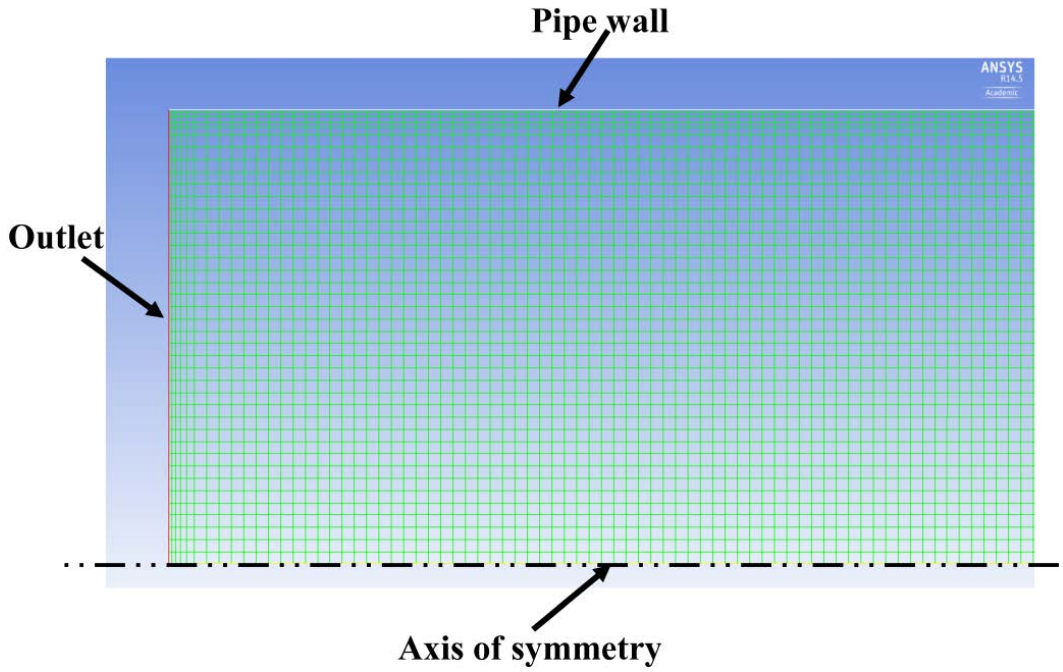

Figure 5.3: 2D computational grid

5.3 Solution Strategy and Settings in ANSYS Fluent

The working fluid, initially at rest, filled the pipe at the initial pressure and temperature before a full bore opening instantaneously occurred (at time t=0). Driven by the large pressure drop at the opening, the gas escaped from inside the pipe into the ambience. The decompression wave front simultaneously receded from the opening. Ahead of the decompression wave front, the fluid remains at rest and at the

initial conditions. The local Mach number ranges from 0 at the decompression front to 1, corresponding to the choked condition, at the full bore opening end.

Because the flow generated after rupture is considered compressible, viscous and turbulent, the turbulence models available in ANSYS Fluent need to be applied. The 'two-layer modelling approach' offered in ANSYS Fluent was used to model the change in properties in the vicinity of the wall. This approach divides the flow domain into a viscosity-affected region (close to the wall) and a fully-turbulent region (away from the wall). The 'realizable' k-ε turbulence model was adopted to model the fully-turbulent region, while the near wall region was treated using the 'enhanced wall treatment' function [136].

The implicit density-based solver was used to solve the unsteady 2D form of the governing flow equations. The default convergence criterion of $1.0\times e^{-03}$ was applied for x- and y-velocities, turbulent kinetic energy, turbulent dissipation energy and energy equation. Based on the accuracy evaluation conducted in Chapter 4, the convective fluxes in the conservation equation have been obtained using the AUSM scheme. A constant time step of 10^{-5} s was used to capture the transient flow features at the monitor point nearest to the full bore opening. The second-order upwind discretisation scheme was used for the momentum equation, turbulent kinetic energy and dissipation of turbulent energy, while the temporal discretisation was treated using the second-order implicit formulation.

The thermodynamic properties required by ANSYS Fluent for calculation are obtained using the 2D structure table shown in Table 5.1. This table is used for all cases studied in this chapter.

Table 5.1: 2D grid table for property calculation

	Pressure (MPa)	Temperature (K)
Min.	0.05	91
Max.	25	313
Increment	0. 14	1
No. of nodes	174	223

5.4 Simulation Results and Validation

The results of the 2D CFD decompression model using the GERG-2008 EOS are presented here. The validation of this model was first performed through comparison with measured results from shock tube tests for natural gas mixtures [59, 158]. The tests were conducted at the TransCanada Pipeline Gas Dynamics Test Facility in Didsbury, Alberta, Canada [13, 59].

In this facility, the main test section of the shock tube had a total length of 172 m. All spools were made from NPS2 x 5.5 mm WT, seamless tube with an internal diameter of approximately 49.3 mm. These spools were designed for a maximum of 22 MPa pressure, with a design factor of 0.8 and location factor of 0.625. The internal surface of the first spool near to the rupture disc was honed to a roughness better than 1.0 μm. In the test, eight pressure transducers and three temperature probes were mounted along the length of the shock tube. The locations of the pressure transducers and temperature probes used for the current simulation are shown in Table 5.2.

Table 5.2: The location of monitoring points

Node	p2	p3	p4	p6	p7
Location from rupture (mm)	59	240	440	840	1240

In this work, three different gas mixtures undergoing decompression were simulated using the CFD model: pure nitrogen, conventional natural gas and rich natural gas. The objective was to examine whether the current CFD model can predict the decompression behaviour of both pure gases and gas mixtures. Firstly, the decompression of pure nitrogen was simulated to examine the decompression behaviour of a single-phase flow. The second set of simulations was performed for conventional lean gas mixture with ~95% methane where the flow was expected to cross the two-phase region. The rich natural gas mixture contained ~80% methane for the third case. The distinctive feature of this mixture is that the two-phase region appears at high pressure (~7.5 MPa), which is close to that of CO_2 mixtures. The predicted results of gas decompression velocity were compared with the measured data of the shock tube tests, and also against results produced by OLGA and GASDECOM.

Table 5.3 lists the initial conditions and the gas compositions of the studied cases. The thermodynamic properties' density, speed of sound, enthalpy and entropy calculated by the GERG-2008 EOS at each node in Table 5.1 for all three cases are presented in Figures 5.4, 5.5 and 5.6, respectively. Those figures illustrate the property change from one- to two-phase regions. For pure nitrogen (Case 1), the two-phase region appears at very low temperatures, which is far from the initial condition of this test, and so the simulation needs to consider only the gas phase.

Table 5.3: Shock tube test conditions and gas compositions

	Case 1	Case 2	Case 3
P_i (MPa)	10.059	10.58	9.94
T_i (K)	260.44	247.65	273.21
C_1 (mole %)	0	95.4741	79.3089
C_2 (mole %)	0	2.9363	14.1967
C_3 (mole %)	0	0.1902	5.2556
iC_4 (mole %)	0	0.0156	0.0114
nC_4 (mole %)	0	0.0253	0.0164
iC_5 (mole %)	0	0.0041	0.0029
nC_5 (mole %)	0	0.003	0.002
C_{6+} (mole %)	0	0.0013	0.0009
N_2 (mole %)	100	0.5689	0.5513
CO_2 (mole %)	0	0.7812	0.6539

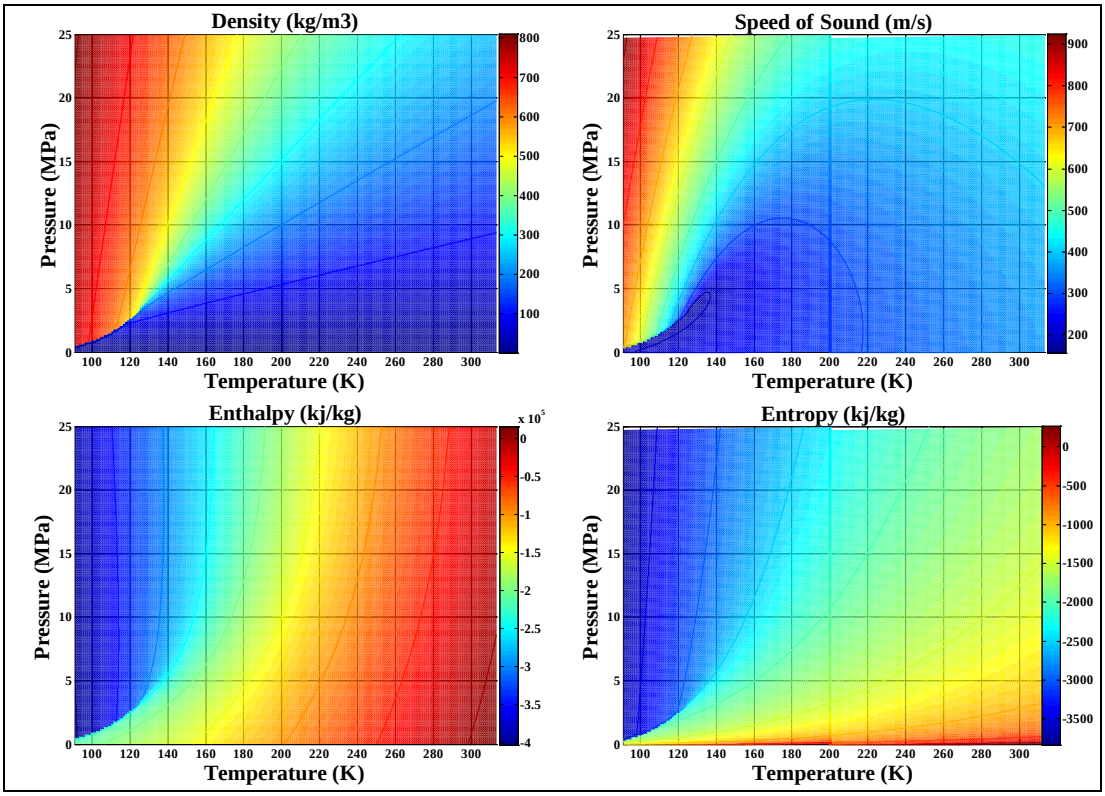

Figure 5.4: Thermodynamic properties calculated by GERG-2008 (Case 1)

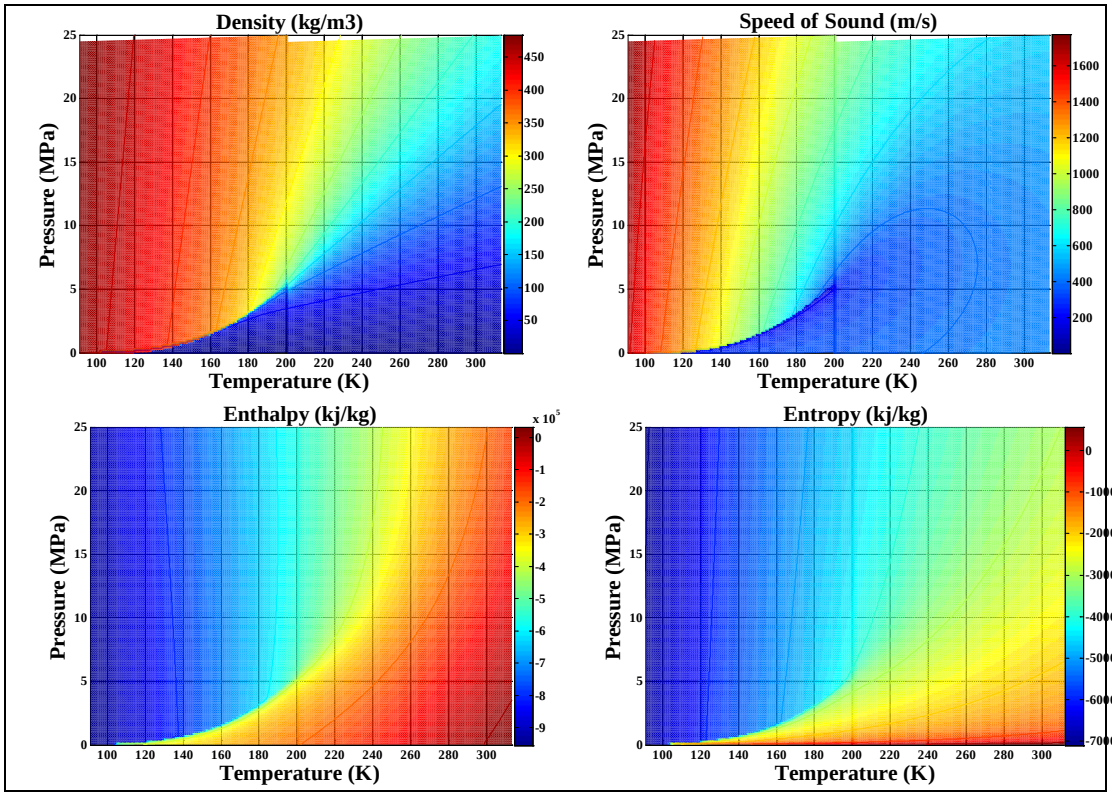

Figure 5.5: Thermodynamic properties calculated by GERG-2008 (Case 2)

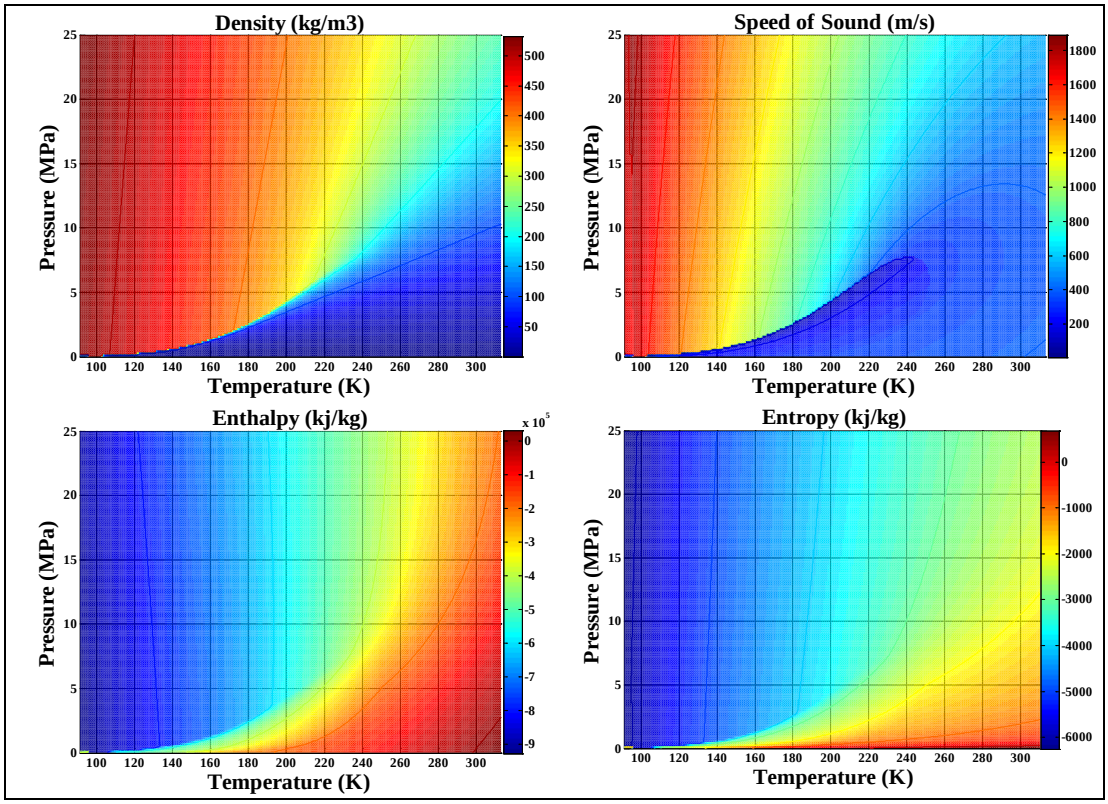

Figure 5.6: Thermodynamic properties calculated by GERG-2008 (Case 3)

A mesh independence study was performed in order to arrive at an optimum mesh size. Seven different element sizes (2, 3, 5, 10, 20, 50 and 100 mm) were tested for each of the studied cases. Figure 5.7 shows a comparison of pressure-time traces predicted using the above element sizes for the mixture in Case 3.

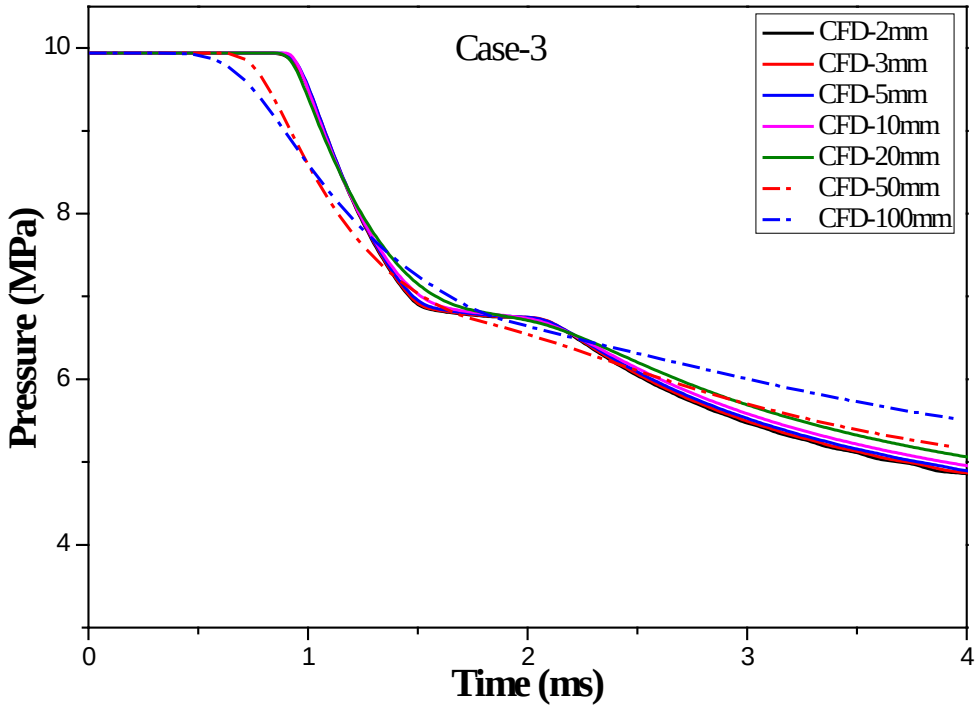

Figure 5.7: Mesh independence study (Case 3)

5.4.1 Verification of GERG-2008 EOS Implementation

In this section, the technique developed to implement the modern multi-component GERG-2008 EOS is tested against the implementation of the PR EOS. The transient behaviour of some parameters required by ANSYS Fluent to activate the real-gas model were monitored. These parameters include pressure, temperature, density and speed of sound. Due to the acceptable accuracy of the PR EOS in predicting the thermodynamic properties of pure gases, Case 1 (pure N_2) was used for the current comparison.

Figure 5.8 compares the density as a function of time as calculated by the PR EOS (black curve) and the GERG-2008 EOS (red curve). From this graph it can be seen that both curves have very similar trends, except slight differences at 0 and 10 s.

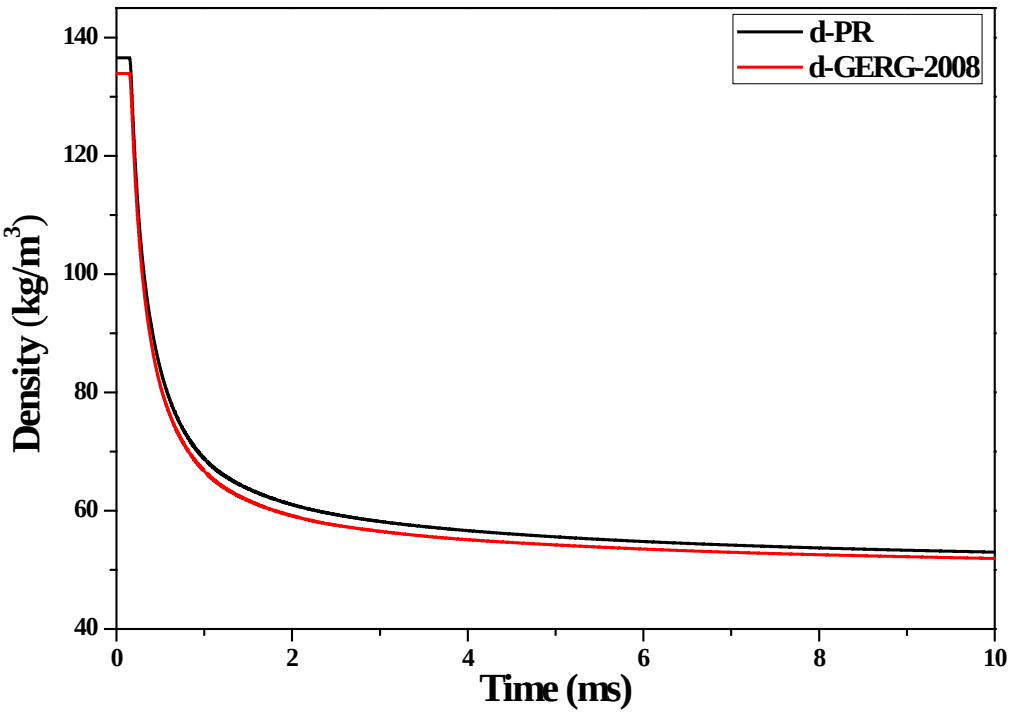

Figure 5.8: Density w.r.t time predicted using both PR EOS and GERG-2008 EOS

The predicted values of the speed of sound as a function of time are compared in Figure 5.9. A similar trend to what was observed in the density is shown here. The maximum discrepancy can be seen at the initial state, which is due to the accuracy variation between the two equations of state. The predicted transient pressure and temperature are shown in Figures 5.10 and 5.11, respectively. Again, in both figures, the results were almost identical despite a minor variation at the later stages of the decompression. The close agreement in the trends illustrates the fact that the current methods used to implement both the PR EOS (direct coding within the UDF) and the multi-component GERG-2008 EOS (indirect implementation using 'property tables'

technique) into ANSYS Fluent is successful and can be used to simulate the transient behaviour of real gases.

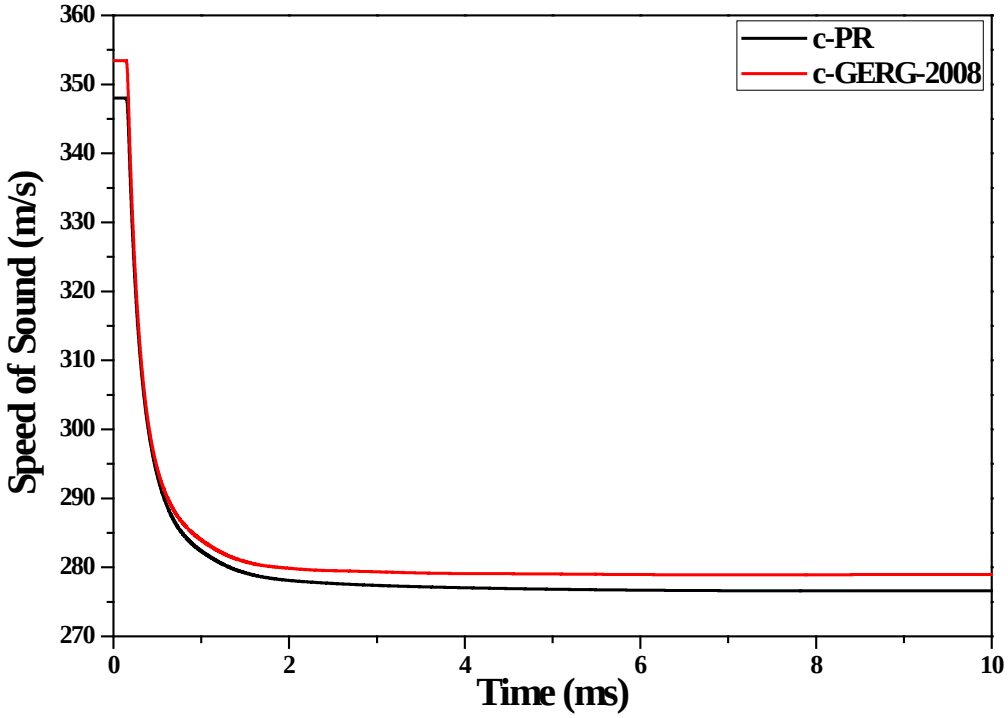

Figure 5.9: Speed of sound w.r.t time predicted using both PR EOS and GERG-2008 EOS

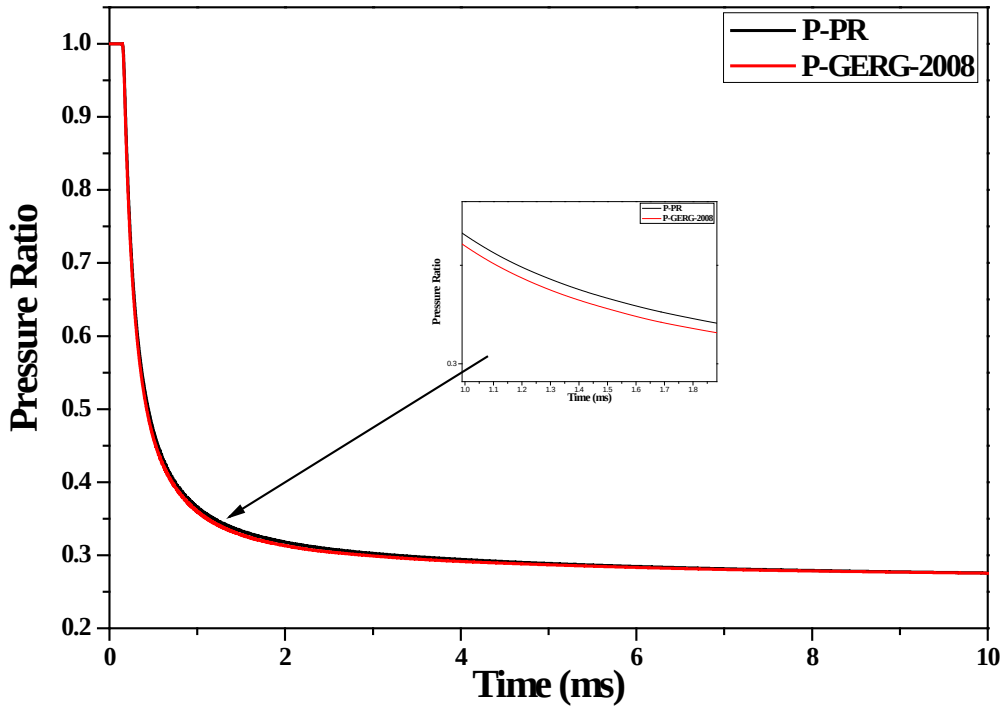

Figure 5.10: Pressure-time traces predicted by PR EOS and GERG-2008 EOS

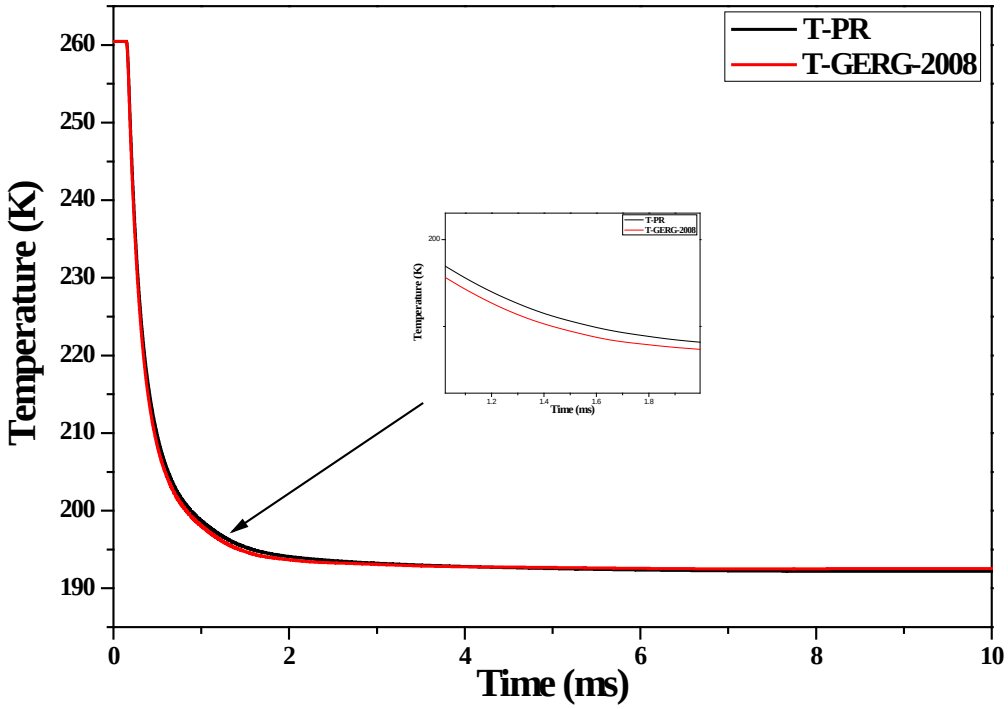

Figure 5.11: Temperature-time traces predicted by PR EOS and GERG-2008 EOS

5.4.2 Calculation of Decompression Wave Speed

Two different methods were used to determine the decompression wave speed. The first method involved calculating the *local* decompression wave speed using Equation 2.4. This was done by monitoring the change in both the speed of sound and the 'outflow' velocity against time. Afterwards, the outflow velocity was subtracted from the speed of sound for several pressures below the initial pressure. However, the *local* gas decompression wave speed could not be deduced from experimental tests such as shock tube tests and/or full-scale burst tests.

In these tests, the gas decompression wave speed w could only be calculated by determining the times at which a certain pressure level reaches several given pressure transducer locations on the pipe. By plotting these locations against time, the decompression wave speed is obtained by performing a linear regression of each

isobar curve. The slope of each regression represents the average decompression wave speed for each isobar. Figure 5.12 illustrates the determination of the decompression wave speed using the pressure-time curves. A linear regression to obtain the average decompression wave speed is shown in Figure 5.13 for Case 3. Both methods can be used in this model to calculate the gas decompression wave speed.

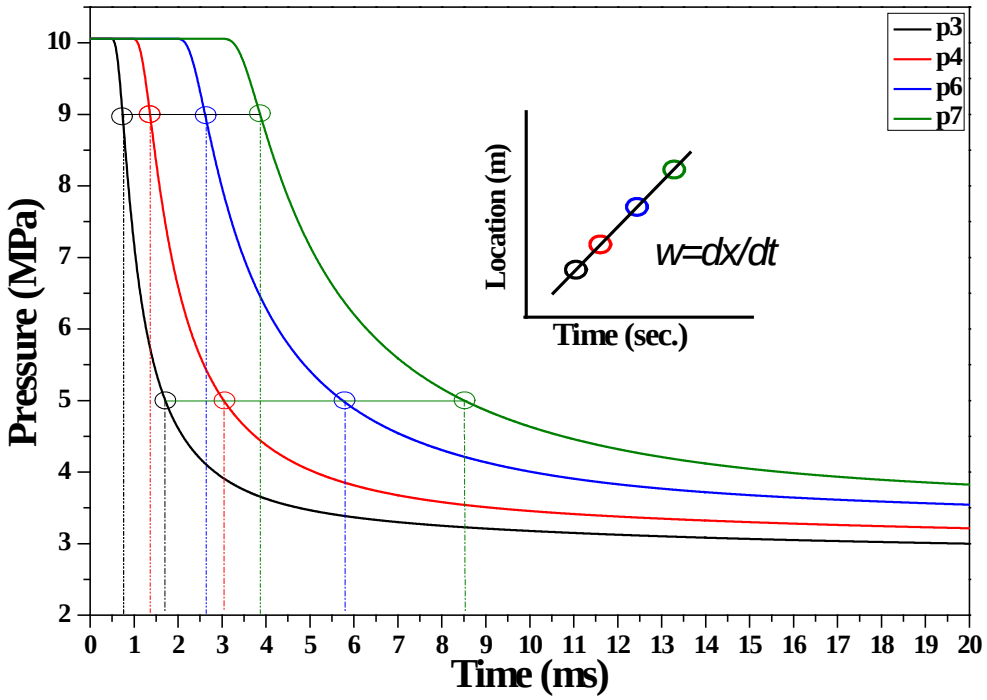

Figure 5.12: Determination of the decompression wave speed from pressure-time traces

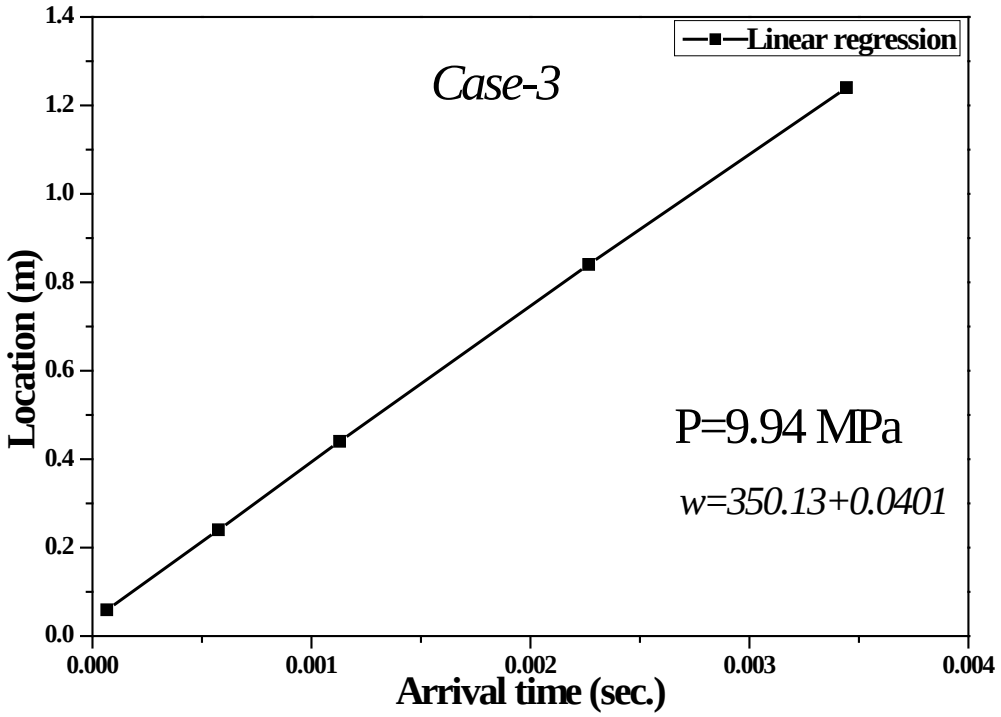

Figure 5.13: Linear regression to obtain the average decompression wave speed

5.4.3 Case 1: Decompression of Pure Nitrogen

Figure 5.14 shows the predicted pressure-time traces of pure nitrogen at four locations: p3, p4, p6 & p7 along the pipeline. It can be seen that the pressure at these monitored points drops rapidly as the decompression wave front passes each location in turn. The pressure becomes gradually steady at pressures below 4 MPa. The rate of change in both speed of sound and outflow velocity as functions of time is presented in Figures 5.15 and 5.16, respectively.

Comparison of the predicted average and local decompression wave speed with the measured data is shown in Figure 5.17. The results of both GASDECOM and OLGA are also presented. The comparison shows that the current 2D CFD decompression model predicts the decompression wave speed well.

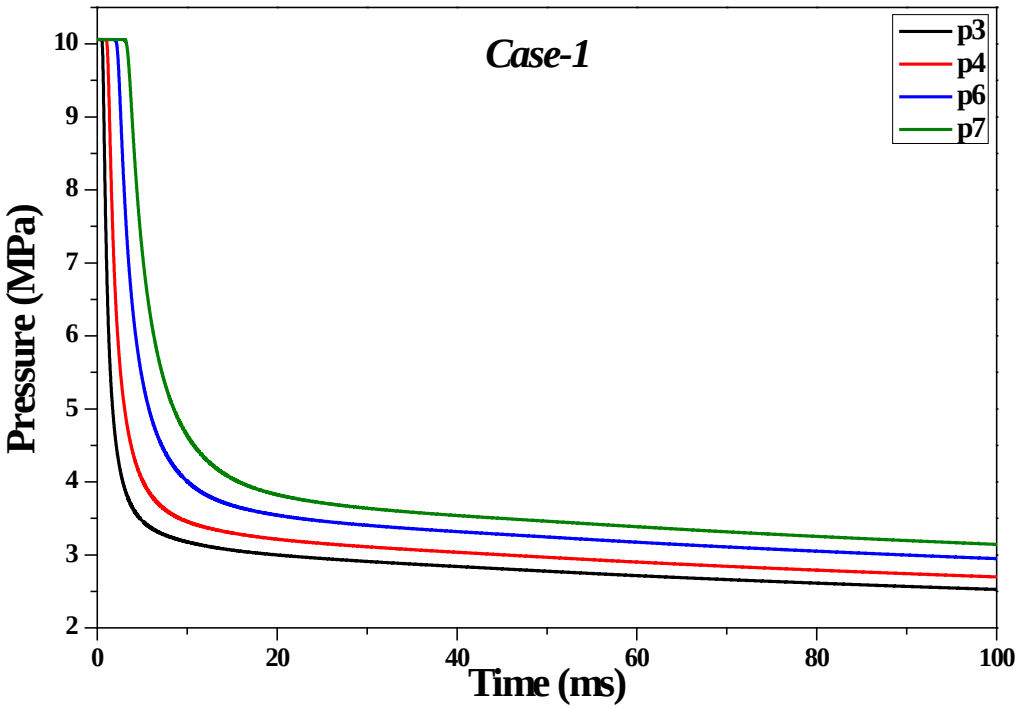

Figure 5.14: Pressure-time traces at four locations (Case 1)

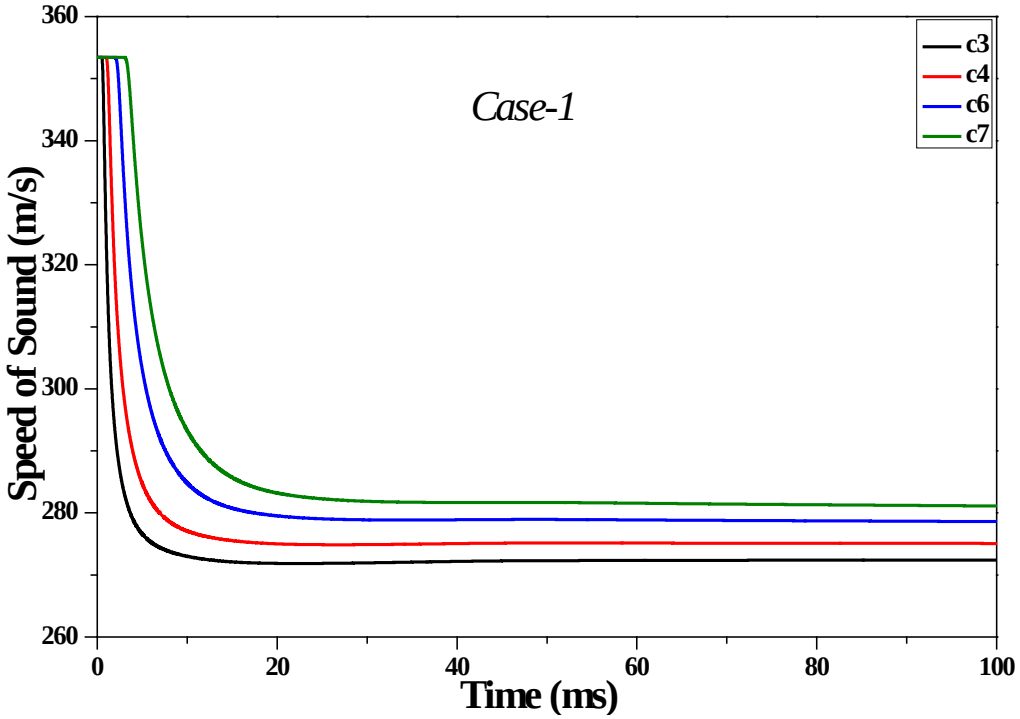

Figure 5.15: Speed of sound-time traces at four locations (Case 1)

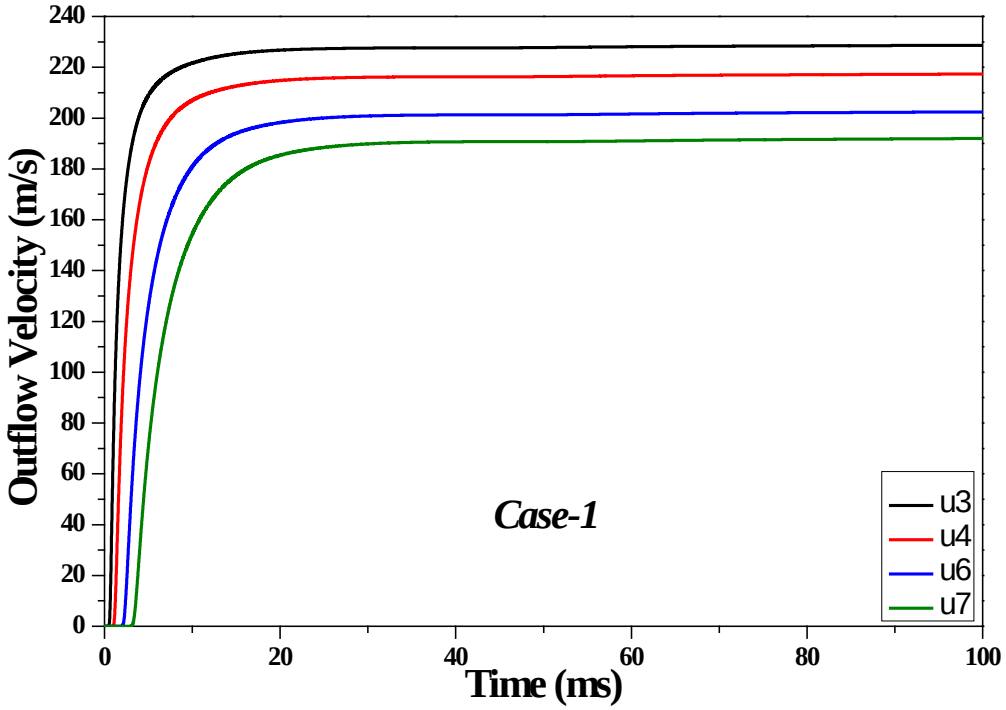

Figure 5.16: Outflow velocity-time traces at four locations (Case 1)

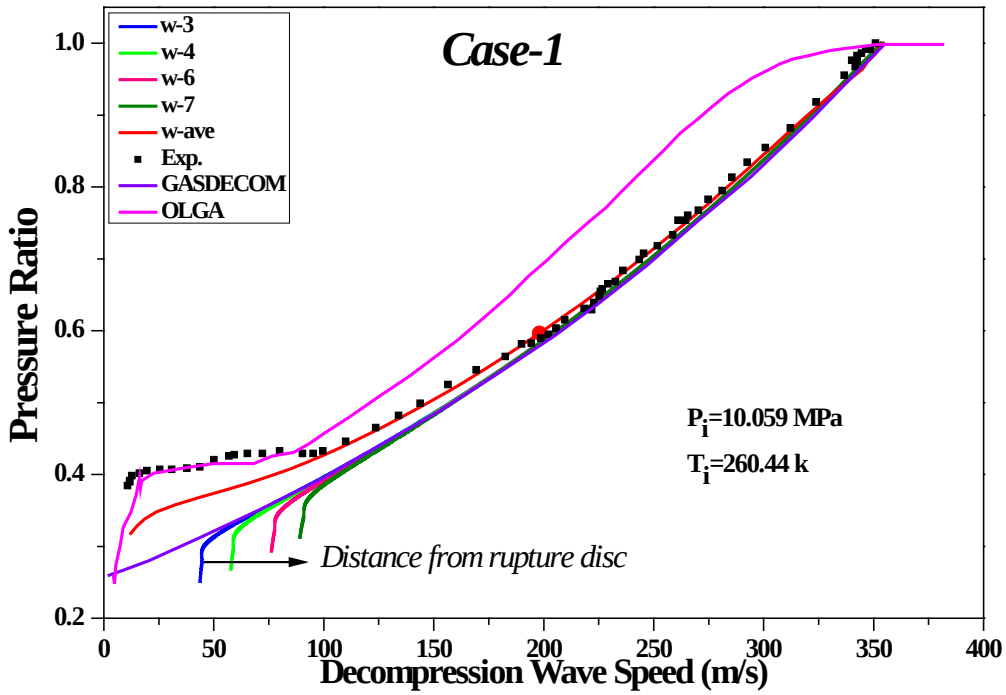

Figure 5.17: Comparison of the predicted decompression wave speed with the measured, GASDECOM and OLGA results (Case 1)

Good agreement can be observed between the measured data and the *average* decompression wave speed calculated using the pressure-time traces. Note that the

measured data of decompression wave speed deviates further to the left, forming a plateau approximately at pressure ratio of 0.4. The local decompression wave speed predicted at the four locations was identical to that predicted by GASDECOM, yet a constant local decompression wave speed was observed at the latter stages of the decompression. This shows that using the same definition of *w*, GASDECOM and the CFD model obtained the same results, indicating that GASDECOM performs as well as CFD (at a fraction of the computation time), despite using a different principle and different EOS. The only difference is that GASDECOM calculates the decompression speed independently of time or location, while the CFD results were predicted at several locations away from the outlet boundary and inherently as functions of the time.

5.4.4 Case 2: Decompression of Lean Natural Gas

Figure 5.18 shows the predicted and the measured pressure-time traces of the lean gas mixture. The predicted pressure starts to fall at nearly the same time as was measured at every monitor location. This indicates that the decompression wave speed was predicted at the correct operating pressure and temperature. The predicted rate of change in pressure was consistent with the experimental results until the appearance of a kink in the pressure-time curves at pressures near 5 MPa. : The kink is due to the discontinuity of the speed of sound across the phase boundary.. After this stage, the measured pressure-time traces became almost steady while the predicted pressure-time traces continued to drop further. The appearance of the kink coincides with a sharp drop in the speed of sound, as shown in Figure 5.19. The observed kink also appeared in the curves of outflow velocity and temperature results, as shown in Figures 5.20 and 5.21, respectively.

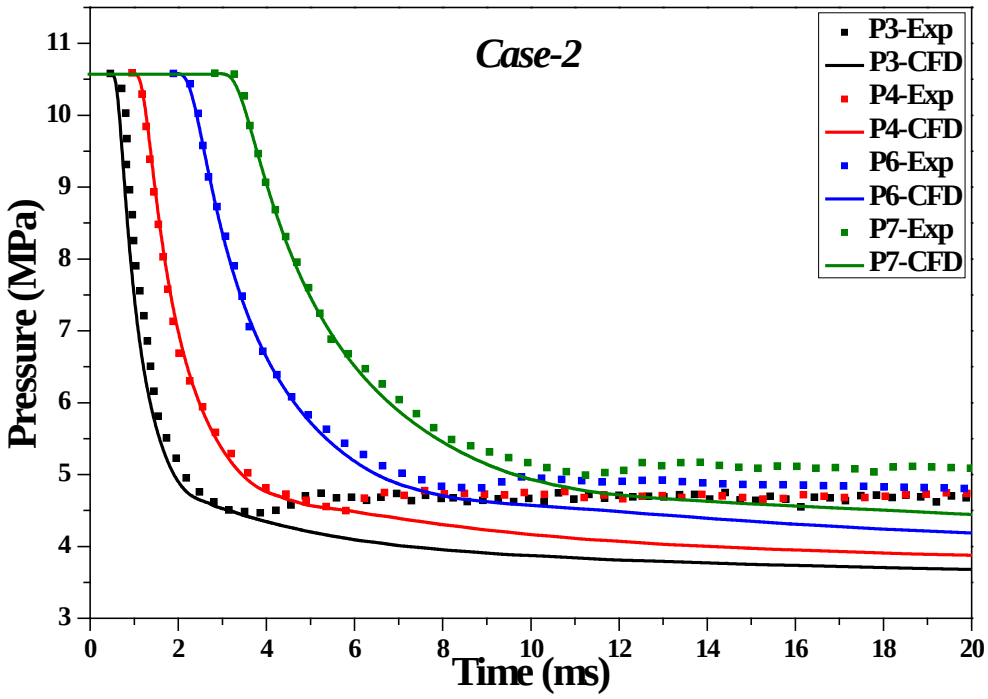

Figure 5.18: Comparison of predicted and measured pressure-time (Case 2)

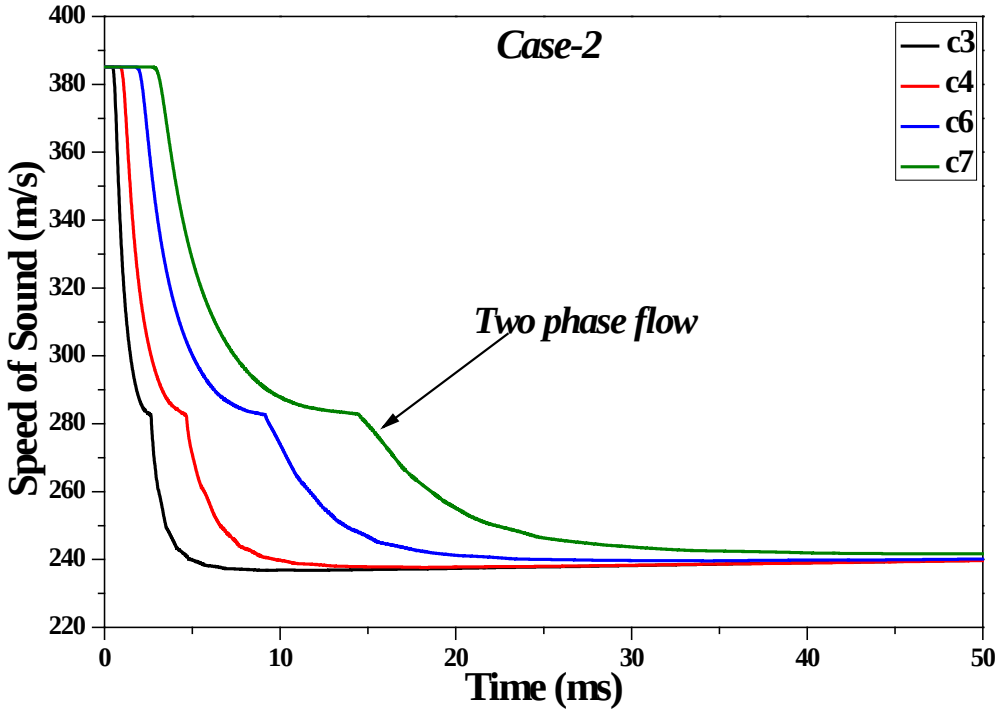

Figure 5.19: Speed of sound-time traces at four locations (Case 2)

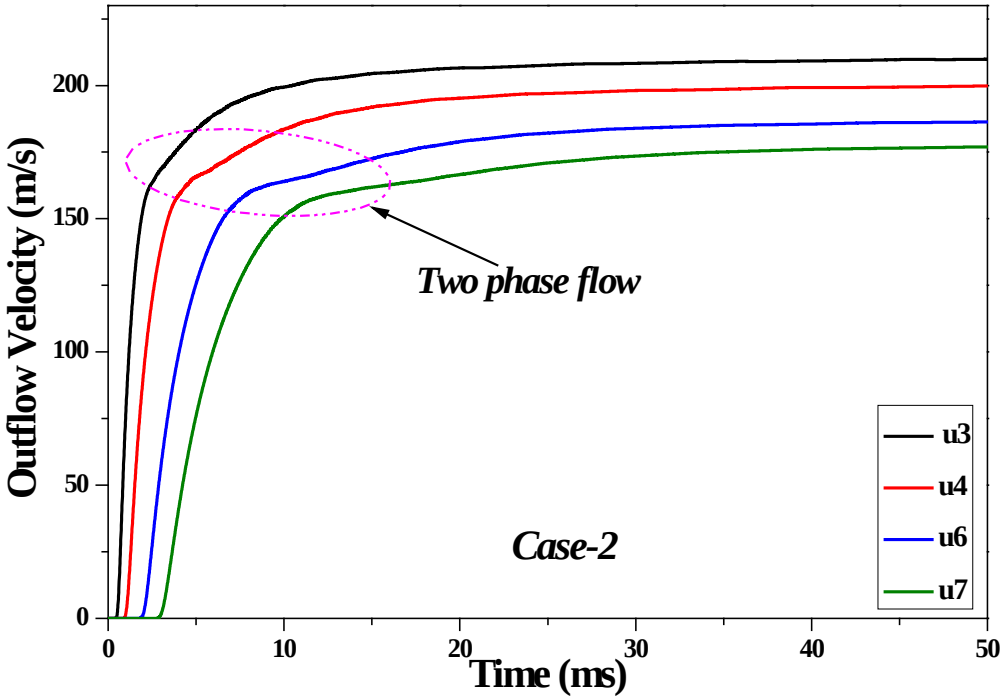

Figure 5.20: Outflow velocity-time traces at four locations (Case 2)

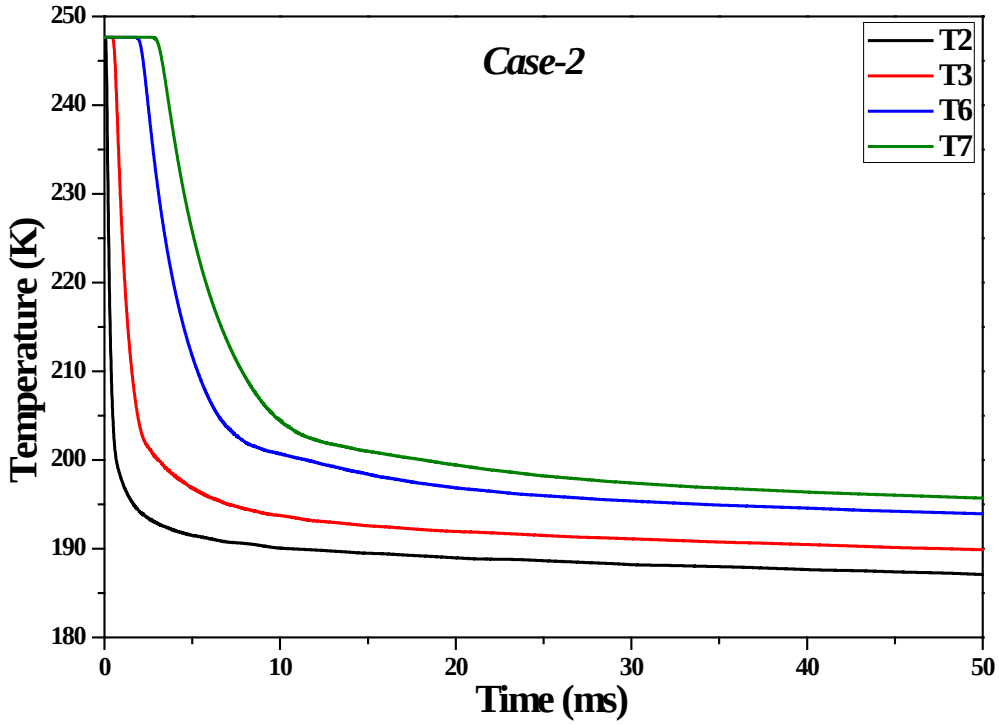

Figure 5.21: Temperature-time traces at four locations (Case 2)

By referring to the pressure and temperature transients, it is seen that the kink at monitor location 2 occurs at P=4.6 MPa and T=200.24 K. This point was found to be exactly on the phase boundary of the mixture, as expected.

Comparison of the predicted decompression speed against the measured data is shown in Figure 5.22. The results predicted by the current CFD model were more consistent with the measured data than those predicted by GASDECOM and OLGA, although there was still some discrepancy at the end of the decompression. Referring to Figure 5.22, a significant reduction in the decompression wave speed is observed, forming a pressure plateau at a pressure ratio of ~0.43 when crossing the phase boundary. Figure 5.23 shows the phase envelope of Case 2 and the point at which the decompression path enters the two-phase region. A significant drop in the speed of sound at a constant pressure occurred during this process.

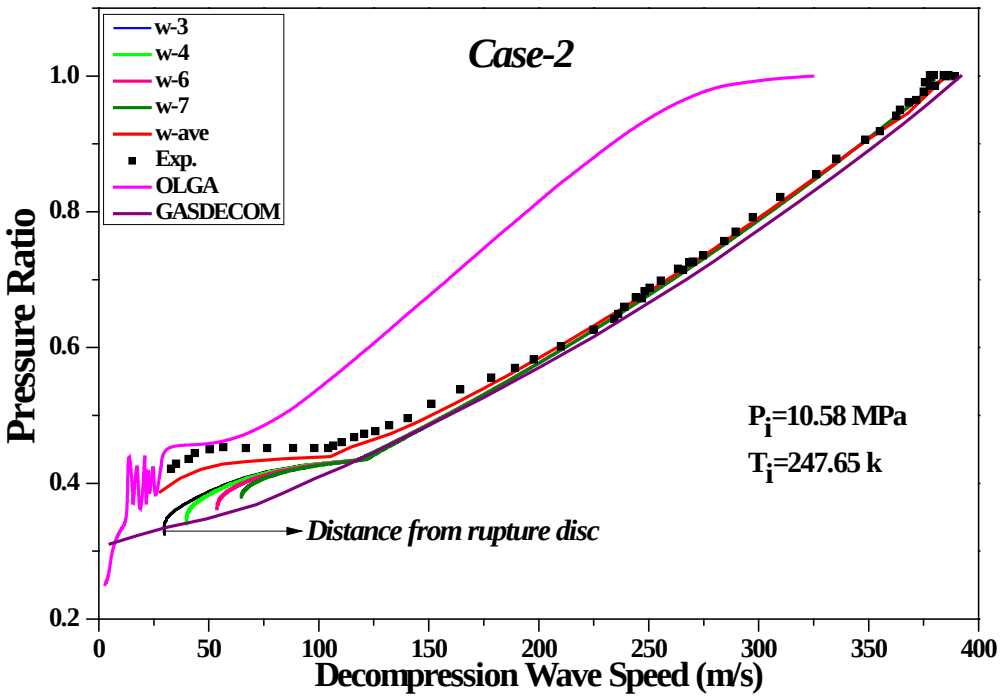

Figure 5.22: Comparison of the predicted decompression wave speed with the measured, GASDECOM and OLGA results (Case 2)

The current CFD decompression model successfully predicted the pressure plateau found in the measured data. The decompression wave speed calculated using the pressure-time traces compared well with the measured results. The appearance of such a plateau for gas mixtures is significant for fracture propagation arrest

requirements, as it can indicate higher minimum arrest toughness. GASDECOM was not able to predict the plateau for this mixture, although its results show good agreement at high pressure ratios, while OLGA predictions were inaccurate for this case as well. The discrepancy in the OLGA prediction can be linked to the method used to calculate the speed of sound [59, 158].

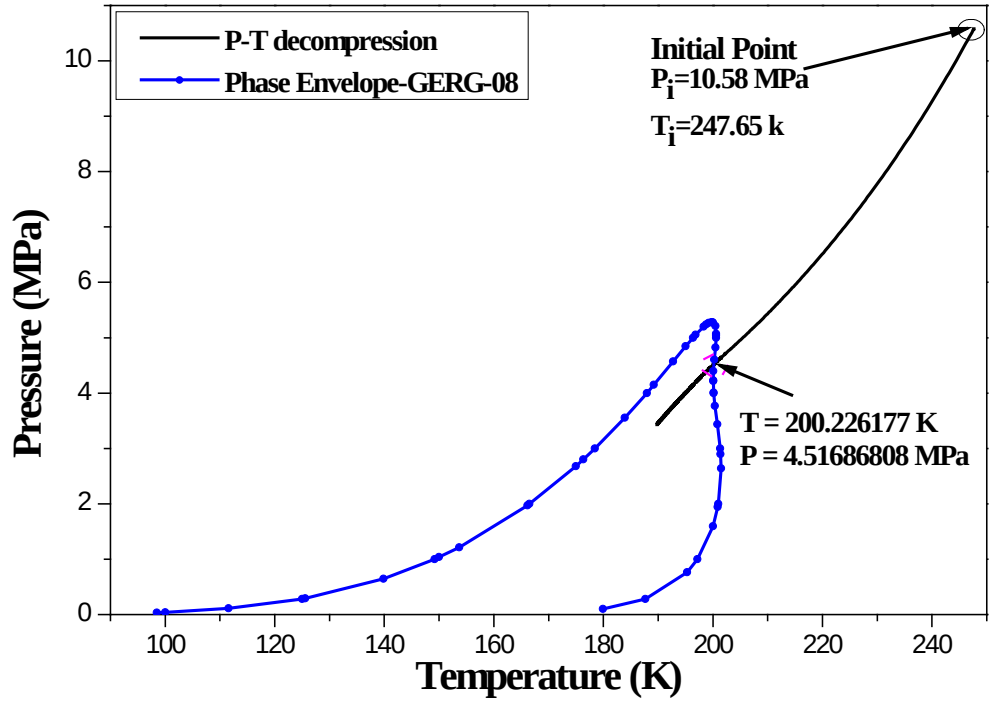

Figure 5.23: The interaction between the decompression behaviour of pressure and temperature with the phase envelope (Case 2)

5.4.5 Case 3: Decompression of Rich Natural Gas

Figure 5.24 shows a comparison between the predicted and experimental results of pressure-time traces of Case 3 recorded at locations 4, 6 & 7. The predicted pressure-time traces were in good agreement with the measured data. The two-phase flow region was predicted and clearly observed on the P-T curves for this mixture. The discrepancy between the predicted and the measured data occurred at pressure lower than 5 MPa.

The calculated speed of sound, outflow velocity and temperature as functions of time are shown in Figures 5.25, 5.26 & 5.27, respectively. In Figure 5.25, a sharp drop in the speed of sound is observed as the decompression wave crossed the two-phase boundary. The sharp drop in the speed of sound coincides with the formation of a plateau in the decompression wave speed transient, as shown in Figure 5.28. From this figure, it can be seen that the predicted average and local decompression wave speed is in good agreement with the measured results, except at low pressure ratios where the predicted results deviate further to the right. The major observation for this mixture is that the speed of sound increases towards the end of the decompression until it finally levels off at around 250 m/s.

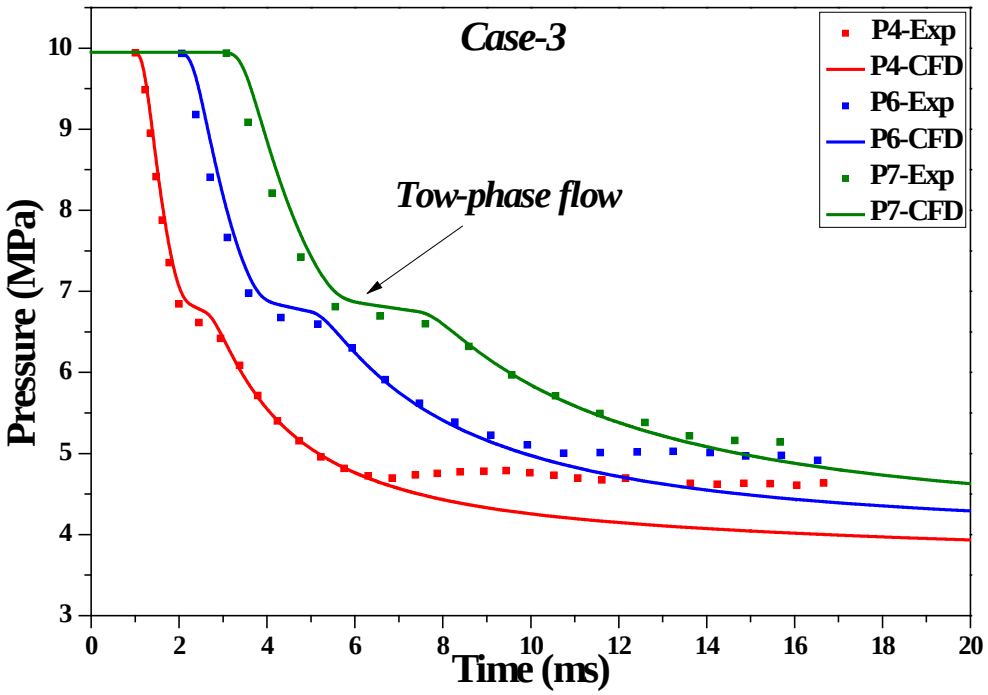

Figure 5.24: Comparison of the predicted and the measured pressure-time (Case 3)

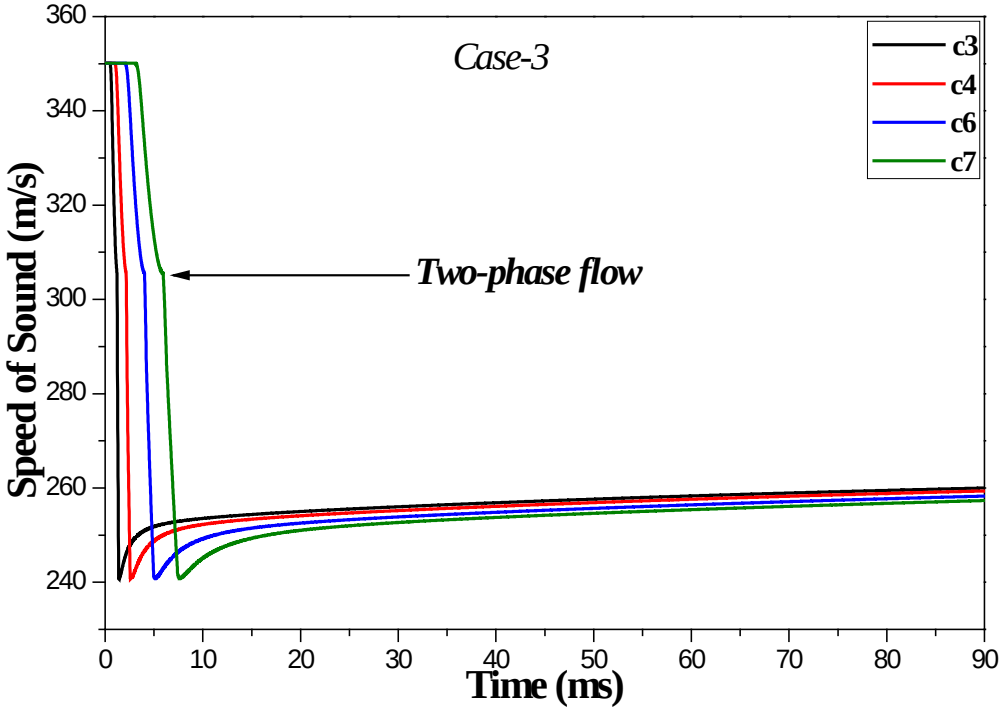

Figure 5.25: Speed of sound-time traces at four locations (Case 3)

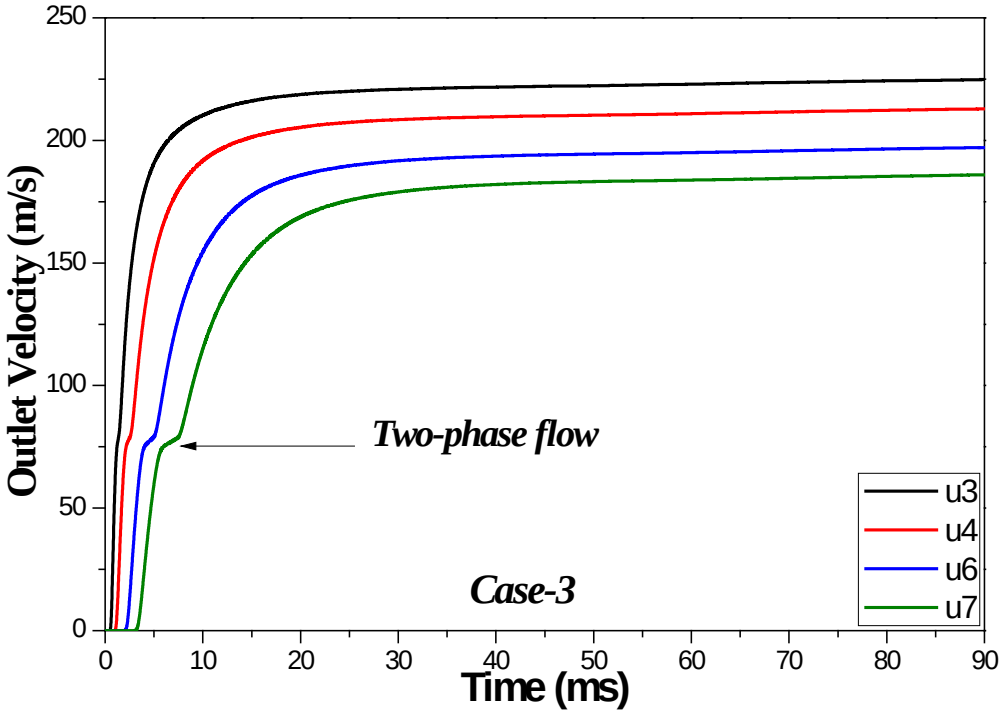

Figure 5.26: Outflow velocity-time traces at four locations (Case 3)

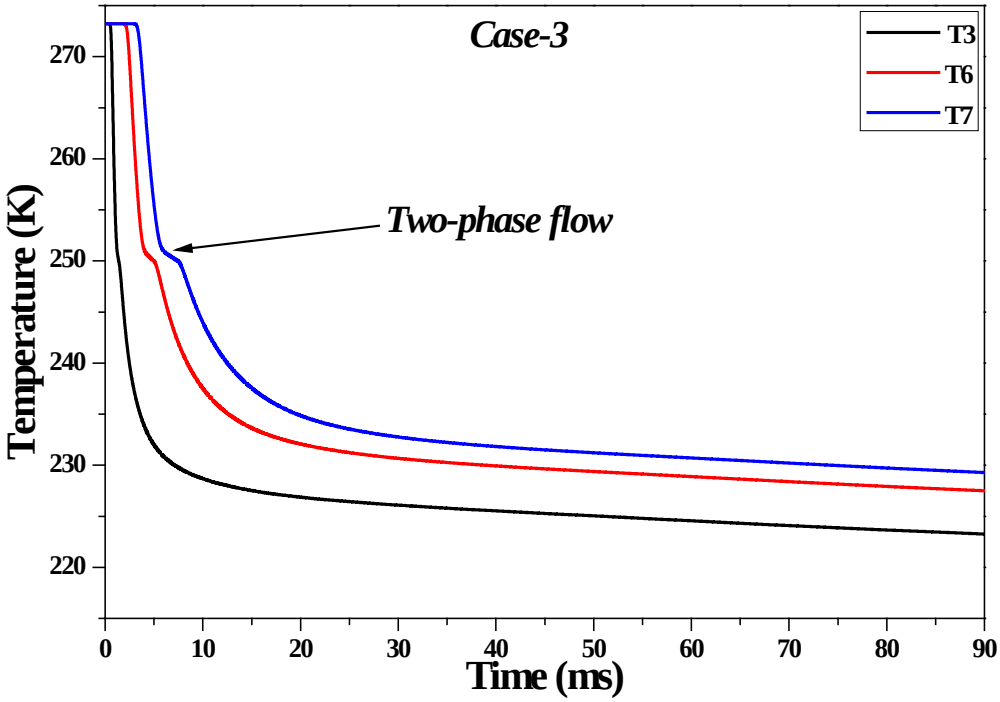

Figure 5.27: Temperature-time traces at four locations (Case 3)

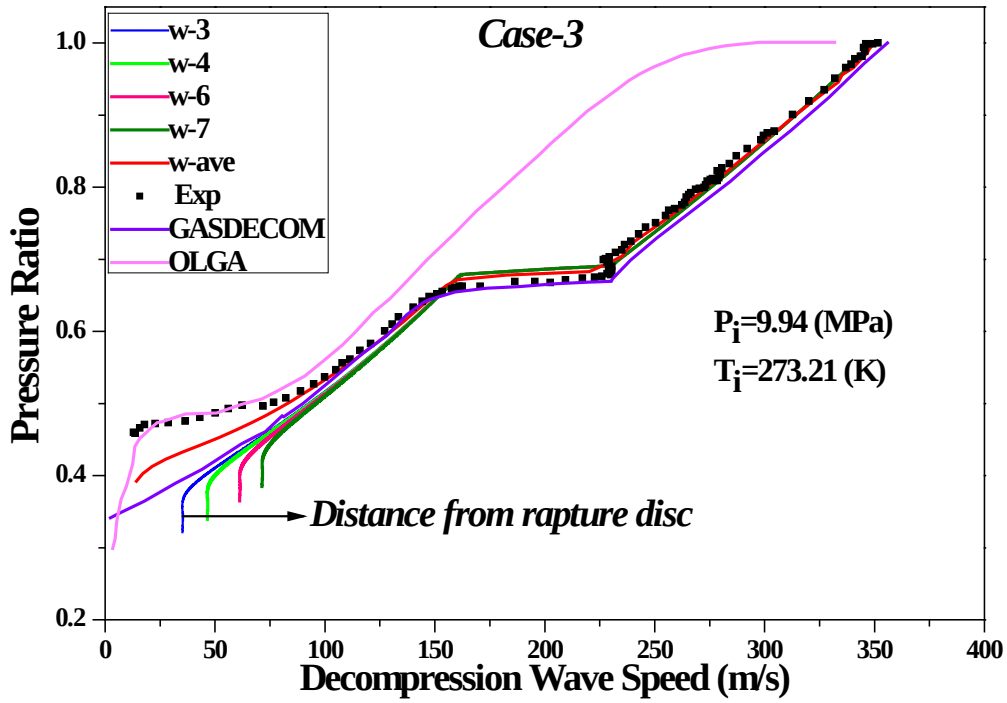

Figure 5.28: Comparison of the predicted decompression wave speed with the measured, GASDECOM and OLGA results (Case 3)

To verify that the CFD model predicted the decompression behaviour of gas mixtures while taking into account phase change, the decompression process was

expressed in the form of a pressure vs temperature curve, and was superimposed on the phase envelope of the mixture. This procedure was also done in the case of the lean gas mixture to find out at which point the flow enters the two-phase region. Figure 5.29 highlights the point where the flow crosses the two-phase boundary.

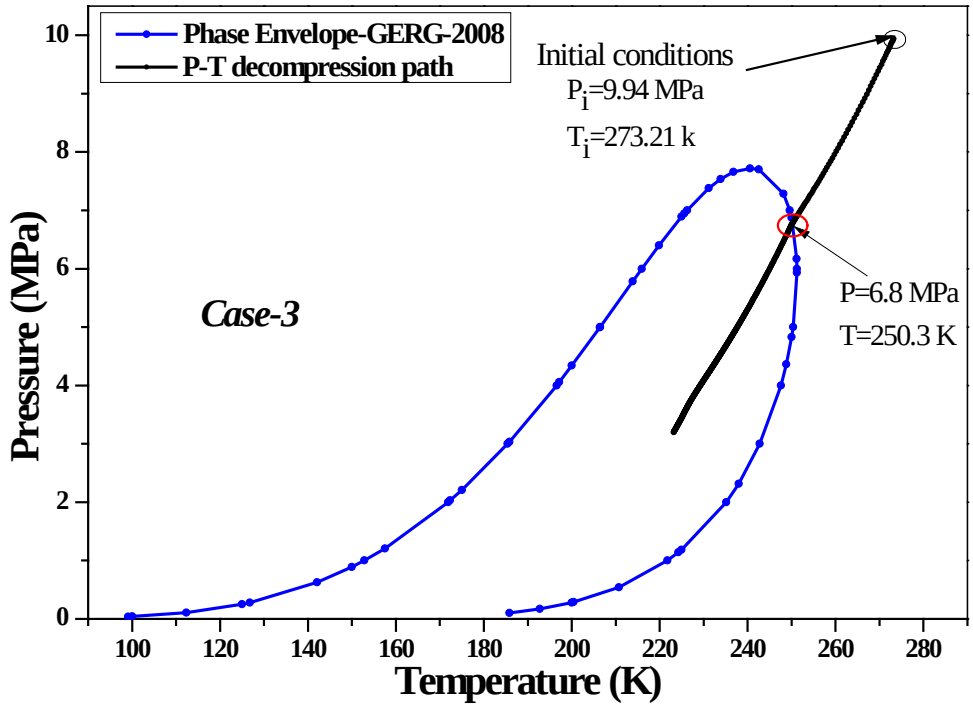

Figure 5.29: The interaction between the decompression behaviour of pressure and temperature with the phase envelope (Case 3)

5.5 Discussion

It was found that if the predicted pressure transient matches the experimental results, the predicted value of the decompression wave speed should be in close agreement with the measured data. As seen from Figures 5.18 and 5.24, there is a slight difference at the plateau between the measured and the predicted results, however, this difference is small (~2.9%–4.8% for Case 2 and 1.5%–1.8% for Case 3). The reason for this difference may be the uncertainties inherent in the numerical method that could possibly be improved. Other factors such as delayed nucleation and/or the rapid dynamics of the phase change (whereas the EOS uses *equilibrium* conditions at

all times), pipe wall roughness, heat transfer effects, etc. can influence the results to various degrees.

The most notable difference between the numerical and measured data is that the measured data shows a pressure drop downstream of the decompression wave, levelling off at the latter stages of the decompression. Experimental measurements show that this levelling off occurs more rapidly at a higher pressure than that predicted by the model. For locations p3 and p4, where results are available for the longest duration of time after the initial arrival of the decompression wave, the difference between the low pressure values is of the order of 0.4–0.8 MPa. This is also reflected on the decompression wave speed curves where, in all cases, the measured data deviates further to the left, creating an apparent second plateau. This is attributed to the piezoelectric pressure transducers used in these particular experiments. The apparent increase in the measured pressure-time traces (Figures 5.18 and 5.24) should be treated with caution at these low pressures. Later tests using Endevco pressure transducers did not show this increase in the pressure-time traces [60, 62].

For the purpose of model validation, the predicted initial decompression wave speed, pressure plateau and its length were compared with the measured data. The variation between the predicted and the measured initial decompression wave speed of all cases is shown in Table 5.4. The comparison shows that the model predicted the initial decompression wave speed precisely for all cases. This is in fact due to the accuracy of the GERG-2008 EOS in predicting the speed of sound at the initial conditions. Table 5.5 compares the predicted extent of the pressure plateau and the measured data once the flow crosses the two-phase region. The difference in the

length of pressure plateau ‘drop in speed of sound’ is shown in Table 5.6. Overall, a very acceptable result with a deviation value below 5% in the worst scenario was revealed, yet the result of Case 3 was the most accurate.

Table 5.4: The deviation between the experimental and the predicted initial decompression wave speed

Cases	**W (Exp)**	**W (CFD)**	**Deviation %**
Case 1	350.92	353.4	~0.71%
Case 2	389.235	385.11	~1.06%
Case 3	351.664	350.13	~0.44%

Table 5.5: The deviation between the experimental and the predicted plateau pressures

Cases	**P (Exp)**		**P (CFD)**		**Deviation %**
	From	To	From	To	
Case 2	0.452	0.44876	0.49955	0.4269	2.6-4.8%
Case 3	0.673	0.6714	0.6825	0.6605	1.47-1.76%

Table 5.6: The drop in speed of sound in two-phase region (plateau length in *w*)

Cases	**Plateau Exp (m/s)**	**Plateau CFD (m/s)**	**Deviation %**
Case 2	102-53=49	105-58=47	4.08%
Case 3	225-157=68	220-155=65	4.4%

The predicted results of decompression wave speed based on the local formulation deviate at the final stage of the decompression process in all cases. The *w* becomes constant with a continuing drop in pressure. This phenomenon begins at different values of pressure ratio and depends on the location. At the location nearest to the

full bore opening, *W* became constant at a lower pressure ratio than that further away from the outlet. This indicates that the difference between the speed of sound and the outflow velocity became constant. This trend is likely to be related to the increase of entropy due to the turbulences at the vicinity of the wall. The increase of entropy limits the decrease of the local speed of sound and limits the rate of increase of the flow velocity. The combined effects on the speed of sound and flow velocity indirectly limit the local decompression wave speed.

Figure 5.30 presents the contour of outflow velocity at several time steps (0.5, 5 & 13 ms) for Case 3. This figure illustrates the effect of the wall on the fluid flow. As the flow progresses, the flow becomes fully developed where the velocity gradually increases towards the centre of the pipe away from the wall boundary, while at the wall boundary the velocity remains very low. This is due to the assumption of no-slip conditions at the wall ($u=0$ *m/s*). As the velocity increases, the friction will increase based on the value of surface roughness ($\varepsilon=1$ μm) defined at the internal surface of the pipe so the entropy will be generated accordingly.

Figure 5.31 presents the entropy generation due to friction effect at the pipe wall. This figure affirms the phenomena that as the outflow velocity increases, the entropy generation increases. However, this impact appears only at the later stages of the decompression process and at pressure levels below choked pressure in all cases. Such an effect can be neglected in terms of predicting the minimum pipe material toughness required for fracture propagation control[82].

This can be further illustrated by comparing property distribution along the pipeline near the wall boundary and at the centre of the pipe. The temperature distribution along the first 10 m of the pipe from the outlet boundary is presented. It can be

noticed that the wall temperature remains slightly high compared to that at the centre of the pipe, which is in fact outside the impact of the boundary layer where the effect of friction is taking place. Figure 5.33 presents the distribution of turbulent kinetic energy at the wall and at the centre of the pipe. It can be seen in Figure 5.34 that the turbulent kinetic energy increases at the wall with the increase in the outflow velocity. Such an effect should be taken into account for longer and smaller diameter pipelines. This has affected the speed of sound, which is re-increased as depicted on Figure 5.35. Notably, the static pressure distribution at both the centre of the pipe and the wall boundary remain almost identical. This explains the difference noticed on Figures 5.17, 5.22 & 5.28 between the local and the average decompression wave speed at the latter stages of the decompression, where the local decompression wave speed became constant while the pressure continued to drop.

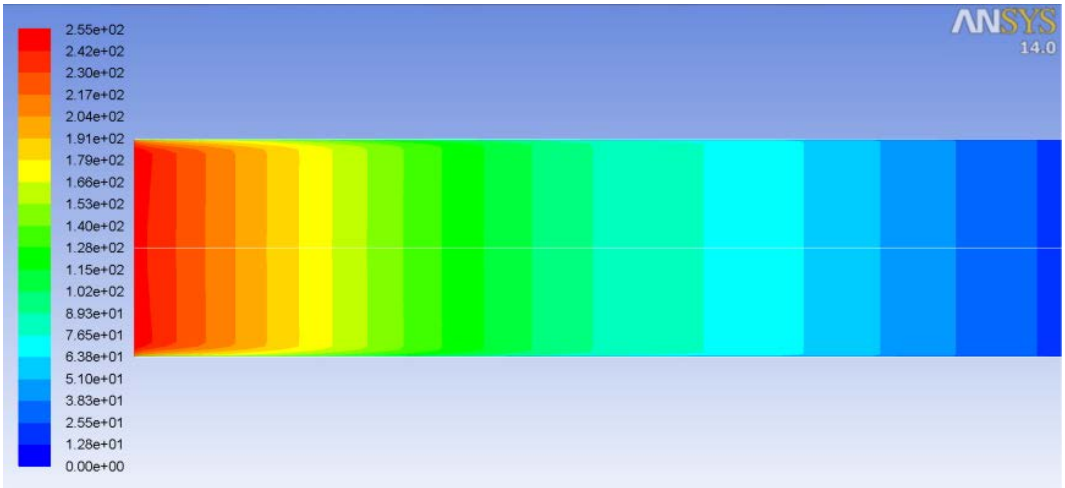

(a) 0.5 ms

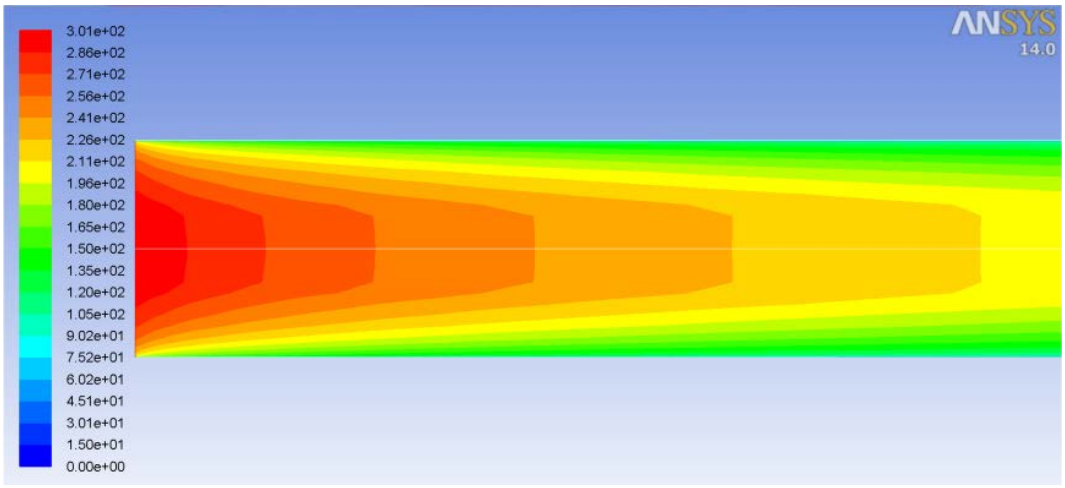

(b) 5 ms

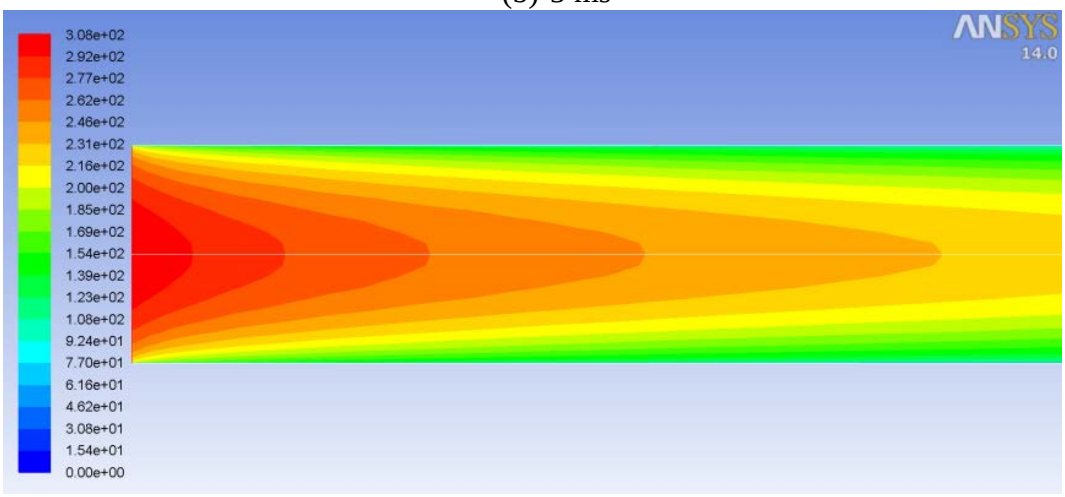

(c) 13 ms

Figure 5.30: Evolution in velocity contours (m/s) (Case 3)

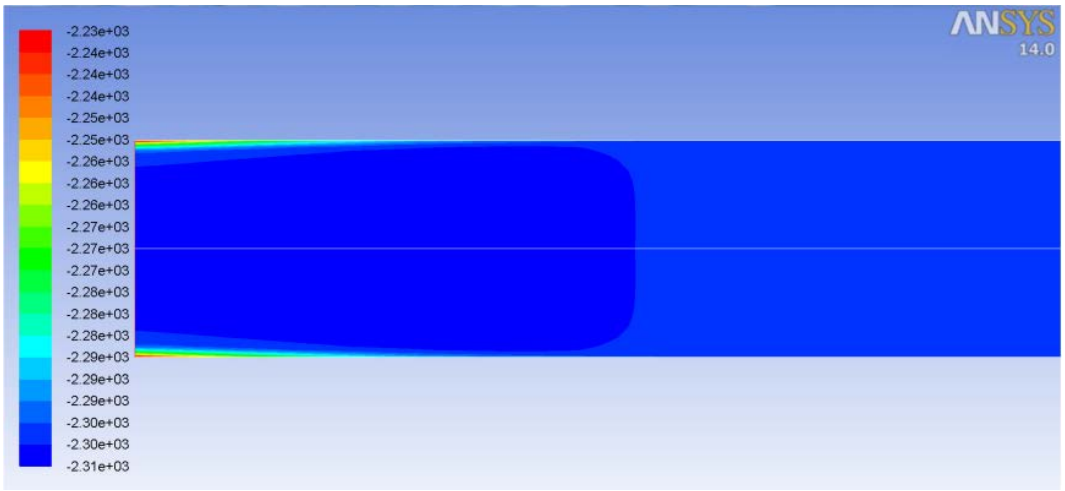

(a) 0.5 ms

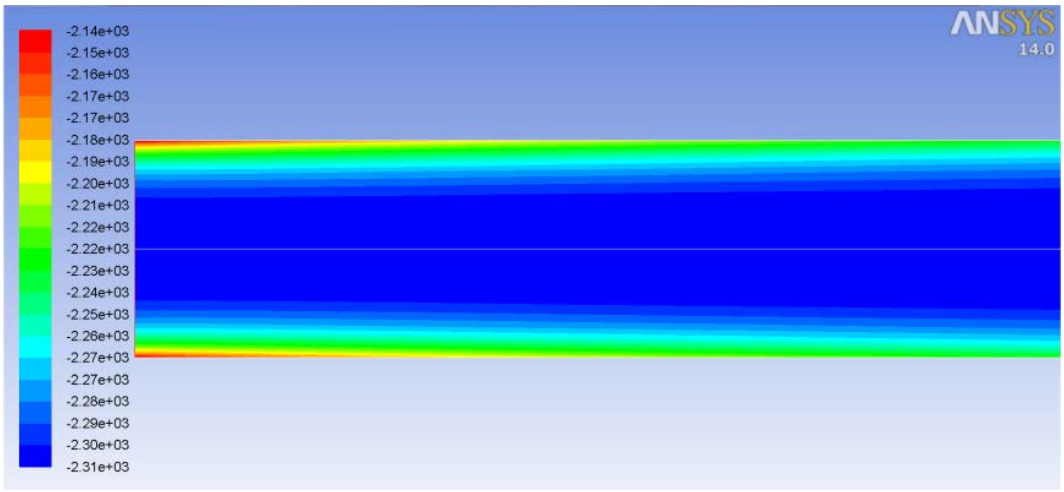

(b) 5 ms

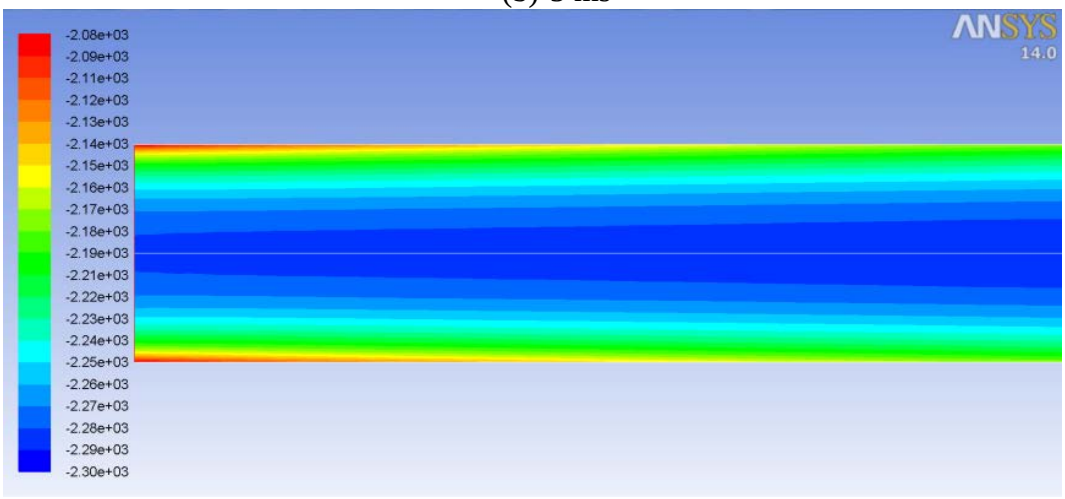

(c) 13 ms

Figure 5.31: Entropy generation contours as the flow evolves

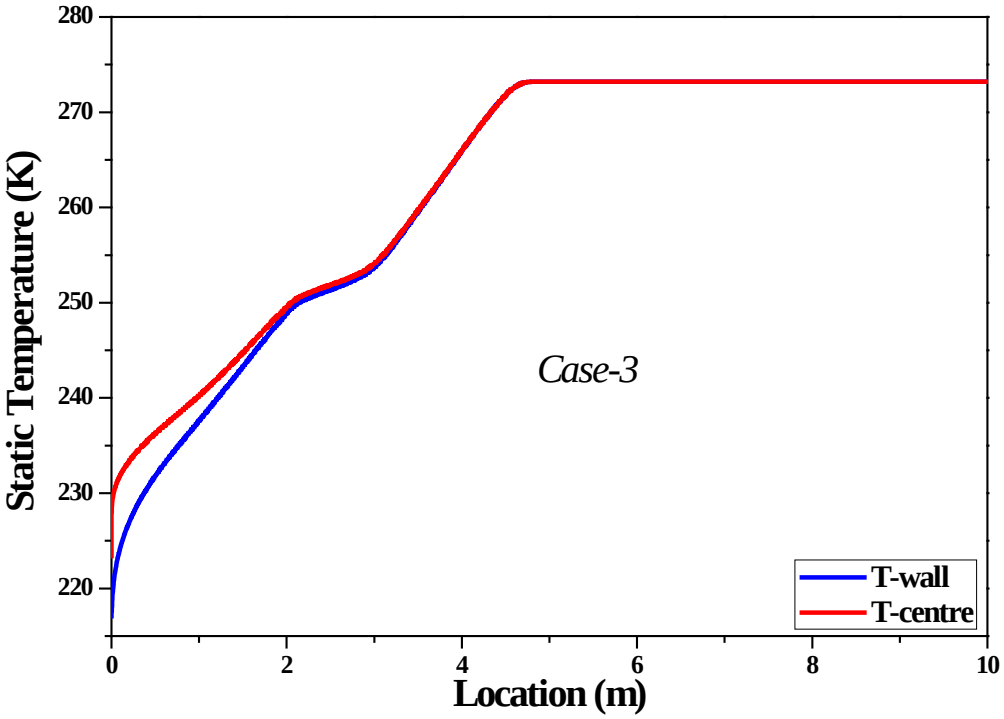

Figure 5.32: Temperature distribution along the first 10 m of the pipe

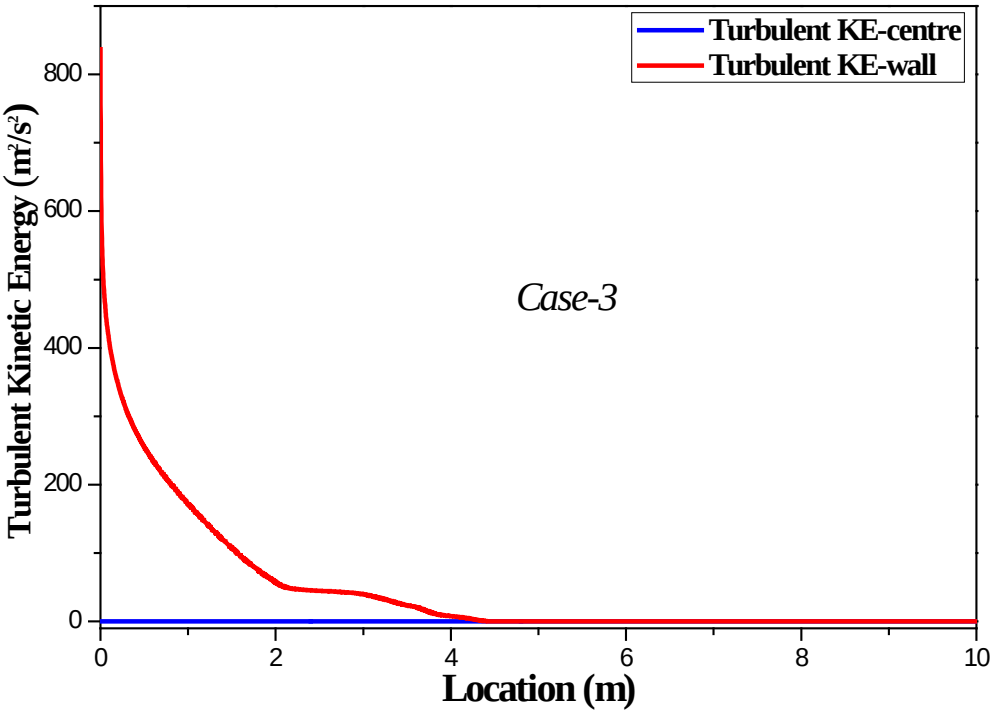

Figure 5.33: Turbulent kinetic energy distribution along the first 10 m of the pipe

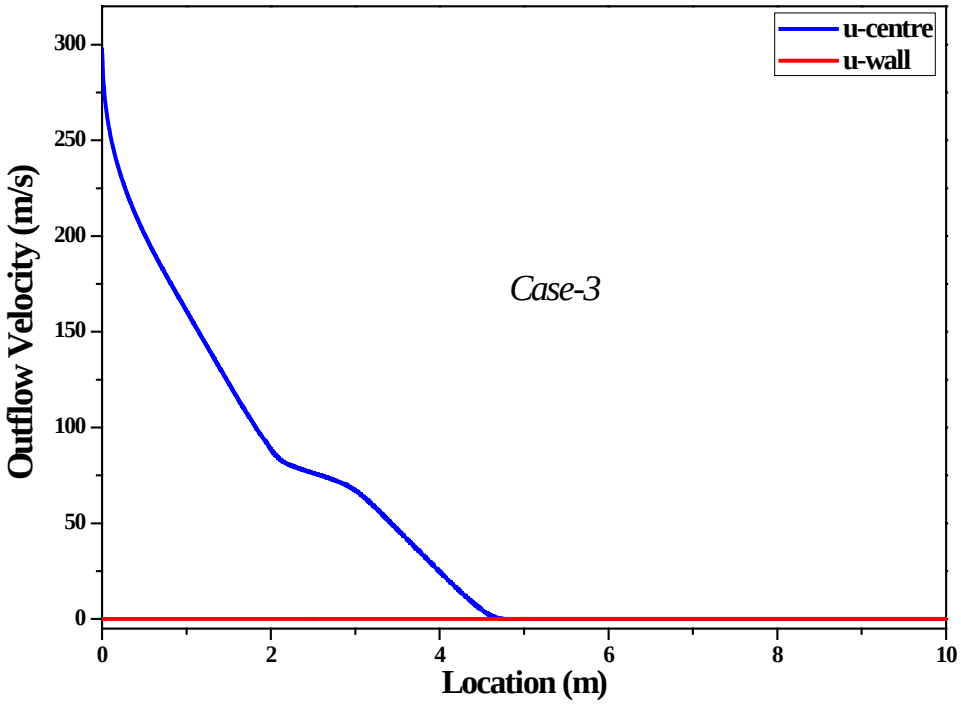

Figure 5.34: Outflow velocity distribution over the first 10 m of the pipe

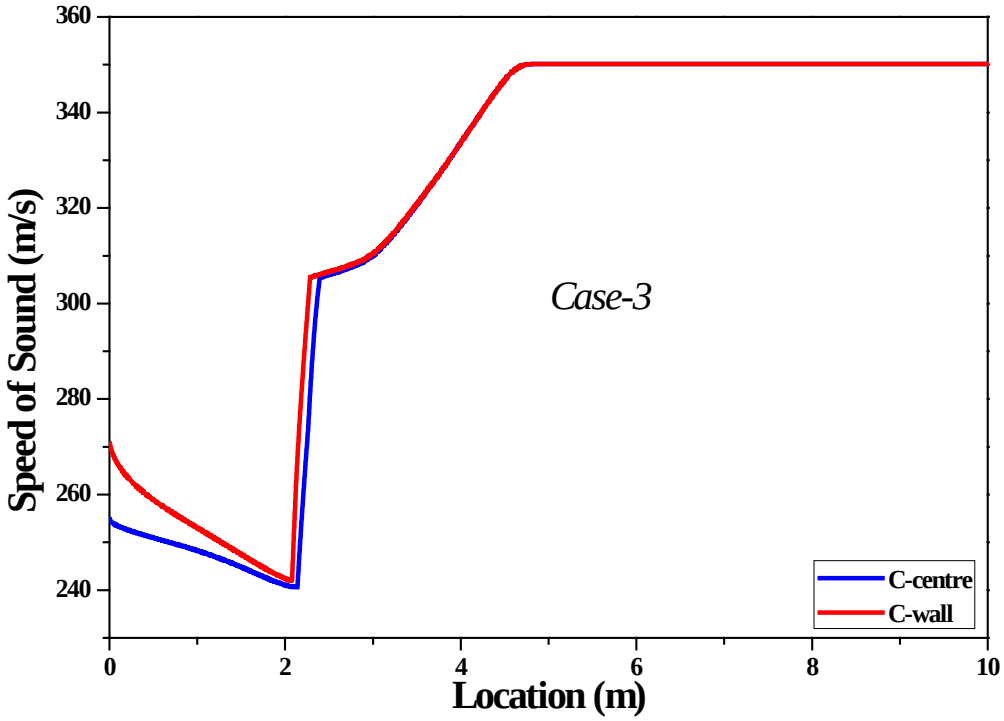

Figure 5.35: Speed of sound distribution over the first 10 m of the pipe

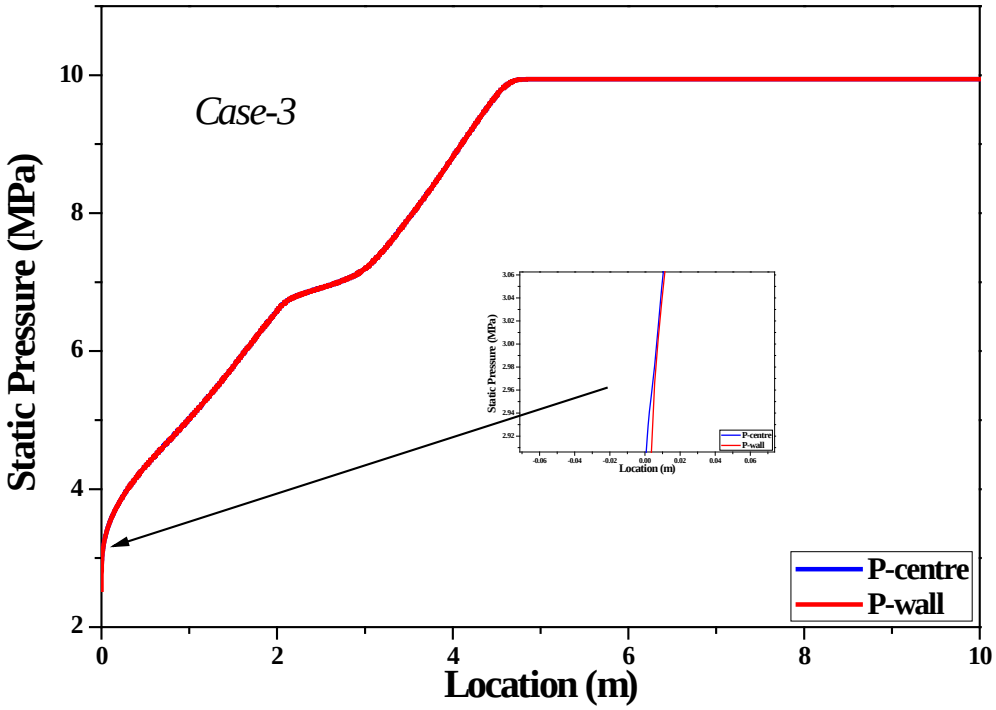

Figure 5.36: Static pressure distribution along the first 10 m of the pipe

5.6 Summary

The findings presented in this Chapter can be summarised as follows:

(a) 2D CFD simulations of the decompression behaviour in gas pipelines were carried out in order to validate the CFD model developed in Chapter 4;

(b) The indirect use of the GERG-2008 EOS was validated against the implementation of the PR EOS. Near-identical trends in all predicted properties were observed, suggesting that the method of implementation of the GERG-2008 EOS was successful;

(c) The results predicted by the current CFD model are in good agreement with experimental results obtained from the shock tube tests studied in this chapter. The results prove the capability of the model in dealing with different gas mixtures and multi-phase flow;

(d) The influence of wall boundary on the behaviour of some properties and its impact on the local and average decompression wave speed is discussed. It was found that the local decompression wave speed will always differ from that obtained from pressure-time traces, especially at the latter stages of the decompression. This difference could be neglected as far as fracture propagation control is concerned, but for longer and smaller diameter pipelines, it may become influential.

The current work demonstrates that the CFD technique can be used to predict rapid and severe gas decompression by solving the governing flow equations, in conjunction with the GERG-2008 EOS. This is shown to be an effective tool for determining the decompression wave speeds for different gas mixtures. In the next chapter, Chapter 6, the model will be used to investigate the decompression behaviour of CO_2 mixtures.

Chapter 6 Decompression Characteristics of CO_2 Mixtures

6.1 Introduction

In this chapter, the 2D CFD decompression model is employed to predict the decompression behaviour of CO_2 mixtures. Two different sets of shock tube tests have been simulated in order to validate the model. The influences of the initial pressure and initial temperature on decompression wave speed are discussed, and the impact of impurities on the decompression behaviour is discussed. In addition, the effects of pipe diameter and pipe wall roughness on decompression wave speed of CO_2 mixtures are investigated. Lastly, based on the predicted decompression curves of the three CCS technologies (post-combustion, pre-combustion and oxyfuel), the arrest toughness is calculated using several initial temperatures, pressures and pipe diameters.

6.2 Simulation Model

Two shock tube tests were modelled. The first test (Case A) was conducted at the TransCanada Pipeline Gas Dynamics Test Facility in Didsbury, Alberta, Canada [54]. The second test (Case B) was commissioned by the National Grid at GL Noble Denton Spadeadam Test Site in Cumbria, UK [55]. In the first test, the main section of the shock tube was 42 m long, the internal diameter (ID) was 38.1 mm and the tube wall thickness was 11.1 mm. In the second test the pipe was 144 m long, the ID was 146.36 mm, and the pipe wall thickness was 10.97 mm. In Case A, a ‘smooth’ pipe surface was used, while in Case B, the pipe has an average surface roughness ranging between 5 and 6.3 μm. The smoothest pipe was placed nearest the rupture disk.

Table 6.1 lists model parameters set up for the current simulations. CFD simulations were carried out for two mixtures: a binary mixture for Case A and a five-component mixture for Case B. Table 6.2 shows the gas compositions and initial conditions of the two tests. The pressure and temperature were monitored as a function of time at several locations along the axial direction, near the exit plane. These locations corresponded to where the pressure transducers and temperature probes were fitted on the shock tubes. Other properties such as the speed of sound and 'outflow' velocity were monitored at the equivalent locations to determine the local decompression wave speed. Table 6.3 shows the locations of pressure and temperature transducers mounted on both shock tube tests. The highlighted cells in Table 6.3 represent locations used for the determination of decompression wave speed in the current simulation.

Table 6.1: Model parameters settings for the current study

Case	Pipe length (m)	Diameter (mm)	Surface roughness (μm)	Turbulence model
Case A	42	38.1	Smooth	Realisable k-ε
Case B	144	146.36	5	Realisable k-ε

Table 6.2: Mixture compositions and initial conditions of shock tube tests

Shock tube test	Mixture components (mole %)					P_i (MPa)	T_i (K)
	CO_2	H_2	N_2	O_2	CH_4		
Case A	72.6	0	0	0	27.4	28.568	313.65
Case B (T31)	91.03	1.15	4	1.87	1.95	14.95	283.15

Table 6.3: Monitor point locations

TEST 1 (Case A)		TEST 2 (Case B)	
Location	Distance from rupture disc (m)	Location	Distance from rupture disc (m)
PT1	0.0295	P2	0.0864
PT1A	0.0924	P4, T4	0.34
PT1B	0.1028	P6	0.54
PT2	0.2	P8	0.74
PT3	0.35	P10	0.94
PT4	0.5	P12	1.24
PT5	0.7	P14, T14	1.84
PT6	0.9	P16	2.44
PT7	1.1	P18	3.64
PT8	3.1	P19	4.84
PT9	5.1	T20	6.04
PT10	7.1	P21	9.04
PT11	9.1	P22	13.54
PT12	13	T23	18.04
PT13	19	P24	22.54
PT14	25	T25	30.04

The thermodynamic properties of each mixture were first produced using the GERG-2008 EOS and then saved into readable files. Table 6.4 shows the structure of the P-T table established for the mixture in Case A. The properties were calculated for all P-T nodes in the Table. Note that the minimum and maximum values of P and T in the main table will vary depending on the initial conditions and phase envelope of

each mixture. A MATLAB code was written to generate plots of the required properties as a function of pressure and temperature. The calculated properties for Case A are presented in Figure 6.1. A smooth distribution was observed for all properties, including the region under the two-phase boundary.

Table 6.4: P-T property structure table

	Pressure (MPa)	Temperature (K)
Min.	0.05	180
Max.	30	320
Increment	0. 1	0.5
No. of nodes	300	281

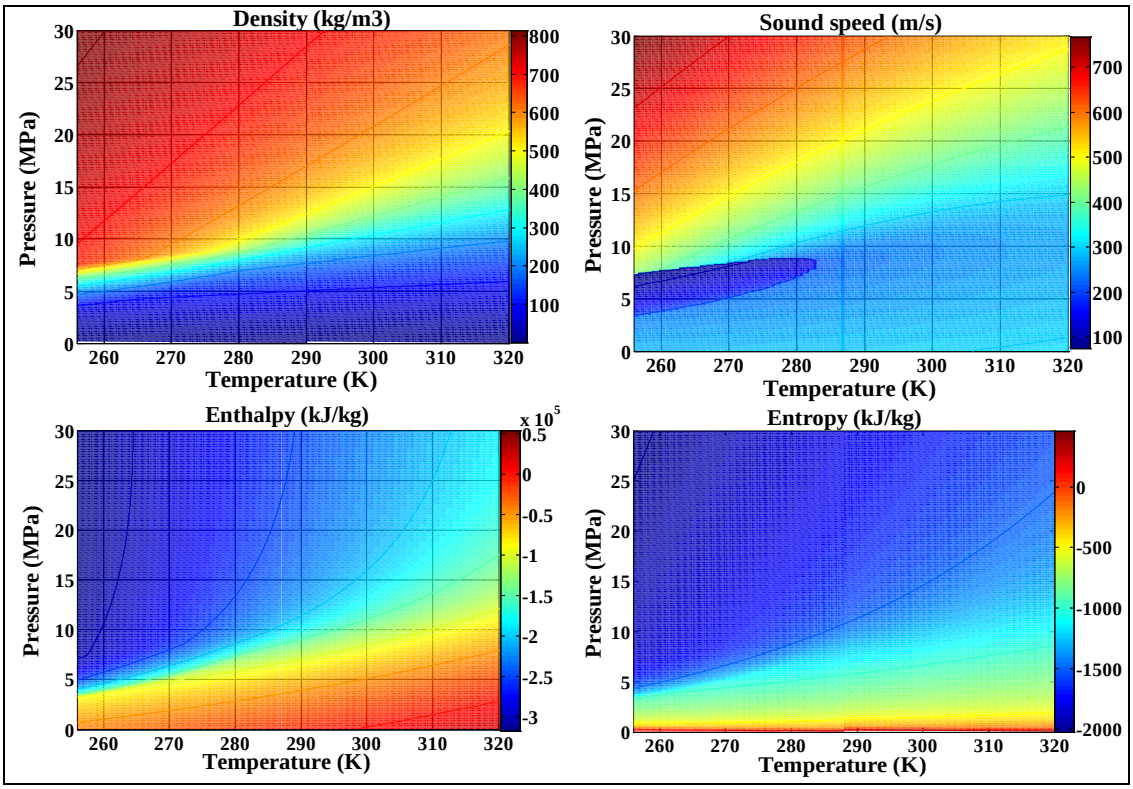

Figure 6.1: Thermodynamic properties calculated by GERG-2008 (CO_2-Case A)

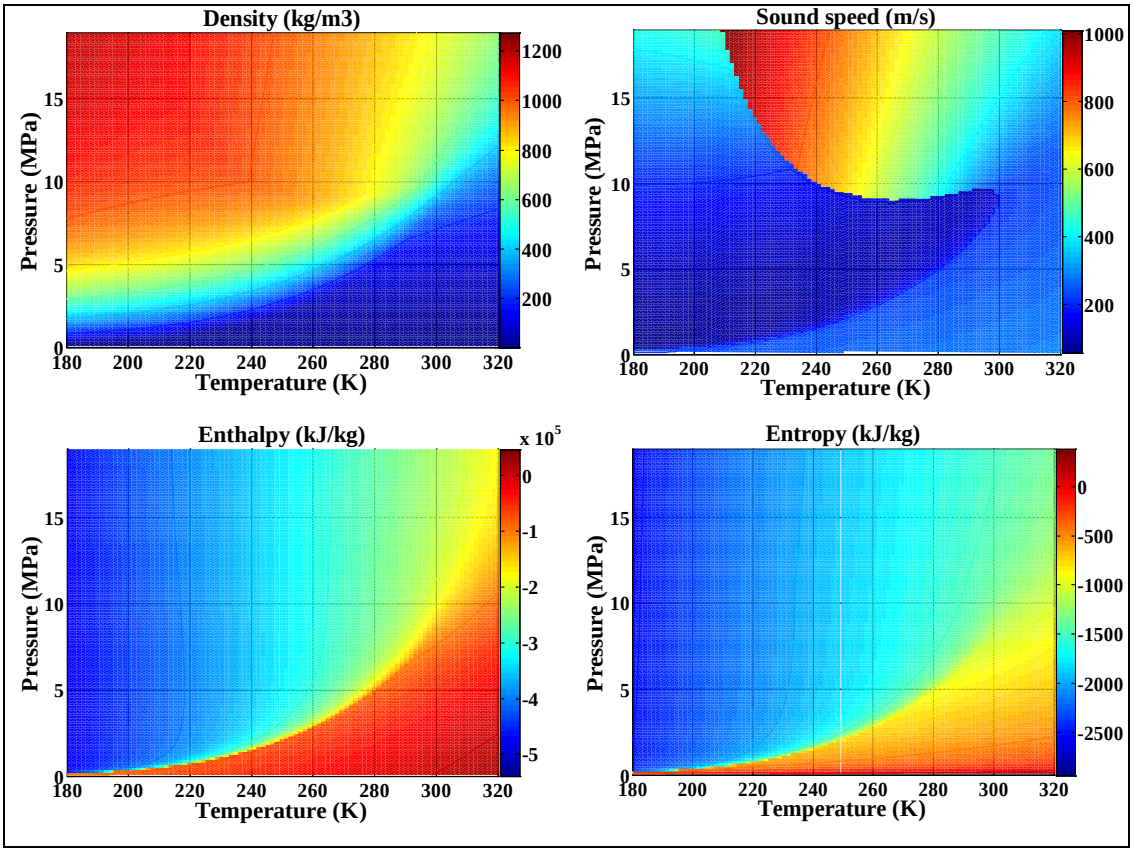

Figure 6.2: Thermodynamic properties calculated by GERG-2008 (CO_2-Case B)

6.2.1 Mesh Independence Study

A mesh-dependence study was carried out for both cases using different element sizes (2, 3, 5, 10, 20, 50, 100 mm). As can be seen from Figures 6.2 and 6.3, an optimum element size was found to be 2 mm, even though for decompression wave speed calculation, an element size up to 10 mm was found acceptable.

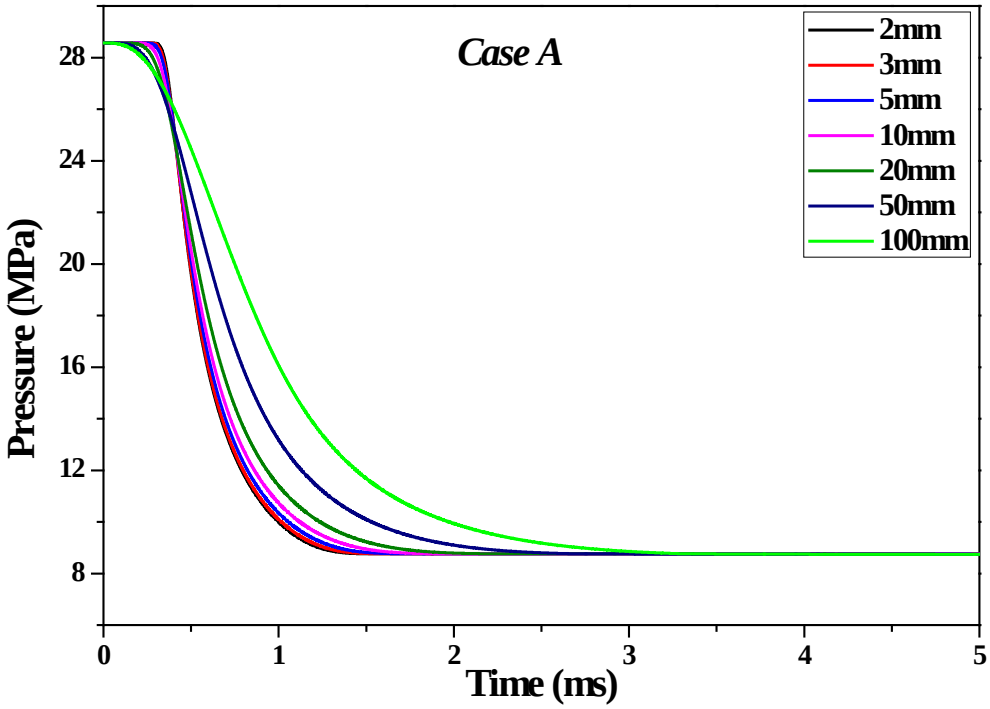

Figure 6.3: Mesh independence for Case A

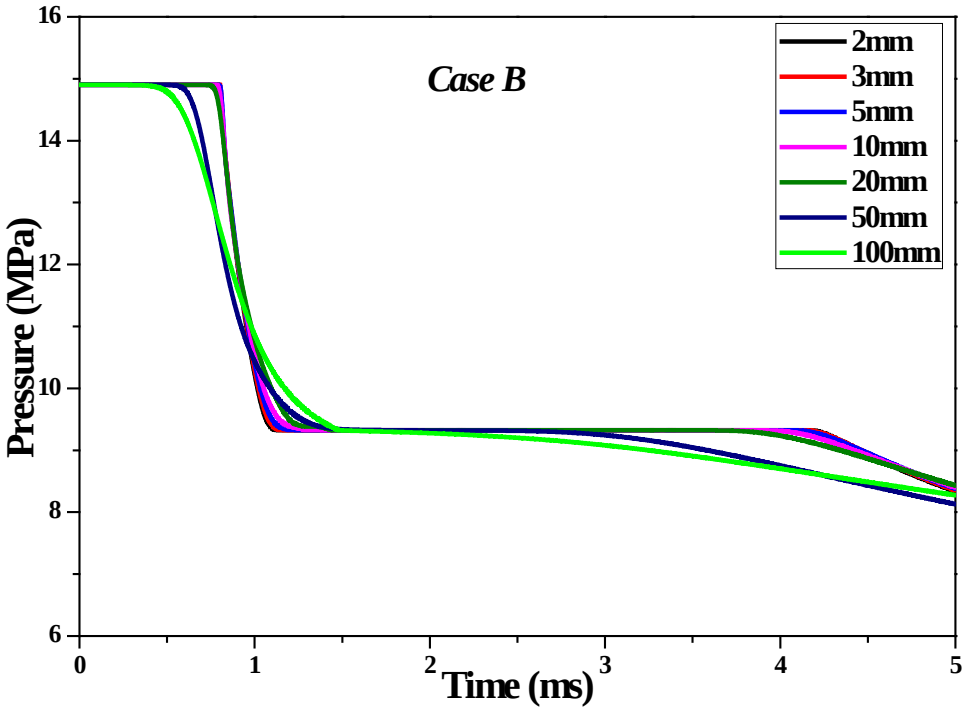

Figure 6.4: Mesh independence for Case B

6.2.2 Simulation Results of Case A

Decompression of the mixture in Case A was simulated first, with a flow domain compatible with the shock tube test described in reference [54]. As Figure 6.5 shows,

the simulated pressure-time histories are in good agreement with the measurements. There was a slight discrepancy between the measured and predicted pressure at pressures between 26 and 27 MPa.

Figure 6.6 shows the transient behaviour of the fluid temperature at the four locations closest to the outlet boundary (rupture disc). The variations in the speed of sound and the outflow velocity are shown in Figure 6.7 and Figure 6.8, respectively. The forms of the pressure-time and temperature-time curves were similar. The fluid temperature suddenly dropped from its initial value to 276 K; the temperature remained steady at this value for several time steps, creating a temperature plateau, before continuing to drop steadily. The predicted speed of sound at the initial conditions was 516.28 m/s. Figure 6.7 shows that the speed of sound gradually decreased to a value close to 258 m/s and then dropped to their lowest level of 105 m/s.

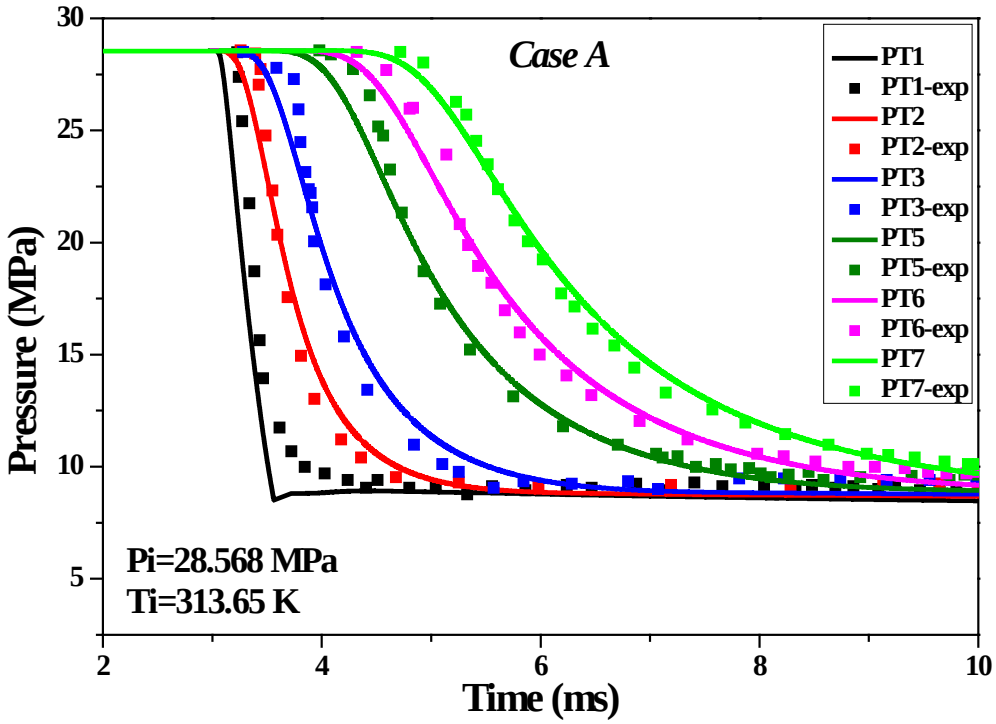

Figure 6.5: Comparison between predicted and measured pressure-time traces (Case A).

Before the rupture disk ruptured, the entire body of gas in the tube was at rest. In the

simulation, as the outlet boundary was subjected to ambient pressure at time t=0+, an expansion (decompression) wave was set off. As the wave propagated away from the opening, the exit velocity was seen to increase. Like the other properties, the outlet velocity remained steady for a short time at 85 m/s before continuing to increase again.

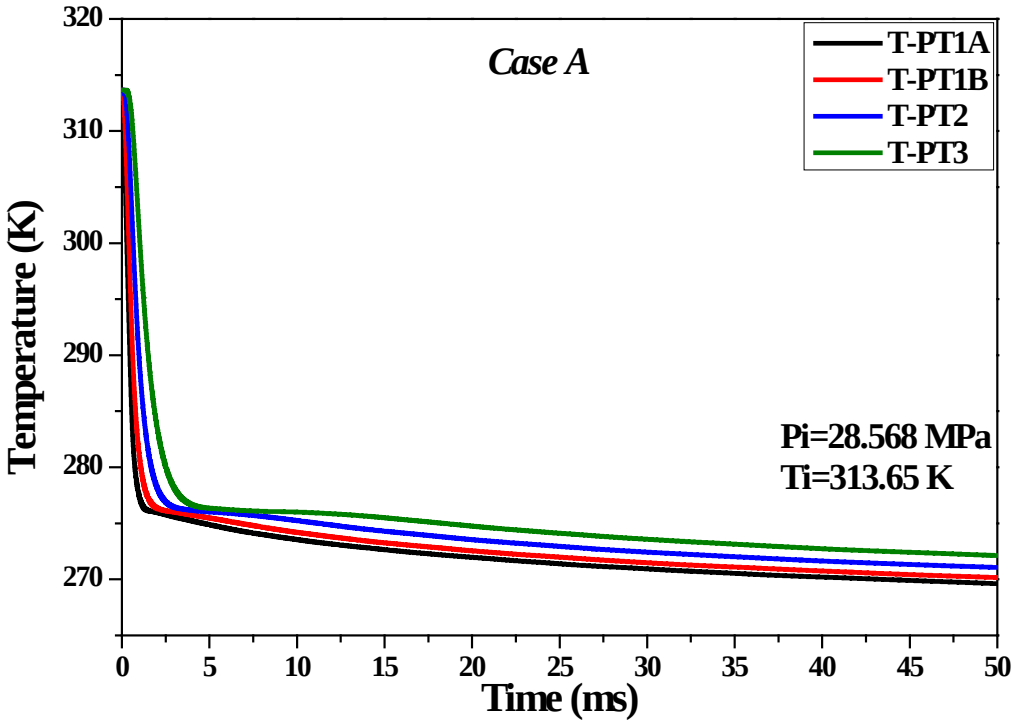

Figure 6.6: Predicted fluid temperature vs time (Case A)

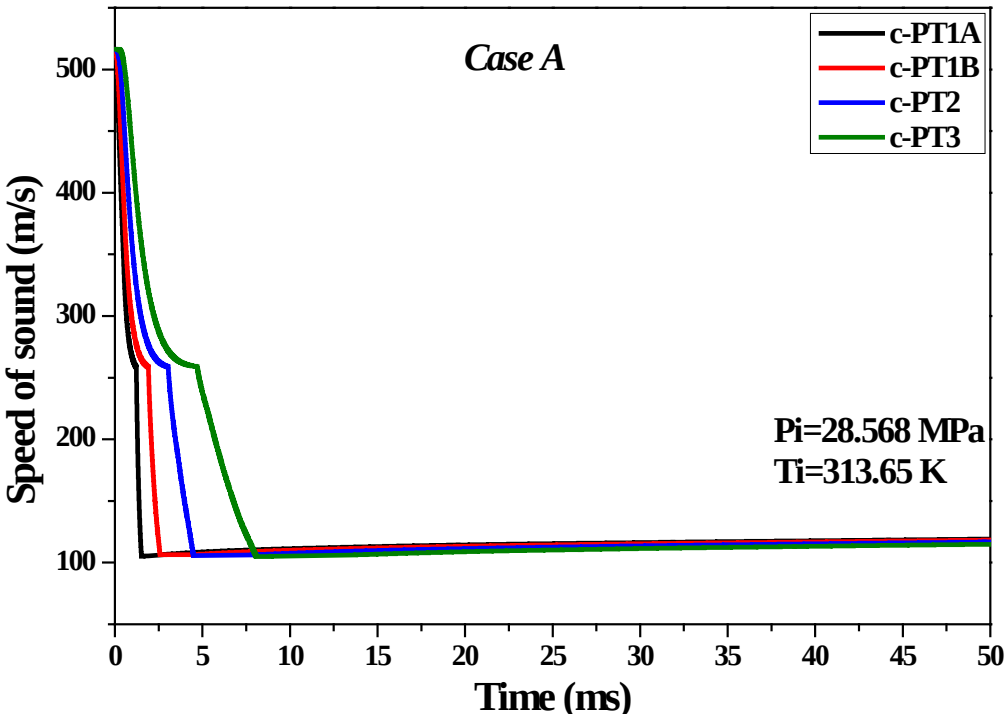

Figure 6.7: Predicted speed of sound vs time (Case A)

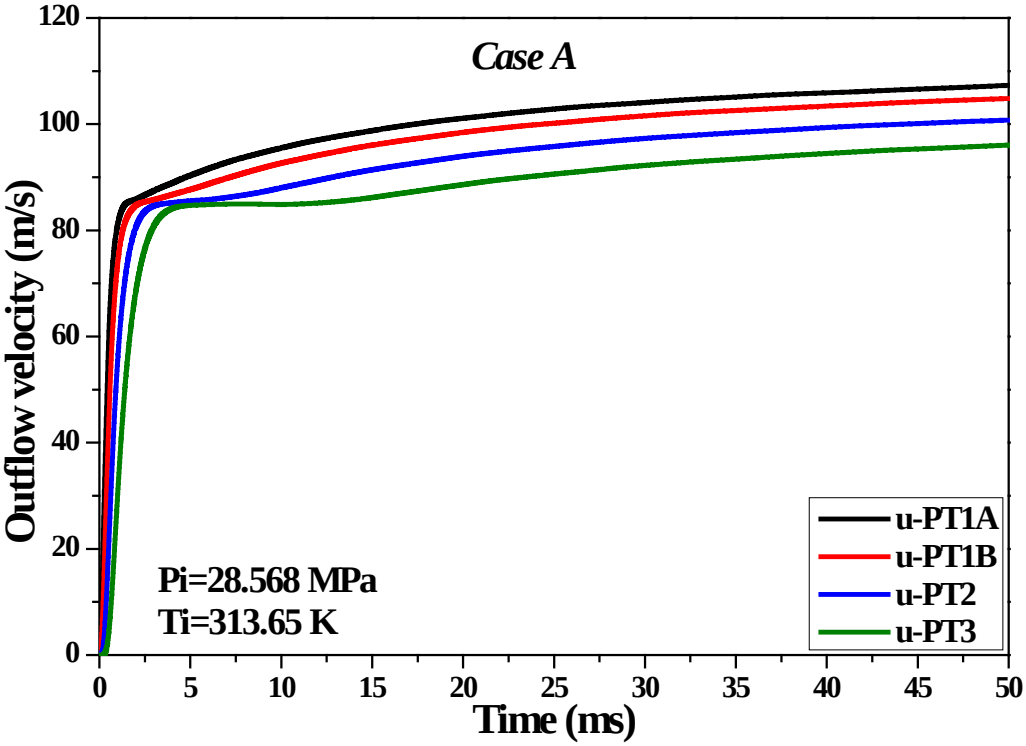

Figure 6.8: Predicted 'outflow' velocity vs time (Case A)

Figure 6.9 shows a comparison between the predicted and experimentally obtained decompression wave speed. The predicted *average* decompression wave speed was

obtained based on readings at the six pressure transducers listed in Table 6.3, whereas the *local* decompression wave speed was determined using the predicted speed of sound and the 'outflow' velocity at 200 mm from the exit. Initially (before the flow commenced), the speed of the decompression wave was equal to the predicted speed of sound in the mixture because the 'outflow' speed was zero. The model predicted the initial decompression wave speed well, differing by only 0.4% from the measured data.

As the pressure decreased, the predicted average decompression wave speed agreed with the measured data, while the local decompression wave speed varied slightly to the right of the experimental curve; because the local decompression wave speed was obtained using the formulation in Equation 2.4, while the average decompression wave speed was calculated using a similar approach to the measured data (based on the pressure-time traces).

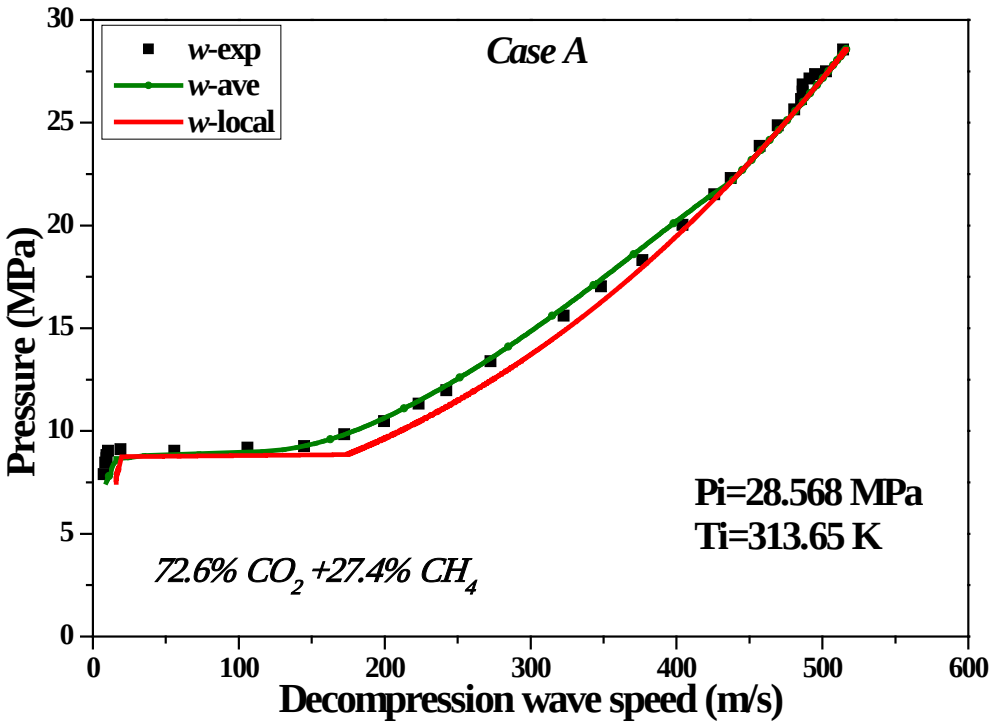

Figure 6.9: Comparison of the predicted and the measured decompression wave speed (Case A)

More importantly, the abrupt drop in the measured decompression wave speed curve which created a long pressure plateau was predicted successfully. According to the BTCM, an accurate determination of the pressure plateau in the decompression wave speed curve is crucial to guarantee an accurate prediction of the required arrest toughness. The current model under-predicted the plateau level slightly. As seen in Figure 6.5, a discrepancy is noticed on the predicted pressure-time curves at the same pressure level. The reason for the discrepancy and its influence is discussed later in this chapter.

The appearance of the plateau can be explained by superimposing the pressure-temperature gradient on the phase envelope, as depicted in Figure 6.10. As the fluid crosses the phase boundary (at T=276 K, P=8.8 MPa), the decompression wave speed experiences a sharp drop which can be attributed to the drop in the speed of

sound, while simultaneously the monitored properties remained constant for several time steps. Clearly, the trend that appeared in all properties stemmed from the discontinuity at the phase boundary. Such outcomes demonstrate that the current CFD model can successfully deal with the phase change predicted implicitly in the property tables.

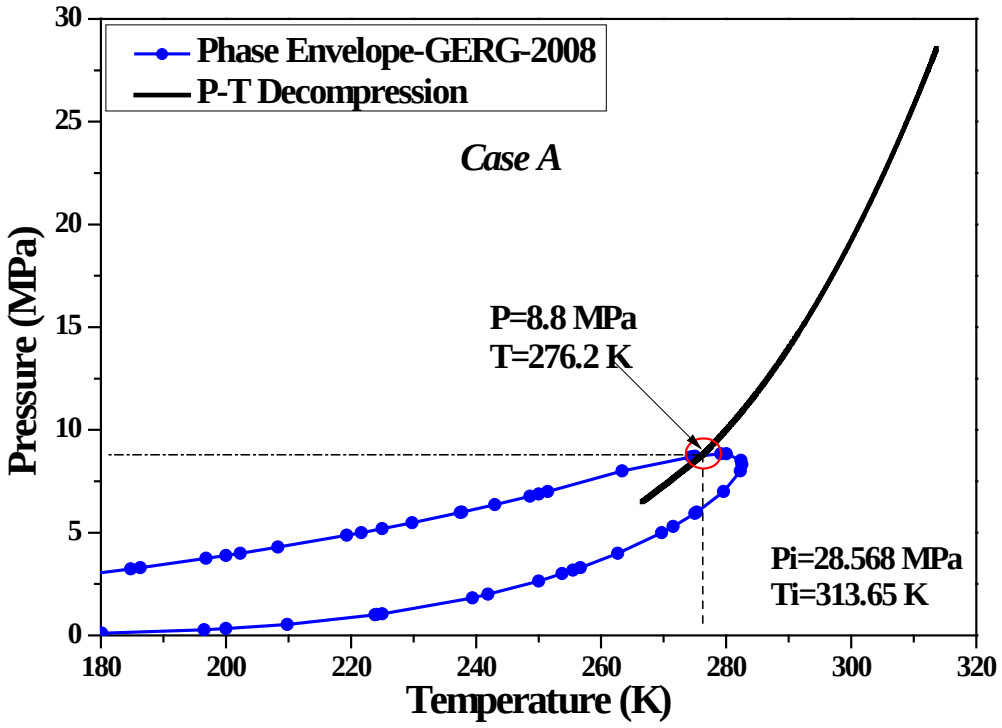

Figure 6.10: The pressure-temperature curve and the phase envelope (Case A)

6.2.3 Simulation Results of Case B

The second simulation was for the mixture in Case B. The computational domain here was based on the physical dimensions of the shock tube test described in reference [55]. Figure 6.11 shows the CFD prediction of pressure-time traces at eight different pressure transducer locations along the pipe, which were given in Table 6.3. A rapid drop in pressure occurred as the decompression wave front passed each location. The appearance of a plateau at about 8 MPa can be ascribed to the phase change that occurred due to the decompression process.

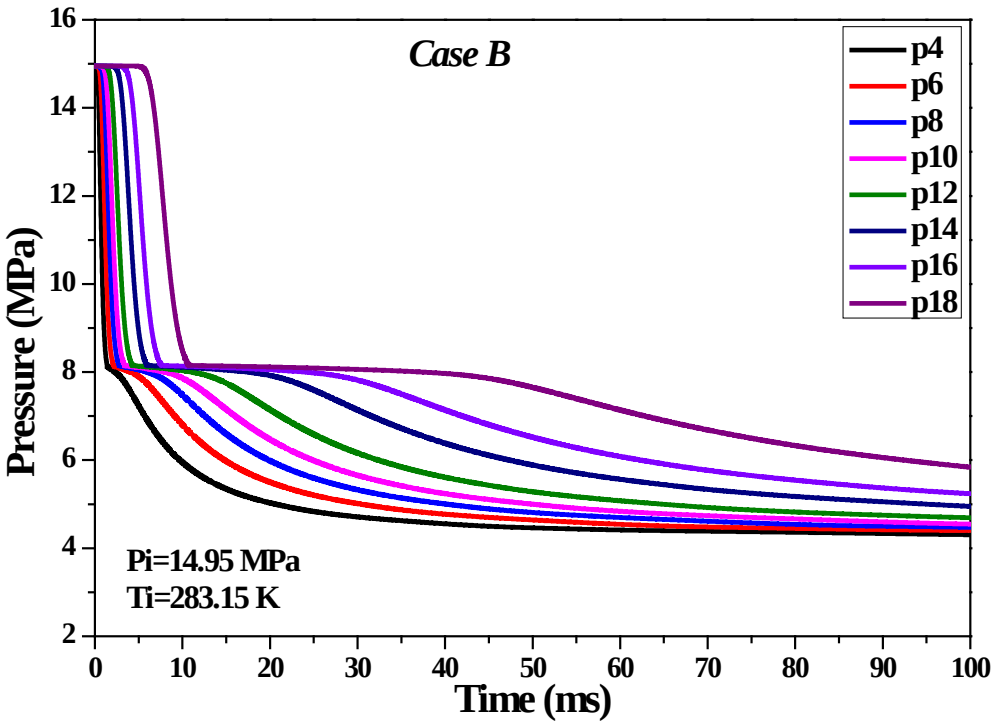

Figure 6.11: Predicted pressure-time traces (Case B)

Figure 6.12 shows the drop in fluid temperature as a function of time at five different locations on the tube. The temperature dropped rapidly from its initial value before flattening out for several time steps at 277 K, creating a plateau in all curves. After this stage, the temperature steadily decreased to its lowest value of 260 K, which was predicted at the closest location to the rupture disc. A comparison with Figure 6.13 confirms that the plateaus occurred at the same pressure level as the point of intersection of the pressure-temperature curve with the phase boundary.

The speed of sound and the outflow velocity were both predicted in order to obtain the local decompression wave speed. The predicted speed of sound versus time for five locations close to the outlet is shown in Figure 6.14, while the predicted outflow velocity is shown in Figure 6.15. At the initial pressure and temperature, the current model predicted the speed of sound as 522 m/s, while the outflow velocity was 0 m/s anywhere inside the tube (before flow commenced). A similar trend that occurred in

the outflow velocity of Case A occurred here, where a kink appeared on all the curves due to phase change. Referring back to the speed of sound curves, the phase change caused a decrease in the speed of sound, and this overall drop in speed of sound due to discontinuity at the phase boundary was ~350 m/s.

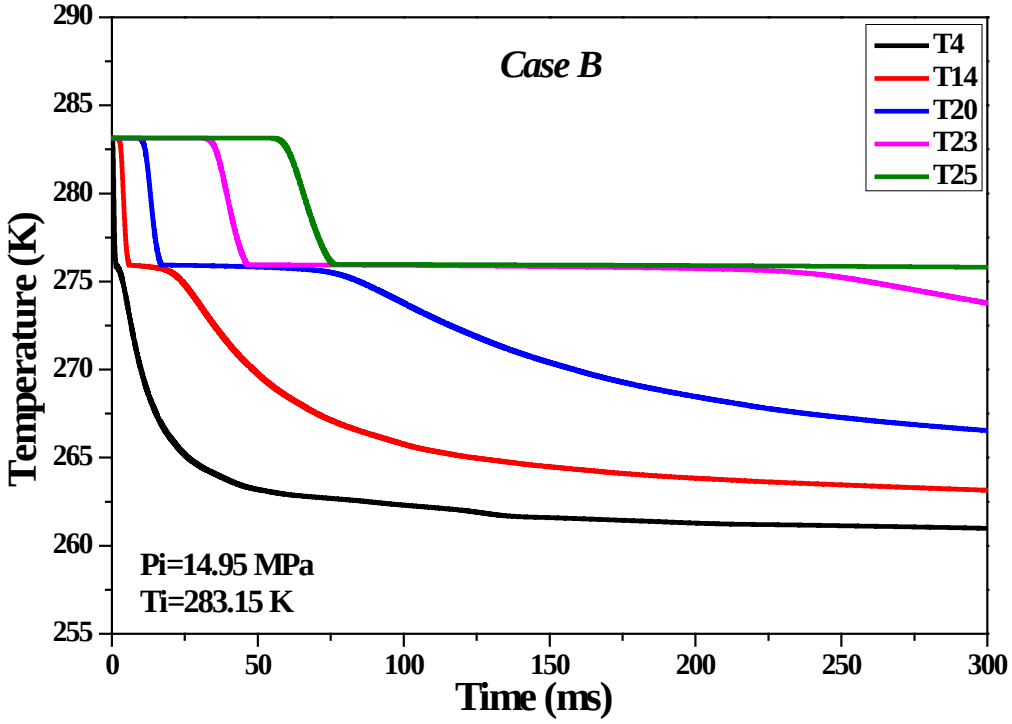

Figure 6.12: Predicted temperature-time traces (Case B)

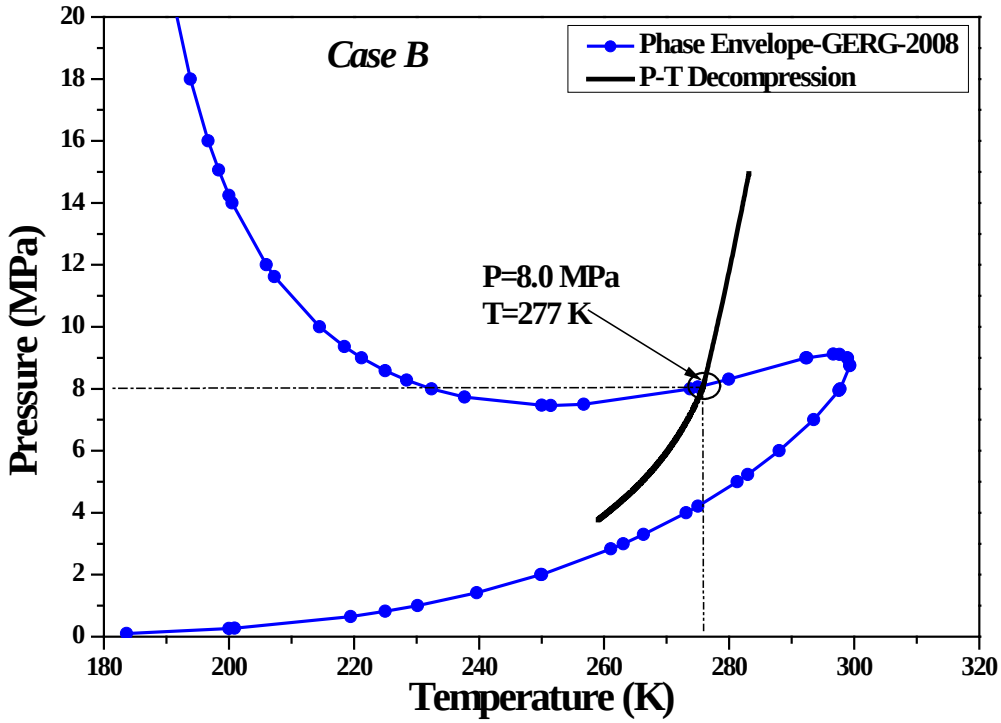

Figure 6.13: The decompression of pressure-temperature compared to phase envelope (Case B)

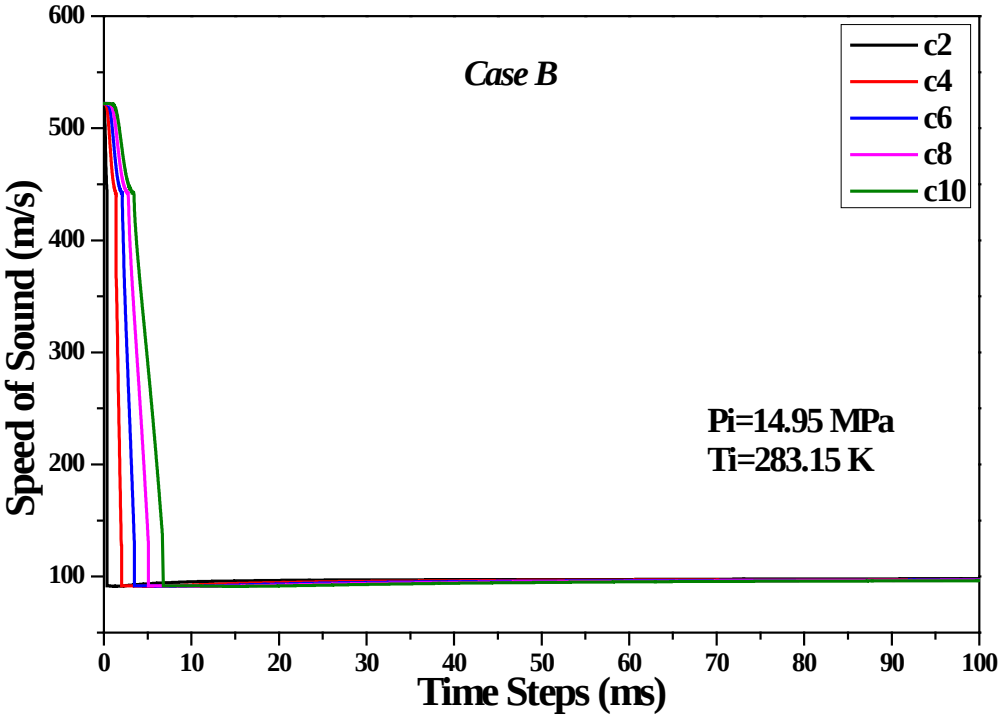

Figure 6.14: The predicted speed of sound vs time (Case B)

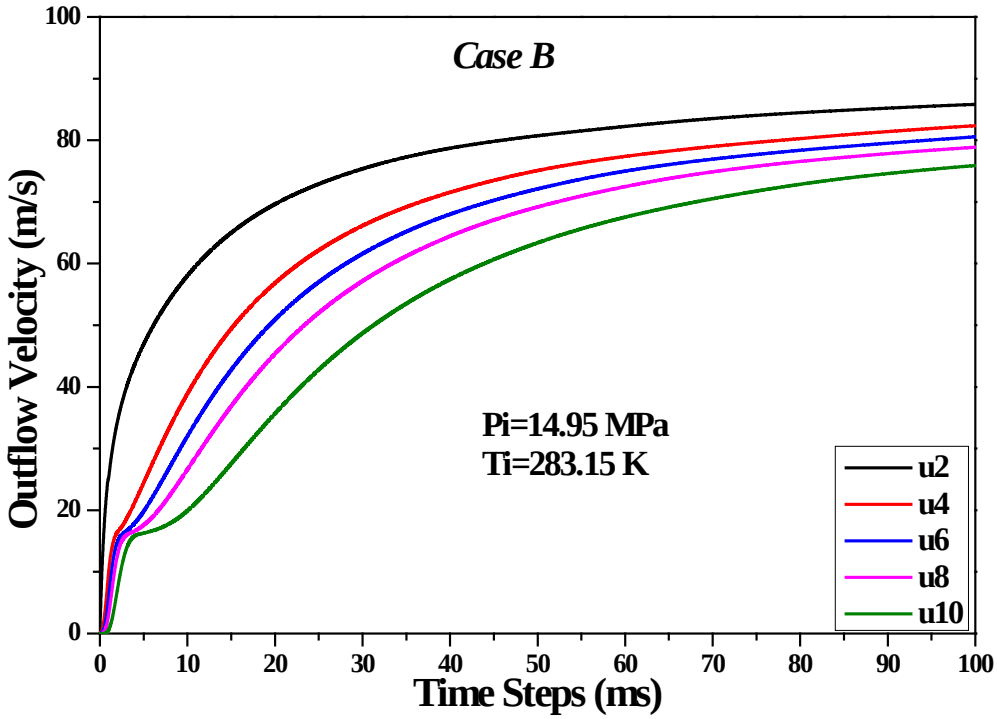

Figure 6.15: The predicted outflow velocity vs time (Case B)

Figure 6.16 shows a comparison between the predicted and experimentally obtained decompression wave speed of Case B, where the initial decompression wave speed predicted by the current model was 521 m/s. This value deviated by approximately +2.4% from the measured result, but the predicted decompression wave speed was consistent with the experimentally obtained value for pressure levels above and below the plateau level. At the plateau there was a discrepancy between the predicted and measured decompression wave speed, even though the plateau began to form close to the pressure level of the measured data. Notably, the length of the predicted plateau in the average decompression wave speed curve was consistent with the measured data. Further discussion is presented hereafter.

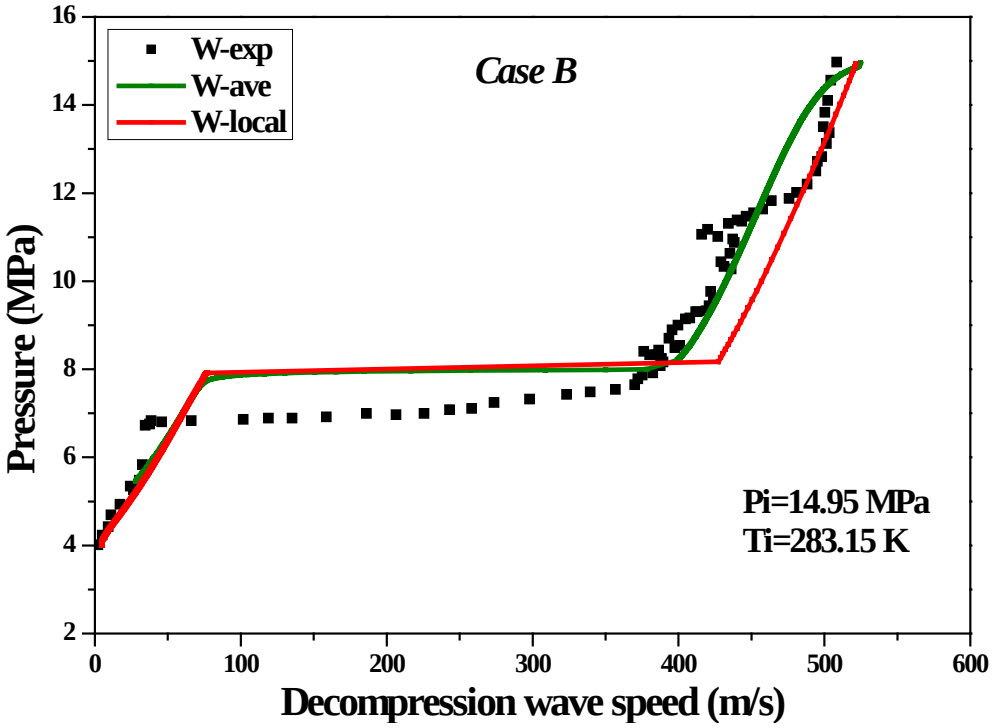

Figure 6.16: Comparison of the predicted decompression wave speed with the measured results (Case B)

6.3 Discussion

If the variation in the simulated pressure matches the experimental results (Figure 6.5), the predicted average value of the decompression wave speed *w* should agree with the measured curve (Figure 6.9); but as Figure 6.9 shows, there was a slight discrepancy at the plateau between the predicted and experimentally obtained decompression wave speed. This variation appeared at the same pressure levels on the pressure-time curves, as Figure 6.5 shows. There was a major difference at the plateau level on the decompression wave speed in the second case, as Figure 6.16 shows. Such a variation may result from uncertainties inherent in the numerical method and/or the way of implementing the GERG-2008 EOS, although factors such as delayed nucleation and/or rapid phase change dynamics (not considered here) can influence the results to varying degrees. Another possible reason for this discrepancy was the actual amount of impurities in the experimental tests, which could be slightly

different from the listed composition.

The speed of sound in the current model can be tracked as a function of time so its relationship with the decompression wave speed can be clearly understood. For instance, Figure 6.16 shows that the 'length' of the pressure plateau (~348 m/s) was almost equal to the sharp drop in the speed of sound due to the phase change, as seen in Figure 6.14. Figure 6.9 and Figure 6.16 show long pressure plateaus that correspond to a significant drop in the decompression wave speed. This would surely influence the ductile fracture propagation control, as outlined in the BTCM.

The pressure plateau level which represents the consequence of phase change on decompression wave speed is an important aspect in determining the required fracture toughness to suppress ductile fracture propagation, so investigating factors that could be sensitive to accurately predict the plateau in decompression wave speed was essential. Further simulations were performed to discuss the influences of initial pressure and temperature, impurities, pipe diameter and surface roughness on the decompression of CO_2 mixtures. In addition, the effect of initial pressure, initial temperature and pipe diameter on arrest toughness will also be investigated in the following sections.

6.3.1 The Effect of Initial Temperature on the Decompression Wave

The influence of initial temperature on the decompression of the CO_2 mixture was examined for Case B. Three different initial temperatures (-20, 35 & 45°C) were used while the initial pressure remained the same as the actual case. These temperatures represent three different phases: liquid, dense liquid and supercritical. Figure 6.17 shows how changing the initial temperature affects the decompression wave speed. Because the initial temperature of Case B was 10°C, the main effect of increasing the

initial temperature (i.e. 35 & 45°C) was decreasing the initial decompression wave speed from 521 to 360 and 312 m/s, respectively; but lowering the initial temperature caused the initial decompression wave speed to increase to 722 m/s.

Moreover, the length and level of the pressure plateaus were affected due to changing the initial temperature – increasing the initial temperature decreased the length of the plateau in the decompression wave speed, and vice-versa. Those observations were consistent with the predicted results of pure CO_2 conducted by reference [24] and for mixtures, for example, references [15, 54]. However, this effect was different in terms of plateau levels for CO_2 mixtures because it depended on the shape of the bubble curve on the phase envelope, which in turn depended on the amount and type of impurities in the CO_2 mixture.

Increasing the initial temperature to 35 and 45°C raised the level of plateaus by a value of 1 MPa above the main test. Interestingly, as Figure 6.17 shows, the apparent plateaus in these two cases occurred at approximately the same level. This can be further explained by representing the pressure-temperature profiles on the phase envelope of the mixture, as depicted in Figure 6.18; but note that the phase change occurred at approximately the same pressure level despite different intercept temperatures with the phase boundary, which were clearly due to the effect of impurities that rose up the bubble curve on the phase envelope. Such a situation cannot occur for pure CO_2.

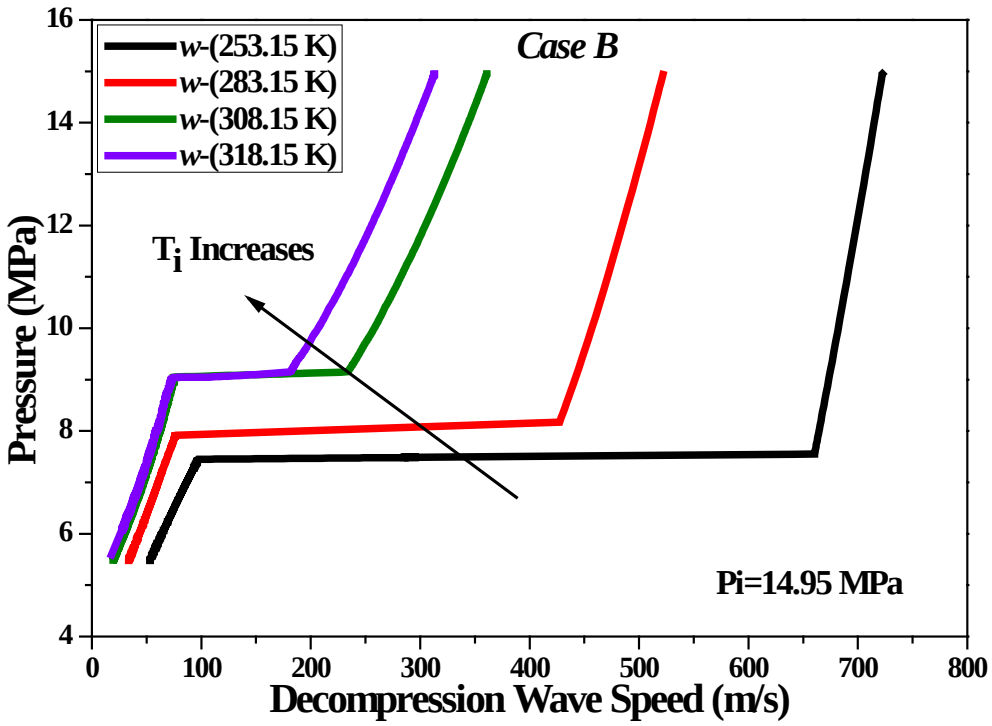

Figure 6.17: Initial temperature effect on decompression wave speed (Case B)

When the initial temperature was -20°C, despite the initial decompression wave speed being much higher than in the main test, the plateau level was predicted at a lower pressure level than the main test by 0.5 MPa. Although this was consistent with the trend in the results of pure CO_2 conducted by reference [24], it cannot be taken as a role for CO_2 mixtures because of the shape of the phase boundary. For instance, if the initial temperature was less than -20°C, the intersection with the phase boundary would take place at a higher pressure level because the bubble curve increased again at temperature levels below that value. So the trend in the results of pure CO_2, which states that as the initial temperature decreases the plateau level in the decompression wave speed decreases, cannot be applied for CO_2 mixtures.

Figure 6.19 presents the effect of increasing the initial temperature on the decompression of the CO_2 mixture from the gas phase. To do that, the initial pressure was set to be below the critical pressure of the mixture, and the initial temperature to

be greater than the critical one. The influence here is that as the initial temperature increases, the plateau level decreases and so low arrest toughness is required for such decompression.

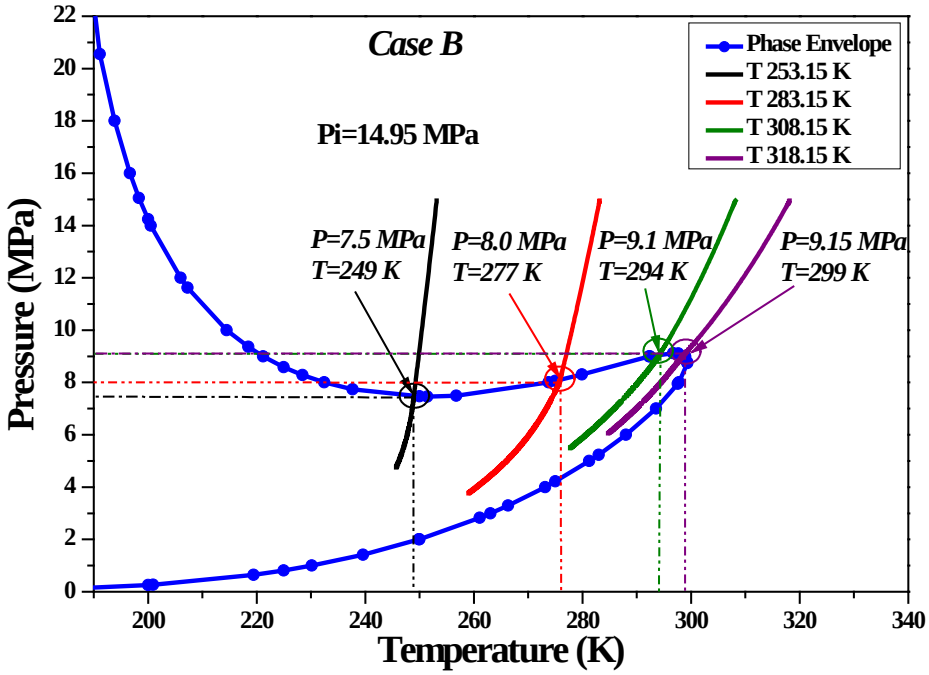

Figure 6.18: Intersection points with the phase envelope for different initial temperatures (Case B)

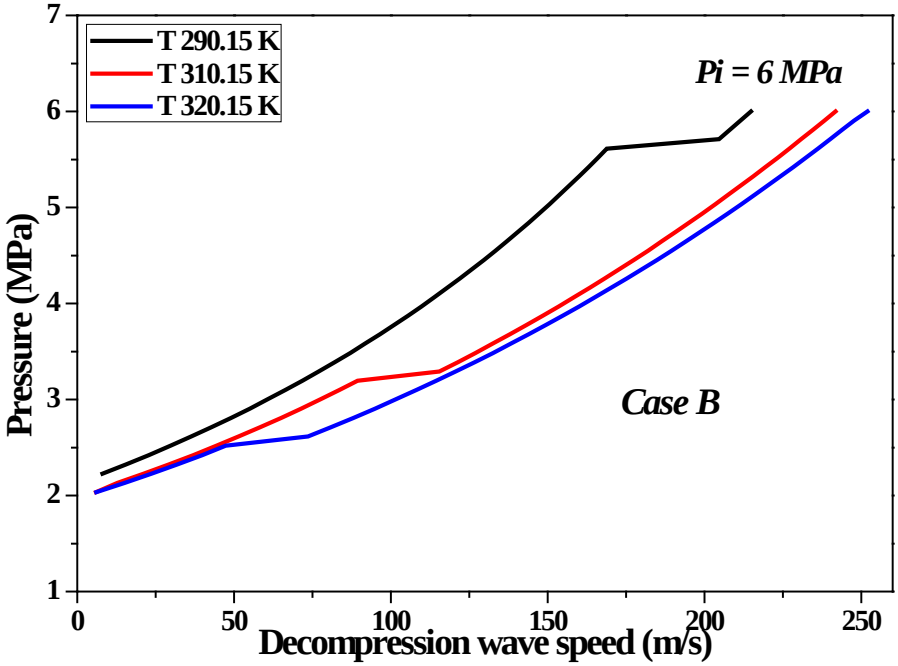

Figure 6.19: Initial temperature effect on decompression wave speed (gas phase)

6.3.2 The Effect of Initial Pressure on the Decompression Wave

The impact of initial pressure on the decompression wave speed is tested using five different pressures (P=10, 14.95, 20, 25 and 30 MPa). Figure 6.20 presents the decompression wave speed of Case B predicted using several initial pressures. As the initial pressure decreases, the plateau length in the decompression wave speed becomes shorter; however, the level of the plateau increases. The result indicates that using lower initial pressure leads to an increase in the minimum required arrest toughness for CO_2 mixtures. Accordingly, it is safer and more efficient to use high initial pressure to transport CO_2 mixtures through pipelines.

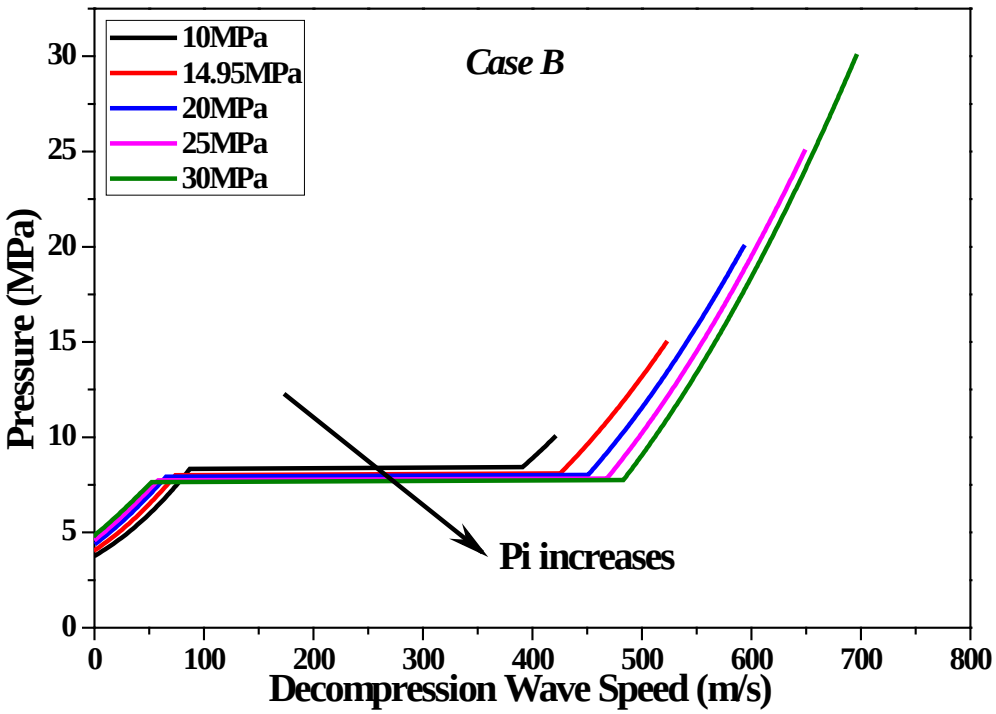

Figure 6.20: Initial pressure effect on decompression wave speed (Case B)

6.3.3 The Effect of Impurities on the Decompression Wave

The effects of several impurities (components other than CO_2) on the decompression of CO_2 pipelines were examined. The impurities that were most likely to exist in CCTs were used [34]. Table 6.5 lists the eight binary CO_2 mixtures studied and the

initial conditions used in the simulation.

Figure 6.21 illustrates the effect of impurities on the phase envelope of CO_2, and show that adding impurities to pure CO_2 shifts the critical point and the bubble curve in the phase envelope. Notably, an additional 5% of hydrogen to the CO_2 had more effect on the phase equilibrium than the other impurities, because it shifted the critical pressure to a value close to 10 MPa. Simulations of decompression with these binary mixtures were conducted using the same flow domain as in Case A. Figure 6.22 shows the influence on the decompression wave speed such that at the same initial conditions and for a fixed fraction of CO_2, each impurity resulted in a different initial decompression wave speed and different pressure plateau level that was clearly related to the phase envelope of the mixture. Adding 5% H_2 to the CO_2 resulted in the highest pressure plateau level (~ 9 MPa). Adding 5% N_2 resulted in a pressure plateau of about 6 MPa. The lowest impact was noticed on the decompression curve of the CH_4 binary mixture – it shows that the level of the plateau is decreased to a value below 5 MPa. These changes in the decompression wave speed will definitely influence the fracture propagation/arrest requirements for CO_2 pipelines.

Table 6.5: The initial conditions and the predominantly CO_2 mixtures

No.	P_i= 15 (MPa)					T_i=283.15 (K)			
	Mixture components (mole %)								
	CO_2	H_2	CO	O_2	N_2	CO	CH_4	Ar	H_2S
1	100	0	0	0	0	0	0	0	0
2	95	5	0	0	0	0	0	0	0
3	95	0	5	0	0	0	0	0	0

4	95	0	0	5	0	0	0	0	0
5	95	0	0	0	5	0	0	0	0
6	95	0	0	0	0	5	0	0	0
7	95	0	0	0	0	0	5	0	0
8	95	0	0	0	0	0	0	5	0
9	95	0	0	0	0	0	0	0	5

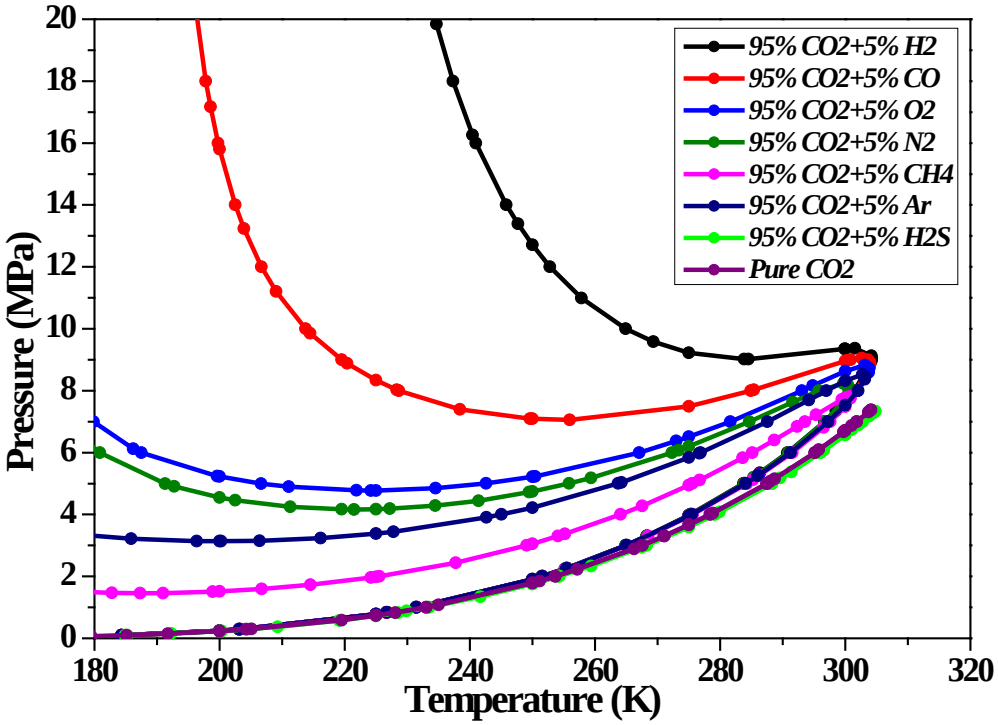

Figure 6.21: Phase envelope of CO_2 mixtures calculated using GERG-2008 EOS

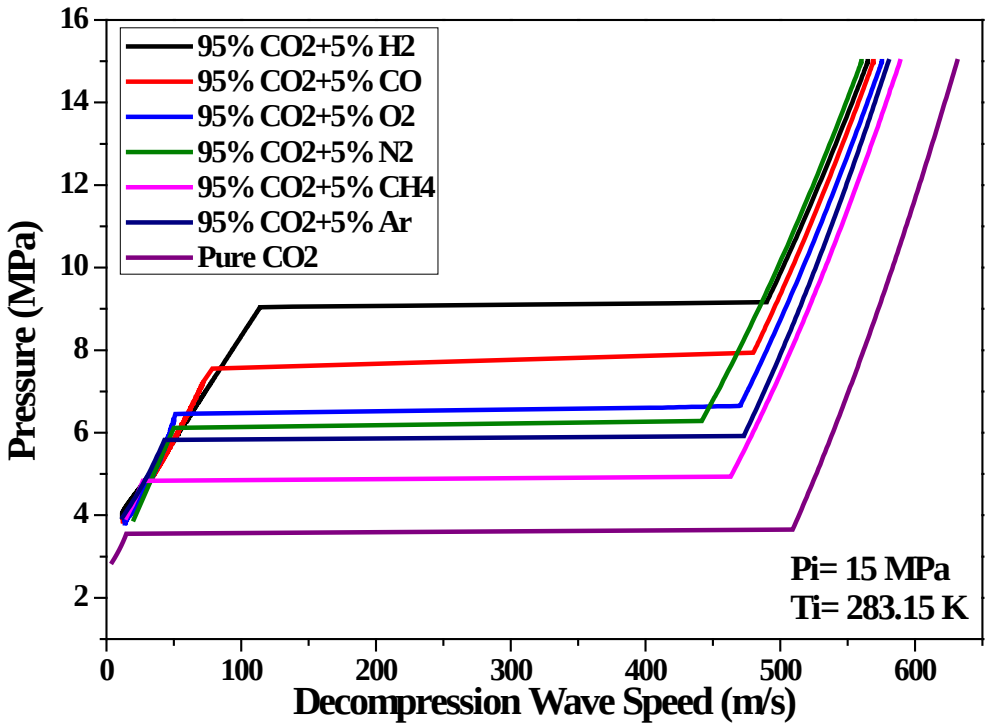

Figure 6.22: Effect of impurities on CO_2 decompression wave speed

6.3.4 Effects of Pipe Diameter and Surface Roughness

The effects of pipe diameter and surface roughness were investigated for the gas composition of Case B. Four different pipe diameters (D=38.1, 250, 500 and 1000 mm) were simulated. The influence of surface roughness was also studied using three various roughness values (ε=5 μm, ε=15 μm and ε=30 μm) for two different diameters (38.1 mm & 250 mm). Figure 6.23 shows the effect of increasing the pipe diameter on the average decompression wave speed. The insert in Figure 6.23 gives the details of P-*w* curves for lower pressures below the saturation pressure.

As the diameter increases from 38.1 mm to 250 mm, the curve of the decompression wave notably decreases at the end of the decompression (low pressure region). In the same time, when *D* further increases to 500 mm, the change in the decompression wave speed curve becomes minor. It is in fact difficult to observe the difference in

the *P-w* curves between *D*=500 mm and *D*=1000 mm. These observations were consistent with the results of Lu et al. [84] and Botros et al. [54] conducted on natural gas mixtures.

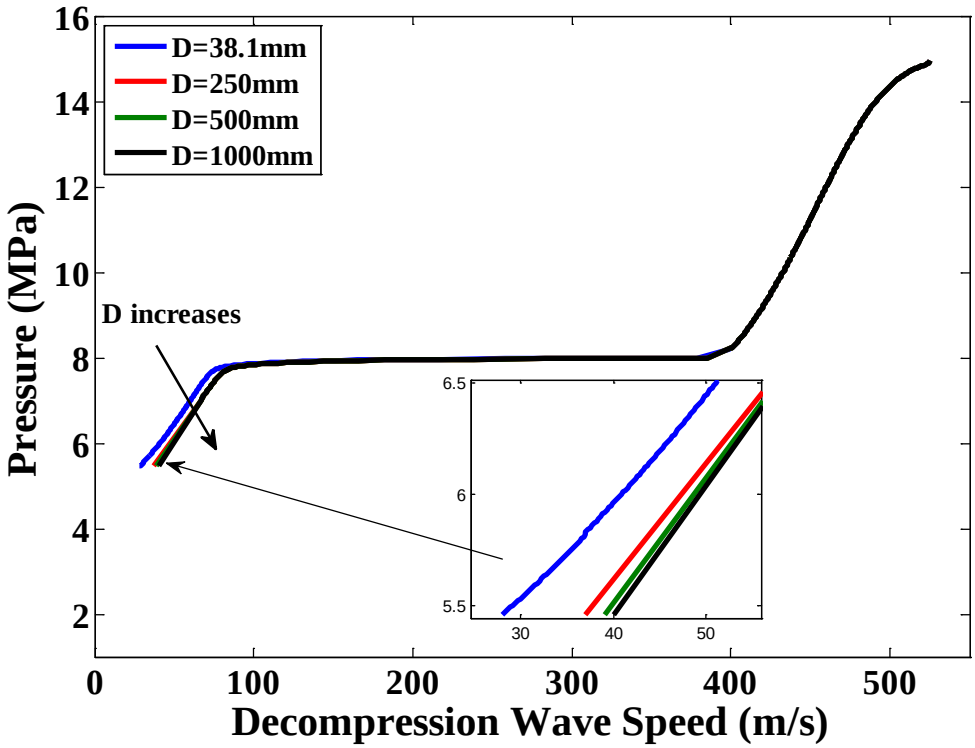

Figure 6.23: Influence of pipe diameter on average decompression wave speed

Figure 6.24 illustrates the average decompression wave speed as a function of pressure for the three roughness values and pipe diameter D=38.1 mm. It can be seen that the decompression curve moves upward as the roughness value increases. This observation again was noticed at low pressure levels below the saturation pressure. As the pressure decreases, the effect of pipe wall roughness generally increases. The effect is hardly seen using the same mixture composition and roughness values for relatively larger pipe diameters, as depicted in Figure 6.25.

It can be observed that even when the pressure dropped to a lower level, the pipe wall roughness only caused a very slight difference in the decompression wave speed. Similar to the effect of the pipe diameter, the pipe wall roughness only causes

a very slight difference in the decompression wave speed at lower pressures. This indicates that the decompression wave speed is independent of the influence of surface roughness for pipe diameters (D≥250 mm). In terms of fracture control philosophy, the effects of pipe wall roughness and pipe diameter on the decompression wave speed are negligible.

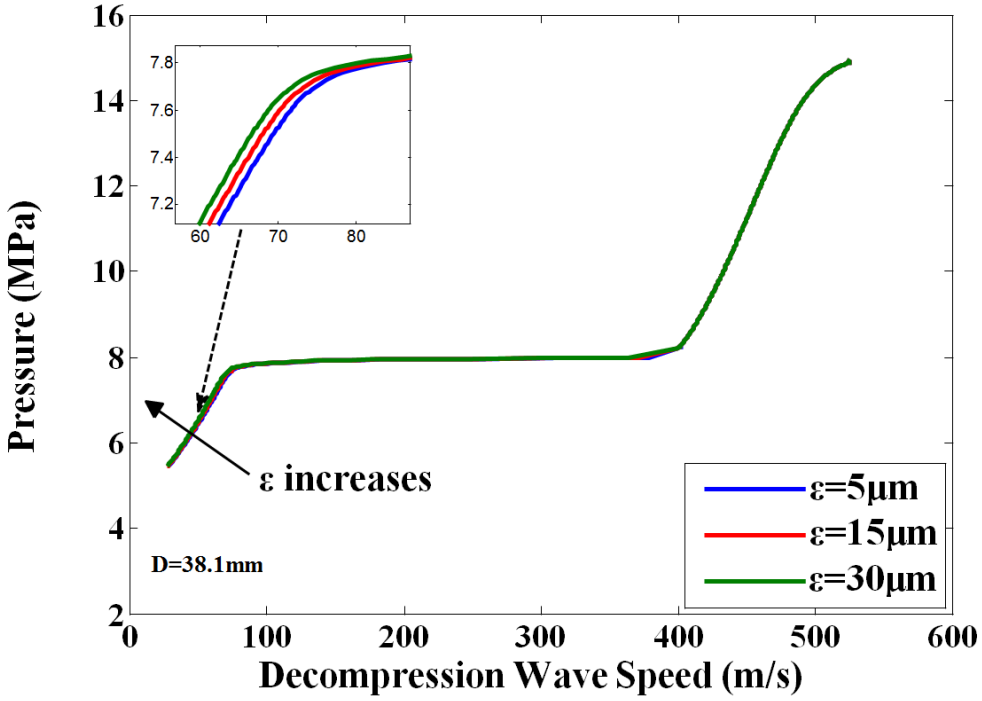

Figure 6.24: Influence of surface roughness on average decompression wave speed for D=38.1 mm

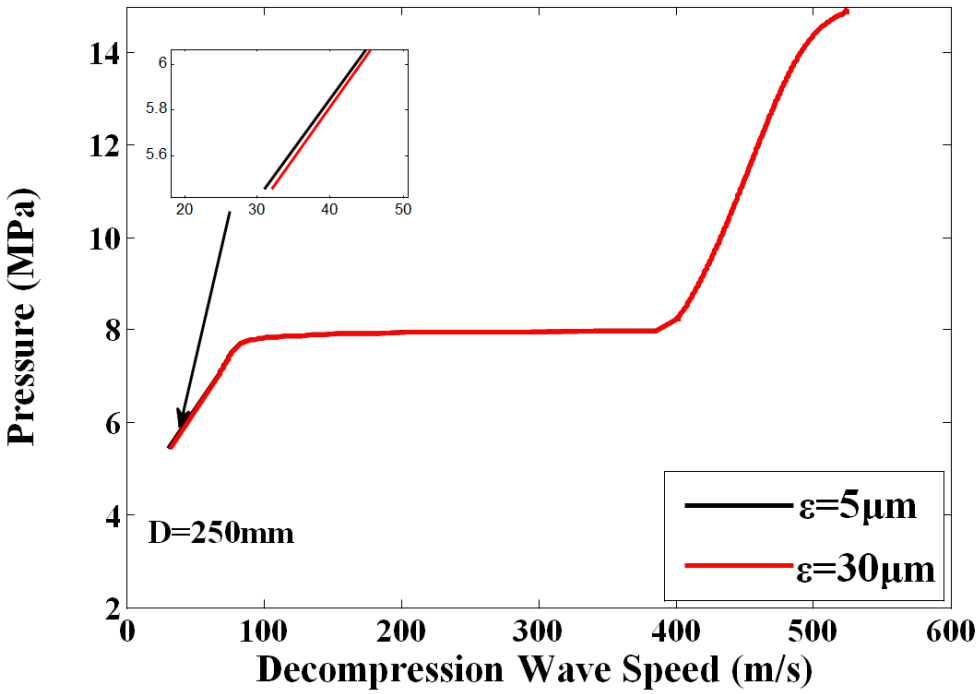

Figure 6.25: Influence of surface roughness on average decompression wave speed for D=250 mm

6.4 Application to the CCS Cases

The composition of the CO_2 stream transported in the pipeline for CCS will depend on its source. Three processes are generally used for capturing CO_2 from power plants: post-combustion, pre-combustion and oxyfuel. Table 6.6 lists typical compositions of CO_2 mixtures captured from these three process routes, which represent typical CO_2 compositions for CCS applications [124].

Table 6.6: CO_2 mixtures captured from post-combustion, pre-combustion and oxyfuel

Gas components	Post-combustion (Mole %)	Pre-combustion (Mole %)	Oxyfuel (Mole %)
CO_2	99.94	95.66	95.87
N_2	0.02	0.43	1.38
O_2	0.02	0.43	1.38

CH_4		2	
H_2		1	
Ar	0.02	0.43	1.37
CO		0.04	
H_2S		0.01	

The 2D CFD model was employed to simulate the above cases for different initial temperatures, initial pressures and pipe diameters. Table 6.7 illustrates the values of the parameters used in the simulations. The effect of these parameters on the arrest toughness was studied for a buried pipeline with steel grade X70. For all cases, the reference initial pressure, initial temperature and pipe diameter used in the simulation were 20 MPa, 10℃ and 914 mm, respectively.

Table 6.7: Values of parameters used in the simulations

Parameters	Values
Initial temperature (T_i), °C	-10, 10, 30
Initial pressure (P_i), MPa	7.5, 10, 20, 25
Pipe diameter/thickness (mm)	305/7.9, 610/15.7, 914/23.6

6.4.1 Post-Combustion Case Study

The effect of initial temperature on the decompression wave speed and accordingly on the predicted fracture propagation velocity for the post-combustion composition is shown in Figure 6.26. The decompression path for the three different initial temperatures is depicted in Figure 6.27. As can be seen, the fluid is in the dense phase for all cases and the plateau level in *P*-*w* curves corresponds to the intersection point of the decompression path with the phase boundary. It was found that the result

of the post-combustion case is similar to that observed in the decompression of pure CO_2. This was attributed to the amount of CO_2 captured by this CCS method (>99%), as it can be observed on the phase diagram also, which is almost identical to the pure CO_2.

The arrest toughness as a function of the initial temperature for three different pipe diameters is shown in Figure 6.28. For the three pipe diameters tested, the arrest toughness increased with the increase in the initial temperature. The highest value of the arrest toughness was observed for pipe diameter of D=914 mm and the initial temperature of 30°C where the arrest toughness was 45 J.

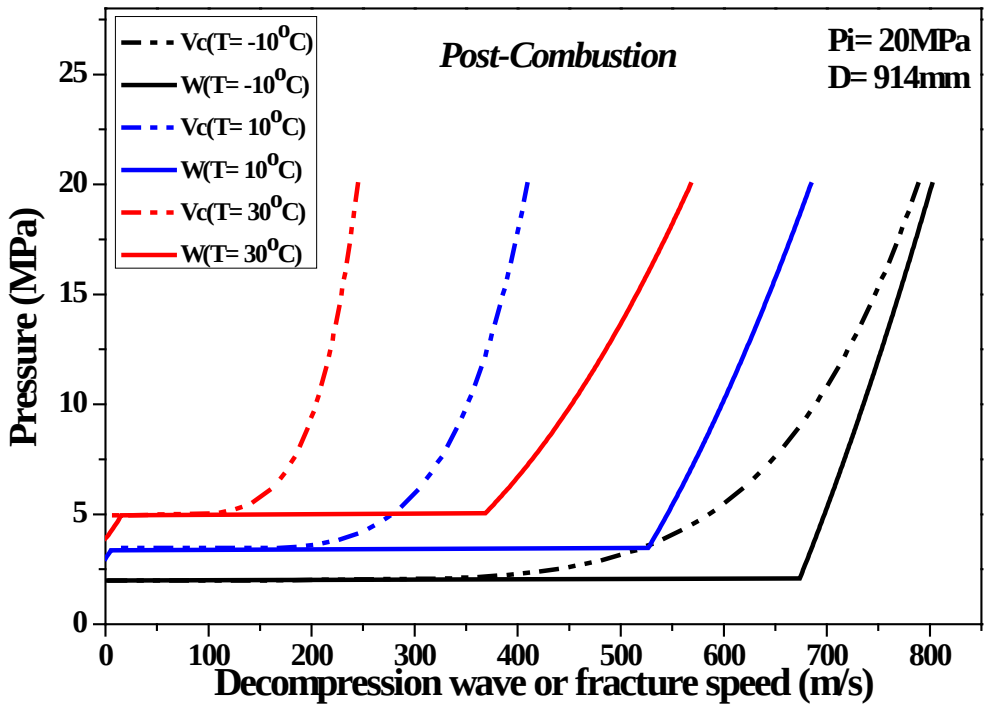

Figure 6.26: Decompression wave and fracture speeds for post-combustion (initial temperature effect)

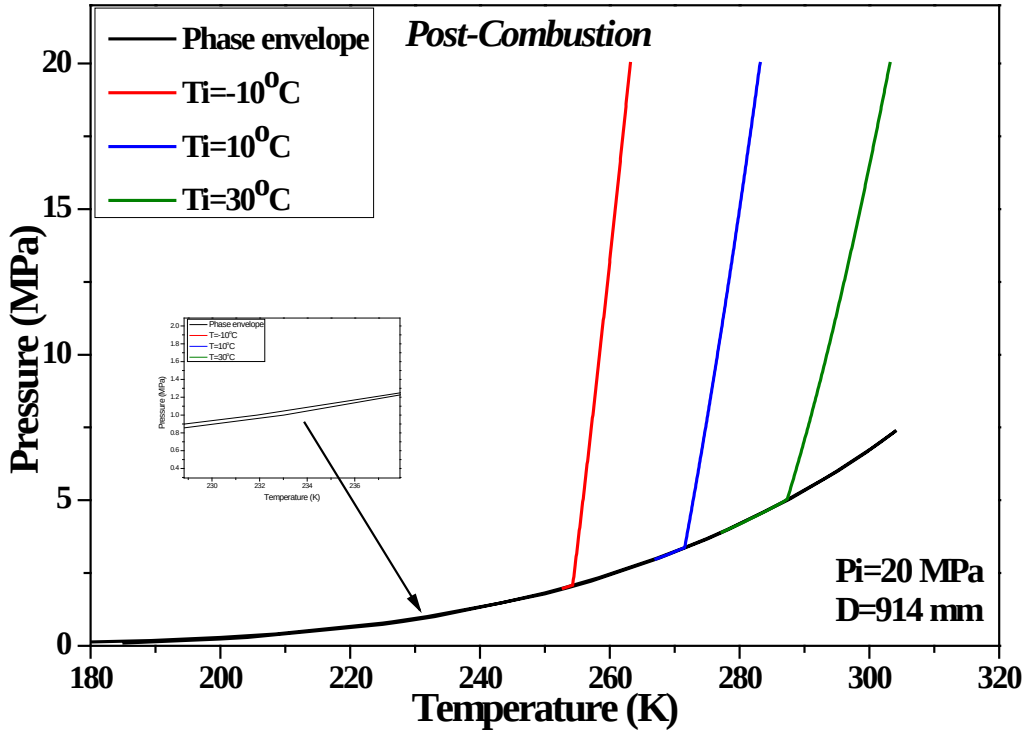

Figure 6.27: Decompression path for three initial temperatures (post-combustion)

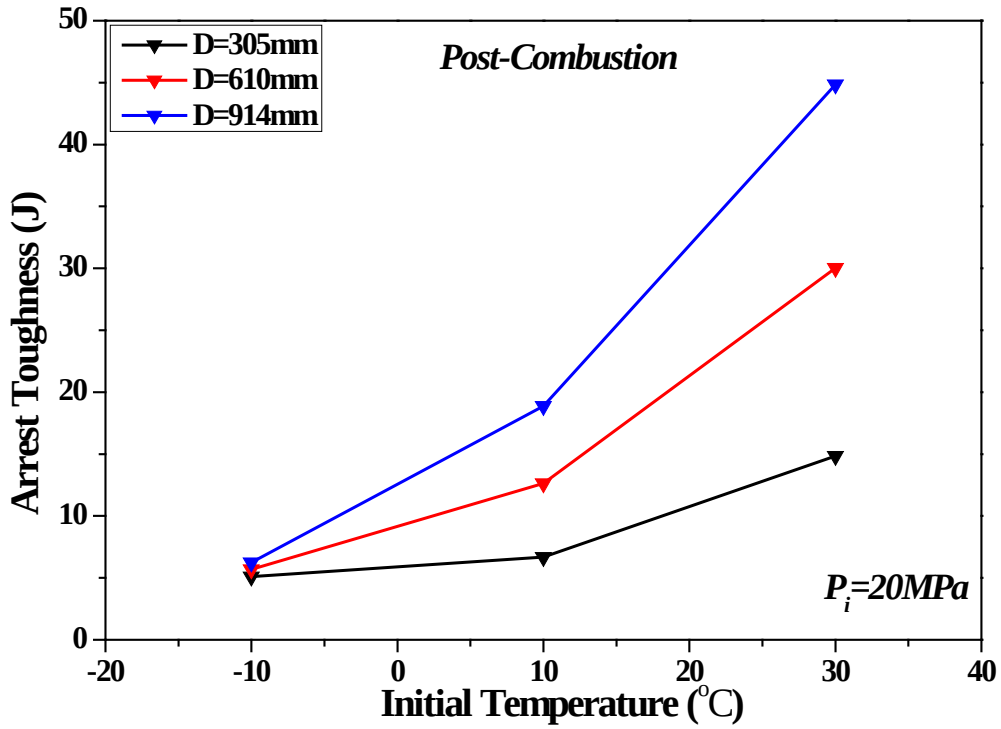

Figure 6.28: Arrest toughness as a function of initial temperature for three pipe diameters for post-combustion case at initial pressure of 20 MPa

Figure 6.29 shows details of the fracture propagation curves and decompression curves for different initial pressures. As can be seen in Figure 6.30, as the initial pressure increases, the intersect point of pressure-temperature decreases and so the required arrest toughness decreases. This is affirmed on Figure 6.31 where the arrest toughness is plotted as a function of the initial pressures listed above. Accordingly, it can be stated that as the initial pressure increases, the required arrest toughness will be decreased and vice-versa; however, this can only be applied for post-combustion composition and/or pure CO_2.

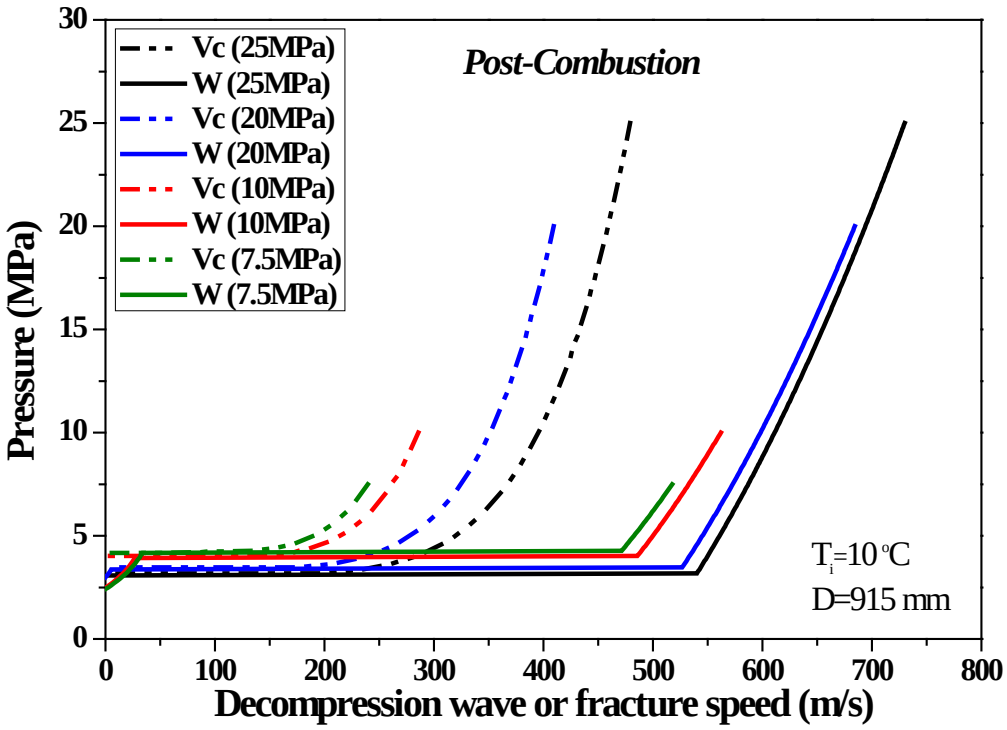

Figure 6.29: Decompression wave and fracture speeds for post-combustion (initial pressure effect)

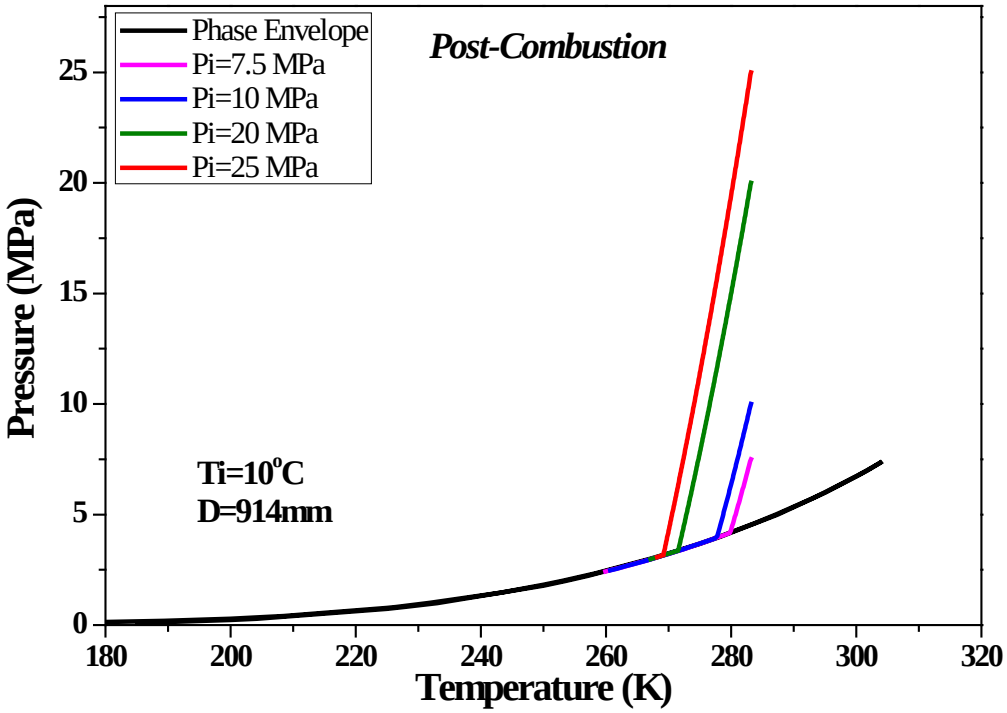

Figure 6.30: Decompression path for four initial pressures (post-combustion)

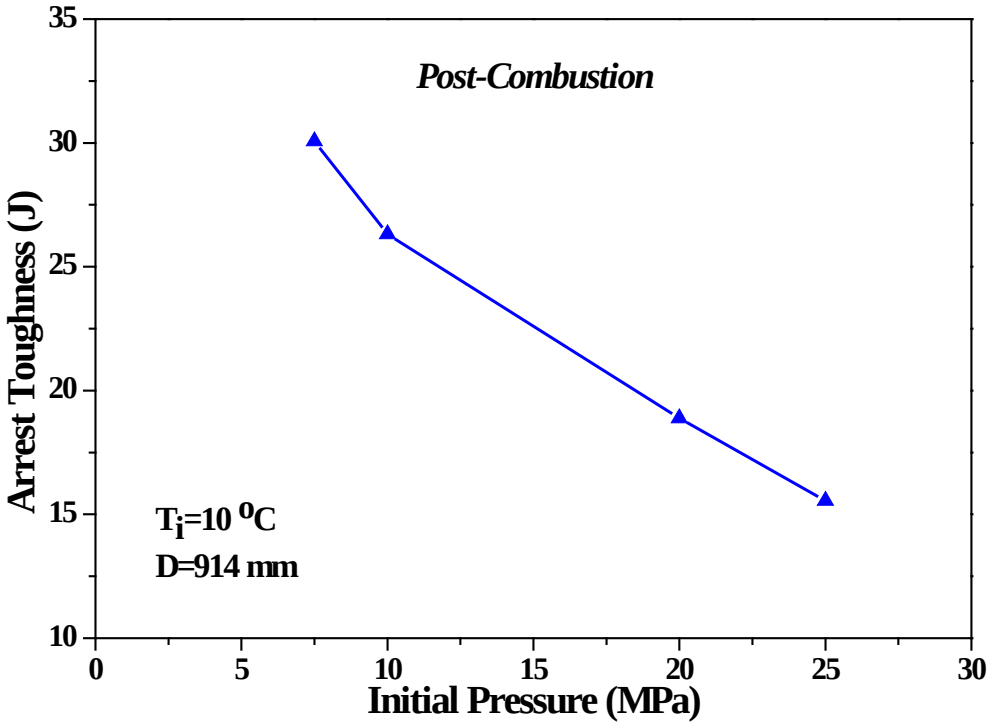

Figure 6.31: Arrest toughness as a function of initial pressure for pipe diameter (D = 914 mm) for post-combustion case at initial temperature of 20 MPa

The decompression curve used to predict the arrest toughness in terms of pipe diameter is obtained using the following conditions (D=914 mm and P_i=7.5 MPa and

T_i=10^{o}C). The pipe diameter has a negligible effect on the gas decompression curve as observed in Section 6.3.4, so only one decompression curve was used. Pipe diameter may influence the fracture propagation curve, as is evident in Figure 6.32. It can be noticed that as the pipe diameter increases, the fracture velocity decreases and so higher required toughness is predicted. This can be further identified from Figure 6.33 where the arrest toughness is plotted as a function of pipe diameter. The result shows that as the pipe diameter increases, the required arrest toughness also increases.

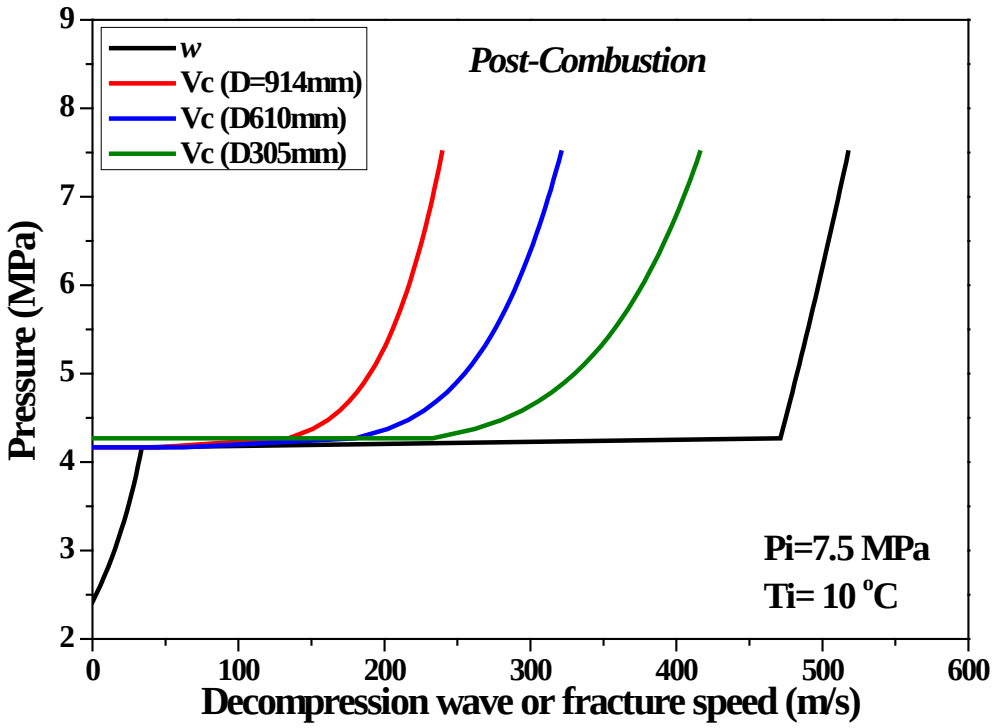

Figure 6.32: Effect of pipe diameter on fracture speed using the same decompression curve of post-combustion.

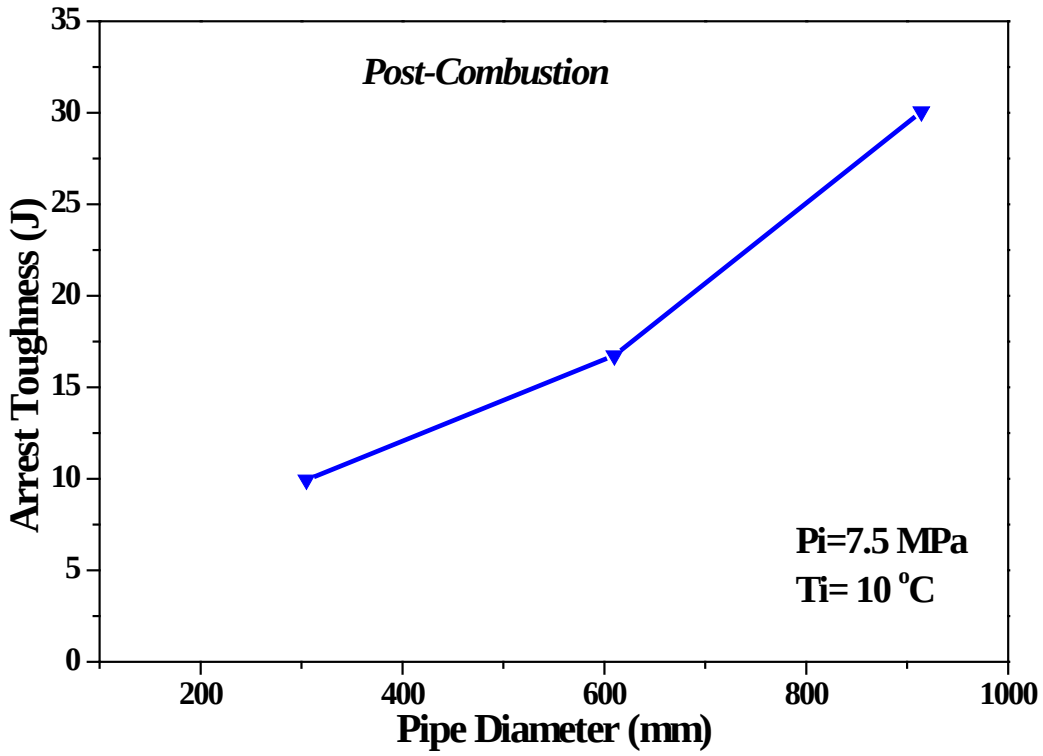

Figure 6.33: The effect of pipe diameter on the arrest toughness of post-combustion case

6.4.2 Pre-Combustion Case Study

To identify the effect of the initial temperature on the arrest toughness of the pre-combustion case, the decompression wave speed was predicted using the three initial temperatures listed in Table 6.7. Figure 6.34 presents the predicted curves of decompression wave and fracture propagation speeds w.r.t. the pressure obtained using the three different initial temperatures. The Figure shows that the plateau level for the pre-combustion case is almost double the level observed in the post-combustion results. This can be further understood from the phase diagram of the mixture where the intersection with the phase boundary occurred at high pressure levels (4.9 MPa, 5.6 MPa and 7 MPa) for the three different initial temperatures of -10^{o}C, 10^{o}C and 30^{o}C, respectively.

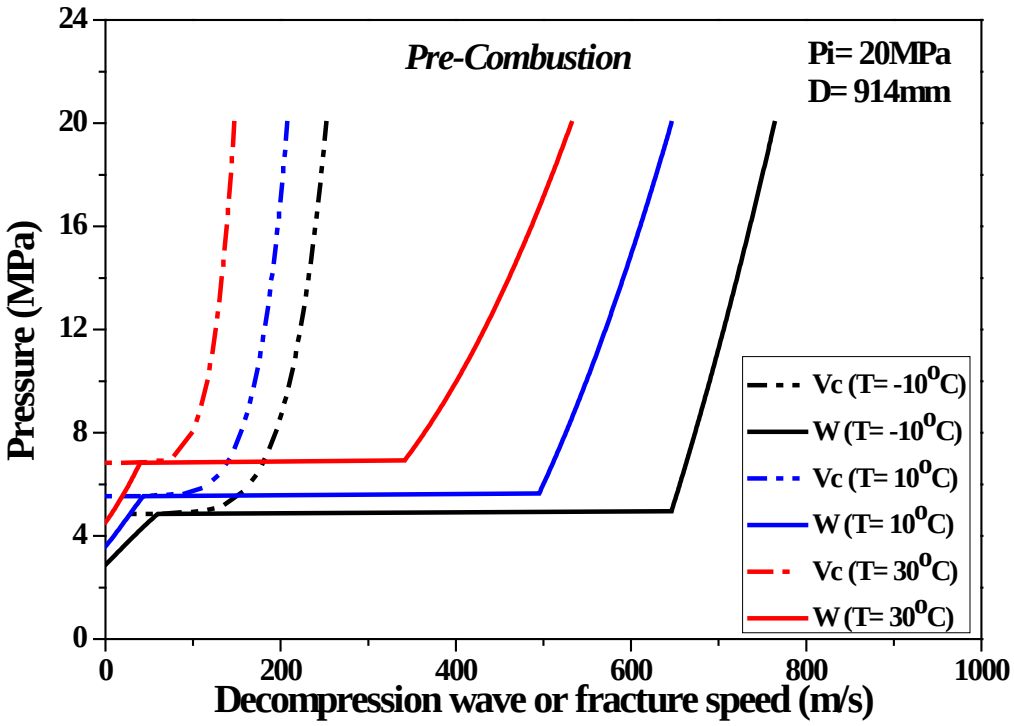

Figure 6.34: Decompression wave and fracture speeds for pre-combustion (initial temperature effect)

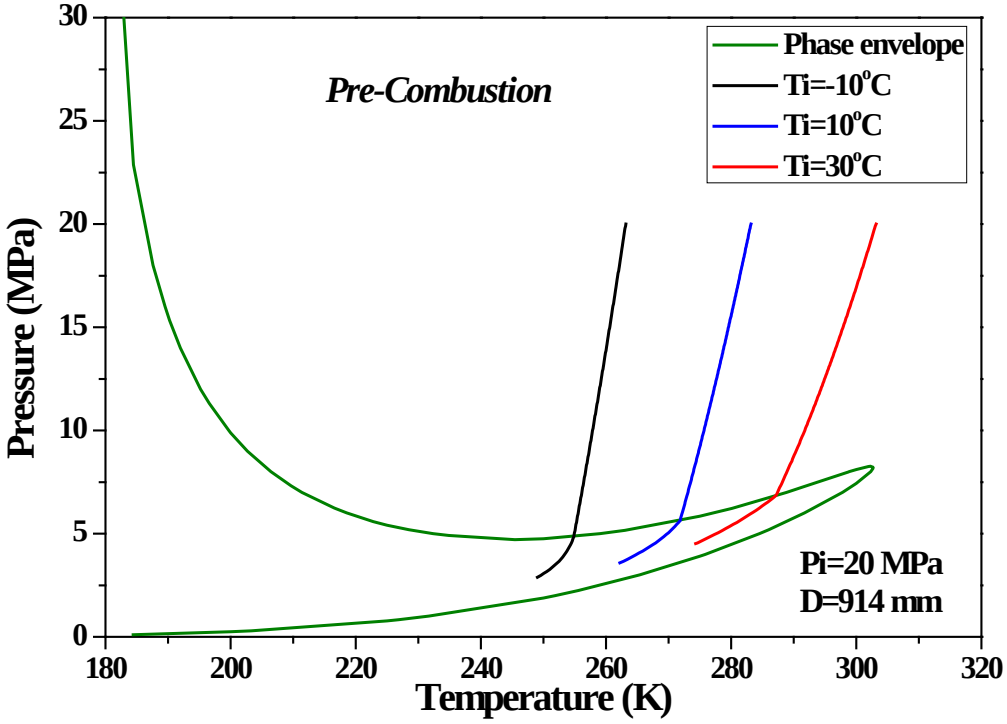

Figure 6.35: Decompression paths for three initial temperatures inserted on the phase envelope of pre-combustion compositions

The increase in the phase envelope for the pre-combustion compositions as shown in

Figure 6.35 will lead to an increase in the required arrest toughness of the pipe. The

arrest toughness as a function of the initial temperature is shown in Figure 6.36. The arrest toughness increases with the increase of initial temperature. However, once the initial temperature is relatively high (30^{o}C), the arrest toughness is increased to over 107 J for relatively large pipeline diameters D>900 mm. Figure 6.34 demonstrates that this is due to the fact that the tangency point is located near the boundary of the plateau region at a fracture speed equal to 40 m/s. The trend observed from the initial temperature effect is consistent with that of the post-combustion case; however, the required arrest toughness in the pre-combustion case is approximately double that needed for transporting the post-combustion composition in the same operating conditions.

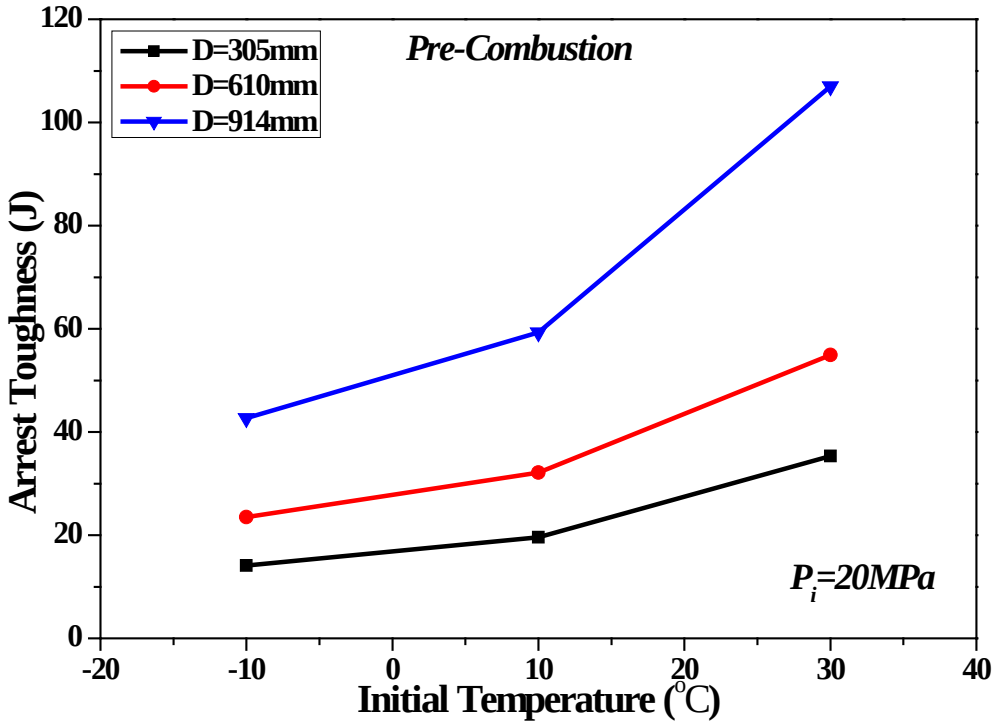

Figure 6.36: Arrest toughness as a function of initial temperature for three pipe diameters for pre-combustion case at initial pressure of 20 MPa

The effect of initial pressure on the arrest toughness was predicted using (T_i=10^{o}C) and (D=914 mm). Figure 6.37 presents the predicted decompression and fracture propagation speeds w.r.t. pressure. The arrest toughness as a function of the initial

pressure is shown in Figure 6.38. As the initial pressure increases, the arrest toughness decreases. At the lower initial pressure (7.5 MPa), the arrest toughness is high. As evident in Figure 6.37, this is due to the tangency point located close to the boundary of the plateau region. The phase envelope and the P-T decompression paths for all initial pressures are depicted in Figure 6.39. For this mixture, the increase in the initial pressure will not always result in a decrease in the arrest toughness, as it can be seen that if the initial temperature is very low (T_i<240 K), the increase in the initial pressure will result in an increase in the required arrest toughness. This is different to the trend of the post-combustion case due to the re-increase in the bubble curve of the pre-combustion case.

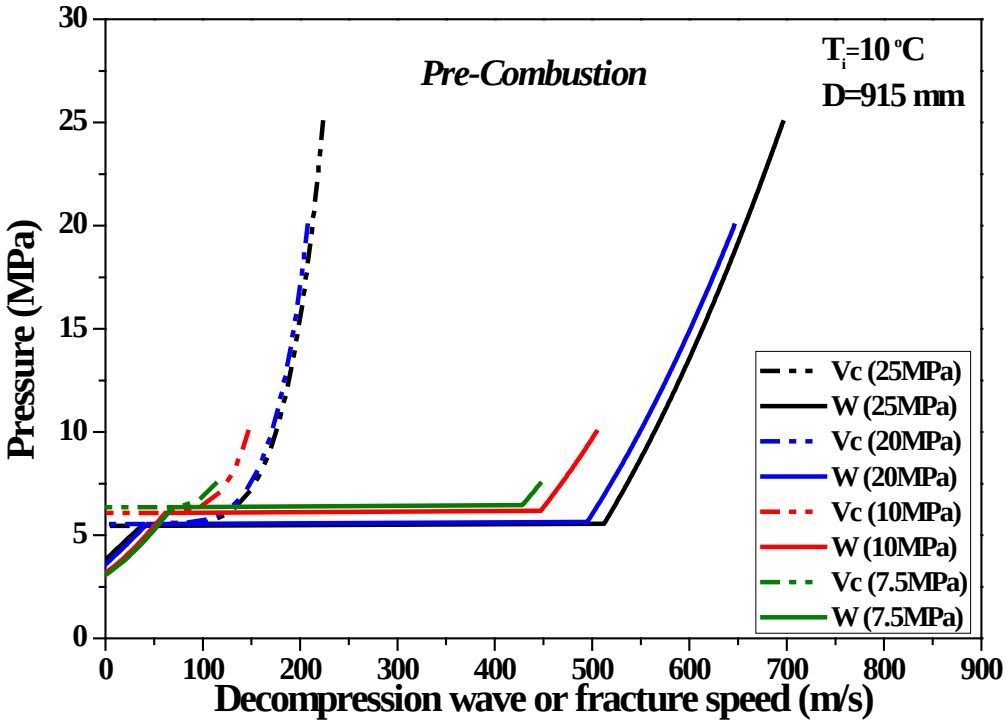

Figure 6.37: Decompression wave and fracture speeds for pre-combustion case (initial pressure effect)

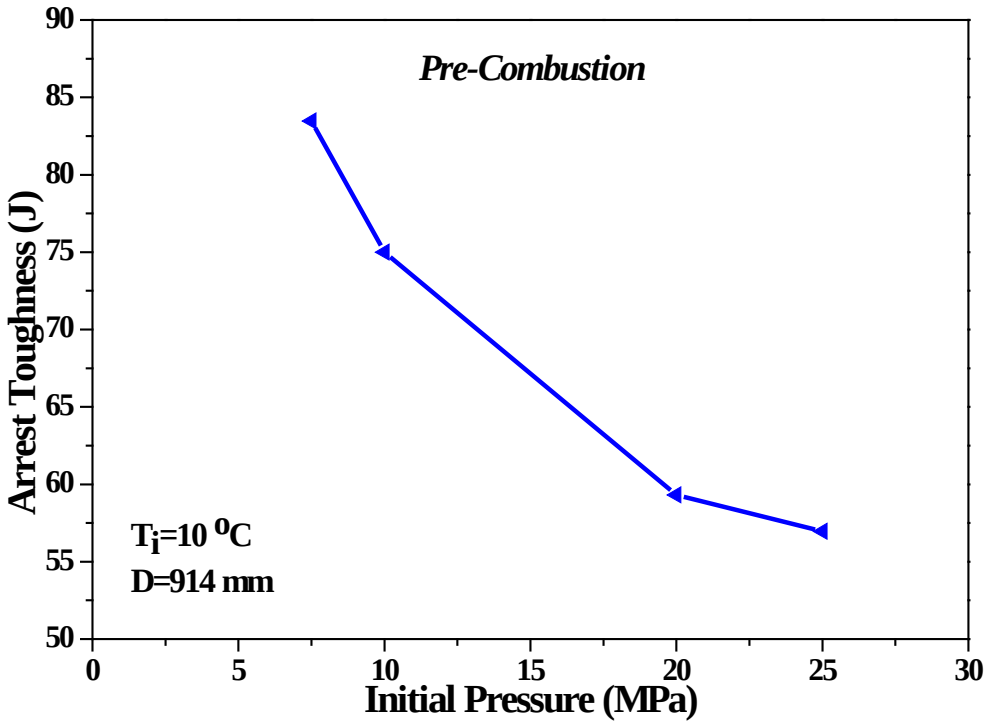

Figure 6.38: Arrest toughness as a function of initial pressure for pipe diameter (D=914 mm) for pre-combustion case at initial temperature of 20 MPa

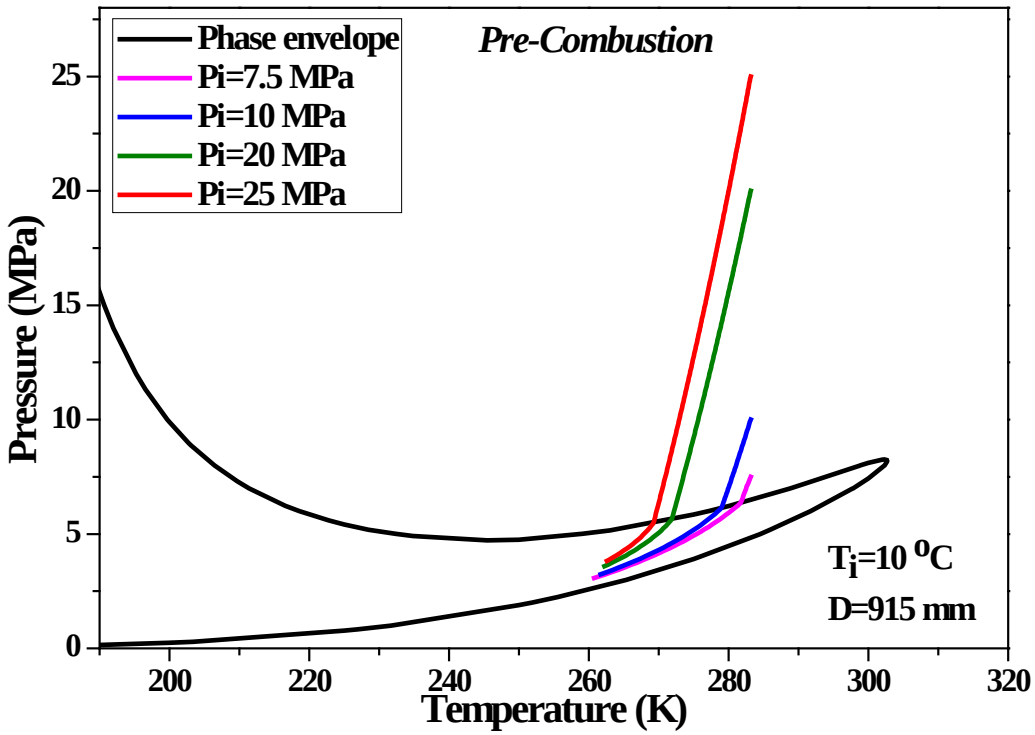

Figure 6.39: Phase envelope and the decompression path for four initial pressures (pre-combustion case)

The arrest toughness as a function of the pipe diameter for P =7.5 MPa and T_i=10^{o}C is shown in Figure 6.40. It can be seen that the arrest toughness increases with the pipe diameter. Figure 6.41 shows the pressure-speed curves. As the pipe diameter increases, the fracture curve moves to the left side, so greater arrest toughness is predicted.

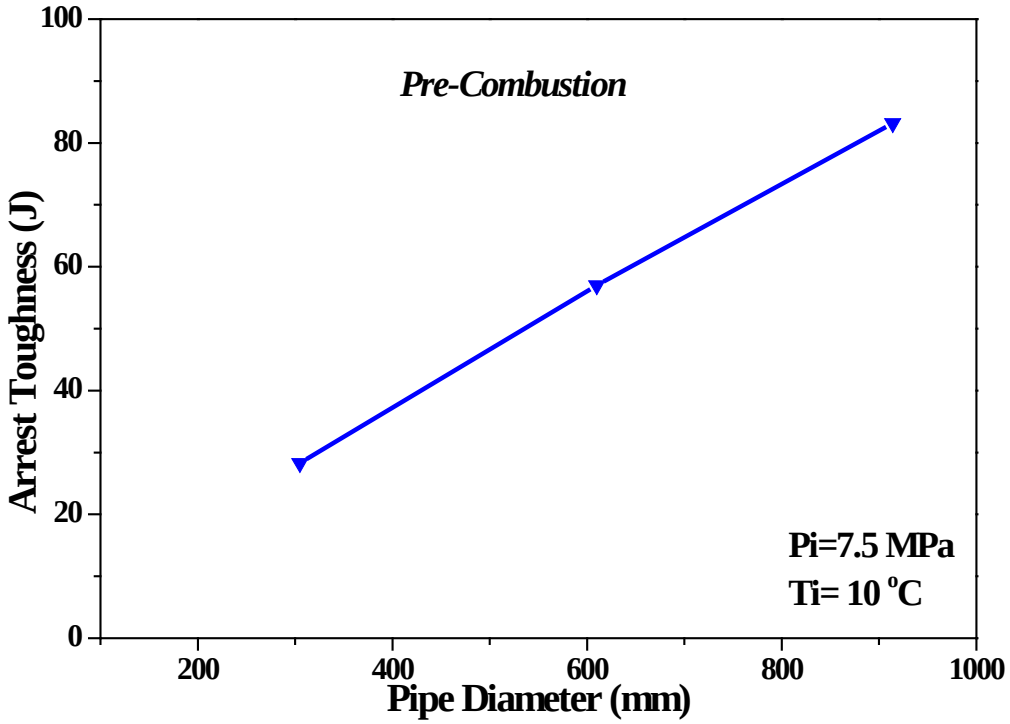

Figure 6.40: The effect of pipe diameter on the arrest toughness of pre-combustion case

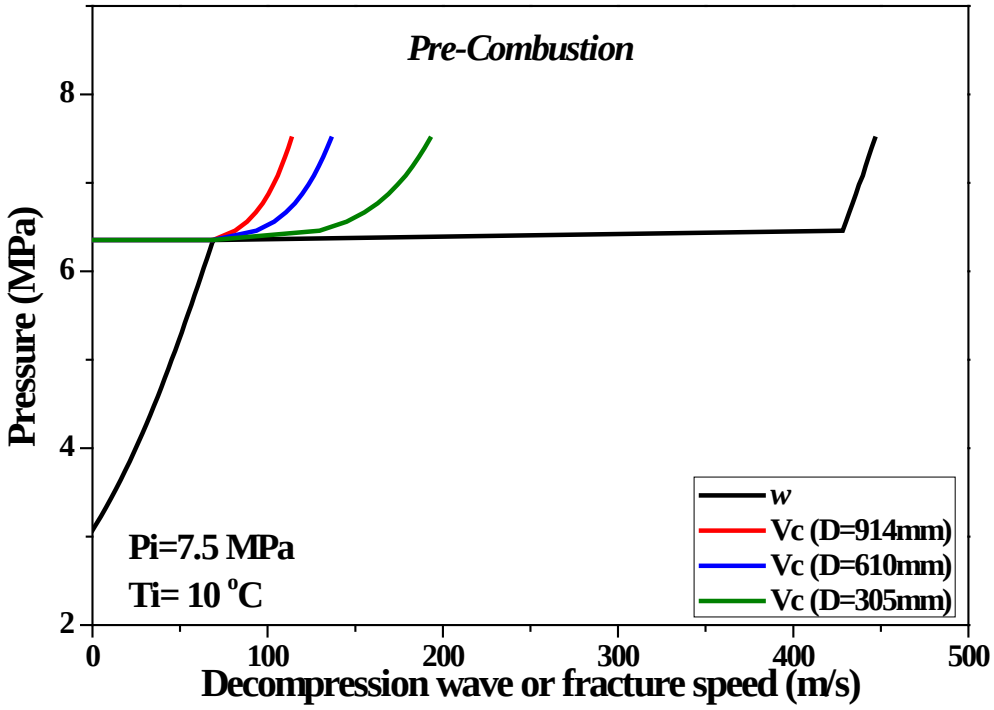

Figure 6.41: Effect of pipe diameter on fracture speed using the same decompression curve as pre-combustion case

6.4.3 Oxyfuel Case Study

The predicted results for oxyfuel were similar to the findings obtained for the pre-combustion case. Accordingly, the figures of the oxyfuel results are inserted in Appendix A.

6.5 Summary

Transporting CO_2 mixtures by pipelines is a challenging issue. In order to improve our knowledge, it is important to develop the modelling tools to simulate the transportation of CO_2 mixtures in pipelines.

In this chapter, 2D CFD simulations were conducted for the CO_2 pipelines, and the predicted results were validated against two separate shock tube tests. The results agreed well with the experimental results.

The following conclusions were made:

- The CFD model successfully tracked the rapid drop in pressure and accounted for the phase change during decompression;
- The decompression wave speed curves in CO_2 mixtures exhibited long pressure plateaus;
- At the same initial pressure, increasing the initial operating temperature decreases the initial decompression wave speed; and lowering the initial temperature increases the initial decompression wave speed;
- A drop in the initial temperature did not always result in a lower pressure plateau level for CO_2 mixtures;
- The existence of hydrogen in the CO_2 stream had a significant impact on decompression, compared to the other impurities tested (e.g. CO, O_2, N_2, … etc.);
- The CFD model was used to investigate the effects of pipe diameter and pipe wall roughness on the decompression wave speed. It was found that the effects of pipe diameter and pipe wall roughness on the decompression wave speed are negligible;
- The model was applied in simulations of pipelines transporting CO_2 mixtures captured from three CCS process routes. The effects of initial temperature, initial pressure and pipe diameter on arrest toughness were investigated;
- If the CO_2 mixture has a dense phase, the arrest toughness increases with decreasing initial pressure, increasing initial temperature and increasing pipe diameter. This indicates that small diameter and high pressure are helpful to control the ductile fracture.

If the CO_2 mixture has a gas phase, the required arrest toughness is generally low. However, the fluid density or mass flow under the same pressure is also low compared to the dense phase.

Chapter 7 3D Simulation of Pressure Distribution behind the Crack Tip

7.1 Introduction

The prediction of the decompression wave speed using the 2D CFD model is in reasonable agreement with results of shock tube tests for a wide range of gaseous mixtures. Recent results of full-scale burst tests using dense phase CO_2 mixtures conducted by National Grid, UK [56], showed that the current form of BTCM for fracture propagation control could not predict accurately the arrest toughness for CO_2 mixtures. Although the outcome of the tests may have been influenced by the line pipe material, it raises the question as to whether the behaviour of the gas was a contributing factor. In this chapter, the difference in pressure distribution along the flaps of a static mouth opening between CO_2 pipelines and nitrogen pipelines is investigated.

According to Freund et al. [159], Parks and Freund [160], the fluid pressure acting on the flaps during the decompression process is a contributing parameter responsible for changing the driving force. The driving force is related to pressure at the crack tip, the length of the pressure decay behind the crack tip, and the shape of the pressure distribution in the flaps region. Some research has been performed to study the pressure distribution along the fractured part of the pipe ‘behind the crack tip’. These studies are mostly based on a one-dimensional steady flow assumption. In the Misawa et al. model [161], the mass flow rate through the fracture opening is considered small. This assumption is suitable for the case with a small puncture in large diameter pipelines. It was also assumed that the outflow occurs under the choked condition. Aursand et al. [162] used a similar assumption for the multi-phase flow of 100% pure CO_2, but the change in the cross-section area was not considered.

The validity of using a one-dimensional analysis to study the pressure distribution behind the fracture front tip was critically studied by Parks and Freund [160]. They mentioned that an acceptable pressure distribution profile can only be predicted if the outflow opening is considered to be large. Accordingly, the assumption of a narrow outlet becomes questionable. In the same work they introduced a 2D model. The crack is considered fully open along its entire length. The geometry is alike a channel of rectangular cross-section. The flow is considered planar between the parallel planes. The full bore opening condition at the section of the crack tip leads to a sonic condition at that plan. Downstream of the crack tip, the flow becomes supersonic following the characteristics of the flow at the exit of a nozzle. The distribution of the pressure along the rectangular flaps was consistent with the experimental result. However, the drop in pressure due to the change in cross-section and that resulting from the escape of the gas cannot be distinguished using this analysis. O'Donoghue et al. [163] mentioned that to precisely simulate the case, a 3D transient flow should be taken into account.

In this chapter, the CFD decompression model developed in Chapter 4 is used in conjunction with a 3D pipe geometry of the mouth opening to simulate the decompression process. The geometry is defined using the Misawa et al. model [161]. The influences of the geometry and length of the mouth on the pressure distribution along the flaps are investigated for CO_2 and Nitrogen. Using this 3D model, the pressure decay due to both the change in cross-section and the outflow behind the crack tip is taken into account.

7.1 3D Pipe Deformation Model

The fracture opening is defined by implementing the model by Misawa et al. [161] into ANSYS DesignModeler using a MATLAB script. Equations 7.1 and 7.2 are used to prescribe the geometry of the pipe. The parameter *w* represents the radial displacement, *v* is the circumferential displacement and R_0 is the radius of the pipe. The radial displacement is a function of the circumferential angle θ and the 'deformation factor' -ψ.

Figure 7.1 illustrates schematically the displacement parameters of the pipe cross-section. In the current study, Equation 7.3 describes the evolution of the deformation factor behind the crack tip, where *x* represents the length of the fracture behind the crack tip. Figure 7.2 shows the geometry of the fracture based on Equation 7.3 for a pipe diameter of 0.914 m and fracture length of 8 m. In the current research, the deformation factor is proportional to the position downstream of the crack tip noted x^2 scaled by a factor S ranging in the (0:1) interval.

$$w(\psi,\theta) = 2R_0\psi\left[1 - cos\left(\frac{\theta}{2}\right)\right] \tag{7.1}$$

$$1 = \left(\frac{w}{R_0} + 1\right)^2 . \left(\frac{1}{R_0}\frac{\partial v}{\partial \theta} + 1\right)^2 + \left(\frac{1}{R_0}\frac{\partial w}{\partial \theta}\right)^2 \tag{7.2}$$

$$\psi(x) = \left(S\frac{x}{x_{max}}\right)^2 \tag{7.3}$$

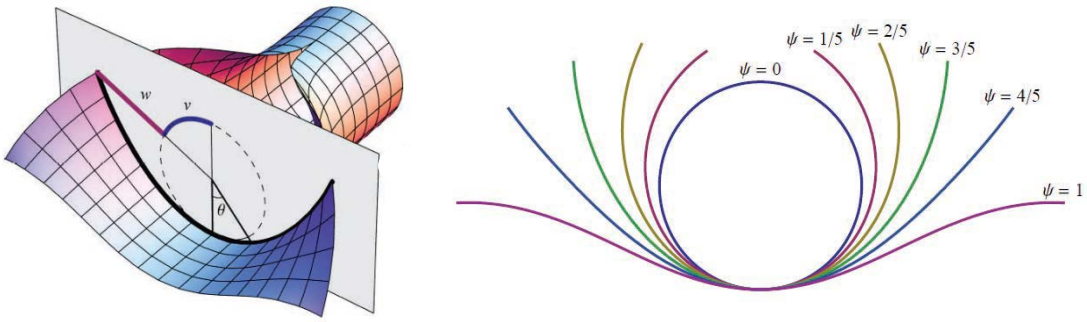

(a) **(b)**

Figure 7.1: (a) Definition of displacement parameters and (b) Deformation behaviour behind the crack tip [161]

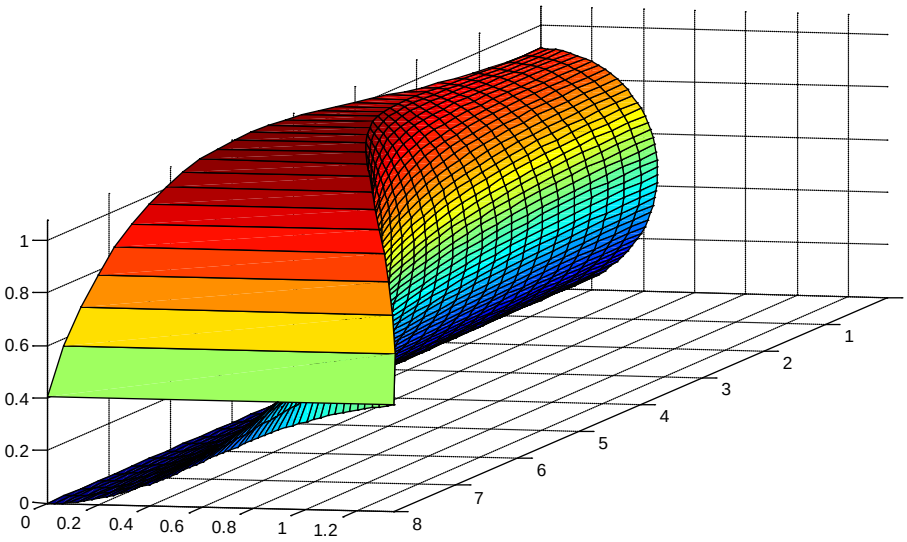

Figure 7.2: Fracture opening geometry for R_0=0.457 m and x=8 m and ψ=0.99 generated using the MATLAB code

To understand why CO_2 produces a high driving force for the fracture during its decompression, the distribution of pressure behind the crack tip is simulated and compared to that resulting from nitrogen decompression. The following sections investigate the effect of fracture length and fracture opening on the pressure distribution.

7.2 Pressure Distribution on the Flap

7.2.1 Simulation of a short fracture

Table 7.1 shows the fluids composition, the initial conditions and the pipe dimensions used in the simulation. Case1 is related to the test conditions used in reference [56]. The same simulation was carried out using Nitrogen (case 2) at the same conditions, allowing for a comparison of the pressure field along the flaps. The total length of the computational domain is 11.4 m. This is half of the vessel length used in the real test [56], taking advantage of the symmetry boundary condition. The total length of the crack along the flaps is 2.5 m. Figure 7.3 shows the computational mesh and the boundary conditions used for the current simulation. The upstream end of the pipe is specified in this simulation as a wall boundary.

Table 7.1: Pipe dimensions, fluid compositions and the initial conditions used in the simulations

	Compositions		**Initial conditions**		**Pipe dimensions**	
	CO_2	N_2	P(MPa)	T(k)	Diameter	Length
Case 1	87.5%	12.5%	14.9	288.35	914mm	22.71m
Case 2	0%	100%	14.9	288.35	914mm	22.71m

The computational mesh contained over 240,000 elements. The maximum length of the elements along the flaps was less than 10 mm. The mesh was swept to an element length up to 80 mm near the upstream end of the pipe. The atmospheric pressure condition (zero gauge pressure) was imposed over the mouth opening (outlet boundary). Two symmetry boundary conditions were imposed. One plane was along

the axial direction and the second was perpendicular to the axial axis, as shown in Figure 7.3.

The solver settings for the numerical solution are as in Chapters 5 & 6. The only difference is that the first-order upwind discretisation scheme was firstly used for the momentum equation, turbulent kinetic energy and dissipation of turbulent energy to get the convergence of the solution quickly, after which the solver switched to second-order formulations. The temporal discretisation was treated using the second-order implicit formulation. The Advection Upstream Splitting Method (AUSM) for the density-based solver [164] was selected. A constant time step of 10^{-6} s was used to capture the transient flow for all cases modelled in this Chapter. A smooth internal pipe surface was specified with an adiabatic wall boundary condition. The 'no-slip' condition was applied at the wall (fluid-solid interface).

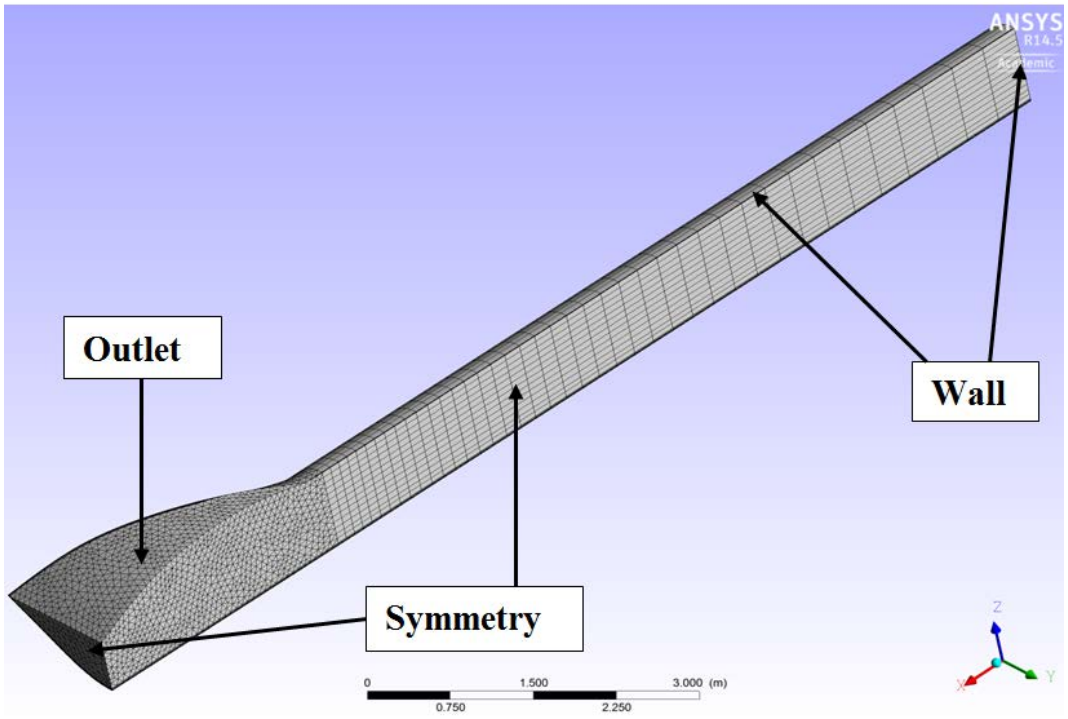

Figure 7.3: 3D computational mesh and boundary conditions

In the simulation, the fracture was static and the geometry followed equation 7.3, with a maximum deformation factor equal to 0.81 at the symmetry plan. Figure 7.4 shows the velocity vector field close to the mouth opening. The flow velocity increases as the fluid progresses towards the outlet, across the divergent geometry created by the opening flaps.

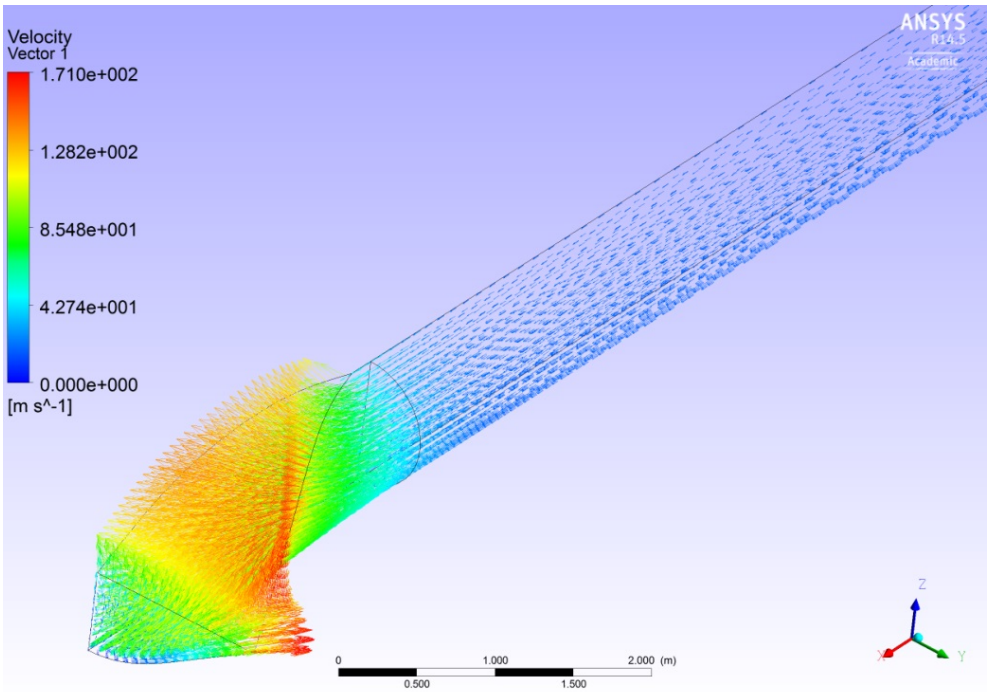

Figure 7.4: Flow velocity field close to the fracture opening

Figure 7.5 (a) & (b) shows the pressure field acting on the pipe wall at t=0.017 s for CO_2 and N_2, respectively. One can observe a comparatively higher pressure distribution in the CO_2 case. Figure 7.5 (c) shows details of the pressure profiles. Initially, the pressure decay occurs faster with CO_2, due to the high decompression wave speed of the fluid in its dense phase (423m/s). However the pressure remains constant as the mixture enters the two phase region. In comparison, Nitrogen has a gradual pressure drop without plateau. The two pressure profiles intersect along the plateau of the CO_2 case. Upstream of this intersection Nitrogen decompresses more slowly than CO_2 due to slower decompression wave speeds above 9 MPa.

Conversely, Nitrogen decompresses downstream of the intersection as the decompression wave speed are faster.

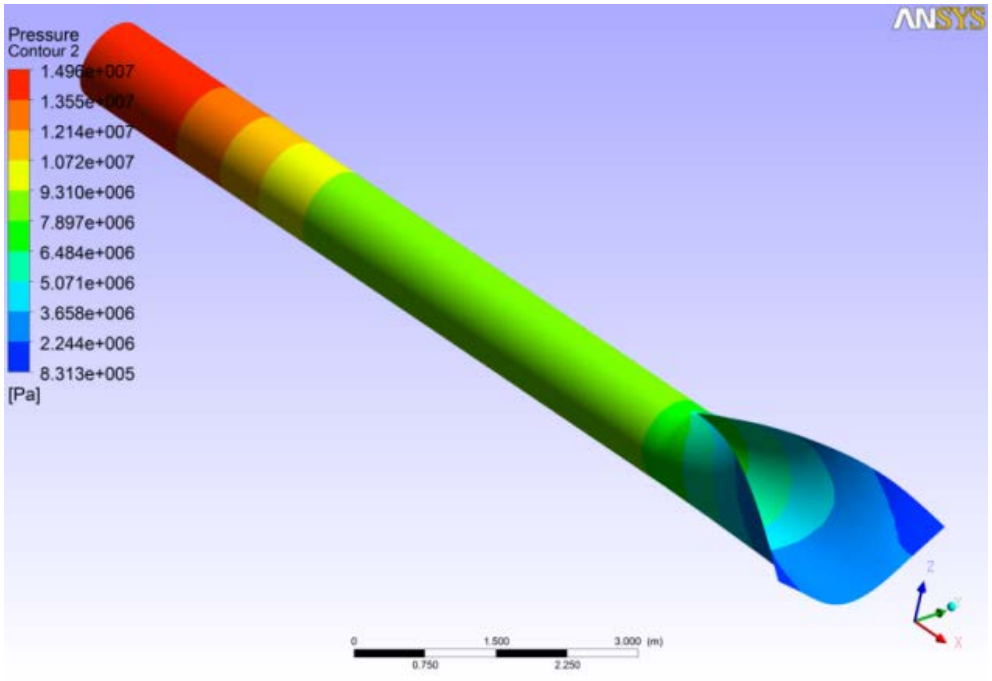

(a) CO_2 (0.017 s)

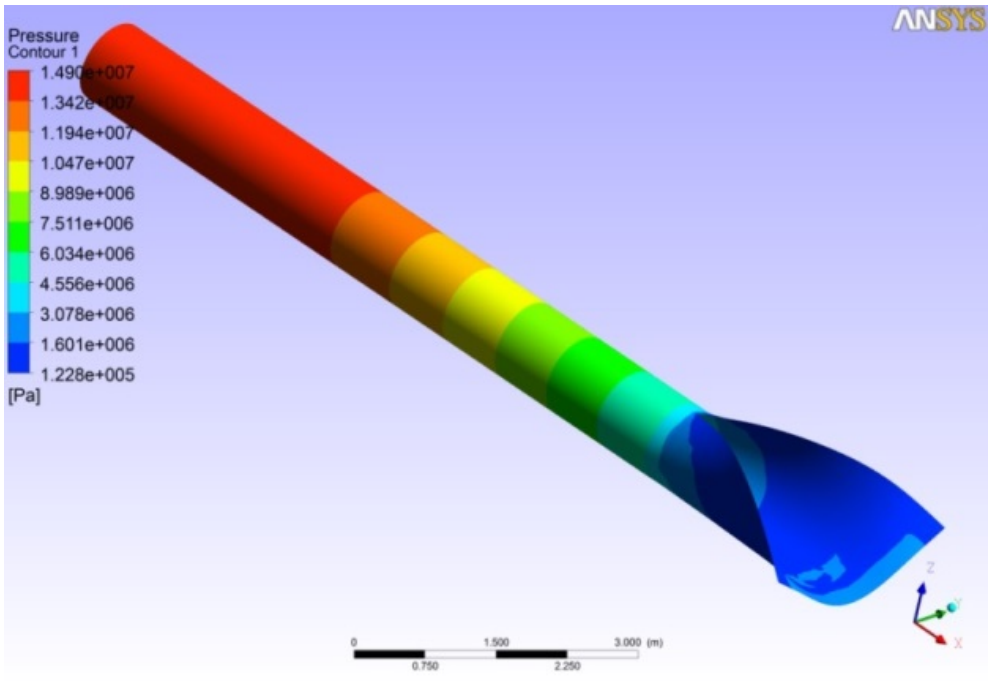

(b) N_2 (0.017 s)

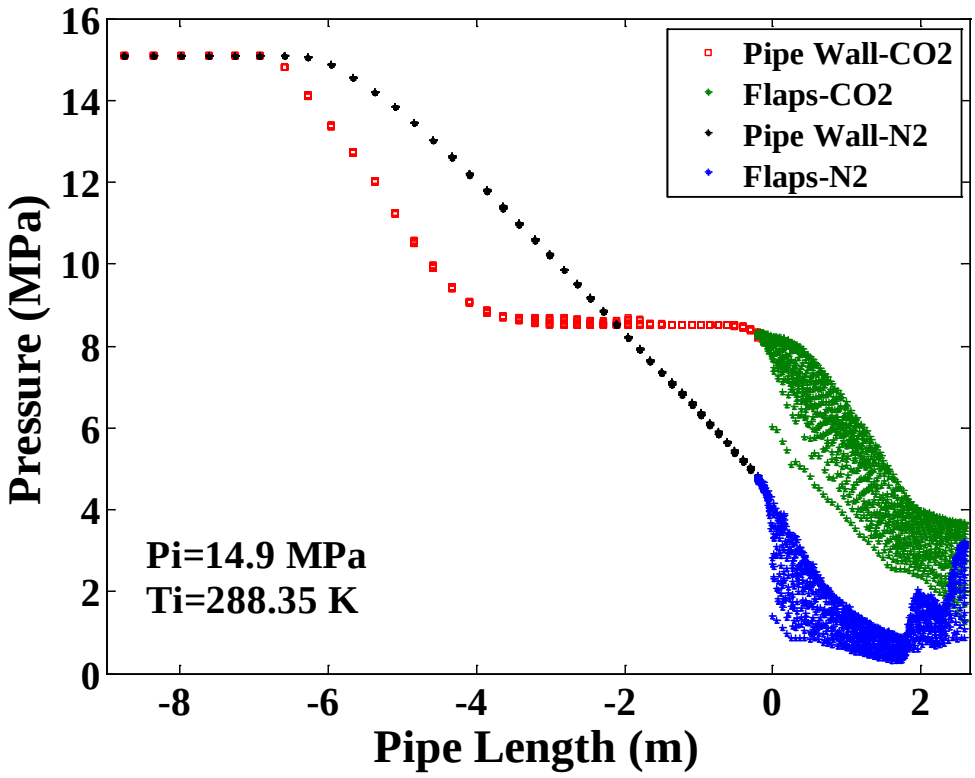

(c)

Figure 7.5: Comparison between the pressure distribution of CO_2 mixture and nitrogen along the pipe length. (0.017 s)

For longer simulation time (t=0.024s), it can be noticed that the crack tip pressure remains at high pressure, (see Figure 7.10 (b)). There are two reasons for this behaviour. First, because the crack length (2.5 m) is relatively short, the flow through the mouth opening is affected by the increase of pressure inherent to the symmetry boundary condition. The flow is forced to turn upward and recompresses. Evidences of this compression are visible in Figure 7.5 (c) for both mixtures. Secondly, the limited size of the outflow surface in conjunction with the symmetry does not allow for a full bore opening to establish. Consequently the choke condition could not take place at the crack-tip cross-section. This suggests that a longer fracture length is required to study the pressure distribution in a full bore opening condition,

representative of a long running fracture. The geometry of the model is altered using a longer fracture to better represent this condition in the following section.

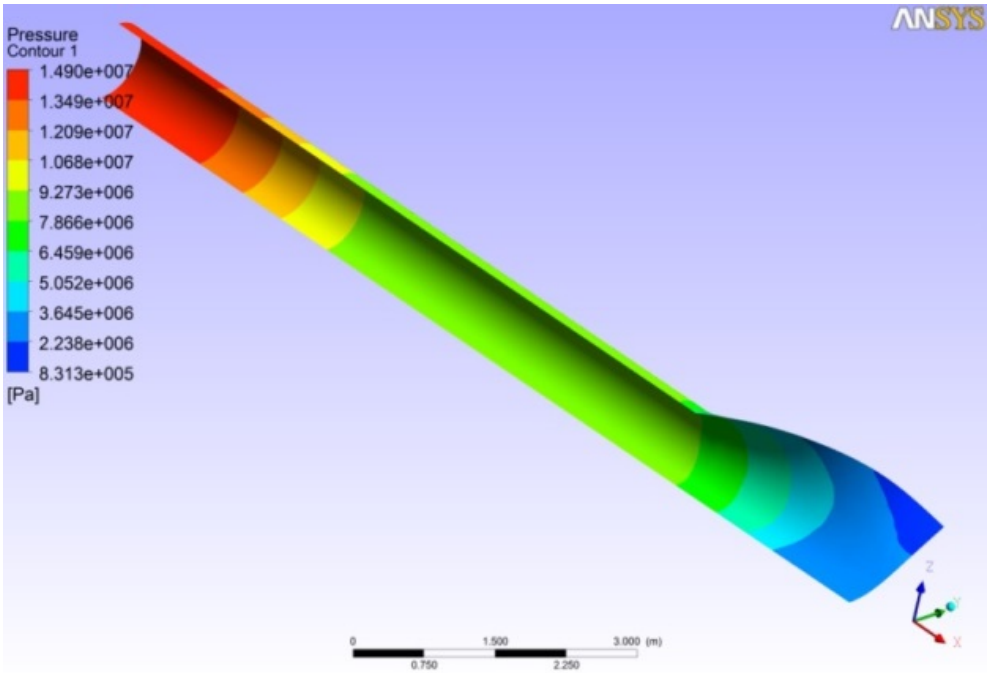

(a) t=0.017 s

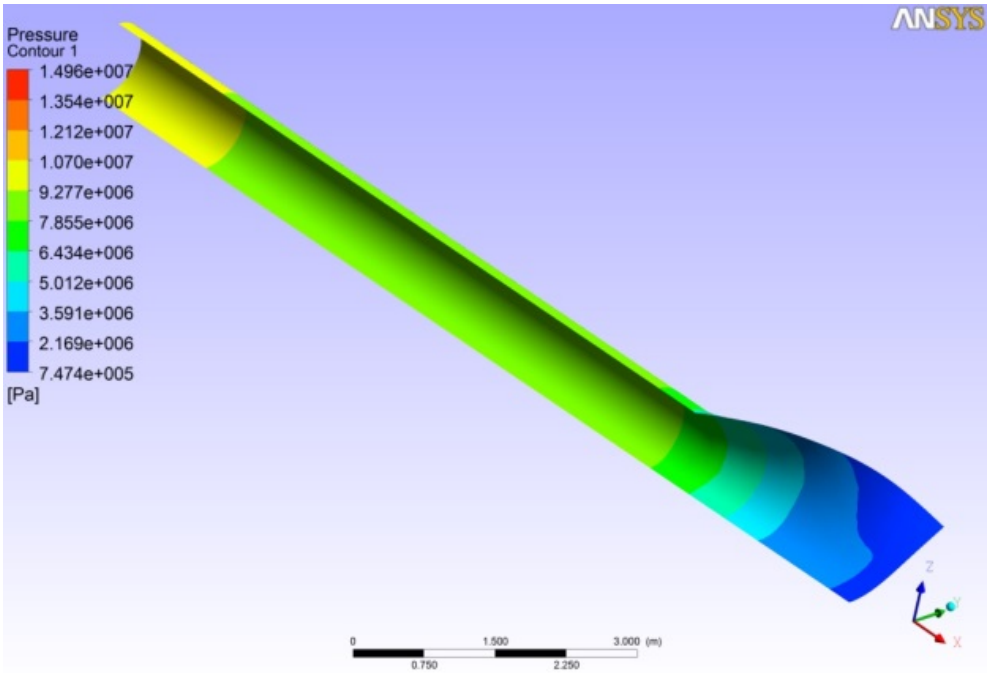

(b) t=0.024 s

Figure 7.6: Pressure contours (a) before and (b) after the reflection of the decompression wave (CO_2 mixture)

7.2.2 Simulation of a long fracture

The pressure distribution acting on the flaps is studied using a longer length of fracture behind the crack tip. The geometry was adjusted by extending the length of crack to 8 m. The remaining of the pipe accounts for 3.34 m. The geometry of the opening flaps is specified using a deformation factor ψ_{end}= 0.64 at x_{max}=8 m following Equation 7.3.

The effect of change in cross-section area behind the crack tip on flow parameters is firstly investigated for the Nitrogen case. The calculated flow parameters are collected at 15 different cross-section areas at several instants before the decompression wave reaches the inlet boundary. Figure 7.7 illustrates the locations of the cross-sections along the flaps. The location at the crack tip is specified as 0m and the rest of the cross sections are set at +0.5m from the previous location up to *x*=6.5m along the axial direction of the flap. Here the last three cross sections from the end of the flap are not included to avoid the effect of symmetry and the reduction in the cross section area after x=6.5m resulted from using Equation 7.3 (see Figure 7.7).

Fluid flow parameters including the average of pressure, Mach number and mass flow rate over each cross section were calculated for pure nitrogen (case 2 in Table 7.2). Figure 7.8 shows the variation of area (A) at each cross-section normalised to the area at the crack tip (At) w.r.t. flap length. Figures 7.9, 7.10 & 7.11 show the flow properties at different A/At normalised to their respective values at the crack tip plane for three different times (20ms, 26ms and 35ms).

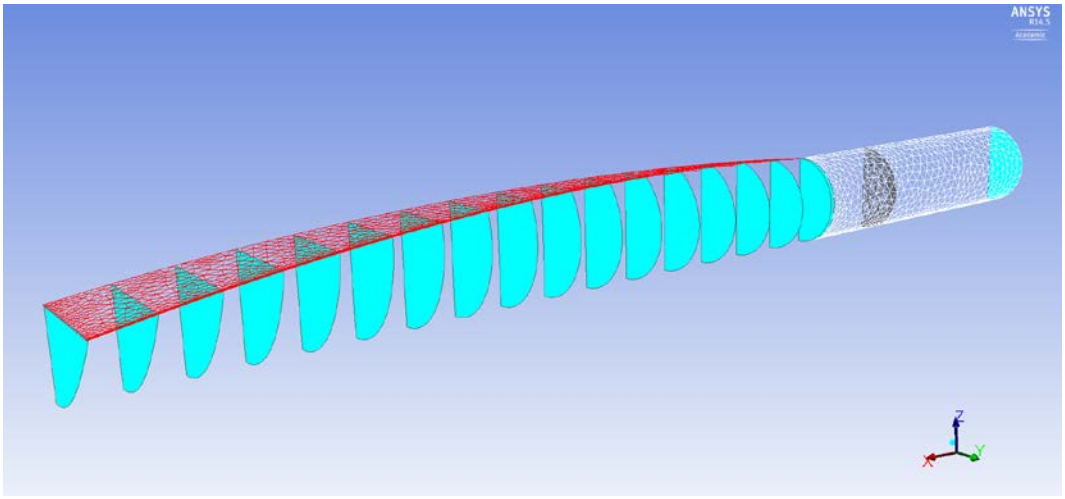

Figure 7.7: Variation in the cross-sections behind the crack tip

In Figure 7.9 the exponential decay of pressure behind the crack tip, similar to that reported by Shim et al. [165], and Parks and Freund [160], is clearly visible. In Figure 7.10 the Mach number at t=26ms and t=30ms reaches sonic condition at the crack tip. The flow becomes increasingly supersonic downstream of this cross-section as the cross-section area increases. At t=20ms the Mach number at the crack tip plane equals to 0.82. The choke condition is not established yet. The pressure decay is equivalent to that of a flow through a convergent-divergent nozzle. The sudden change in the Mach number curves at the end of the considered A/At is due to the equality between the cross sectional areas at x=6m and x=6.5 as it can be seen from Figure 7.8.

The change in mass flow rate through each cross section at 20 ms, 26 ms and 30 ms is depicted in Figure 7.11. This change is due to (a) the mass lost through the mouth opening and (b) the nature of the flow which becomes steadier with time. As the cross-section area increases, the mouth opening widens and the loss of mass flow rate increases. The change in the mass flow rate w.r.t time is nearly steady after 26

ms. Other flow variables, such as the Mach number, are still showing some transient behaviour towards the tail of the flaps.

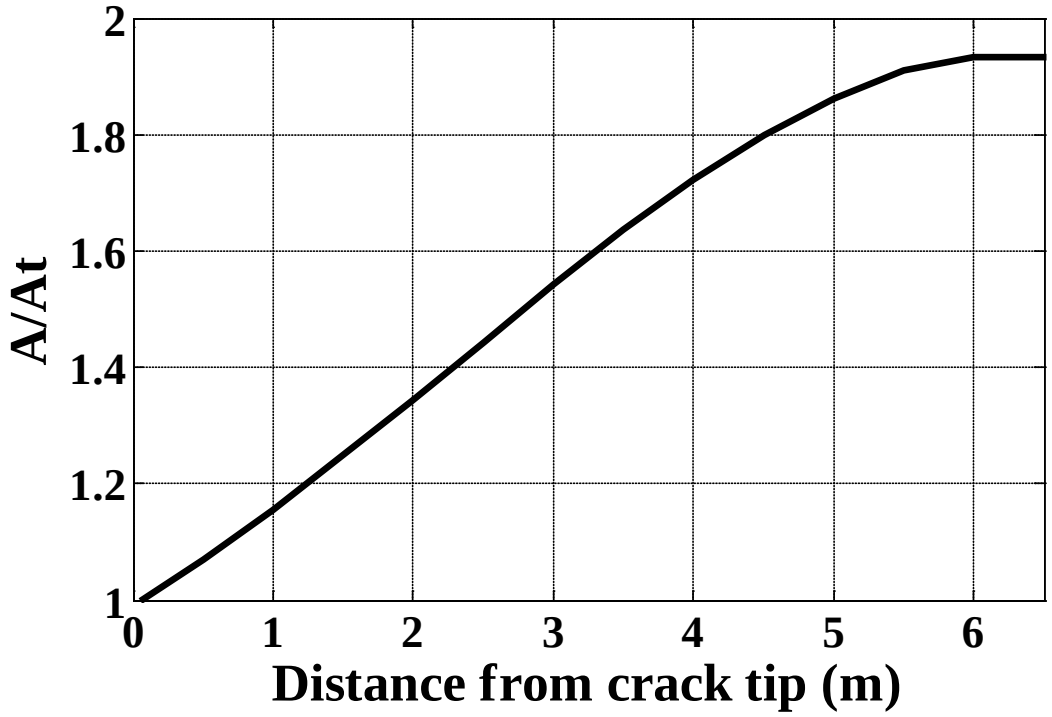

Figure 7.8: Normalised cross-sectional areas by the cross-section area at the crack tip as a function of flap length for Nitrogen

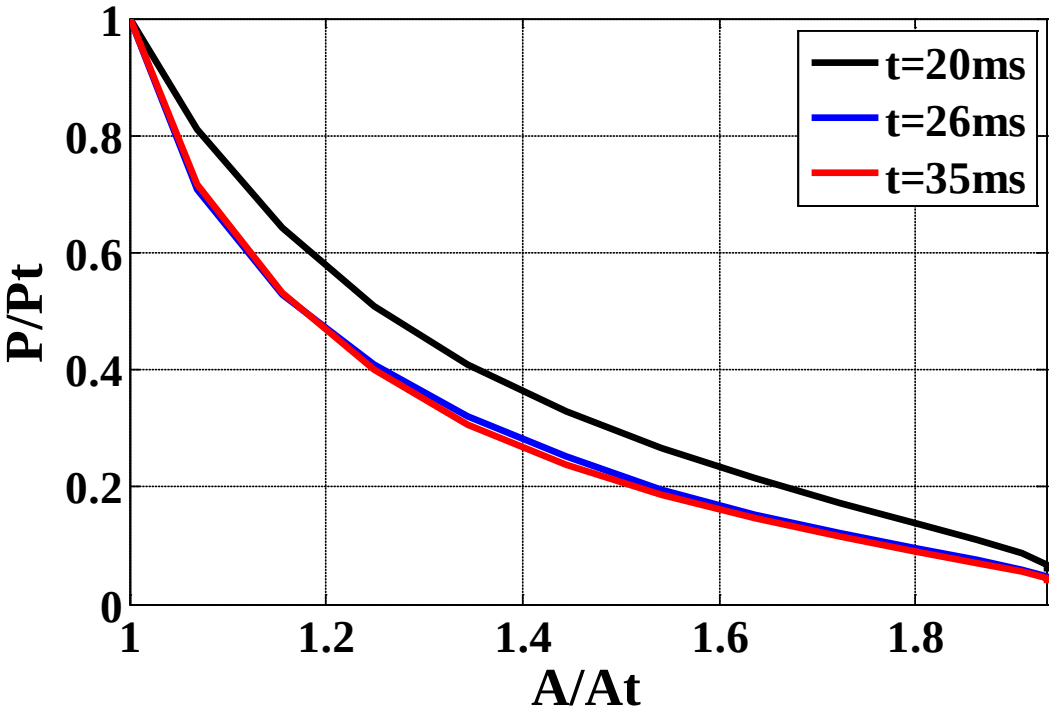

Figure 7.9: Normalised pressure distribution as a function of the normalised cross-sectional areas for Nitrogen

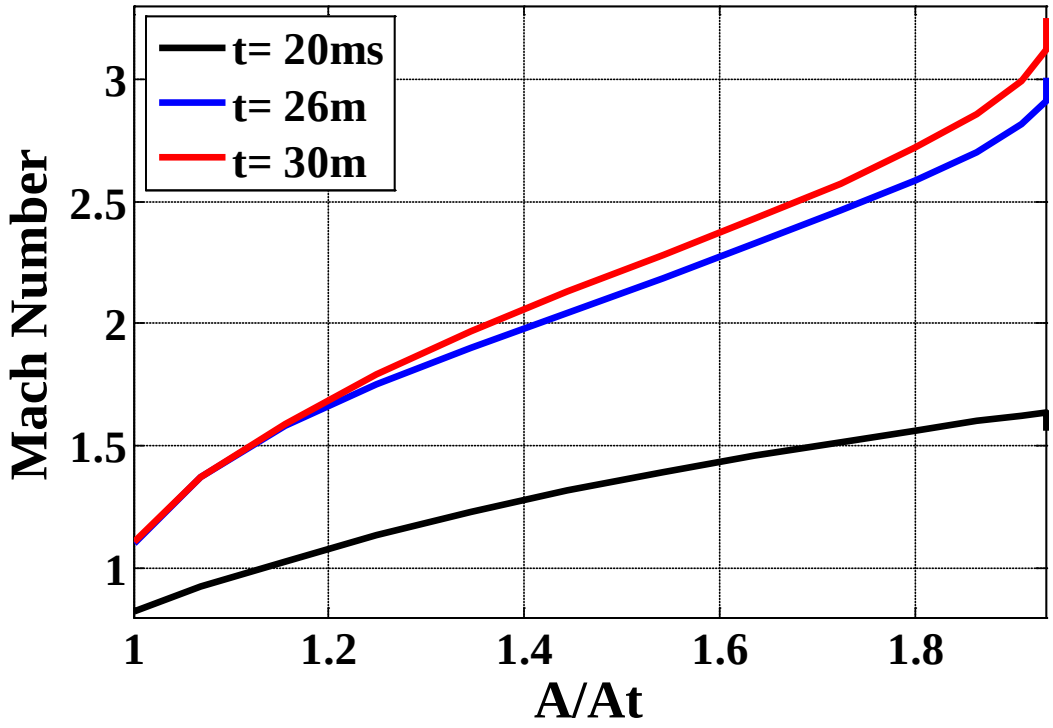

Figure 7.10: Mach number as a function of the normalised cross-sectional areas for Nitrogen

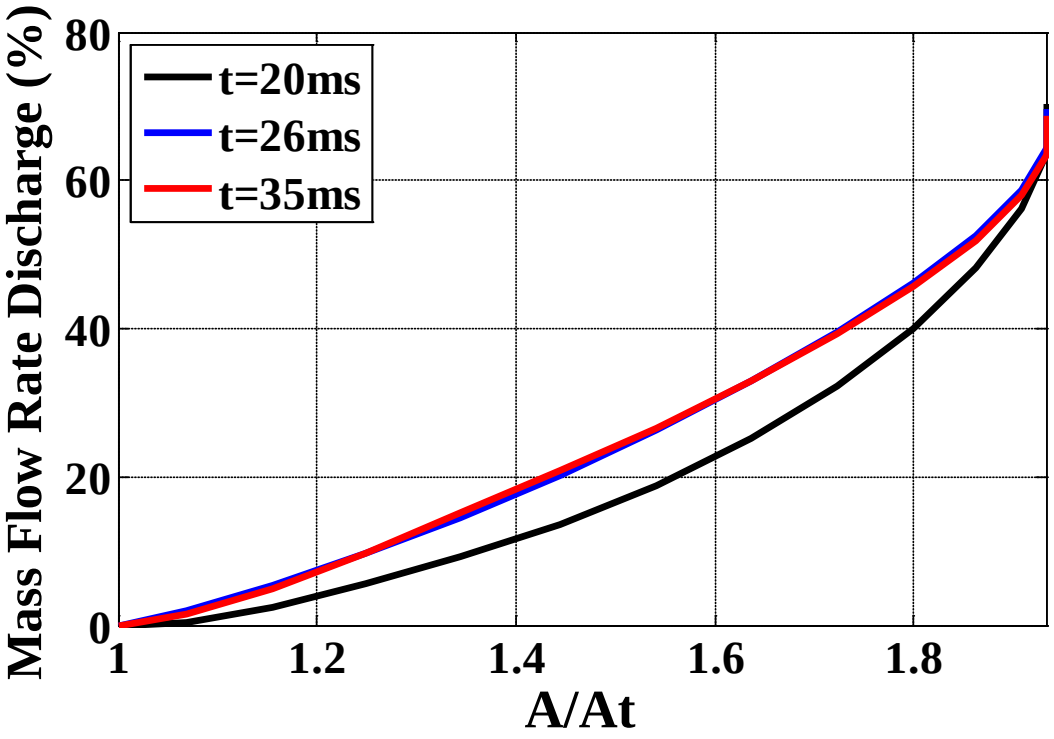

Figure 7.11: Normalised mass flow rate discharge as a function of the normalised cross-sectional areas for Nitrogen.

The above results confirm that the pressure distribution behind the crack tip is affected by the change in the cross section area and the outflow.

The distribution of pressure behind the crack tip resulted from the decompression of CO_2 rich mixture (case 1) was recorded and compared to that resulting from nitrogen decompression (case 2) using the 8 m flap length. The simulation time for the current analysis is specified to the time taken by the decompression wave speed to reach the inlet boundary and before the appearance of the effect of the symmetry boundary condition at the far end of the flap. This is to avoid the effects of those two boundary conditions on the pressure distribution. Other transient data were recorded.

The mass flow rate as a function of time for both mixtures at the outlet boundary was monitored and shown in Figure 7.12. It can be seen that the change in the mass flow rate lessens after 25 ms for Nitrogen and 29 ms for the CO_2 mixture. Again the solution did not reach a steady state as discussed previously. The mass flow rate throughout the outlet boundary of the CO_2 mixture was relatively high compared to that observed for nitrogen at the same instants due to a larger density despite a lower outflow velocity. In numbers, the CO_2 mixture produces a mass flow rate approximately 40-50% higher than that of nitrogen for the same initial operating for the investigated flaps' geometry.

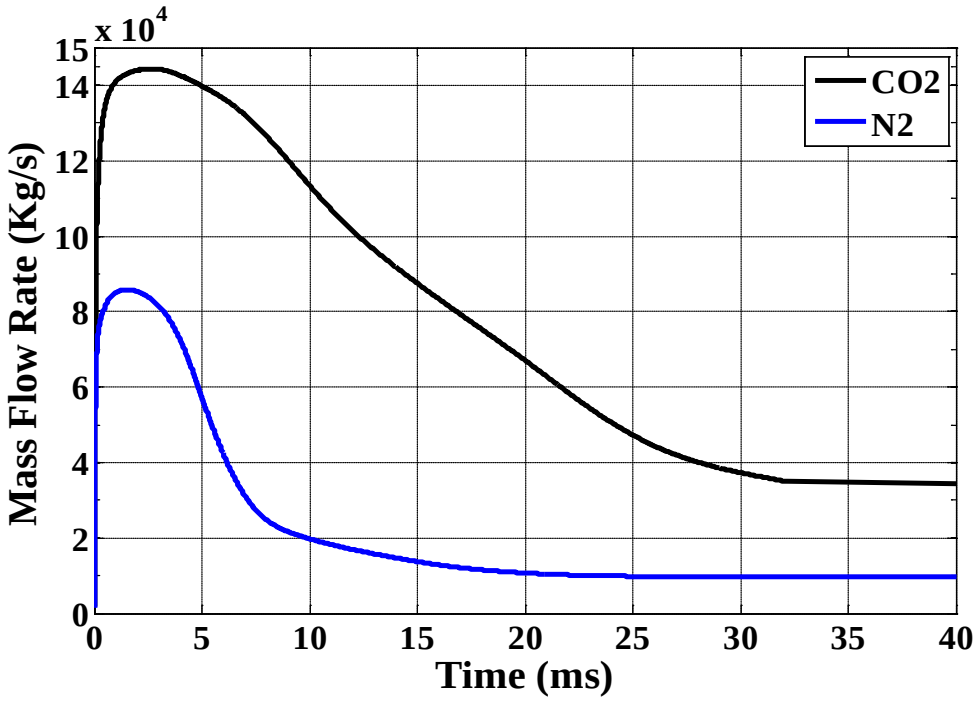

Figure 7.12: Mass flow rate as a function of time

A comparison between the pressure distributions of the two cases along the pipe wall is shown in Figure 7.13. The comparison was conducted at t=20ms. In this figure, the pressure distribution on the internal surface of the pipe upstream of the fracture tip is represented by the blue and black colors for CO_2 and N_2 respectively. The pressure distribution downstream is shown in red for CO_2 and in green for N_2. Similar to the analysis carried out with the short fracture length, the drop in pressure for CO_2 is faster than that of N_2 for most of the region upstream of the fracture tip. The CO_2 mixture reaches a pressure plateau corresponding to the pressure at the crossing of the two phase boundary (~9MPa). As illustrated on the figure, the plateau starts at a location of 1.8m in front of the crack tip and is sustained approximately 1 m downstream of the crack tip for the region at the bottom of the pipe. For a given cross-section downstream of the crack tip, the lowest pressure over the circumference is observed close to the mouth opening whereas the highest pressure is found at the bottom of the pipe wall. This observation holds for both mixtures and in

qualitative agreement with the behaviour reported by Shim et al.[165]. Compared to the short fracture length, the effect of the symmetry boundary condition is lessen.

Figure 7.14 shows the normalised pressure distribution (w.r.t. the initial operating pressure) at each normalised cross section area. The CO_2 pressure acting on the flaps remains high, ranging between 55 and 63% of the initial operating pressure for A/At<1.3. In the nitrogen case, the pressure distribution acting on the flaps is relatively low, ranging between 17 and 37% of the initial pressure. The difference in the normalised pressure distribution between the two cases along the flaps region is depicted in Figure 7.15. The comparison reveals that the pressure acting on the flaps during the decompression of the rich CO_2 mixture is higher than that for nitrogen, by more than 20% for A/At<1.65. This indicates that the driving force of the CO_2 mixture is likely to be higher than that of nitrogen. A higher force is therefore acting on that surface during this time interval.

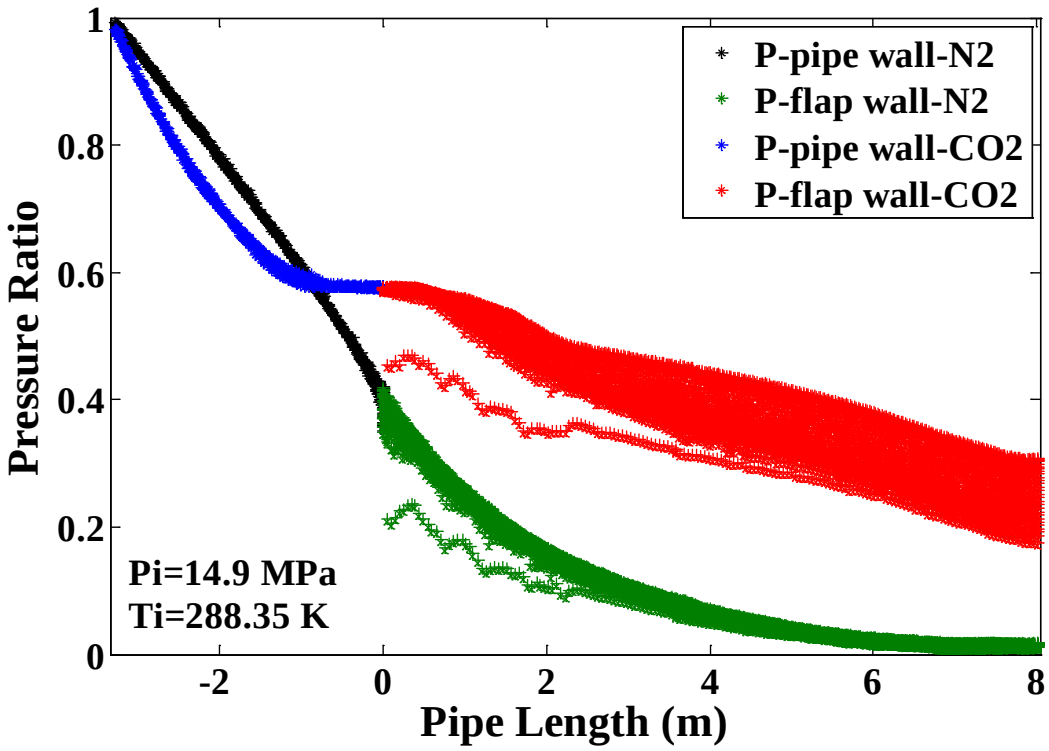

Figure 7.13: Comparison between the pressure distribution on the wall along the pipe length for CO_2 and N_2 cases at t=20ms

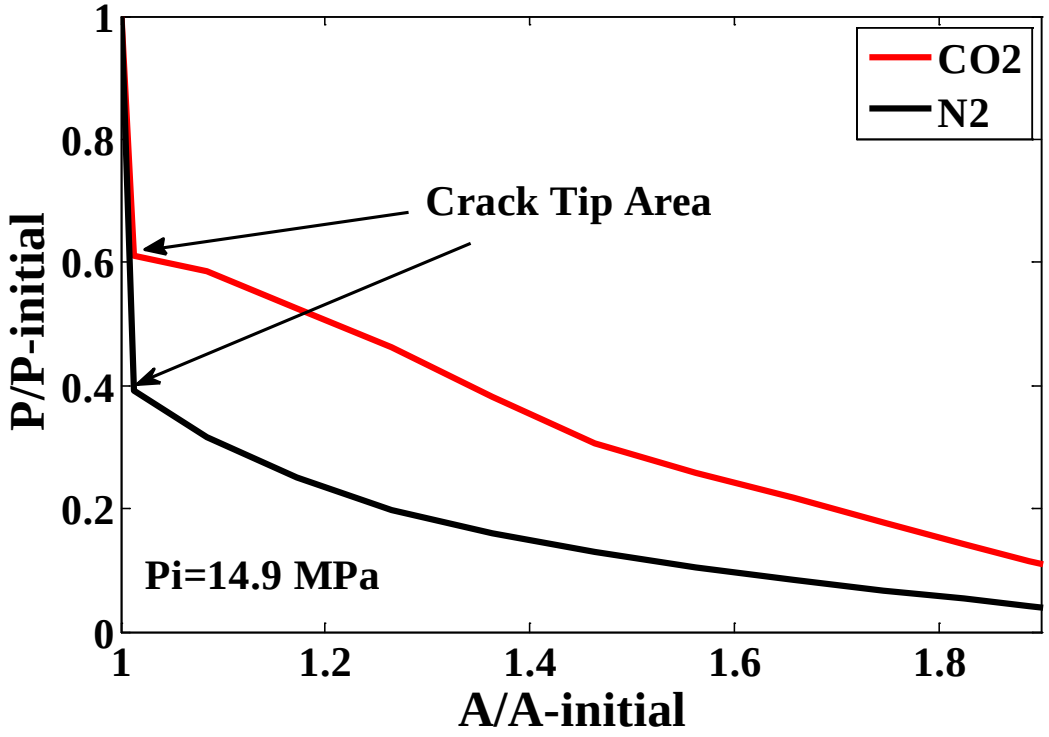

Figure 7.14: Pressure distribution along the pipe length normalised to the initial pressure as a function in the variation in cross-section area at t=20ms

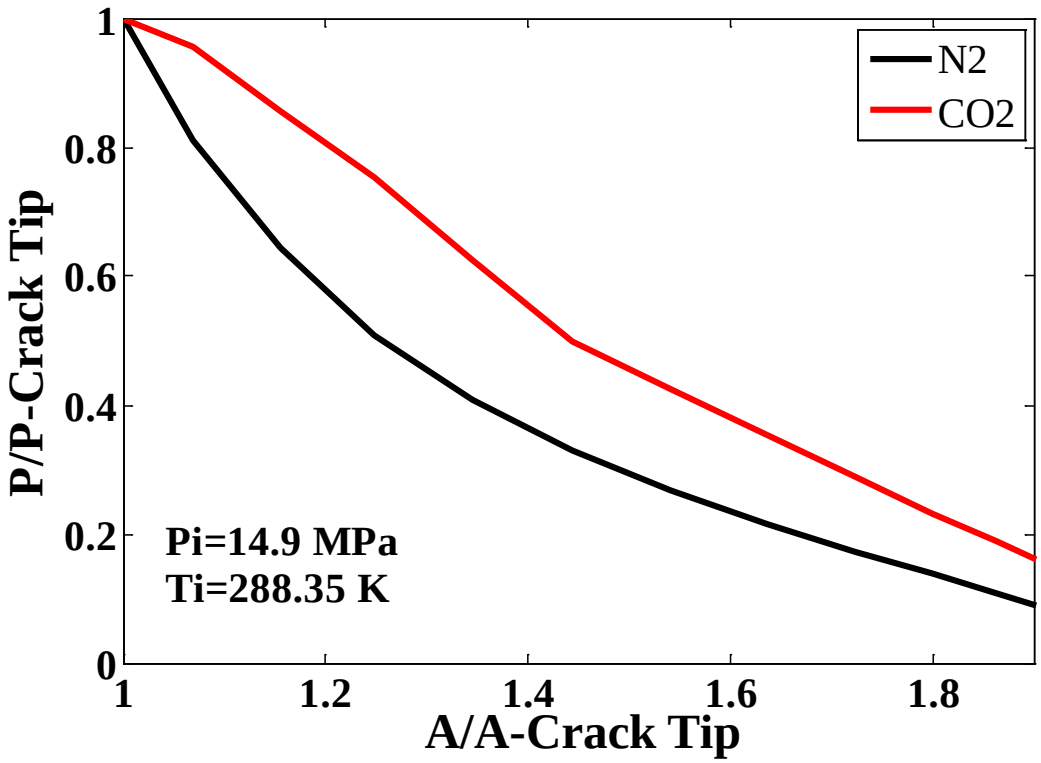

Figure 7.15: Pressure distribution along the flaps length as a function of the cross-section area at t=20ms

7.2.3 Fracture Opening Effect on Pressure Distribution

The influence of fracture opening behind the crack tip on the pressure distribution was investigated using transient simulation. This is because in gas pipelines, the opening of a running fracture is a narrow gap at the initiation of the fracture that becomes progressively wider [74]. In the current investigation, the fracture length behind the crack tip was specified to 8 m.

Table 7.3 shows the parameters used for the simulation. Several mouth opening geometries are constructed by using different values of deformation factor ψ_{end} . ψ_{tip} is equal to zero in all cases. Figure 7.16 compares the pressure distribution on the internal surface of the pipe wall for nitrogen using three different mouth openings for the first 10 ms, at which time the pressure distribution between the cases varies

noticeably. The fluid pressure acting on the internal surface of the pipe wall was affected by the increase of the fracture opening angle and the geometry of the flaps.

Table 7.2: Mouth opening based on the deformation factor using Equation 7.3

Fracture Opening	
L (m)	ψ_{end}
8	0.16
8	0.36
8	0.64

As can be noticed, the pressure distribution drops to lower levels as the opening increases. This is consistent with the increase of the outflow surface area and the larger increase of the axial cross-section areas. For a smaller opening (ψ_{end}=0.16), the pressure remains at high levels, possibly providing a high driving force for running the crack. In this case the pressure at the crack tip was more than 75% of the initial pressure. As the mouth opening widens, the crack tip pressure is lowered to 65% and 60% in the cases of ψ_{end}=0.36 and 0.64, respectively. However the three geometries do not lead to a full bore condition at the crack tip cross-section area. The flow does not choke at this location within the first 10 ms.

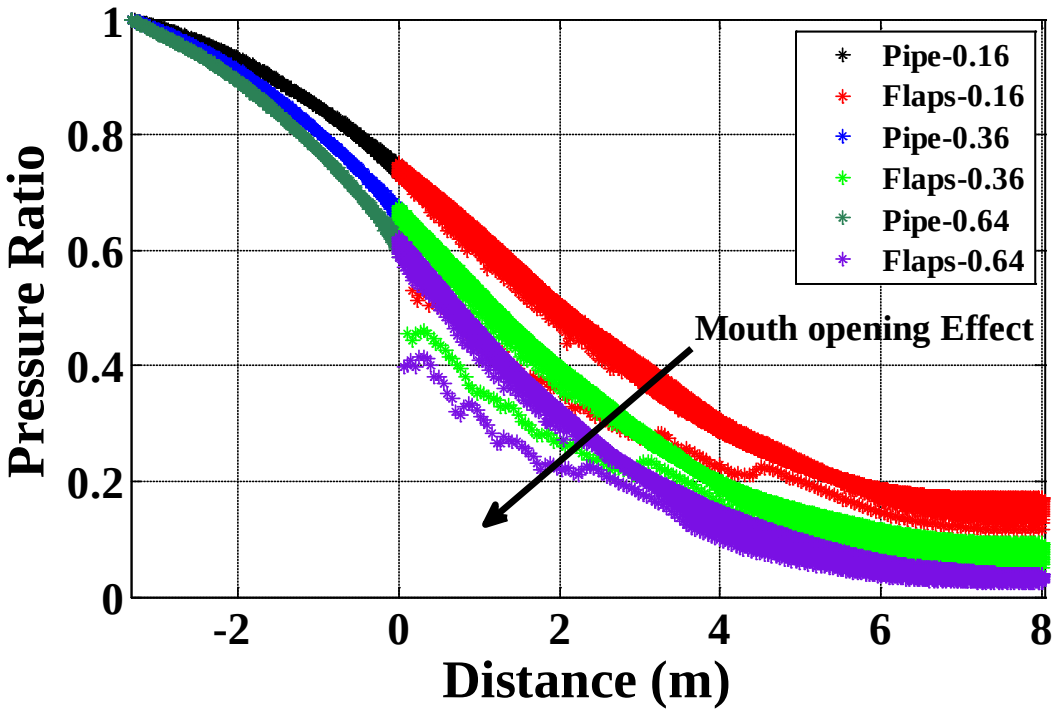

Figure 7.16: The effect of mouth opening on the pressure distribution using (ψ_{end}=0.16, 0.36 & 0.64) t=10ms.

7.3 Summary

The decompression behaviour of CO_2-rich mixtures was studied using a 3D CFD model. A pipe opening geometry model developed by Misawa et al. [161] was adopted and implemented into the CFD decompression model to investigate the effect of the fracture opening on the decompression of the fluid in a ruptured high pressure pipelines. The results show that the pressure distribution behind the crack tip is affected by the change in the cross-sectional area and mouth opening. The exponential pressure decay behind the crack tip is , qualitatively, consistent with that reported in the literature.. A comparison between the pressure distribution downstream the fracture of CO_2 mixtures and nitrogen was conducted. For CO_2 rich mixture undergoing a two-phase flow, the pressure behind the static crack tip was found to remain at a high pressure level, close to the saturation pressure, at 20 ms.

The effect of mouth opening on the fluid pressure acting on the flaps was studied using three different pipe openings. For a narrow opening (ψ_{end}=0.16), the pressure along the flaps was up to 75% of the operating pressure at 10 ms. Wider mouth opening lead to a low pressure of 65% and 60% for ψ_{end}=0.36 and 0.64, respectively, at the same instant of the simulation. This shows that the pressure decay in front of the crack tip is affected by the width of the mouth opening until the full-bore condition is reached. The obtained results of pressure distribution behind the crack tip can be used in conjunction with other structure simulation tools in order to calculate the driving force of the crack.

Chapter 8 Conclusions and Future Work

8.1 Summary

The decompression of CO_2 in pipelines was simulated using a new multi-dimensional model developed using the CFD software, ANSYS Fluent. The simulations gave valuable insight into a number of factors that affect the decompression characteristics of pure CO_2 and CO_2 mixtures, and highlighted the distinguishing features of CO_2 decompression compared to other gases. The model predictions were validated against measured data obtained from various shock tube tests and full-scale burst tests conducted using natural gas and dense-phase CO_2 mixtures.

This research has assessed the suitability and the applicability of three different currently available equations of state used in the gas pipeline industry for calculating the thermodynamic properties of CO_2-based mixtures, and identified the GERG-2008 EOS as the most suitable. This is significant, since no EOS was recommended in the past to be used for calculating the properties of CO_2 mixtures. This was done by conducting a critical comparison of the performance of three equations of state in calculating the densities and speeds of sound of some mixtures related to CCS technology, against currently available measured data found in the literature. It was concluded that the GERG-2008 EOS exhibits better accuracy and better computing convergence than other equations of state over most of the range of the tested conditions.

The decompression simulations were performed for natural gas and CO_2 in pipelines using a multi-dimensional model using the implementation of the GERG-2008 EOS in the CFD code ANSYS Fluent, for the first time. This novel implementation technique can be used to incorporate any other future EOS into the model.

The 2D CFD simulations of the decompression behaviour in gas pipelines were in good agreement with experimental results obtained from shock tube tests. The simulations showed that the model successfully tracked the rapid drop in pressure observed in the experiments. The model also captured the discontinuity in fluid properties occurring due to the appearance of the two-phase region.

The model was employed to predict the decompression characteristics of several CO_2 mixtures relevant to CCS technologies, and the simulation results were validated against two shock tube tests. The decompression wave speed curves in CO_2 mixtures exhibited longer pressure plateaus compared to natural gas mixtures. The impact of several factors on the decompression wave speed was also investigated. Those factors include: the initial temperature, initial pressure, fluid composition, pipe diameter and internal surface roughness.

It was found that increasing the initial operating temperature decreases the initial decompression wave speed, and lowering the initial temperature increases the initial decompression wave speed. Also, an increase the initial temperature leads to a higher pressure plateau for temperatures below the critical temperature. However, a drop in the initial temperature does not always result in a lower pressure plateau level for CO_2 mixtures. This is because of the influence of shape of the bubble curve on the phase envelope, which in turn depends on the amounts and types of impurities in the CO_2 mixture. Among the impurities investigated, the existence of hydrogen in the CO_2 stream had a maximum impact on the decompression, compared to the other impurities tested (e.g. N_2, O_2, CH_4, Ar, CO and H_2S). It was also found that the effects of pipe diameter and pipe wall roughness on the decompression wave speed are negligible for pipe diameters greater than 250 mm. Increasing the initial pressure

was found to lower the pressure plateau, implying that using lower initial pressure leads to an increase in the required arrest toughness for pipelines transporting CO_2 mixtures. This suggests that it is safer and more efficient to use high initial pressure to transport CO_2 mixtures through pipelines.

The model was used in simulations of pipelines transporting CO_2 mixtures captured from three CCS process routes. The effects of initial temperature, initial pressure and pipe diameter on the arrest toughness were investigated. If the CO_2 mixture is initially a dense-phase fluid, the arrest toughness increases with decreasing initial pressure, increasing initial temperature and increasing pipe diameter. This indicates that small diameter and high pressure are helpful to control the tendency for ductile fractures. On the other hand, if the CO_2 mixture has decompressed from an initial gas phase, the required arrest toughness is generally low. However, the fluid density or mass flow under the same pressure is also low compared to the dense phase.

3D simulations were conducted to simulate the pressure distribution acting on the flaps behind the crack tip, in order to gain insight into the driving force for fracture in CO_2 pipelines. The results show that the pressure distribution behind the crack tip is affected by the change in the cross-sectional area and mouth opening. The exponential pressure decay behind the crack tip is qualitatively, consistent with that reported in the literature. A comparison between the pressure distribution downstream of the fracture in pipelines carrying CO_2 mixtures and pure nitrogen was conducted. The comparison showed that CO_2 fluid pressure acting on the flaps remains high, between 55 and 63% of the initial operating pressure, for several cross-sections behind the crack tip. In the nitrogen case, the pressure acting on the flaps is

relatively low, ranging between 17 and 37% of the initial pressure for the same range of cross-sections.

The effect of mouth opening on the fluid pressure acting on the flaps was studied using three different pipe openings. For a narrow opening (ψ_{end}=0.16), the pressure along the flaps was up to 75% of the operating pressure at 10 ms. Wider mouth opening lead to a low pressure of 65% and 60% for ψ_{end}=0.36 and 0.64, respectively, at the same instant of the simulation. This shows that the pressure decay in front of the crack tip is affected by the width of the mouth opening until the full-bore condition is reached. Such information is valuable, as the predicted pressure acting on the flaps can be used in conjunction with other simulation tools to determine the force driving the fracture.

8.2 Recommendations

For future work, it is recommended that the current model be further developed to account for the propagation of the crack for the decompression simulation, as the fracture opening results show that the pressure distribution acting on the flaps is influenced by the change in the shape of the pipe opening. This can be conducted using the 'dynamic mesh' feature available in ANSYS Fluent. It is possible that more accurate predictions can be gained by defining a suitable fracture speed that can be used to deform the mesh. This will lead to the possibility of developing a fully coupled 3D fluid-structure model to simulate fracture propagation in CO_2 and/or natural gas pipelines.

REFERENCES

1. IE, 2011 *Building Essential Infrastructure for Carbon Capture and Storage*. *Insight Economics Pty Ltd (IE)*: Melbourne. p. 43.
2. Li, H. and J. Yan, 2009, *Evaluating cubic equations of state for calculation of vapor–liquid equilibrium of CO2 and CO2-mixtures for CO2 capture and storage processes.* Applied Energy. **86**(6): p. 826-836.
3. Metz, B., O. Davidson, H.d. Coninck, M. Loos, and L. Meyer, 2005 *IPCC Special Report on Carbon Dioxide Capture and Storage*. Intergovernmental Panel on Climate Change: New York. p. 443.
4. Zhang, Y., X. Ji, and X. Lu, 2014, *Energy consumption analysis for CO2 separation from gas mixtures.* Applied Energy. **130**(0): p. 237-243.
5. IEA, 2010 *CO_2 pipeline Infrastructure: An analysis of global challenges and opportunities*. *International Energy Agency Greenhouse Gas Programme*. p. 1-134.
6. DNV, 2010, *Recommended Practice DNV-RP-J202 "Design and Operating of CO_2 Pipelines".*
7. Cosham, A. and R.J. Eiber, 2008b, *Fracture control in carbon dioxide pipelines - the effect of impurities. Proceedings of the Biennial International Pipeline*. p. 229-240.
8. Parfomak, P.W. and P. Folger, 2008 *CRS Report for Congress on Carbon Dioxide (CO_2) Pipelines for Carbon Sequestration: Emerging Policy Issues*. *Congressional Research Service CRS*. p. 1-21.
9. Cosham, A. and R.J. Eiber, 2008a, *Fracture propagation in CO2 pipelines.* The Jornal of Pipeline Engineering. **4**: p. 281-291.
10. Li, H. and J. Yan, 2009, *Impacts of equations of state (EOS) and impurities on the volume calculation of CO2 mixtures in the applications of CO2 capture and storage (CCS) processes.* Applied Energy. **86**(12): p. 2760-2770.
11. Maxey, W.A., J.F. Kiefner, and R.J. Eiber,1976 *Ductile fracture arrest in gas pipelines*. Related Information: A. G. A. Cat. No. L32176. Medium: X; Size: Pages: 46.
12. Kiefner, J.F., W.A. Maxey, R.J. Eiber, and A.R. Duffy, 1973 *Failure Stress Levels of Flaws in Pressurized Cylinders* Progress in Flaw Growth and Fracture toughness Testing, ASTM STP 536, American Society for Testing and Materials. p. 461-481.
13. Botros, K.K., W. Studzinski, J. Geerligs, and A. Glover, 2004, *Determination of Decompression Wave Speed in Rich Gas Mixtures. The Canadian Journal of Chemical Engineering*. **82**(5): p. 880-891.
14. Cosham, A. and R.J. Eiber, 2008a, *Fracture propagation in CO_2 pipelines. The Jornal of Pipeline Engineering*. **vol. 4**(no. 2): p. 281-291.
15. Cosham, A., R.J. Eiber, and E.B. Clark, 2010, *GASDECOM: Carbon Dioxide and Other Components. ASME Conference Proceedings*. **2**: p. 777-794.
16. Rothwell, A.B., 2000, *Fracture propagation control for gas pipelines—past, present and future. In: Denys R, editor. Proceedings of the 3rd International Pipeline Technology Conference*. **1**: p. 387–405.
17. Calabrese, F. Masserano, and M.J. Blunt, 2005 *Simulation of physico-chemical processes during carbon dioxide sequestration in geological structures*, in *Proceedings of the 2005 SPE Annual Technical Conference and Exhibition*: Dallas, Texas, USA, 9–12 October 2005.
18. Gale, J. and J. Davison, 2004, *Transmission of CO_2-safety and economic considerations. Energy*. **29**(9-10): p. 1319-1328.

19. Koornneef, J., M. Spruijt, M. Molag, A. Ramírez, W. Turkenburg, and A. Faaij, 2010, *Quantitative risk assessment of CO_2 transport by pipelines--A review of uncertainties and their impacts. Journal of Hazardous Materials*. **177**(1-3): p. 12-27.
20. Barrie, J., K. Brown, P.R. Hatcher, and H.U. Schellhase, 2004, *Carbon Dioxide Pipelines: A Preliminary Review of Design and Risks. 7th International Conference on Greenhouse Gas Technologies*.
21. Berstad, T., C. Dørum, J.P. Jakobsen, S. Kragset, H. Li, H. Lund, A. Morin, S.T. Munkejord, M.J. Mølnvik, H.O. Nordhagen, and E. Østbya, 2011, *CO_2 pipeline integrity: A new evaluation methodology*. Energy Procedia. **4**: p. 3000-3007.
22. Bliss, K., 2005 *Carbon Capture and Storage: A Regulatory Framework for States*. *Interstate Oil and Gas Compact Commission IOGCC*: Oklahoma. p. 1-80.
23. Castillo, R., 2009, *Technical evaluation of CO2 compression and purification in CCS power plants.* Fourth International Conference on Clean Coal Technologies Dresden, Germany, 18–21 May. p. 1-25.
24. Cosham, A., 2009, *CO_2: "It's a gas, Jim, but not as we Know it". Pipeline Technology Conference*. p. 1-16.
25. Doctor, R., A. Palmer, D. Coleman, J. Davison, C. Hendriks, O. Kaarstad, M. Ozaki, and M. Austell. 2005 *Chapter 4: Transport of CO_2,* in *IPCC Spccial Report on Carbon Dioxide Capture and Storage*, R. Pichs-Madruga and S. Timashev, Editors, Cambridge University Press: Cambridge.
26. Eldevik, F., 2008 *Safe Pipeline Transmission of CO_2. Pipeline & Gas Journal*. **235**(11): p. 76-77.
27. Heggum, G., T. Weydahl, R. Mo, M. Molinvik, and A. Austegaard. 2005 *CO_2 Conditioning and Transportation*, in *Carbon Dioxide Capture for Storage in Deep Geological Formations*, D.C. Thomas and S.M. Benson, Editors, Elsevier Ltd. p. 925-936.
28. Mazzoldi, A., T. Hill, and J.J. Colls, 2011, *Assessing the risk for CO_2 transportation within CCS projects, CFD modelling. International Journal of Greenhouse Gas Control*. **In Press, Corrected Proof**.
29. Nimtz, M., M. Klatt, B. Wiese, M. Kühn, and H. Joachim Krautz, 2010, *Modelling of the CO_2 process- and transport chain in CCS systems--Examination of transport and storage processes. Chemie der Erde - Geochemistry*. **70**(Supplement 3): p. 185-192.
30. Workman, M., N. McGlashan, H. Chalmers, and N. Shah, 2011, *An assessment of options for CO_2 removal from the atmosphere. Energy Procedia*. **4**: p. 2877-2884.
31. Raine, A., 2008, *Transboundary Transportation of CO_2 Associated with Carbon Capture and Storage Projects: An Analysis of Issues under International Law CCLR The Carbon & Climate Law Review*. **2**(4): p. 353-365.
32. Barrie, J., K. Brown, P. Hatcher, and H. Schellhase, 2004, *Carbon dioxide pipelines: A preliminary review of design and risks.* Greenhouse Gas Control Technologies. **7**: p. 315-320.
33. Eldevik, F., B. Graver, L.E. Torbergsen, and O.T. Saugerud, 2009, *Development of a Guideline for Safe, Reliable and Cost Efficient Transmission of CO_2 in Pipelines. Energy Procedia*. **1**(1): p. 1579-1585.

34. Seevam, P.N., J.M. Race, M.J. Downie, and P. Hopkins, 2008, *Transporting the Next Generation of CO[sub 2] for Carbon, Capture and Storage: The Impact of Impurities on Supercritical CO2 Pipelines*. ASME Conference Proceedings. **2008**(48579): p. 39-51.
35. Race, J., 2006 *Designing a Safe Carbon Dioxide Transport Infrastructure for the UK*. Presentation to CCSA – 24th July 2006 Newcastle University.
36. Cabral, M.A. and M.J. Kimber, 1997, *PIPELINE FRACTURE EXPERIENCES IN AUSTRALIA AND NORTH AMERICA.* Pipeline Fracture Experience. **3**: p. 21.
37. Brown, S.F., 2011 *CFD Modelling of Outflow and Ductile Fracture Propagation in Pressurised Pipelines*, in *Department of Chemical Engineering*. University College London: London. p. 227.
38. Rudland, D.L., G.M. Wilkowski, S. Kawaguchi, and N. Hagiwara, 2005, *Determination of Conditional Probability of Dynamic Ductile Axial Crack Arrest for Conventionally-Rolled, Lower-Toughness Linepipe Materials. Journal of Pressure Vessel Technology*. **vol. 127**(no. 2): p. 143-150.
39. Leis, B. and R. Eiber, 1998, *Relationship Between Apparent Charpy V-Notch Toughness and the Corresponding Dynamic Crack-Propagation Resistance.* International Pipeline Conference, Calgary, Alberta, Canada.
40. Rothwell, A., 1997, *Fracture propagation control measures for gas pipelines. In: Proceedings of international seminar on fracture control in gas pipelines.* WTIA, Sydney, Australia. **part. 6–1. ISBN 0 909539-73-1.**
41. Carbon Storage Taskforce, 2009 *National Carbon Mapping and Infrastructure Plan – Australia*. Full Report, Department of Resources, Energy and Tourism Canberra.
42. Zhuang, Z. and P.E. O'Donoghue, 2000, *The recent development of analysis methodology for rapid crack propagation and arrest in gas pipelines. International Journal of Fracture*. **Vol. 101**: p. 269-290.
43. Rudland, D., D.J. Shim, H. Xu, D. Rider, P. Mincer, D. Shoemaker, and G. Wilkowski, 2007 *FIRST MAJOR IMPROVEMENTS TO THE TWO CURVE DUCTILE FRACTURE MODEL PART I MAIN BODY*. U.S. Department of Transportation Research and Special Programs Administration Washington DC 20590 and Pipeline Research Council International, Inc. Arlington, VA 22209. p. 300.
44. 1981 *Final Report on the Test Program at the Northern Alberta Burst Test Facility*. Foothills Pipe Lines (Yukon) Ltd. : Calgary, Alberta, Canada.
45. Andrews, R.M., N.A. Millwood, A.D. Batte, and B.J. Lowesmith. 2004, *The fracture arrest behaviour of 914 mm diameter X100 grade steel pipelines*. in *IPC 2004*: ASME.
46. Eiber, B., L. Carlson, B. Leis, and A. Gilroy-Scott, 1999 *Full-scale tests confirm pipe toughness for North American pipeline*, in *Oil & Gas Journal*. PennWell Corporation: United States, Tulsa. p. 48-54.
47. Eiber, R. and L. Carlson. 2000, *Fracture control for the alliance pipeline*. in *ASME International pipeline conference IPC-2000*. Calgary, Alberta, Canada
48. Eiber, R.J. and W.A. Maxey, 1977, *Full-scale experimental investigation of ductile fracture behavior in simulated arctic pipeline.* Materials Engineering in the Arctic , Proceedings of Int. Conf., St. Jovite, Quebec, Canada, Sept 27-Oct 1, 1976, also Canadian Arctic Gas Study Limited (CAGSL), Engineering in the Arctic/ASM, St. Jovite, Quebec,.

49. Groves, T.K., P.R. Bishnoi, and J.M.E.W. allbridge, 1978, *Decompression Wave Velocities In Natural Gases In Pipe Lines. Canadian Journal of Chemical Engineering*. **56**(1): p. 664-668.
50. Igi, S., S. Kawaguchi, and N. Suzuki, 2009 *Running ductile fracture analysis for X80 pipeline in JGA burst tests*, in *Pipeline Technology Conference*: Oct 12-14, Ostend, Belgium.
51. Kawaguchi, S., N. Hagiwara, T. Masuda, C. Christensen, H. Nielsen, P. Ludwigsen, D. Rudland, and G. Wilkowski. 2004, *Application of X80 in Japan: fracture control*. in *4th International Conference On Pipeline Technology, Ostend. Belgium*.
52. Makino, H., I. Takeuchi, and R. Higuchi. 2008, *Fracture Propagation and Arrest in High-Pressure Gas Transmission Pipeline by Ultra High Strength Line Pipes*. in *7th International Pipeline Conference, IPC2008*. Calgary, Alberta, Canada: ASME.
53. Kawaguchi, S., K. Murai, Y. Hashimoto, N. Hagiwara, H. Yajima, and M. Toyoda. 2008, *Full-scale burst tests of ultra-high pressured rich-gas pipelines under buried and unburied conditions*. in *Proceedings of IPC 2008 7th International Pipeline Conference*. Calgary, Alberta, Canada.: ASME.
54. Botros, K.K., E.H. Jr, and P. Craidy, 2013b, *Measuring decompression wave speed in CO2 mixtures by a shock tube.* Pipelines International. (16).
55. Cosham, A., D.G. Jones, K. Armstrong, D. Allason, and J. Barnett. 2012a, *The Decompression Behaviour oF Carbon Dioxide in The Densephase*. in *Proceedings of the 2012 9th International Pipeline Conference*. Calgary, Alberta, Canada: ASME.
56. Cosham, A., D.G. Jones, K. Armstrong, D. Allason, and J. Barnett. 2012b, *RUPTURES IN GAS PIPELINES, LIQUID PIPELINES AND DENSE PHASE CARBONDIOXIDE PIPELINES*. in *Proceedings of the 2012 9th International Pipeline Conference*. Calgary, Alberta, Canada: ASME.
57. Botros, K.K., J. Geerligs, A. Glover, and B. Rothwell, 2001, *Expansion tube for determination of the decompression wave speed for dense/Rich gases at initial pressures of up to 22 Mpa.* International Gas Research Conference (IGRC), Amsterdam, The Netherlands, November 5–8.
58. Botros, K.K., J. Geerligs, L. Fletcher, B. Rothwell, P. Venton, and L. Carlson, 2010d, *Effects of Pipe Internal Surface Roughness on Decompression Wave Speed in Natural Gas Mixtures.* ASME Conference Proceedings. **2010**(44212): p. 907-922.
59. Botros, K.K., J. Geerligs, J. Zhou, and A. Glover, 2007, *Measurements of flow parameters and decompression wave speed following rupture of rich gas pipelines, and comparison with GASDECOM. International Journal of Pressure Vessels and Piping*. **84**(6): p. 358-367.
60. Botros, K.K., J. Geerligs, B. Rothwell, L. Carlson, L. Fletcher, and P. Venton, 2010b, *Transferability of decompression wave speed measured by a small-diameter shock tube to full size pipelines and implications for determining required fracture propagation resistance. International Journal of Pressure Vessels and Piping*. **87**(12): p. 681-695.
61. Phillips, A.G. and C.G. Robinson, 2005 *Gas Decompression Behavior following the Rupture of High Pressure Pipelines – Phase 2: Modeling Report, PRCI Contract PR-273-0135*.
62. Botros, K.K., J. Geerligs, and R.J. Eiber, 2010a, *Measurement of Decompression Wave Speed in Rich Gas Mixtures at High Pressures (370*

bars) Using a Specialized Rupture Tube. Journal of Pressure Vessel Technology. **vol. 132**(no. 5): p. 051303-15.
63. Eiber, R., T. Bubenik, and W. Maxey, 1993 *GASDECOM, computer code for the calculation of gas decompression speed that is included in fracture control technology for natural gas pipelines. NG-18 Report 208*. American Gas Association Catalog.
64. Starling, K.E. and J.E. Powers, 1970, *Enthalpy of Mixtures by Modified BWR Equation.* Industrial & Engineering Chemistry Fundamentals. **9**(4): p. 531-537.
65. Hopke, S.W. and C.J. Lin, 1974 *Application of BWRS Equation to Natural Gas Systems*, in *76'h National AIChE Meeting, American Institute of Chemical Engineers*: Tulsa, Oklahoma, USA.
66. Phillips, A.G. and C.G. Robinson, 2002 *Gas decompression behavior following the rupture of high pressure pipelines - Phase 1, PRCI Contract PR-273-0135*. *Pipeline Research Council International, Inc.* p. 1-52.
67. Johnson, D.M., P.S. Cumber, N. Horner, L. Carlson, and R. Eiber. 2000, *Full-Scale Fracture Propagation Experiments: A Recent Application and Future Use for the Pipeline Industry*. in *Proceedings of the ASME International Pipeline Conference*. Calgary, Alberta Canada: ASME.
68. Gibbons, R.M. and A.P. Laughton, 1984, *An equation of state for polar and non-polar substances and mixtures.* Journal of the Chemical Society, Faraday Transactions 2: Molecular and Chemical Physics. **80**(9): p. 1019-1038.
69. Redlich, O. and J.N.S. Kwong, 1949, *On the Thermodynamics of Solutions. V. An Equation of State. Fugacities of Gaseous Solutions.* Chemical Reviews. **44**(1): p. 233-244.
70. Peng, D.-Y. and D.B. Robinson, 1976, *A New Two-Constant Equation of State.* Industrial & Engineering Chemistry Fundamentals. **15**(1): p. 59-64.
71. Soave, G., 1972, *Equilibrium constants from a modified Redlich-Kwong equation of state.* Chemical Engineering Science. **27**(6): p. 1197-1203.
72. Jones, D.G. and D.W. Gough, 1981, *Rich Gas Decompression Behaviour in Pipelines.* AGA-EPRG Linepipe Research Seminar IV, Duisburg.
73. Makino, H., T. SUGIE, T. KUBO, T. SHIWAKU, S. ENDO, T. INOUE, Y. KAWAGUCHI, Y. MATSUMOTO, and S. MACHIDA, 2001, *Natural Gas Decompression Behavior in High Pressure Pipelines.* ISIJ Int (Iron Steel Inst Jpn). **41**(4): p. 389-395.
74. Qiu, W., J. Gong, and J. Zhao, 2011, *A Study on Natural Gas Decompression Behavior. Petroleum Science and Technology*. **vol. 29**(no. 1): p. pp29 - 38.
75. Xu, X.-X. and J. Gong, 2008, *A united model for predicting pressure wave speeds in oil and gas two-phase pipeflows.* Journal of Petroleum Science and Engineering. **60**(3–4): p. 150-160.
76. Lemmon, E.W., M.L. Huber, and M.O. McLinden, 2010 *NIST Standard Reference Database 23: Reference Fluid Thermodynamic and Transport Properties-REFPROP*. National Institute of Standards and Technology: Gaithersburg.
77. Span, R. and W. Wagner, 1996, *A New Equation of State for Carbon Dioxide Covering the Fluid Region from the Triple-Point Temperature to 1100 K at Pressures up to 800 MPa. ISSN*. **25**(6): p. 1509-1596.
78. Kunz, O., R. Klimeek, W. Wagner, and M. Jaeschke, 2007 *The GERG-2004 Wide-Range Equation of State for Natural Gases and Other Mixtures-GERG Technical Monograph 15*. Groupe Européen de Recherches Gazières.

79. Picard, D.J. and P.R. Bishnoi, 1988, *The Importance of Real-Fluid Behavior and Nonisentropic Effects in Modeling Decompression Characteristics of Pipeline Fluids for Application in Ductile Fracture Propagation Analysis. THE CANADIAN JOURNAL OF CHEMICAL ENGINEERING*. **66**(1): p. 3-12.
80. Picard, D.J. and P.R. Bishnoi, 1989, *The Importance of Real-Fluid Behavior in Predicting Release Rates Resulting From High-Pressure Sour-Gas Pipeline Ruptures. THE CANADIAN JOURNAL OF CHEMICAL ENGINEERING*. **67**(1): p. 3-9.
81. Mahgerefteh, H., S. Brown, and G. Denton, 2012, *Modelling the impact of stream impurities on ductile fractures in CO2 pipelines.* Chemical Engineering Science. **74**(0): p. 200-210.
82. Mahgerefteh, H., S. Brown, and S. Martynov, 2012, *A study of the effects of friction, heat transfer, and stream impurities on the decompression behavior in CO2 pipelines.* Greenhouse Gases: Science and Technology. **2**(5): p. 369-379.
83. Jie, H.E., B.P. Xu, J.X. Wen, R. Cooper, and J. Barnett. 2012, *Predicting The Decompression Characteristics of Carbon Dioxide Using Computational Fluid Dynamics*. in *Proceedings of the 2012 9th International Pipeline Conference*. Calgary, Alberta, Canada ASME.
84. Lu, C., G. Michal, A. Elshahomi, A. Godbole, P. Venton, K.K. Botros, L. Fletcher, and B. Rothwell. 2012, *Investigating The Effects of Pipe Wall Roughness and Pipe Diameter on The decompression Wave Speed in Natural Gas Pipelines*. in *9th International Pipeline Conference 2012*. Calgary, Alberta, Canada: ASME.
85. Botros, K.K., L. Carlson, and M. Reed, 2013a, *Extension of the semi-empirical correlation for the effects of pipe diameter and internal surface roughness on the decompression wave speed to include High Heating Value Processed Gas mixtures.* International Journal of Pressure Vessels and Piping. **107**: p. 12-17.
86. Botros, K.K., B. Rothwell, L. Carlson, and P. Venton, 2012 *Semi-Empirical Correlation to Quantify the Effects of Pipe Diameter and Internal Surface Roughness on the Decompression Wave Speed in Natural Gas Mixtures* in *9th International Pipeline Conference IPC2012*. ASME: ,Calgary, Alberta, Canada
87. Chen, J.R., S.M. Richardson, and G. Saville, 1995, *Modelling of two-phase blowdown from pipelines—II. A simplified numerical method for multi-component mixtures.* Chemical Engineering Science. **50**(13): p. 2173-2187.
88. Bendiksen, K.H., D. Maines, R. Moe, and S. Nuland, 1991, *The Dynamic Two-Fluid Model OLGA: Theory and Application.* SPE Production Engineering. **6**(2): p. 171-180.
89. Zucrow, M.J. and J.D. Hoffman,1976 *Gas Dynamics*. New York: John Wiley and Sons.
90. Mahgerefteh, H., A. Oke, and O. Atti, 2006, *Modelling outflow following rupture in pipeline networks.* Chemical Engineering Science. **61**(6): p. 1811-1818.
91. Mahgerefteh, H., Saha, Pratik, Economou, and I. G., 1999, *Fast numerical simulation for bore rupture of pressurized pipelines.* American Institute of Chemical Engineers. AIChE Journal. **45**(6): p. 1191-1191.

92. Starling, K.E. and J.L. Savidge, 1994 *Compressibility Factors of Natural Gas and Other Related Hydrocarbon Gases*. American Gas Association, Transmission Measurement Committee Report No.8, and American Petroleum Institute, MPMS Chapter 14.2 Second Edition.
93. Savidge, J.L., 2001 *Report to AGA Transmission Measurement Committee Task Group 13 on A.G.A. Report No.10 , Speed of Sound*: 2000 AGA Operations Conference, Marriott, Denver.
94. Ahmed, T. 2010 *CHAPTER 7 - Equations of State*, in *Working Guide to Vapor-liquid Phase Equilibria Calculations*, T. Ahmed, Editor, Gulf Professional Publishing: Boston. p. 59-96.
95. Poling, B.E., J.M. Prausnitz, J.P. O'Connell, and Ebrary,2001 *The properties of gases and liquids*. 5th ed. ed., New York: McGraw Hill Companies 5th ed.
96. Smith, J.M., H.C.V. Ness, and M.M. Abbott,1996 *Introduction to chemical engineering thermodynamics* 5th ed ed. McGraw-Hill chemical engineering series. New York McGraw-Hill 763.
97. Valderrama, J.O., 2003, *The State of the Cubic Equations of State.* Industrial & Engineering Chemistry Research. **42**(8): p. 1603-1618.
98. Wei, Y.S. and R.J. Sadus, 2000, *Equations of state for the calculation of fluid-phase equilibria.* AIChE Journal. **46**(1): p. 169-196.
99. Elshahomi, A., C. Lu, G. Michal, X. Liu, A. Godbole, and P. Venton, 2015, *Decompression wave speed in CO2 mixtures: CFD modelling with the GERG-2008 equation of state.* Applied Energy. **140**: p. 20-32.
100. Benedict, M., G.B. Webb, and L.C. Rubin, 1940, *An Empirical Equation for Thermodynamic Properties of Light Hydrocarbons and Their Mixtures I. Methane, Ethane, Propane and n-Butane* Journal of Chemical Physics **8**(4): p. 12.
101. Morsy, T.E., 1970, *Extended Benedict-Webb-Rubin equation of state. Application to eight fluorine compounds.* Journal of Chemical & Engineering Data. **15**(2): p. 256-265.
102. Mills, M.B., M.J. Wills, and V.L. Bhirud, 1980, *The calculation of density by the BWRS equation of state in process simulation contexts.* AIChE Journal. **26**(6): p. 902-910.
103. Lin, C.J. and S.w. Hopke, 1973 *Application of the BWRS Equation to Methane, Ethane, Propane and Nitrogen systems*, in *75'h National AIChE Meeting, American Institute of Chemical Engineers*: New Orleans, Louisiana, USA.
104. Sander, S.I.,1999 *Chemical and engineering thermodynamics*. third ed., New Yourk: Wiley.
105. Wagner, W., 2009 *Description of the Software Package for the Calculation of Thermodynamic Properties from the GERG-2004 XT08 Wide-Range Equation of State for Natural Gases and Other Mixtures*. Ruhr-Universitat Bochum. p. pp.76.
106. Kunz, O. and W. Wagner, 2012, *The GERG-2008 Wide-Range Equation of State for Natural Gases and Other Mixtures: An Expansion of GERG-2004.* Journal of Chemical & Engineering Data. **57**(11): p. 3032-3091.
107. Picard, D.J. and P.R. Bishnoi, 1987, *Calculation of the thermodynamic sound velocity in two-phase multicomponent fluids.* International Journal of Multiphase Flow. **13**(3): p. 295-308.
108. Li, H., J.P. Jakobsen, Ø. Wilhelmsen, and J. Yan, 2011, *PVTxy properties of CO2 mixtures relevant for CO2 capture, transport and storage: Review of*

available experimental data and theoretical models. Applied Energy. **88**(11): p. 3567-3579.
109. Patel, N.C. and A.S. Teja, 1982, *A new cubic equation of state for fluids and fluid mixtures.* Chemical Engineering Science. **37**(3): p. 463-473.
110. Yu, J.-M., B.C.Y. Lu, and Y. Iwai, 1987, *Simultaneous calculations of VLE and saturated liquid and vapor volumes by means of a 3P1T cubic EOS.* Fluid Phase Equilibria. **37**(0): p. 207-222.
111. Ely, J.F., J.W. Magee, and W.M. Haynes, 1987 *CO2PAC, Program*. available at the NatL Bur. Stand: Boulder, Colorado.
112. Anguus, S., B. Armstrong, and K.M. de Reuck,1976 *International Thermodynamic Tables of the Fluid State - 3 Carbon Dioxide*. Pergamon, New York.
113. Duschek, W., R. Kleninrahm, W. Wanger, and J. Chem,1990 *Thermodyn. 22, 841*.
114. Gilgen, R., R. Kleinrahm, W. Wanger, and J. chem,1992 *Thermodyn. 24, 1943*.
115. Pitzer, K.S. and D.R. Schreiber, 1988, *Improving equation-of-state accuracy in the critical region; equations for carbon dioxide and neopentane as examples.* Fluid Phase Equilibria. **41**(1–2): p. 1-17.
116. Chen, Z.Y., A. Abbaci, S. Tang, and J.V. Sengers, 1990, *Global thermodynamic behavior of fluids in the critical region.* Physical Review A. **42**(8): p. 4470-4484.
117. Novikov, I.I. and Y.S. Trelin, 1962 *Teploenergetica 9, 2, 79*.
118. Botros, K.K., 2010c, *Measurements of Speed of Sound in Lean and Rich Natural Gas Mixtures at Pressures up to 37 MPa Using a Specialized Rupture Tube.* International Journal of Thermophysics. **31**(11): p. 2086-2102.
119. Munkejord, S.T., J.P. Jakobsen, A. Austegard, and M.J. Mølnvik, 2010, *Thermo- and fluid-dynamical modelling of two-phase multi-component carbon dioxide mixtures.* International Journal of Greenhouse Gas Control. **4**(4): p. 589-596.
120. Lemmon, E.W., M.L. Huber, and M. Mclinden, 2007, *NIST Standard Reference Database 23: Reference Fluid Thennodynamie and Transport Properties-REFPROP, Version 8.0, National Institute of Standards andTechnology, Standard Reference Data Program, Gaithersburg.*
121. Stryjek, R. and J.H. Vera, 1986, *PRSV: An improved peng—Robinson equation of state for pure compounds and mixtures.* THE CANADIAN JOURNAL OF CHEMICAL ENGINEERING. **64**(2): p. 323-333.
122. Baudouin, O., S. Dechelotte, P. Guittard, and A. Vacher. 2008 *Simulis® Thermodynamics: an open framework for users and developers*, in *Computer Aided Chemical Engineering*, B. Bertrand and J. Xavier, Editors, Elsevier. p. 635-640.
123. Lemmon, E.W., M.L. Huber, and M.O. McLinden, 2013 *NIST Standard Reference Database 23: Reference Fluid Thermodynamic and Transport Properties-REFPROP, Version 9.1*.
124. Seevam, P., J. Race, M. Downie, J. Barnett, and R. Cooper. 2010, *Capturing Carbon Dioxide: The Feasibility of Re-Using Existing Pipeline Infrastructure to Transport Anthropogenic CO2*. in *8th International Pipeline Conference IPC2010*. Calgary, Alberta, Canada: ASME.

125. Magee, J. and J. Ely, 1988, *Isochoric (p, v, T) measurements on CO2 and (0.98 CO2+ 0.02 CH4) from 225 to 400 K and pressures to 35 MPa.* International Journal of Thermophysics. **9**(4): p. 547-557.
126. Herget, C.M., 1940, *Ultrasonic velocity in carbon dioxide and ethylene in the critical region.* The Journal of Chemical Physics. **8**(7): p. 537-542.
127. Brugge, H.B., J.C. Holste, K.R. Hall, B.E. Gammon, and K.N. Marsh, 1997, *Densities of Carbon Dioxide + Nitrogen from 225 K to 450 K at Pressures up to 70 MPa.* Journal of Chemical & Engineering Data. **42**(5): p. 903-907.
128. Muirbrook, N.K., 1964 *Experimental and thermodynamic study of the high-pressure vapor-liquid equilibria for the nitrogen-oxygen-carbon dioxide system*: Berkeley-California.
129. Arai, Y., G.-I. Kaminishi, and S. Saito, 1971, *The experimental determination of the p-v-t-x relations for the carbon dioxide-nitrogen and the carbon dioxide-methane systems.* Journal of Chemical Engineering of Japan. **4**(2): p. 113-122.
130. Mallu, B.V. and D.S. Viswanath, 1990, *Compression factors and second virial coefficients of H2, CH4, {xCO2 + (1 − x)H2}, and {xCO2 + (1 − x)CH4}.* The Journal of Chemical Thermodynamics. **22**(10): p. 997-1006.
131. Sarashina, E., Y. Arai, and S. Sasato, 1971, *The PVTX relation for the carbon dioxide-argon system.* Journal of Chemical Engineering of Japan. **4**(4): p. 379-381.
132. Mallu, B.V., G. Natarajan, and D.S. Viswanath, 1989, *(p, Vm, T, x) and virial coefficients of {xCO2 + (1 − x)CO}.* The Journal of Chemical Thermodynamics. **21**(9): p. 989-996.
133. Stouffer, C.E., S.J. Kellerman, K.R. Hall, J.C. Holste, B.E. Gammon, and K.N. Marsh, 2001, *Densities of Carbon Dioxide + Hydrogen Sulfide Mixtures from 220 K to 450 K at Pressures up to 25 MPa.* Journal of Chemical & Engineering Data. **46**(5): p. 1309-1318.
134. ANSYS, 2010, *ANSYS Fluent 13.0 Getting Started Guide.* (13.0): p. viii, 18.
135. Brid, R.B., W.E. Stewart, and E.N. Lightfoot,1960 *Transport Phenomena*. New York: John Wiley & Sons
136. ANSYS, 2010 *ANSYS Fluent 13.0 Theory Guide* p. xxviii, 720.
137. Kay, J.M. and R.M. Nedderman,1985 *Fluid Mechanics and Transfer Processes*: Cambridge University Press.
138. Versteeg, H.K. and W. Malalasekera,2007 *An introduction to computational fluid dynamics : the finite volume method* 2nd ed., New York: Pearson Education Ltd.
139. ANSYS/Fluent, 2010, *ANSYS Fluent user's Guide.* p. 2334.
140. Tóth, P., A. Fritzsch, and M. Lohász. 2008, *Application of computational fluid dynamics softwares for 2d acoustical wave propagation*. in *Proceedings of Gépészet 2008 Conference*
141. BARTH, T. and D. JESPERSEN. 1989, *The design and application of upwind schemes on unstructured meshes*. in *AIAA, Aerospace Sciences Meeting, 27 th, Reno, NV*.
142. Liou, M.S., 1996, *A sequel to AUSM: AUSM+*. Journal of Computational Physics. **129**(2): p. 364-382.
143. Roe, P.L., 1986, *Characteristic based schemes for the Euler equations.* Annual Review of Fluid Mechanics. **18**: p. 337–365.

144. Spalart, P. and S. Allmaras, 1992 *A one-equation turbulence model for aerodynamic flows. Technical Report AIAA-92-0439*. American Institute of Aeronautics and Astronautics.
145. Launder, B.E. and D.B. Spalding, 1974, *The numerical computation of turbulent flows.* Computer Methods in Applied Mechanics and Engineering. **3**(2): p. 269-289.
146. Yakhot, V. and S.A. Orszag, 1986, *Renormalization group analysis of turbulence. I. Basic theory.* Journal of scientific computing. **1**(1): p. 3-51.
147. Shih, T.-H., W.W. Liou, A. Shabbir, Z. Yang, and J. Zhu, 1995, *A new k-ε eddy viscosity model for high reynolds number turbulent flows.* Computers & Fluids. **24**(3): p. 227-238.
148. Nikuradse, J., 1937 *Laws of flow in rough pipes*. NACA Tech. Mem. 1292: Washington.
149. Adams, T., C. Grant, and H. Watson, 2012, *A Simple Algorithm to Relate Measured Surface Roughness to Equivalent Sand-grain Roughness.* International Journal of Mechanical Engineering and Mechatronics. **1**(2): p. 66-71.
150. Wagner, W., 2009 *Description of the Software Package for the Calculation of Thermodynamic Properties from the GERG-2004 XT08 Wide-Range Equation of State for Natural Gases and Other Mixtures*. RUHR-UNIVERSITÄT BOCHUM. p. 76.
151. Çengel, Y.A. and M.A. Boles,2011 *Thermodynamics: an engineering approach*. McGraw-Hill series in mechanical engineering. New York: McGraw-Hill Higher Education. xxxvi, 988 p.
152. Cheremisinoff, N.P.,1984 *Fluid flow pocket handbook*. Houston, Tex.: Gulf Pub. Co., Book Division. xii, 199 p.
153. Eckert, E.R.G. and R.M. Drake,1971 *Analysis of heat and mass transfer*. McGraw-Hill series in mechanical engineering. New York: McGraw-Hill. xxi, 806 p.
154. Klimeck, R., R. Span, R. Kleinrahm, and W. Wagner, 1996 *Fundamental equation for calorific properties. Collecting of data and test of existing equations. Final report to GERG WG 1.3, Lehrstuhl für Thermodynamik*. Ruhr-Universität Bochum.
155. ADLER, S.B., C.F. SPENCER, H. OZKARDESH, and C.-M. KUO. 1977 *Industrial Uses of Equations of State: A State-of-the-Art Review*, in *Phase equilibria and fluid properties in the chemical industry estimation and correlation: a symposium*, T.S. Storvick and S.I. Sandler, Editors, AMERICAN CHEMICAL SOCIETY. p. pp. 150-199.
156. Andresen, T. and G. Skaugen. 2007, *Lookup Tables Based on Gibb's Free Energy for Quick and Accurate Calculation of Thermodynamic Properties for CO_2*. in *22nd International Congress of Refrigeration : Refrigeration creates the future*. Beijing: International Institute of Refrigeration.
157. Mahgerefteh, H., O. Atti, and G. Denton, 2007, *An Interpolation Technique for Rapid CFD Simulation of Turbulent Two-Phase Flows.* Process Safety and Environmental Protection. **85**(1): p. 45-50.
158. Botros, K.K., J. Geerligs, and R. Given, 2004 *Decompression Response of High-Pressure Natural Gas Pipelines Under Rupture or Blowdown Conditions*. Pipeline Research Council International, Inc.

159. Freund, L.B., D.M. Parks, and J.R. Rice. 1976 *Running ductile fracture in a pressurized line pipe*, in *Mechanics of crack growth, ASTM STP 590, American Society for testing and Materials* Philadelphia. p. 243-262.
160. Parks, D. and L. Freund, 1978, *On the gasdynamics of running ductile fracture in a pressurized line pipe.* Journal of Pressure Vessel Technology. **100**(1): p. 13-17.
161. Misawa, K., y. Imai, and S. Aihara. 2010, *A new Model For Dynamic Crack Propagation and Arrest in Gas Pipelines*. in *The 8th International Pipeline Conference IPC2010*. Calgary, Alberta, Canada: ASME.
162. Aursand, E., P. Aursand, T. Berstad, C. Dørum, M. Hammer, S.T. Munkejord, and H.O. Nordhagen, 2013, *CO2 pipeline integrity: A coupled fluid-structure model using a reference equation of state for CO2*. Energy Procedia. p. 1-10.
163. O'Donoghue, P.E., M.F. Kanninen, C.P. Leung, G. Demofonti, and S. Venzi, 1997, *The development and validation of a dynamic fracture propagation model for gas transmission pipelines. International Journal of Pressure Vessels and Piping*. **vol. 70**(no. 1): p. 11-25.
164. Liou, M.S., 1993, *A new flux splitting scheme*. Journal of Computational Physics. **107**(1): p. 23-39.
165. Shim, D.-J., G. Wilkowski, D. Rudland, B. Rothwell, and J. Merritt. 2008, *Numerical simulation of dynamic ductile fracture propagation using cohesive zone modeling*. in *2008 7th International Pipeline Conference*: American Society of Mechanical Engineers.

APPENDICES

Appendix A: Oxyfuel case study results

Effect of Initial Temperature:

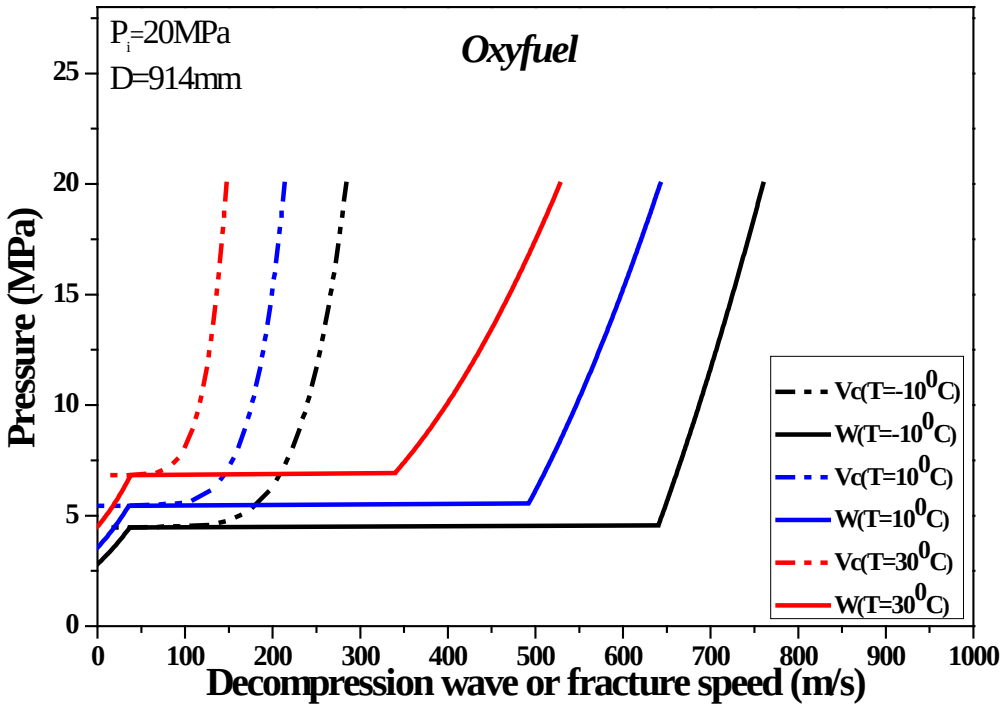

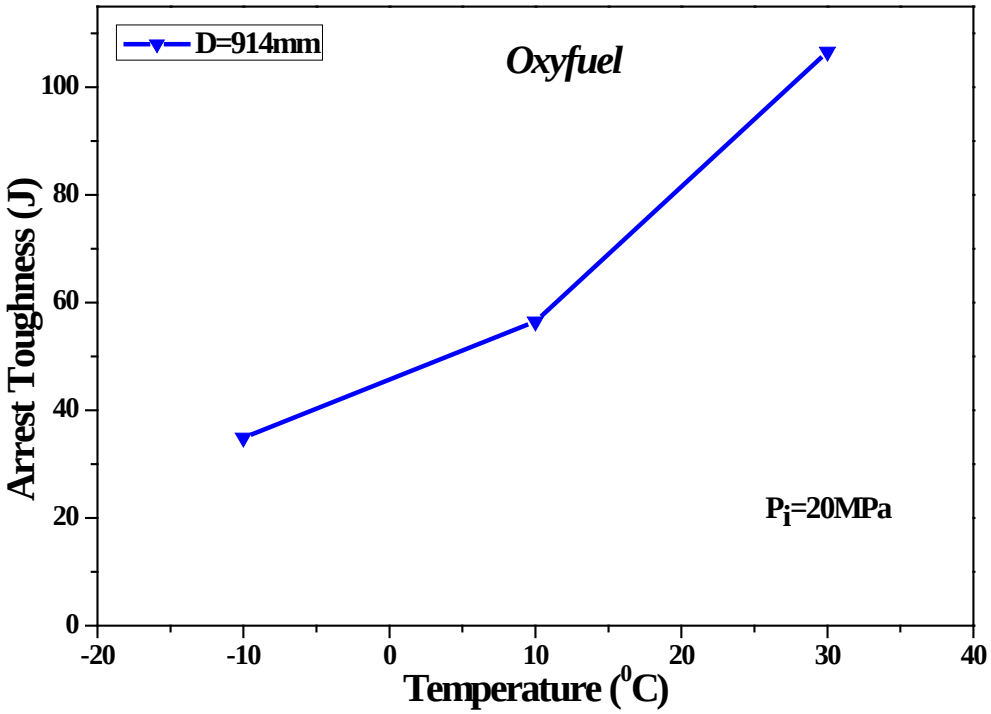

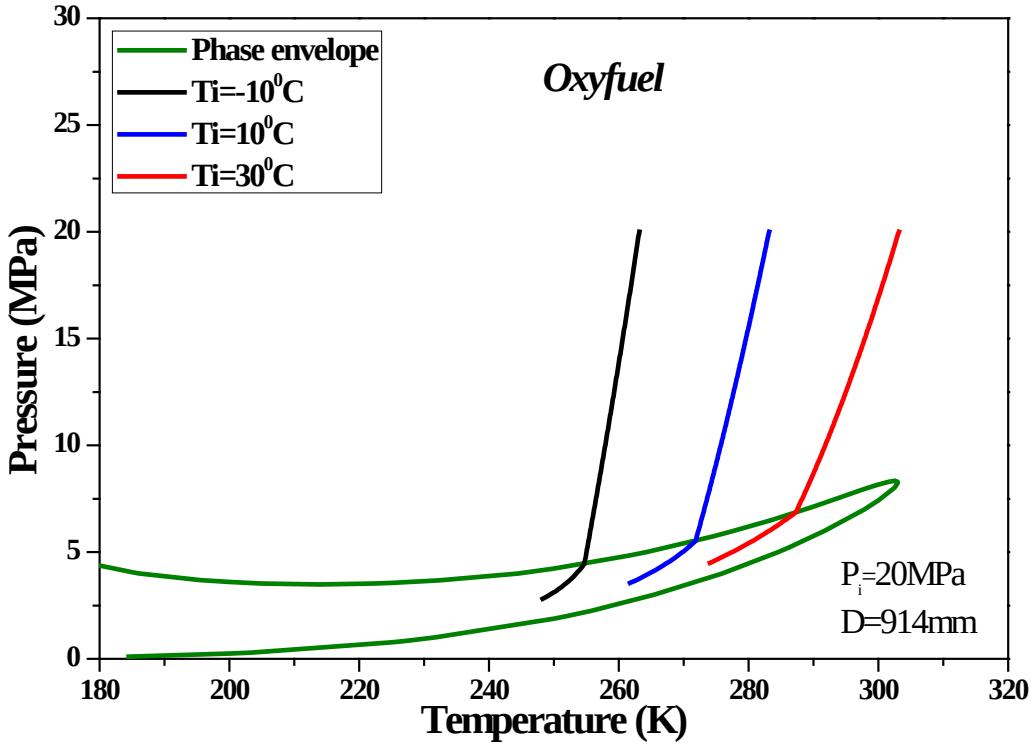

Effect of Initial Pressure:

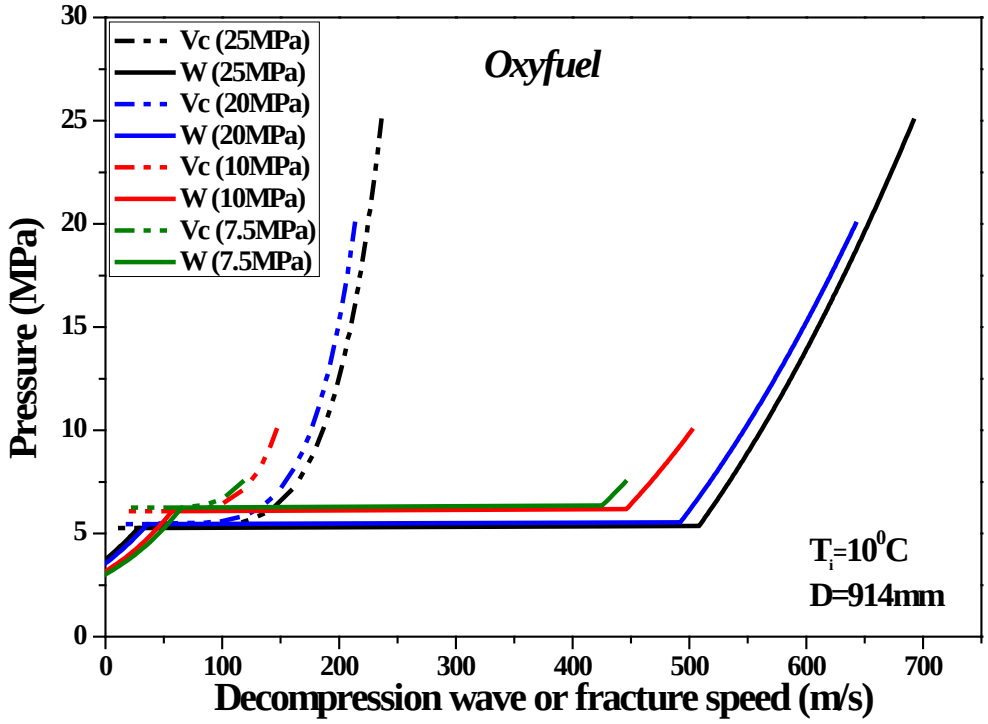

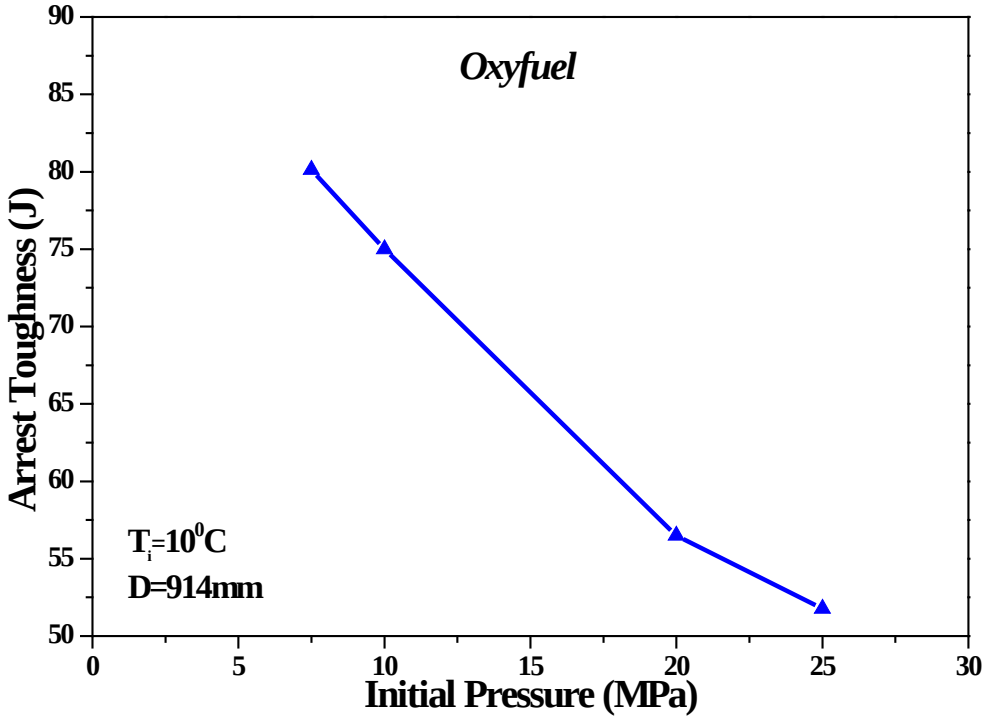

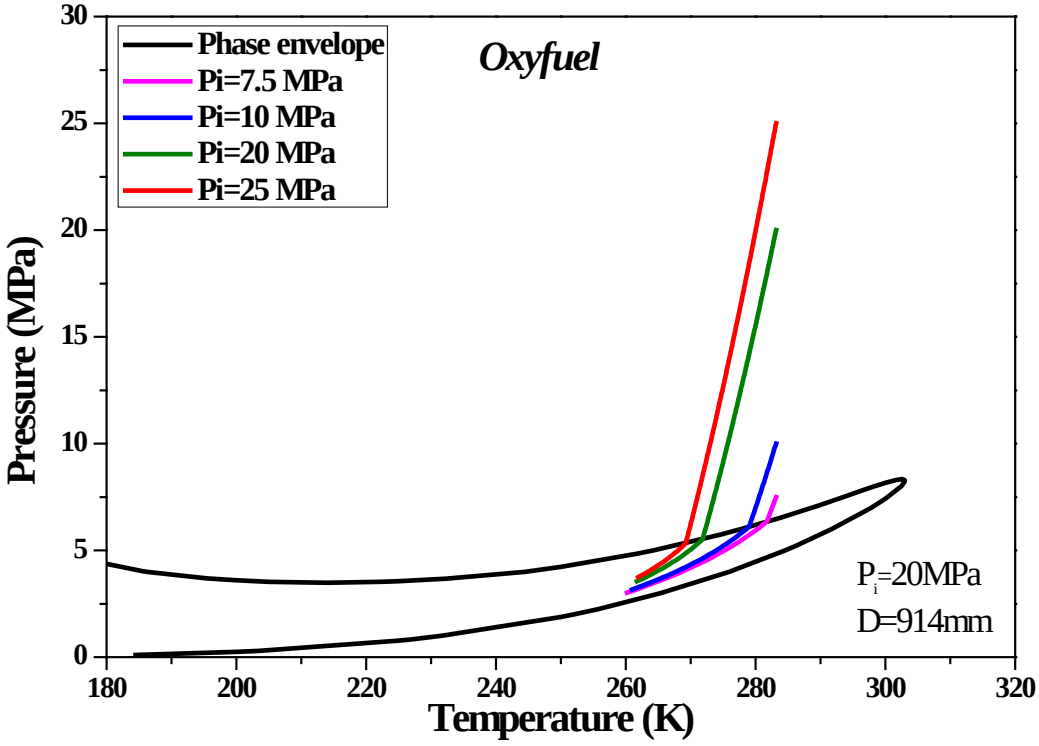

Effect of Diameter:

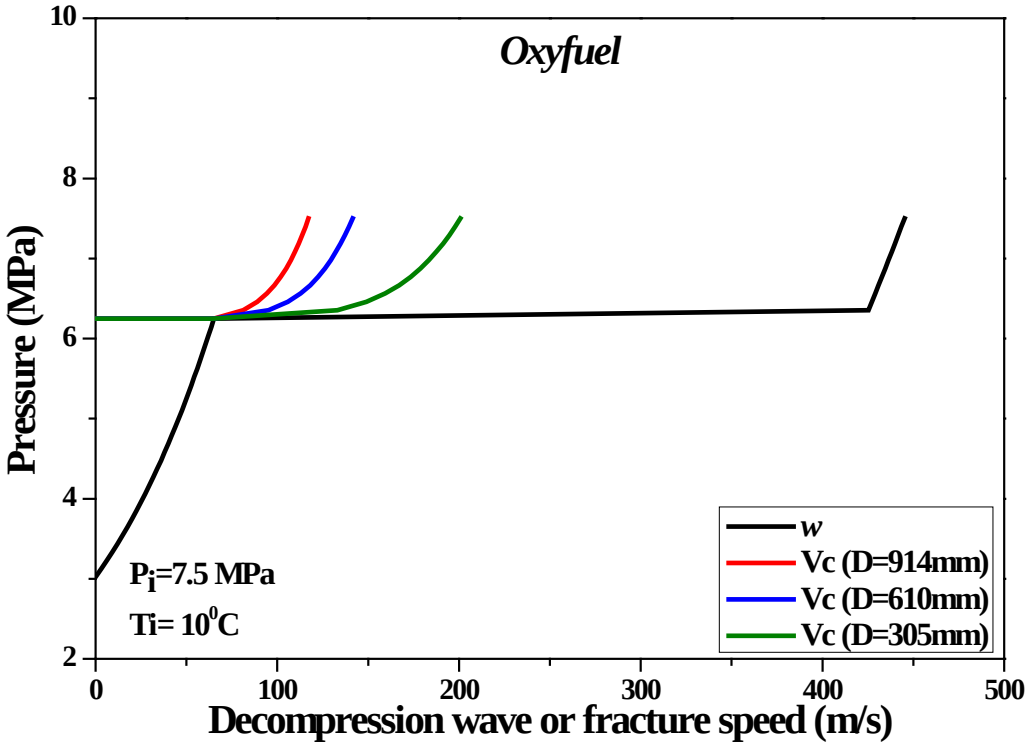
Oxyfuel
Pressure (MPa)
Decompression wave or fracture speed (m/s)
w
Vc (D=914mm)
Vc (D=610mm)
Vc (D=305mm)
Pi=7.5 MPa
Ti= 10⁰C
10
8
6
4
2
0
100
200
300
400
500

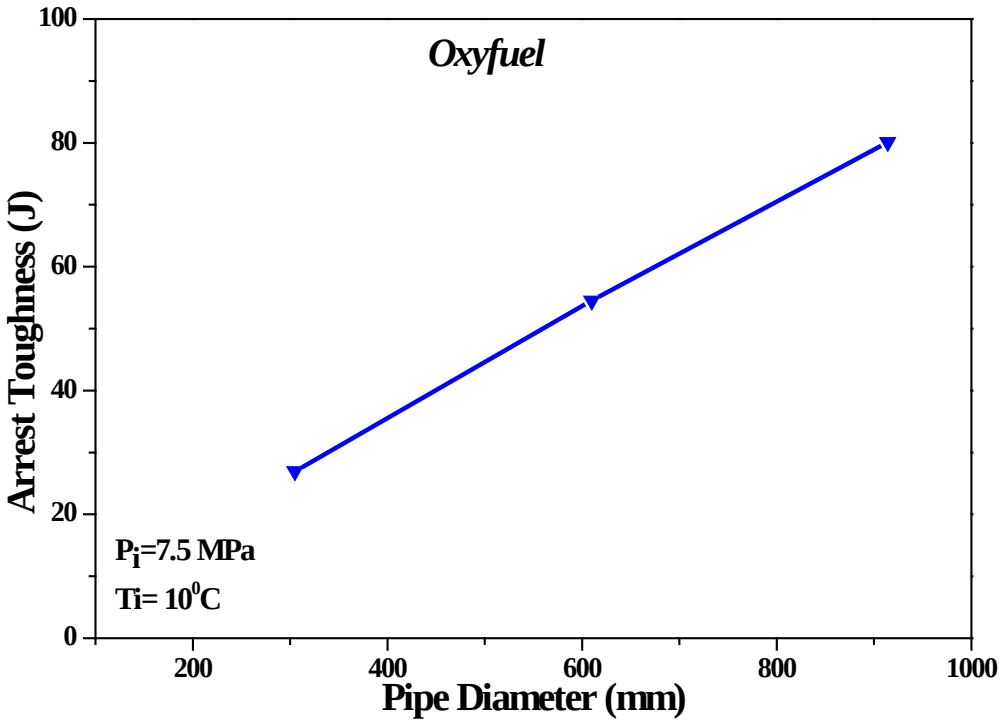
Oxyfuel
Arrest Toughness (J)
Pipe Diameter (mm)
Pi=7.5 MPa
Ti= 10⁰C
100
80
60
40
20
0
200
400
600
800
1000